ISSN 0915-6348

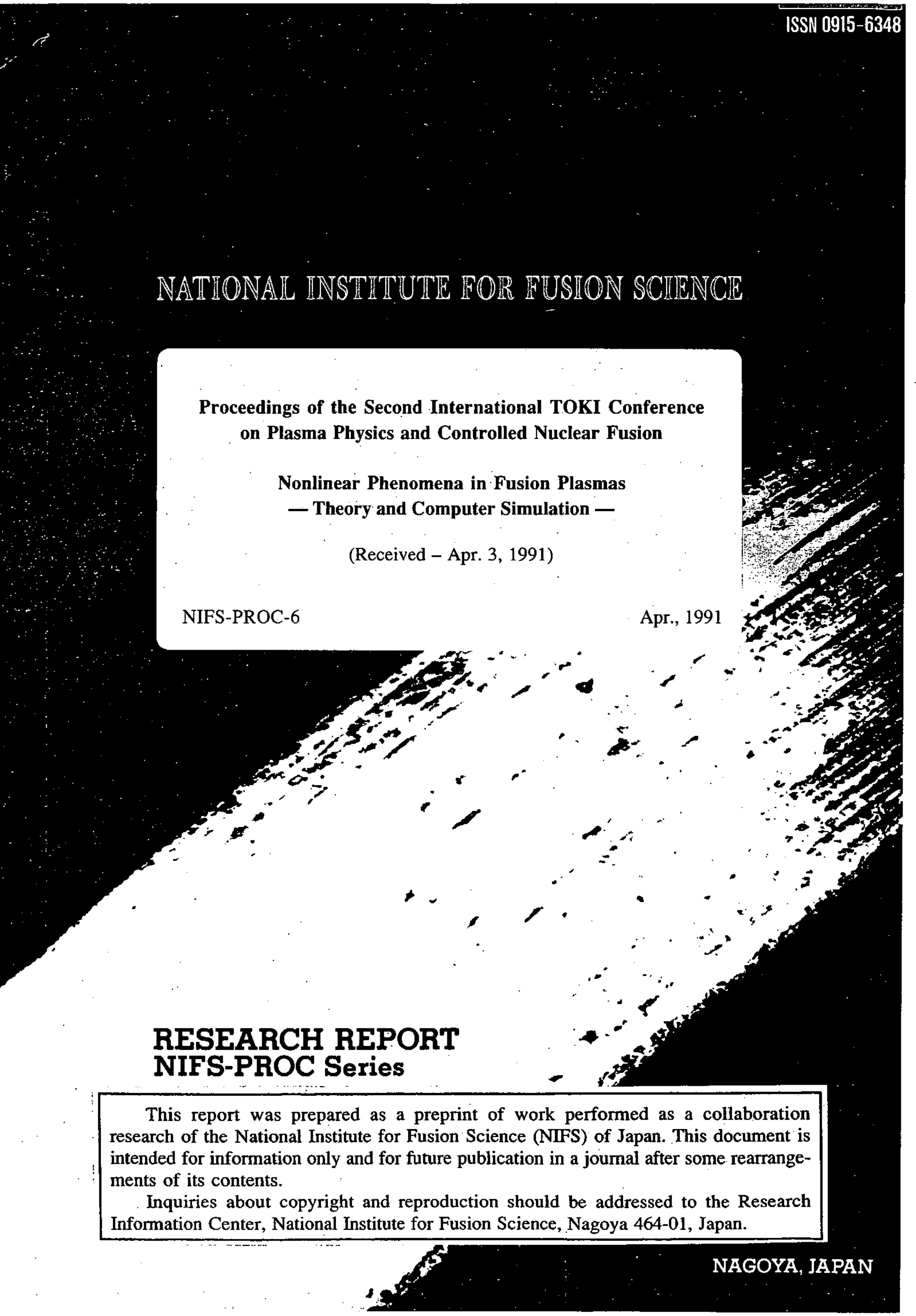

NATIONAL INSTITUTE FOR FUSION SCIENCE

Proceedings of the Second International TOKI Conference on Plasma Physics and Controlled Nuclear Fusion

Nonlinear Phenomena in Fusion Plasmas
— Theory and Computer Simulation —

(Received – Apr. 3, 1991)

NIFS-PROC-6 Apr., 1991

RESEARCH REPORT
NIFS-PROC Series

NAGOYA, JAPAN

PROCEEDINGS of THE SECOND INTERNATIONAL TOKI CONFERENCE
on PLASMA PHYSICS and CONTROLLED NUCLEAR FUSION

NONLINEAR PHENOMENA IN FUSION PLASMAS
— THEORY AND COMPUTER SIMULATION —

November 27-30, 1990
Toki-shi Bunka Plaza, Toki City, Japan

National Institute for Fusion Science
Nagoya 464-01, Japan

Keywords; proceedings, the second international Toki conference,
nonlinear phenomena, fusion plasmas, theory,
computer simulation

CONTENTS

Preface ---------- 1

Session I Keynote lecture

Nonlinear Phenomena and Processes in High Energy Plasmas
B.Coppi (MIT) ---------- 3

Session II MHD Relaxation

Self-Organizing Processes in Magnetically Confined Plasma
T.Sato (NIFS) ---------- 8
Current Sheet Formation and Rapid Reconnection in the Solar Corona
A.Bhattacharjee (Columbia Univ.) ---------- 12
Log-Stable Distribution of Energy Dissipation in Turbulence
S.Kida (Kyoto Univ.) ---------- 13
Statistical Properties of Two-dimensional Magnetohydrodynamic Turbulence
D.Biskamp (Max Plank Inst.) ---------- 17
Turbulent Dynamo and Subgrid-Scale Modeling of MHD Turbulence
A.Yoshizawa (Tokyo Univ.) ---------- 18

Session III Transport I

Hybrid Fluid/Kinetic Descriptions of Tokamak Plasmas
J.D.Callen (Univ. of Wisconsin) ---------- 22
The Theory of Turbulence and Anomalous Transport in Plasmas: Past, Present, and Future
J.A.Krommes (PPPL) ---------- 26
Ion Temperature Gradient Turbulence and Coherent Structures
D.Choi (Korea Advanced Inst.) ---------- 30

Three-Dimensional Particle Simulation of Trapped Electron Instabilities in Tokamaks
C.Z.Cheng (Princeton Univ.) ---------------------------- 31
Edge Anomalous Transport in Heliotron/Torsatron
M.Wakatani (Kyoto Univ.) -------------------------------- 32

Session IV Helical Plasmas

Optimization, Non-local MHD-Mode, and α -Particle Confinement Behaviour of Helias Equilibria
J.Nuhrenberg (Max Planck Inst.)------------------------- 37
Equilibrium Beta Limit of Helical Systems
T.Hayashi (NIFS)-- 41
Suppression and Control of Magnetic Islands in Toroidal Plasmas
A.Bhattacharjee (Columbia Univ.) ----------------------- 45
Theoretical Studies of Nonlinear Sheath Dynamics
J.K.Lee (POSTECH)--- 53

Session V Laser Plasmas

Hydrodynamic Instabilities in Laser Driven Implosion
K.Mima (Osaka Univ.) ------------------------------------ 57
Solitons and Chaos in Laser-Plasma Interaction
C.S.Liu (Univ. of Maryland)------------------------------ 61
Nonlinear Evolution of 2D and 3D Rayleigh-Taylor Instability at Stagnation Phase in Laser Implosion
K.Nishihara (Osaka Univ.) ------------------------------- 62

Session Ⅵ Transport Ⅱ

Models for Collisional Transport across a Magnetic Field with Destroyed Surfaces
G.Laval (Ecole Polytechnique) ---------- 66

Issues in Direct Numerical Simulation of Plasma Turbulence and Transport
A.Thyagaraja (Culham Lab.) ---------- 70

Anomalous Transport Due to the Skin Size Electromagnetic Drift Mode in Tokamaks
A.Hirose (Univ. of Saskatchewan) ---------- 74

Session Ⅶ Space Plasmas

Magnetohydrodynamical Formation of Astrophysical Jets from Gravitationally Collapsing Objects
Y.Uchida (Univ. of Tokyo) ---------- 78

Computer Simulation of Solar Wind-Magnetosphere Interaction
K.Watanabe (NIFS) ---------- 79

Rapid Acceleration of Protons in a Nonlinear Magnetosonic Wave and Their Energy Spectrum
K.Ohsawa (Nagoya Univ.) ---------- 83

Session Ⅷ Poster Session

1. Effect of Pressure on Mode Transition Point of Partially Relaxed States with Peripheral Loss
Y.Kondoh (Gunma Univ.) ---------- 87

2. Relaxed State and Entropy Production
T.Kato (Waseda Univ.) ---------- 91

3. Simulation Study of MHD Relaxation and Reconnection Processes
K.Kusano (Hiroshima Univ.) ---------- 95

4. Finite β Equilibrium for a Pressure Configuration
S.Kajita (Gifu Univ.) ---------- 98

5. Application of Mathematica to Energy Principle
T.Yamagishi (Fukui Inst. of Technology) ······ 102
6. Direct Ion Heating in MHD Relaxation
Z.Yoshida (Univ. of Tokyo) ······ 106
7. Helical Field Effect in Solar/Stellar Wind
H.Washimi (Nagoya Univ.) ······ 107
8. Self-Similar Evolution of Nonlinear Magnetic Buoyancy Instability
K.Shibata (Aichi Univ.) ······ 111
9. Turbulent Mixing due to Rayleigh-Taylor Instabilities in Laser Driver Implosion
H.Takabe (Osaka Univ.) ······ 115
10. Electrostatic Particle Simulations of Density and Temperature Driven Modes in a Toroidal Plasma
M.LeBrun (Univ. of Texas) ······ 119
11. Internal Kink Mode Simulation by 3-D Gyrokinetic Code
H.Naitou (Yamaguchi Univ.) ······ 123
12. Particle Simulation Study on the Tilt Stabilization of the FRC Plasma
R.Horiuchi (NIFS) ······ 127
13. 3-D Electromagnetic Macroscale Particle Simulation of Inhomogeneous, Magnetized Plasmas
M.Tanaka (NIFS) ······ 131
14. Study of Kink Instability and Current Relaxation by Three Dimensional Macroscale Particle Simulation
H.Takamaru (NIFS(Hiroshima Univ.)) ······ 135
15. Nonadiabatic Behavior of the Magnetic Moment of a Charged Particle in a Dipole Magnetic Field
S.Murakami (NIFS(Hiroshima Univ.)) ······ 139
17. Numerical Study of Ion Temperature Gradient Modes in a Tokamak
M.Yagi (JAERI) ······ 143
18. Nonlinear Behavior and Transport Property of Multiple-Helicity Resistive Interchange Modes near Marginally Stable State
H.Sugama (NIFS) ······ 144

19. Nonlinear Computer Analysis of Backward Wave Oscillator
T.Watanabe (NIFS) ---------- 148
20. Mode Conversion of Alfven Waves Induced by Quadrupole Magnetic Field Modulation
H.Hojo (Univ. of Tsukuba) ---------- 154
21. Numerical Simulation of Potential-Driven Ion Cyclotron Oscillation
S.Ishiguro (Tohoku Univ.) ---------- 158
22. Dynamics of Interfaces with Internal Structures
T.Kawakatsu (Kyushu Univ.) ---------- 162
23. Nonlinear Equations for weakly unstable modes
N.Nakajima (NIFS) ---------- 164
24. Hole Dynamics of One-Dimensional Plasma
K.Kitahara (Tokyo Institute of Tech.) ---------- 168
25. Shock and Soliton Structures Induced by Poloidal Flow in Tokamaks
T.Taniuti (Chubu Univ.) ---------- 169
26. Soliton Phenomena in Electron Beam Plasma
T.Yajima (Univ. of Tokyo) ---------- 170
27. Point Vortex Description of a Modon solution
C.Matsuoka (Nagoya Univ.) ---------- 174
28. Structures of Magnetic Field Lines in the Helical Torus
T.Hatori (NIFS) ---------- 177
29. Regular Motion and Symmetry in the Relativistic Standard Map
Y.Nomura (NIFS) ---------- 180
30. Diffusion and Relaxation in Hamiltonian Chaos
T.Konishi (Nagoya Univ.) ---------- 184

Session Ⅸ Tokamak

Non-Linear Behaviour in Tokamaks
J.A.Wesson (JET) ---------- 187
Fluctuation Spectrum of Ion Temperature Gradient Driven Modes in Sheared Magnetic Fields
T.Tuda (JAERI) ---------- 194

Equilibria and Dynamics of Temperature in a Fusion Reactor Plasma
H.Wilhelmsson (Univ. of Technology) ·················· 198
Model for Marfe-Detached Plasma Transition in Tokamak
P.K.Kaw (Inst. for Plasma Research) ·················· 202
Propagations of Drift Waves in Toroidal Plasma Systems
S.Yoshikawa(PPPL) ·················· 203

Session X Chaos·Soliton

Statistical Mechanics Using Symbolic Dynamics
R.White (Princeton Univ.) ·················· 204
Diffusion Through Stochastic Webs in Two and More Dimensions
A.J.Lichtenberg (UC Berkeley) ·················· 208
Formation and Dynamics of Solitary Waves and Vortices in Driven and Damped Systems
K.H.Spatschek (Universitat Dusseldorf) ·················· 212
Solitons and Chaos in Plasma
Y.Ichikawa (NIFS) ·················· 216

Appendix I Program of Conference ·················· 220

Appendix II List of Participants ·················· 227

Preface

The National Institute for Fusion Science was established on the 29th of May, 1989 as the major university fusion research center in Japan. The Institute of Plasma Physics in Nagoya University, part of the Plasma Physics Laboratory in Kyoto University, and the Institute for Fusion Theory in Hiroshima University were fused into this institute. Present major activities include the design and construction of the Large Helical Device (LHD) as well as the formulation of a more complete theory of nonlinear plasmas based on simulation and analytical methods. One of our obligations as the central laboratory is to promote international collaboration. The International Toki Conference is a part of our collaboration program. Every year we host this conference on various topics. In the first International Toki Conference held in 1989 we discussed next-generation helical device projects which exist around the world. Among these, the LHD project is now in progress as a main activity of our institute.

This past year we focused on another main task of our institute which is the promotion of theory and computer simulation research of various plasmas. We placed particular emphasis on the nonlinear physics of fusion and related plasmas. The most prominent feature of plasma physics, more so than other fields, is its intrinsic nonlinearity. Plasma theorists are responsible for taking the leadership in developing a new concept and methodology that can systematically elucidate the highly complex and nonlinear behavior of nature and lead us to its intuitive comprehension. We are presently in the midst of a fog. Recent, rapid progress of computer simulations have given us a light of hope, though faint, in front of us. In this, the 2nd Toki conference, we aimed to brighten, to whatever extent possible, this glimmer of hope.

More than twenty famous theorists from ten foreign countries and more than a hundred domestic participants from universities, institutes and industrial companies gathered at this conference. The topics discussed were rich in variety. I believe that we have been able to sow the seeds of highly nonlinear physics in this conference. Until the buds bloom, we must persevere for some time.

On behalf of the organizing and executive committee members I would like to express my sincere thanks to all participants, particularly the foreign participants, without whom we would not have been able to have such a successful meeting. I would also like to thank the many other people who worked so kindly and effectively behind the scenes.

SATO, Tetsuya
Chairman
The Organizing Committee of
The 2nd Int'l Toki Conference

Organization

Organizing Committee

T.Sato (NIFS) : Chairman

M.Okamoto (NIFS)

T.Hatori (NIFS)

K.Mima (Osaka Univ.)

M.Wakatani (Kyoto Univ.)

T.Takeda (JAERI)

Executive Committee

T.Sato (NIFS) : Chairman
M.Okamoto (NIFS)
T.Hatori (NIFS)
H.Sanuki (NIFS)
T.Hayashi (NIFS)
M.Tanaka (NIFS)
K.Watanabe (NIFS)
R.Horiuchi (NIFS)
N.Nakajima (NIFS)
H.Sugama (NIFS)

Sponsorship

∗ Host Organization

National Institute for Fusion Science

Ministry of Education, Science and Culture

∗ Supporting Organization

Toki City

Fusion Science Association

The Japan Society of Plasma Science and Nuclear Fusion Research

Nonlinear Phenomena and Processes in High Energy Plasmas*

B. Coppi
Massachusetts Institute of Technology, Cambridge, MA 02139

Introduction

Both in space physics and in the field of high energy laboratory plasmas where, for instance, fusion burn conditions can be achieved a large class of observed phenomena require the understanding of the nonlinear processes that underlie them. Nonlinear plasma physics has had a rather humble but clearly formulated beginning: experiments on plasma waves and their nonlinear interactions have, in fact, confirmed the theories [1] that had been developed for instance on mode couplings, nonlinear Landau damping, etc. The phenomena that confront us at present are considerably more complex but their importance is such that tentative and rudimentary theoretical descriptions have to be given of them. While accepting the fact that the analytical tools we have generated are not adequate to the task, I think that our explanations should be based on clear concepts and start from complete and correct linearized theories. In order to be specific on some of the issues involved, two rather general areas will be considered: magnetic reconnection in collisionless plasmas, and transport processes in magnetically confined plasmas.

I. Collisionless Magnetic Reconnection

The importance of understanding processes that lead to transitions of magnetic field topology (commonly referred to as reconnection) has come to light first in space physics. These processes have in fact a key role in explaining the interaction of the solar wind with the earth's magnetic field and the development of large scale solar flares. On the other hand, although the first theory [2] of collective modes producing magnetic reconnection in collisionless plasmas was reported more than 25 years ago, laboratory experiments attaining the very high temperature regimes where these modes can be excited have come into reality only recently [3]. These experiments involve magnetically confined toroidal plasmas where electron temperatures in the 5 to 10 keV range have been obtained by suppressing the onset of macroscopic modes producing magnetic reconnection due to the effects of finite electrical resistivity [4]. The latter type of mode is in fact considered to be responsible for the crash phase of the so-called "sawtooth oscillations" of the central part of the plasma column. The suppression of these occurs when a significant population of "high energy" nuclei is injected into the plasma column.

The high temperature regimes thus obtained are subject to sudden collapses (so-called "monster sawteeth") that we attribute to collisionless modes producing magnetic reconnection [5] and having a prevalent poloidal number $m^o = 1$. We observe that the earlier analyses that were carried out for space physics [6] had shown that collisionless reconnection tends to develop only weakly in plasma configurations that have a relatively large stability margin against the onset of ideal MHD mode. On the other hand, a magnetically confined axisymmetric plasma of the type embodied by the experiments of Ref. [3], can have relatively low stability margin against ideal MHD ($m^o = 1$) modes and consequently is susceptible to strong collisionless reconnecting modes. We find that the relevant growth rates have numerical values consistent with the characteristic times of the observed collapses [3]. The smallest characteristic distance involved in the spatial structure of these modes is the inertial skin depth $d_e = c/\omega_{pe}$ and therefore they can be classified as of the "inertial" type [2], even though, unlike the modes treated in Ref. [2], they cannot be described by fluid equations. The second characteristic distance is the ion gyroradius ρ_i and the third is the radius r_1 where $q(r_1) = B_\phi r_1/(B_\theta R) = 1$. We refer, for simplicity to a toroidal configuration with a large aspect ratio ($r/R << 1$, R being the major radius) and circular magnetic surfaces where the magnetic field is represented by $\underset{\sim}{B} \simeq B_\phi(r)\underset{\sim}{e}_\phi + B_\theta(r)\underset{\sim}{e}_\theta$. The mode growth rate is about [5]

$$\gamma \simeq \left[V_A d_e + \frac{1}{5}\, c\lambda_{De}\left(1 + \frac{T_i}{T_e}\right)^{1/2}\right]/(r_1 L_s)$$

where $1/L_s = (r_1/R)dq/dr$.

Another attractive aspect of the linearized theory is that it produces the appropriate reconnected magnetic field configuration. However, this theory breaks down for very small values of the perturbed magnetic field $\tilde{B}_r$, when the size of the magnetic island $\delta_I \sim d_e$. We note that $\delta_I \propto \tilde{B}_r^{1/2}$. A theoretical model to extend the analysis beyond the point where $\delta_I \sim d_e$ is proposed [5] and is based on the assumption that the electrons are scattered over the region δ_I and lose momentum at a rate corresponding to a magnetic diffusion coefficient $D_m \sim \gamma\delta_I^2$. This leads to δ_I replacing d_e as the smallest scale distance of the problem and to preserve γ of the order of $c\lambda_{De}/(r_1 L_s)$ while a new form of the relevant dispersion equation, that is similar to that of the linearized theory, is solved. The latter feature is consistent with the experimentally observed fact that the growth rate of the instability remains about constant well beyond the limits of the linearized theory.

A theoretical model that could reasonably cover the range where $\delta_I > \rho_i$ remains to be formulated. An important guidance for this can come from the particle simulation codes that have been recently developed. In fact, we consider existing codes that are based on fluid equations as important steps in the direction of understanding how reconnection develops in low temperature regimes but inadequate for high temperatures. To illustrate this point we note that experimental evidence has been provided of the fact that a steepened plasma pressure gradient resulting from the injection of pellets in high temperature plasmas, can suppress, or render more difficult to excite, the modes responsible for the crash phase of sawtooth oscillations [7]. This can most easily be explained by the importance [8] that the frequencies $\omega_{*j} = -(c/r_1)\ (dp_j/dr)/(ne_j B)$ have on the dynamics of the considered modes that existing fluid codes do not usually include.

II. Transport Issues

The description of transport in regimes where the effects of collective modes are dominant over those of collisions is frequently considered an obscure art where predictions cannot be made, given the nature of the processes involved and their intrinsic nonlinearities, and where the main physical factors are impossible to isolate. Examples are then given to illustrate that this image of the field is not quite accurate.

a) Peaked Density Regimes

These regimes were originally suggested [9] on the basis of the linear and non-linear theory [10] of the so-called η_i-modes ($\eta_i = d\ln T_i/d\ln n$) in order to redress the deteriorated confinement of the Alcator-C experiment. Therefore knowledge of the main ingredients of the theory, in spite of the rudimentary state of its nonlinear part, led to the production of peaked density profiles and to successfully raising the confinement parameter $n_o\tau_E$ to its expected record values. By now, a variety of interesting properties have been found [7] to be associated with peaked particle density regimes. These findings require more than the near-suppression of η_i-modes in order to be explained.

b) Profile Consistency and Coupled-Mode Transport

A substantial body of experimental evidence has been accumulated, since the "principle of profile consistency" [11] was proposed more than 10 years ago, on the fact that the experimentally observed temperature profiles correspond to an effective thermal conductivity κ_{eff} that is a monotonically increasing function of the plasma radius. Typically κ_{eff} enters an equation of the form

$$S = -\frac{1}{r}\frac{d}{dr}\left[r\kappa_{eff}\frac{dT}{dr}\right],$$

where S is the energy deposition function and $T(r)$ is the temperature. The observed typical dependence of κ_{eff} on r is forced by the fact that the observed electron temperature profiles fall within a rather specific class.

We deduce, from this, the conclusion that no single mode, among those that are presently known can produce the observed typical form of κ_{eff}. We consider, for instance, the diffusion coefficient [10] that has been associated with the excitation of drift modes

$$D_d \sim \frac{cT}{eB}\frac{\rho_i}{r_p}\frac{\lambda_{\parallel}}{r_p}$$

where $\lambda_{\parallel}$ is the mode longitudinal wavelength and r_p is the pressure gradient scale distance. The profile of $\kappa_d = nD_d$ is definitely not of the type that can match the observations. The second conclusion we draw is that the spatial coupling of the effect of two kinds of modes can produce the desired form of κ_{eff}. The considered situation may, in fact, be compared to having two electrical conductors in series. The first kind of mode is excited within the main body of the plasma column and the second kind is excited at the edge. A specific example that is proposed as realistic for current experiments is the trapped electron mode, so called ubiquitous [12], that is driven primarily by the electron pressure gradient in combination with the collisional impurity density gradient driven mode at the edge of the plasma column [13]. Thus a diffusion coefficient is derived and shown to reproduce the observed temperature profiles, to imply a scaling of the energy confinement time consistent with scalings inferred from the available experiments, and to account for the so-called isotopic effect [13]. A model for the nonlinear interaction of modes that are localized in different regions of the plasma column is being analysed in collaboration with P. Kaw.

c) Related Energy and Current Density Transport

The redistribution of the current density in a high temperature plasma is usually described in terms of the magnetic field "diffusion" associated with the collisional resistivity, as it is generally concluded that the order of magnitude of the time scales involved in the current density redistribution are consistent with the collisional resistive times. Yet there are indications that it should not be sufficient to relate the applied electric field $E_{\|}$ to $J_{\|}$ through the collisional resistivity η only, in order that the appropriate current density profiles be reproduced. In particular in regimes where a significant fraction of the electron population is trapped and the collisional resistivity is given by the so-called "neoclassical" expression, the resulting current density profile is "strange" if the electron temperature radial profile is close to a Gaussian.

To deal with this problem we assume that in ohmic regimes, where the applied electric field drives the current and at the same time heats the plasma, the transport of the electron thermal energy and the redistribution of the current density are strongly coupled. We consider a matrix equation that describes the transport for both quantities under steady state conditions, we postulate symmetry properties of the elements of this matrix and use them to define two transport coefficients: an effective thermal conductivity and a thermal-viscous coefficient [14].

The requirement that the adopted transport coefficients comply with the principle of profile consistency and generate acceptable profiles both for the electron temperature and the current density is used together with the predicted [11] experimental observation that the loop voltage falls within a relatively small range of values for the most disparate types of ohmic experiments. An integro-differential equation is derived from the matrix transport equation and the resulting steady state electron temperature and current density profiles are obtained from appropriate numerical solutions. These show that the thermal-viscous coefficient leads to a broadening of the current density profile and to an increase of the central electron temperature, while the temperature profile remains largely unchanged [15].

We propose that the degradation that occurs in the presence of injected heating is associated with the decoupling between the thermal energy transport and the current energy transport when the electric field is no longer the source for both. In this case we argue that the contribution to the electron thermal energy diffusion coefficient by collective modes that do not depend directly on the current density distribution (such as those [13] mentioned in part b) of this section) becomes prevalent.

References

[1] B. Coppi, M.N. Rosenbluth and R.N. Sudan, *Ann. Phys.* **55**, 207 (1960).

[2] B. Coppi, *Phys. Letters* **11**, 226 (1964).

[3] D.J. Campbell, et al., *Phys. Rev. Letters* **60**, 2148 (1988).

[4] B. Coppi, P Detragiache, F. Pegoraro, and F. Porcelli, *Phys. Rev. Letters* **63**, 2733.

[5] B. Coppi and P. Detragiache, Massachusetts Institute of Technology, R.L.E., Report PTP-90/14 (Cambridge, MA 1990). Submitted to *Phys. Rev. Letters.*

[6] B. Coppi, G. Laval and R. Pellat, *Phys. Rev. Letters* (1966).

[7] Y. Kamade, T. Takizuka, M. Nagami and T. Ozeki, *Nucl. Fusion* **31**, 23 (1991).

[8] G. Ara, B. Basu, B. Coppi, G. Laval, M. Rosenbluth, and B. Waddell, *Ann. Phys.* **112, 443** (1978).

[9] B. Coppi, S. Cowley, P. Detragiache, R. Kulsrud, F. Pegoraro, in *Plasma Physics and Controlled Nuclear Fusion Research 1984*, (Publ. I.A.E.A. Vienna 1985) 93.

[10] B. Coppi, M.N. Rosenbluth, R.Z. Sagdeev, *Phys. Fluids* **10**, 582 (1967).

[11] B. Coppi, in *Comm. Plasma Phys. Cont. Fusion* 5 (1980) 261.

[12] B. Coppi and G. Rewoldt, *Phys. Rev. Letters* **33** (1974) 1329, and B. Coppi and F. Pegoraro, *Nucl. Fusion* **17** (1977) 1963.

[13] B. Coppi, in *Plasma Physics and Controlled Nuclear Fusion Research 1990*, (Publ. I.A.E.A., Vienna 1991), paper I-2-6.

[14] B. Coppi, R. Englade, M. Nassi, F. Pegoraro, L. Sugiyama, in *Plasma Physics and Controlled Nuclear Fusion Research 1990* (Publ. I.A.E.A., Vienna, 1991) paper D-4-14.

[15] B. Coppi and F. Pegoraro, *Massachusetts Institute of Technology*, R.L.E., Report PTP-90/2 (Cambridge, MA 1990). Submitted to *Physics of Fluids.*

*Sponsored in part by the U.S. Department of Energy

SELF-ORGANIZING PROCESSES IN MAGNETICALLY CONFINED PLASMA

T. SATO, R. HORIUCHI, K. WATANABE, T. HAYASHI
and K. KUSANO*)

National Institute for Fusion Science
*)Faculty of Science, Hiroshima University

Fig. 1 shows three snapshots of a self-organizing magnetohydrodynamic plasma [1]. We take a cylinder with rectangular cross section in which a magnetized plasma is filled. We assume periodicity along the axis (z) and that plasma is confined by a perfect conductor with a toroidal system in mind. The initial condition is a force-free equilibrium. Neither plasma flow nor pressure exists in the initial state. Furthermore, we make an important assumption that ohmically heated plasma is instantaneously cooled by radiation loss. This is equivalent to assuming that entropy produced during the dynamical process is thrown away from the system. We neglect the role of the plasma pressure.

The initial force-free equilibrium includes free magnetic energy because plasma itself carries currents. In the present case, the free magnetic energy is sufficiently large that an ideal current-driven (helical kink) instability arises. Accordingly, plasma (magnetic field configuration) is deformed. Because of resistivity, whatever small it is, magnetic reconnection is driven at places where antiparallel field condition is realized. At reconnection points where antiparallel field condition is satisfied currents are largely enhanced because of $\mu_0 \boldsymbol{J} = \nabla \times \boldsymbol{B}$. Therefore, free magnetic energy is strongly dissipated there due to enhanced ohmic dissipation $\eta \boldsymbol{J}^2$. Simultaneously reconnection changes magnetic topology. If there exists a minimum energy magnetic field configuration other than the vacuum field configuration, it is expected that the system realizes a new ordered magnetic field configuration with the minimum energy.

Fig. 1 depicts a trace of a constant axial (toroidal) magnetic field intensity. The upper panel shows the initial equilibrium configuration, the second an intermediate configuration where the initial magnetic structure is torn in peaces at converging points of plasma flows by reconnection driven by an ideal helical kink instability. The bottom panel shows a clear helical structure which is established after disordered magnetic energy is dissipated by ohmic heating which in turn is thrown away from the system by radiation loss. Summing up, we can say that a simple ordered structure (a helical structure in this case) is created from a once disordered structure (middle panel) when the entropy produced during the process is swept out from the system.

The above example suggests that the magnetohydrodynamic self-organization requires :

1) Existence of a sufficient free (magnetic) energy that can drive a current-driven (helical kink) instability.

2) Plasma flows induced by the current-driven instability drive reconnection at their converging points whereby magnetic topology is changed.

3) Disordered magnetic energy (entropy) is swiftly removed. Actually, disordered magnetic energy is transferred into thermal energy through ohmic heating enhanced by driven

reconnection which, in turn, is removed from the system by radiation. This process takes place in the magnetohydrodynamic time scale rather than the resistive time scale.

Fig. 2 shows the time evolutions of the magnetic energy W and the magnetic helicity K. Note that the initial state at this example is different from that of Fig. 1. As one sees in this figure, the helicity decreases slowly and smoothly, while the energy exhibits a stepwise decrease.

Incidentally, the evolutions of W and K are given by

$$\frac{\partial W}{\partial t} = -2 \int \eta \boldsymbol{J} \cdot \boldsymbol{J} \, dV \tag{1}$$

$$\frac{\partial K}{\partial t} = -2 \int \eta \boldsymbol{J} \cdot \boldsymbol{B} \, dV \tag{2}$$

where η is the resistivity. These equations indicate that, generally speaking, both W and K decrease with the time scale of ohmic dissipation.

The fact that W and K behave very differently during the self-organization process must tell us some important physical law underlying the process. It is natural to infer that the driven reconnection process must hold the key. The simulation result indicates that the magnetic field completely vanishes at the reconnection point.

Recalling Eqs. (1) and (2) we find a beautiful dispensation of Nature that the current driven instability deforms the magnetic field and generates a completely antiparallel magnetic field configuration where W is drastically decreased but K is not influenced (complete reconnection) as if the system knew its destination and the shortest path. The topology of the magnetic field thereby is globally changed.

In conclusion, the magnetohydrodynamic self-organization is governed by the nonlinearly driven reconnection whereby the magnetic helicity is conserved but the magnetic energy is stepwise decreased. This reminds us the mystery and dispensation of Nature.

In this regard we shall examine the time evolutions of the average wavenumber of the magnetic energy and the magnetic helicity. This is shown in Fig. 3 for the same example as that of Fig. 2. It is interesting to observe that the energy spectrum cascades normally, while the helicity spectrum cascades inversely. Higher mode spectrum of the energy as a matter of fact swiftly disappears, resultantly, the (magnetic) entropy in the system decreases to create a new ordered structure which has a simpler helical structure.

In the case of tokamak, on the other hand, there is a strong toroidal (potential) field which is supplied from an external coil current and a relatively peak current flows in the toroidal direction which produce a relatively weak poloidal field convertible to kinetic and thermal energies. Even though current driven instabilities occur by releasing the free (small) poloidal magnetic energy, the released (flow) energy is not sufficiently large that the massive toroidal field is folded to make a completely antiparallel field configuration. This indicates that the magnetic field would never vanish at a reconnection point, in other words, only the poloidal field components can experience reconnection (incomplete or partial reconnection). Therefore, $\boldsymbol{J} \cdot \boldsymbol{B}$ would be enhanced at a reconnection point rather than being minimized, thus the helicity could not be conserved. This is the reason why the tokamak configuration cannot be obtained by Taylor's theory[3] assuming the helicity conservation. The sawtooth oscillations in tokamaks, therefore, should be a partial self-organization process which exhibits a slight topological change due to partial reconnection.

Since resistivity is intrinsic to the reconnection process, it is conceivable that self-organization should take place in the time scale dependent strongly on the resistive time scale t_R. As we will see in Figs. 2 and 3, however, the actual evolution time scale of the self-organization is much smaller than, and rather independent of, the resistive time scale. The time scale is of the order of a few tens of the Alfven transit time, t_A, where the Reynolds number $R = t_R/t_A$.

The magic of this fact time scale can be well explained in terms of a driven type reconnection[4]. A physical difference between the spontaneous reconnection and driven reconnection is depicted in Fig. 4. As we can see in the upper part of this figure, in a spontaneous reconnection process antiparallel field components must exist initially where the current is locally peaked. Subject to a finite resistivity, the current peak tends to be flattened. The time scale of this flattening is naturally governed by the resistive diffusion because the resistivity is the direct cause of reconnection. In a tearing mode instability, feedback flows leading to enhancement of the neutral point current exist, thereby, the current flattening is enhanced. Nevertheless, the process is still largely dependent on the resistivity because the flows are the effect of the resistivity induced reconnection.

On the other hand, in the case of driven reconnection which is depicted in the lower part the current peaking is locally created at a converging point of the plasma flows driven externally or induced internally by an ideal MHD instability, notably, a current-driven helical kink instability. In this case the time scale of current peaking is determined by the strength of the flow amplitude. Therefore, the flows are the cause of reconnection and the dissipation is determined by $\boldsymbol{J}^2$ rather than η. This indicates that the time scale of the self-organization is governed by the MHD (i.e., MHD flows) time scale[4].

When the magnetic free energy is sufficient, the current driven instability deforms the magnetic field so largely that completely antiparallel field points are created somewhere inside the system whereby the magnetic topology is globally changed and a minimum energy topology of magnetic field is realized. It is noted that the magnetic helicity is conserved during this proccess, while the magnetic energy is drastically decreased. The reversed field pinch (RFP) relaxation is a typical example of this type [2].

When the free energy is not so large, only partially antiparallel field configuration is formed where only partial reconnection occurs. Partial reconnection can not globally change the magnetic topology. The magnetic helicity is not conserved in this case because $\boldsymbol{J}\cdot\boldsymbol{B} \neq 0$ at the reconnection point. A typical example of the latter is the tokamak sawtooth relaxation[5].

1. R. Horiuchi and T. Sato, Phys. Fluids, **29**, 4174, 1986.
2. K. Kusano and T. Sato, Nucl. Fusion, **27**, 821, 1987.
3. J. B. Taylor, Phys. Rev. Lett., **33**, 1139, 1974.
4. T. Sato, R. Horiuchi and K. Kusano, Phys. Fluids, **B1**, 255, 1989.
5. T. Sato, Y. Nakayama, T. Hayashi, K. Watanabe and R. Horiuchi, Phys. Rev. Lett., **63**, 525, 1989.

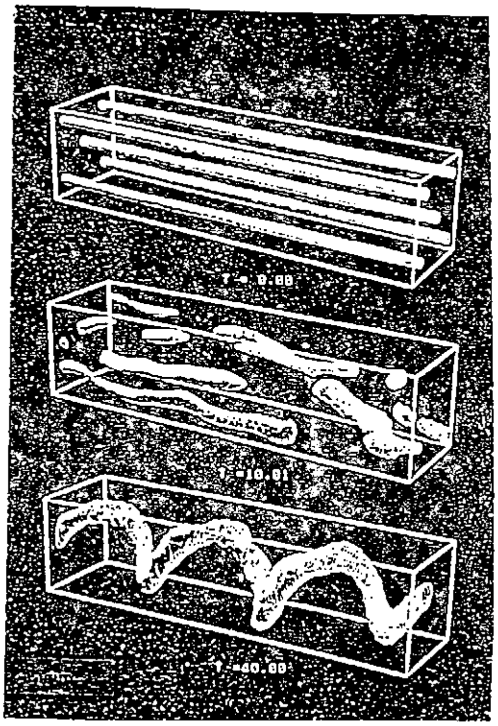

Figure 1. The snapshots of a self-organizing magnetohydrodynamic plasma.

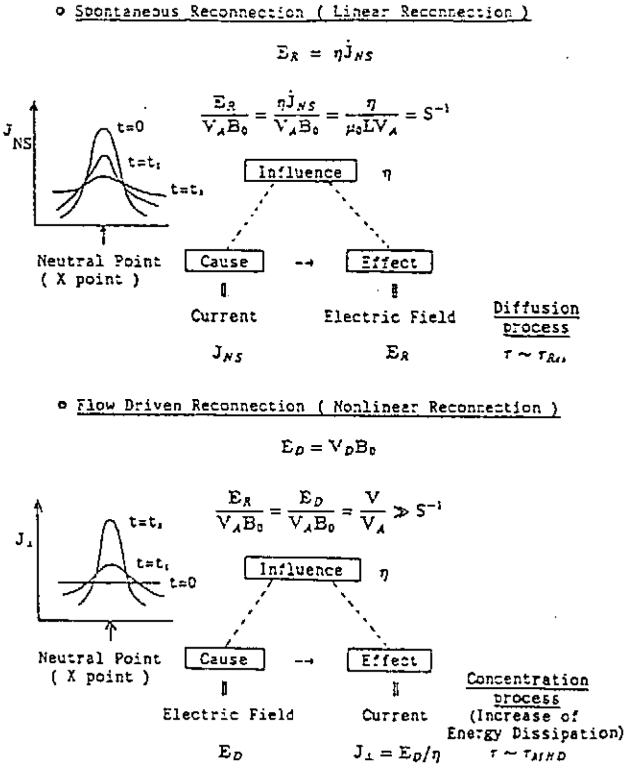

Figure 4. A physical difference between the spontaneous reconnection and driven reconnection.

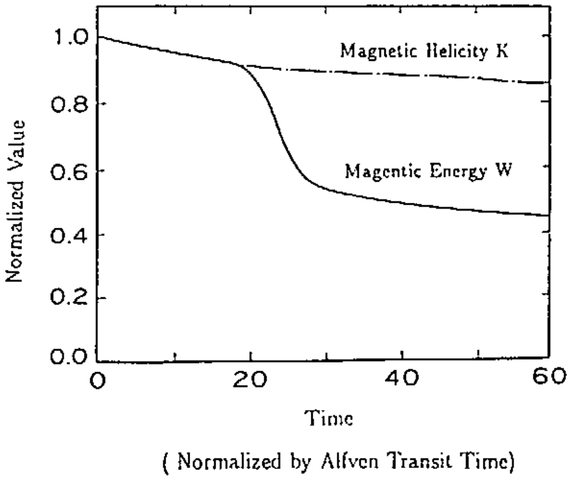

Figure 2. Time evolutions of the magnetic energy W and the magnetic helicity K.

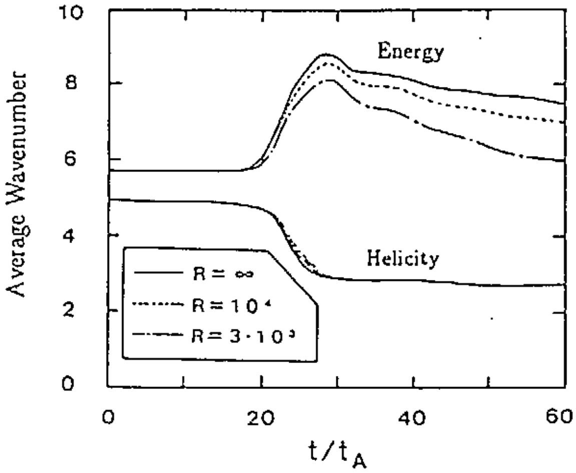

Figure 3. The time evolutions of the average wavenumber of the magnetic energy and the magnetic helicity.

Current Sheet Formation and Rapid Reconnection in the Solar Corona

A. Bhattacharjee and Xiaogang Wang
Department of Applied Physics
Columbia University
New York, New York 10027

It is shown that a current sheet is formed in Parker's model of the solar corona (Parker 1972) from the requirement that magnetic helicity is conserved in the presence of a very small but finite plasma resistivity. The presence of dissipation permits slippage of field-lines with respect to the plasma, and makes Van Ballegooijen's theorem (1985) inapplicable. A current sheet can thus be formed in the presence of smooth photospheric flows. The structure of the current sheet encompasses a thin strip spanning two Y-points. It is shown that the rapid reconnection involved in the formation of the current sheet justifies the use of helicity conservation. Implications for coronal heating and numerical simulations of the corona are discussed.

Log-Stable Distribution of Energy Dissipation in Turbulence

Shigeo KIDA

Research Institute for Mathematical Sciences, Kyoto University, Kyoto 606, Japan

The statistical properties of small-scale motion of turbulence, especially the low-order moments such as the energy spectrum function, are well described by the Kolmogorov similarity theory. But the higher-order statistics of the derivatives of velocity increasingly deviate from the Kolmogorov prediction. Since the intermittent property of velocity field had been recognized experimentally, lots of intermittency theories have been proposed by incorporating the intermittent structure of flow field, especially of the fluctuations of the energy dissipation rate field. They describe the intermittency effects qualitatively, but the quantitative agreement is still controversial. Here, we propose a new intermittency theory and compare the results with experiments.

Consider the fluctuations of the energy dissipation rate field

$$\epsilon(\boldsymbol{x}) = \frac{\nu}{2}\sum_{i,j=1}^{3}\left(\frac{\partial u_i}{\partial x_j} + \frac{\partial u_j}{\partial x_i}\right)^2. \tag{1}$$

We introduce a spatial average of $\epsilon(\boldsymbol{x})$ as

$$\epsilon_r(\boldsymbol{x}) = \frac{1}{V_r}\int_{V_r(\boldsymbol{x})} \epsilon(\boldsymbol{x}')\mathrm{d}\boldsymbol{x}', \tag{2}$$

where $V_r(\boldsymbol{x})$ is the volume of a sphere of radius r centered at $\boldsymbol{x}$, and introduce the logarithm of the breakdown coefficient ϵ_r/ϵ_l $(r < l)$

$$a_{r,l} = \ln\frac{\epsilon_r(\boldsymbol{x})}{\epsilon_l(\boldsymbol{x}')}, \tag{3}$$

where the positions $\boldsymbol{x}$ and $\boldsymbol{x}'$ are assumed to be close to each other in the sense that $|\boldsymbol{x} - \boldsymbol{x}'| \leq 2(l-r)$.

Now we make an assumption that (i) $P_a(a|\frac{r}{l})$, the probability density function (*pdf*) of $a_{r,l}$, is a function of ratio $\frac{r}{l}$ and is independent of positions $\boldsymbol{x}$ and $\boldsymbol{x}'$, (ii) the *pdf*s of $a_{r,\rho}$

and $a_{\rho,l}$ $(r < \rho < l)$ are independent of each other, (iii) the form of $P_a(a|\frac{r}{l})$ is the same if variable a is appropriately shifted and scaled by a linear transformation as $a \to (a-d)/c$, where c (> 0) and d are functions of $\frac{r}{l}$, and (iv) $\langle \mathrm{e}^{pa} \rangle_{r/l}$, the p-th order moment of $\mathrm{e}^{a_{r,l}}$ exists for any $p \geq 0$.† Then, the *pdf* of $a_{r,l}$ is uniquely given by a special case of the Lévy stable distributions, the characteristic function of which is written as

$$\varphi_a\left(z|\tfrac{r}{l}\right) = \left(\tfrac{r}{l}\right)^{\frac{\mu}{2^\alpha-2}\left[\mathrm{i}z-\left(z\mathrm{e}^{\mathrm{i}\pi/2}\right)^\alpha\right]}, \tag{4}$$

where $-\pi \leq \arg(z) \leq 0$. This distribution has two free parameters, i.e., the intermittency parameter μ (> 0) and the characteristic exponent of the distribution α $(0 < \alpha \leq 2)$.

Using eq. (4), we can show that the asymptotes of $P_a\left(a|\frac{r}{l}\right)$ for large values of $|a|$ for $1 < \alpha < 2$ is

$$P_a\left(a|\tfrac{r}{l}\right) \sim \begin{cases} |a|^{-(\alpha+1)} & \text{as } a \to -\infty, \\ \exp\left[-Aa^{\alpha/(\alpha-1)}\right] & \text{as } a \to \infty, \end{cases} \tag{5}$$

where

$$A = \frac{\alpha - 1}{\alpha^{\alpha/(\alpha-1)}\left(\frac{\mu}{2^\alpha-2}\ln\frac{r}{l}\right)^{1/(\alpha-1)}}. \tag{6}$$

The p-th order moment of $\epsilon(\boldsymbol{x})$ is calculated as follows. Using eqs. (3) and (4), we obtain

$$\left\langle\left(\frac{\epsilon_r}{\epsilon_l}\right)^p\right\rangle = \langle \mathrm{e}^{pa}\rangle_{r/l} = \varphi_a\left(-\mathrm{i}p \mid \tfrac{r}{l}\right) = \left(\tfrac{r}{l}\right)^{-\mu(p-p^\alpha)/(2^\alpha-2)}. \tag{7}$$

If we put $l = L$, the integral scale of turbulence, and neglect fluctuations of $\epsilon_L(\boldsymbol{x})$, then eq. (7) becomes

$$\frac{\langle {\epsilon_r}^p\rangle}{{\epsilon_L}^p} = \left(\tfrac{r}{L}\right)^{-\mu(p-p^\alpha)/(2^\alpha-2)} = \left(\tfrac{r}{L}\right)^{-\mu_p}, \tag{8}$$

where μ_p is the scaling exponent of the p-th order moment of $\epsilon(\boldsymbol{x})$. Then we find

$$\mu_p = \mu\frac{p^\alpha - p}{2^\alpha - 2} \qquad \text{for } 0 < \alpha \leq 2. \tag{9}$$

It may be interesting to note the asymptotic form of the *pdf* of ϵ_r at small and large values of ϵ_r. We can show, using asymptotes (5), that for $1 < \alpha < 2$,

$$P_\epsilon\left(\epsilon_r|\tfrac{r}{l}\right) \sim \begin{cases} \frac{1}{\epsilon_r(-\ln\epsilon_r)^{\alpha+1}} & \text{as } \epsilon_r \to 0, \quad \text{(10a)} \\ \exp\left[-A(\ln\epsilon_r)^{\alpha/(\alpha-1)}\right] & \text{as } \epsilon_r \to \infty. \quad \text{(10b)} \end{cases}$$

---

† The moment $\langle \mathrm{e}^{pa}\rangle_{r/l}$ for negative p does not exist.

Asymptote (10a) implies that the *pdf* diverges nearly inversely proportionally to ϵ_r at the origin. Therefore, the moment of ϵ_r of any negative power does not exist. Asymptotic expression (10b) at large ϵ_r shows that the *pdf* decreases faster than any power decay.

The present results (9) of the scaling exponents of the energy dissipation rate may be compared with experiments. Since, however, $\epsilon(\boldsymbol{x})$ is difficult to measure in laboratory experiments, we compare here our results with experimental measurements of scaling exponents of Δv_r, the velocity difference at two points separated by r. If $\langle(\Delta v_r)^p\rangle$, the p-th order moment of Δv_r, has a power dependence on r,

$$\langle(\Delta v_r)^p\rangle \sim r^{\zeta_p}, \tag{11}$$

then we find, using (8), (9) and relation

$$\Delta v_r \sim \epsilon_r{}^{\frac{1}{3}} r^{\frac{1}{3}}, \tag{12}$$

that

$$\zeta_p = \frac{p}{3} - \mu \frac{\left(\frac{p}{3}\right)^\alpha - \frac{p}{3}}{2^\alpha - 2}. \tag{13}$$

Exponents ζ_p were measured by Anselmet *et al.* (1984) up to $p = 18$ in a jet turbulence at $R_\lambda = 852$. We compare our results (13) with their data by the least-squares method to obtain the best fit with $\mu = 0.20$ and $\alpha = 1.65$. In Fig. 1, we plot the variation of exponent ζ_p against p for various values of α and for $\mu = 0.2$ together with the experimental values. For $\alpha = 2$, exponent (13) reduces to the prediction

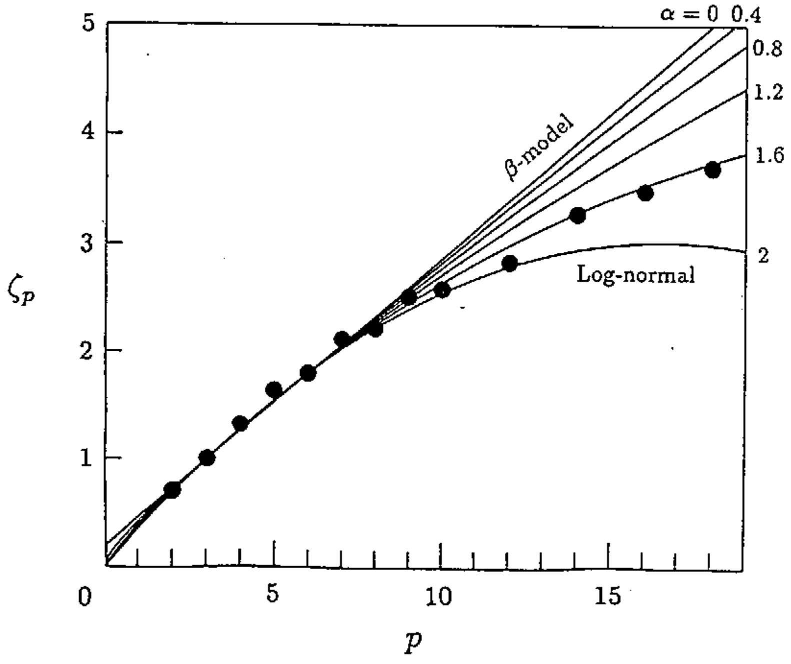

Fig. 1. Scaling exponents ζ_p of velocity differences.

of the log-normal theory, while it coincides with that of the β-model in the limit $\alpha \to 0$. The experimental data are distributed between these two extremes. They are very close to our theory with $\alpha \approx 1.6$ over $2 \leq p \leq 18$.

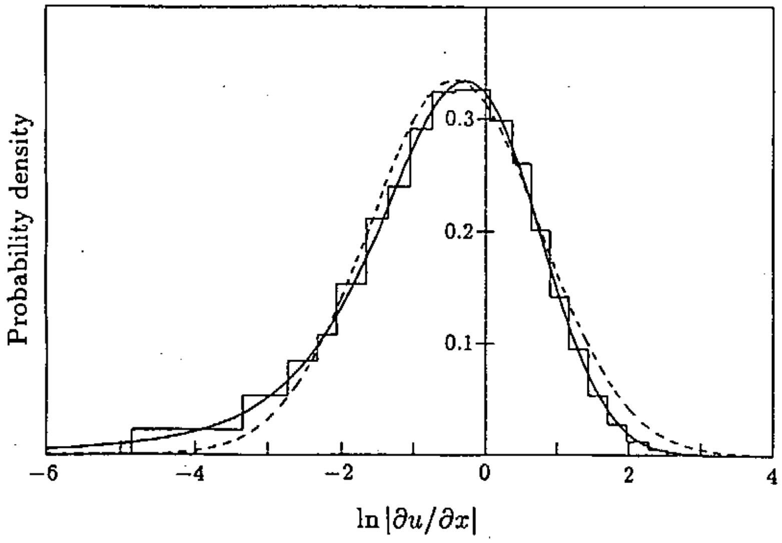

Fig. 2. The probability density function for $\ln|\partial u/\partial x|$.

Another independent comparison is made in Fig. 2, where we plot, with bar graph, the *pdf* of the logarithm of absolute value of the derivative of velocity in a turbulent boundary layer measured by Stewart *et al.* (1970). The solid and broken curves are the log-stable distribution (with $\mu = 0.2$ and $\alpha = 1.65$) and the log-normal distribution, respectively. Both of these theoretical distributions are shifted and scaled appropriately so that they are best fitted to the measured probability density by the least squares method. It is well known that the *pdf* of $\ln|\partial u/\partial x|$ is asymmetric with respect to the mean value; it has a longer tail for very small values of $\ln|\partial u/\partial x|$ than for very large values so that the skewness is negative. Therefore the log-normal distribution, which is symmetric, inevitably underestimates (overestimates) it for small (large) values of $\ln|\partial u/\partial x|$. It is seen that the observed distribution is in excellent agreement with the log-stable distribution over the whole range shown in the figure. Remember that this agreement is achieved by using the values of parameters μ and α determined by comparing with an independent experiment. This suggests the possibility that these parameters may be universal independent of the kinds of turbulence. A theoretical determination of them is however left for a future study.

References

F. Anselmet, Y. Gagne, E.J. Hopfinger & R.A. Antonia: J. Fluid Mech. **140** (1984) 63.
R.W. Stewart, J.R. Wilson and R.W. Burling: J. Fluid Mech. **41** (1970) 141.

Statistical Properties of Two-dimensional Magnetohydrodynamic Turbulence

D. Biskamp and H. Welter
Max-Planck-Institut für Plasmaphysik
8046 Garching bei München, Germany

After a brief introduction to the basic properties of MHD turbulence the statistical properties are discussed more in particular as obtained by evaluating a number of numerical turbulence simulation computations. First the probability distributions (PD) of various dynamical quantities are presented. For the field differences $\delta\vec{v}(\vec{r},\tau)$ $(=\vec{v}(\vec{x}+\vec{r},t+\tau)-\vec{v}(\vec{x},t))$, $\delta\vec{B}(\vec{r},\tau)$ the PDs are Gaussian at large separations $\vec{r}$ or τ, while they become approximately exponential for $\vec{r},\tau \rightarrow 0$. This behavior is very similar to that observed for Navier-Stokes turbulence and appears to depend only on the quadratic nonlinearity, as is shown by a simple probabilistic argument. The PD of the local energy dissipation rate $\epsilon(\vec{x},t)$ is consistent with a log-normal distribution at larger ϵ but exhibits a different behavior at small ϵ. In order to discuss intermittency the β-model developed for hydrodynamic turbulence is adapted to MHD. Comparison of simulation results of energy spectra with the β-model predictions shows intermittency corrections to be small, regarding both the spectral index of the inertial range and the dissipative scale. Fourth order correlations seem to exhibit a stronger intermittency effect, in particular a Reynolds number dependence of the flatness factor $F \propto R_\lambda^{1/2}$. Arguments are given that this behavior is, however, not yet characteristic of the asymptotic regime $R_\lambda \rightarrow \infty$, where a constant value of F is expected. (A similar conclusion was recently reached by R. Kraichnan.) As a result intermittency appears to be a weaker effect than presently assumed.

Turbulent dynamo and subgrid-scale modeling of MHD turbulence

Akira Yoshizawa
Institute of Industrial Science
University of Tokyo
7-22-1, Roppongi, Minato-ku, Tokyo 106

A bulk turbulent dynamo model is presented for understanding of the effects of MHD fluctuations. This model can explain some interesting properties of the steady state of MHD turbulence that are related to RFP and Earth's magnetic fields. A subgrid-scale model is also derived as a numerical approach for investigating the intermittent properties in these phenomena that are beyond the reach of the bulk dynamo model.

I . Effects of MHD fluctuations

The magnetic induction equation and the Navier-Stokes equation for a viscous, incompressible electrically conducting fluid are given by

$$\partial B/\partial t = \nabla \times (u \times B - \lambda j), \quad \nabla \cdot B = 0, \tag{1}$$

$$j = \nabla \times B = (1/\lambda)(E + u \times B), \tag{2}$$

$$\partial u/\partial t + \nabla \cdot (uu - BB) + 2\Omega \times u = -\nabla p_M + \nu \Delta u, \quad \nabla \cdot u = 0. \tag{3}$$

Here B is the magnetic field, u is the velocity, j is the electric current, E is the electric field,

p_M (= $p + B^2/2$; p is the pressure) is the MHD pressure, λ is the magnetic diffusivity (resistivity), ν is the kinematic viscosity, and Ω is the angular velocity of the rotating system. The Coriolis effect related to Ω is very important in Earth's magnetic dynamo.

We divide f into the ensemble-mean part or the filtered part $\bar{f}$ and the deviation f'; namely,

$$f = \bar{f} + f', \quad \bar{f} = \langle f \rangle \quad \text{or} \quad \int G(x-y) f(y) dy \qquad (4)$$

[$G(x)$ is the filter function]. The ensemble-mean or filtered equations of (1)-(3) are

$$\partial \bar{B}/\partial t = \nabla \times (\bar{u} \times \bar{B} + E_T - \lambda \bar{j}), \quad \nabla \cdot \bar{B} = 0, \qquad (5)$$

$$\bar{j} = \nabla \times \bar{B} = (1/\lambda)(\bar{E} + \bar{u} \times \bar{B} + E_T), \qquad (6)$$

$$\partial \bar{u}/\partial t + \nabla \cdot (\bar{u}\bar{u} - \bar{B}\bar{B}) + 2\Omega \times \bar{u}$$
$$= - \nabla p_M + \nabla \cdot R + \nu \Delta \bar{u}, \quad \nabla \cdot \bar{u} = 0. \qquad (7)$$

Here E_T and R are the so-called turbulent electromotive force and the Reynolds stress, respectively, which are defined by

$$E_T = \overline{u' \times B'} + E_{DF}, \qquad (8)$$

$$R = - (\overline{u'u'} - \overline{B'B'}) + R_{DF}, \qquad (9)$$

where the subscript DF means the double filtering effect, which will be neglected in this work.

II. Bulk dynamo model

In the bulk modeling based on the ensemble-mean quantities, we first express E_T etc. as[1]

$$E_T = \alpha \bar{B} - \beta \bar{j} + \gamma (\Omega + \bar{\omega}/2), \qquad (10)$$

with the aid of the results from a two-scale DIA[2]

[ω (= $\nabla \times u$) is the vorticity). The first two terms are very familiar as the alpha and beta effects, respectively.

In order to express α etc., we introduce the following one-point quantities;

$$K = (\overline{u'^2} + \overline{B'^2})/2 \text{ (MHD turbulent energy)}, \tag{11a}$$

$$W = \overline{u' \cdot B'} \text{ (cross helicity)}, \tag{11b}$$

$$H = \overline{B' \cdot j'} - \overline{u' \cdot \omega'} \text{ (residual helicity)}, \tag{11c}$$

$$\varepsilon = \nu \overline{(\partial u_j' / \partial x_i)^2} + \lambda \overline{(\partial B_j' / \partial x_i)^2}$$

$$\text{(energy dissipation rate).} \tag{11d}$$

Using (11), α etc. are modeled as

$$\alpha = C_1 H \varepsilon / K, \quad \beta = C_2 K^2 / \varepsilon, \ \cdots\cdot. \tag{12}$$

In order to close the equations for $\overline{B}$ and $\overline{u}$, we similarly model the transport equations for K, ε, W, and H. This system of equations is called the four-equation model in the terminology of fluid turbulence.

The bulk dynamo model is very useful in discussing about the steady global properties of phenomena, for instance, the validity of the concept of the helicity injection by the so-called F-Θ pumping.[3,4]

Ⅲ. SGS modeling

A major motivation of the SGS modeling is that the kinematic viscosity ν of plasma cannot be estimated experimentally, but that its magnitude has much influence on the level of MHD fluctuations.[5]

In the SGS modeling, the original ν is replaced by the turbulent viscosity ν_T, which is much larger than ν. Therefore the above difficulty can be avoided.

The policy of the SGS modeling is to construct a model as simple as possible and make full use of a large computer. At this time, the motion on the small energy-dissipative scale at high Reynolds numbers are estimated using the conservsation properties of the MHD energy, cross helicity, etc. For instance, let us consider the equation for K that

$$\partial K/\partial t + \nabla\cdot(\bar{u}K) = P_K - \varepsilon + \nabla\cdot T_K, \qquad (13)$$

where P_K (= $R_{ij}\partial \bar{u}_j/\partial x_i - E_T\cdot\bar{j}$) is the production rate and T_K is the transport rate. In the nearly steady state, we have

$$\int \varepsilon\, dV = \int P_K dV. \qquad (14)$$

We relax the condition to assume the local balance;

$$\varepsilon \fallingdotseq P_K. \qquad (15)$$

From (15), we can estimate ν_T, β, etc. in the functional form of $\nabla\bar{B}$ and $\nabla\bar{u}$.[6]

[1] A. Yoshizawa, Phys. Fluids B2, 1589 (1990).

[2] A. Yoshizawa, Phys. Fluids 28, 3313 (1985).

[3] A. Yoshizawa, Phys. Fluids B1, 983 (1989).

[4] F. Hamba, Phys. Fluids B (to appear).

[5] E.J. Caramana, Phys. Fluids B1, 2186 (1989).

[6] A. Yoshizawa, J. Phys. Soc. Jpn. 60, No.1 (to appear).

Hybrid Fluid/Kinetic Descriptions of Tokamak Plasmas*

J.D. Callen, Z. Chang, J.B. Hollenberg, J.P. Wang
University of Wisconsin, Madison, WI 53706-1687 USA

Introduction. Collisional fluid moment descriptions (resistive/neoclassical MHD, Braginskii equations [1], etc.) have provided many useful theoretical models of the macroscopic behavior [2], microscopic fluidlike instabilities, and equilibrium transport properties [3, 4] of tokamak plasmas. Such descriptions are considered useful because the distribution functions in tokamaks are experimentally measured to be nearly Maxwellian with small ($< 10^{-2}$) flow, etc. distortions, and because they embody the simplest representations of the (nonlinear) conservation of density, momentum and energy in tokamaks. However, the usual fluid moment descriptions neglect many important kinetic effects -- magnetic particle trapping, Landau damping, finite Larmor radius (FLR) effects, etc. At the other extreme, at least the simplest "collisionless" kinetic treatments of plasma instabilities (drift waves, trapped-particle instabilities, etc.) often do not include many important semi-collisional and nonlinear fluid effects -- momentum-conserving collisional friction between species, poloidal flow damping, bootstrap current, lack of transport for $\mathbf{E} + \mathbf{V} \times \mathbf{B} = 0$ perturbations, magnetic island structures, etc. In order to bridge this gap and to provide a comprehensive nonlinear theory of tokamak plasmas that includes both types of effects, we have developed [5] an exact Chapman-Enskog-like approach for determining the "small" kinetic distortions of species distribution functions that are needed to calculate the fluid moment closure relations -- primarily the stress tensors $\underline{\Pi}$, $\underline{\Theta}$. A first step in the hybrid fluid/kinetic direction was the development of neoclassical MHD [6], which extended the reduced resistive MHD equations [7] from the collisional Pfirsch-Schlüter regime into the long mean free path banana-plateau collisionality regime. Below, we briefly discuss neoclassical MHD, our new Chapman-Enskog-like approach, neoclassical MHD and linearized kinetic closure relations, the determination of net transport in our hybrid fluid/kinetic approach, and provide a brief summary of the status and future directions of this work.

Neoclassical MHD. The fundamental physical effect added to resistive MHD to obtain the neoclassical MHD equations [6] is the viscous damping of poloidal flows in tokamak plasmas. Mathematically, the parallel viscous force $\mathbf{B} \bullet \nabla \bullet \underline{\Pi}_{\parallel}$ is added to the parallel momentum balance equation. The addition of the consequent "magnetic pumping" produces poloidal flow damping, an enhanced polarization drift, the bootstrap current, and the electrical conductivity diminution due to trapped particles. In the original neoclassical MHD work [6] only the transport equilibrium ($\partial/\partial t << \nu$), flux-surface-averaged parallel viscous force $< \mathbf{B} \bullet \nabla \bullet \underline{\Pi}_{\parallel} >$ was available -- from the neoclassical transport work by Hirshman and Sigmar [4]. With our recent development of the Chapman-Enskog-like approach we have been able to more directly derive [8] this viscous force, and obtain its non-flux-surface-averaged form (see below). Further extensions of the parallel (and other) viscous force terms are currently being explored using our new Chapman-Enskog-like approach.

Chapman-Enskog-Like Approach. An Ansatz of a heat flow distorted distribution function not far from a flow-shifted local "dynamic" Maxwellian and fluid moment equations for n, T, V, q have been used [5] to recast the full kinetic equation (with a complete linearized Fokker-Planck Coulomb collision operator) into an equation for F -- the departure of the distribution function from its lowest order Maxwellian with "dynamic" fluid moments n(x, t), T(x,t), V(x, t), q(x, t). The needed closure relations are obtained by calculating the viscous stress tensor $\underline{\Pi}$, and heat stress tensor $\underline{\Theta}$ from solutions of the kinetic equation for F. Both the test particle and field particle (or momentum, energy restoring [9]) parts of the Coulomb collision operator are retained and shown to cancel various frictional force and dissipation terms. A drift-kinetic limit of the dynamics has also been developed [5] and found to be of the form (for $\nabla \bullet \mathbf{V} \cong 0$, $\mathbf{q} = 0$ for simplicity here)

$$\frac{\partial\langle F\rangle}{\partial t} + \left(v_{\|} + \mathbf{V}\right) \bullet \nabla \langle F\rangle - \left\langle C_R\left(\langle F\rangle\right)\right\rangle = \left(m/T\right)\left(v_{\|}^2 - v_{\perp}^2/2\right)\left(\mathbf{V} \bullet \nabla\ \ell n B\right) f_M + v_{\|}\, \mathbf{b} \bullet \nabla \bullet \underline{\Pi}\, f_M\ , \qquad (1)$$

where the < > brackets indicate averages over a gyroperiod. This Chapman-Enskog-like result clearly exhibits the fact that magnetic pumping ($\mathbf{V} \bullet \nabla\ \ell n\, B$) drives the $P_2\,(v_{\|}\,/\,v)$ or stress distortions of the distribution function.

Neoclassical Viscous Force. The parallel viscous force obtained from an equilibrium ($\partial/\partial t << \nu$) solution of Eq. (1) for an axisymmetric tokamak yields a parallel viscous force of the form $\mathbf{B} \bullet \nabla \bullet \underline{\Pi} = mn\mu\, U_\theta \langle B^2\rangle\ \hat{f}_T\,(\theta)$ where μ is the viscous damping coefficient ($\sim \sqrt{\varepsilon}\,\nu$ in the banana collisionality regime), and $U_\theta^{(\Psi)} = \mathbf{V} \circ \nabla\theta\ /\ \mathbf{B} \circ \nabla\theta$ is the poloidal flow flux function. The spatial shape factor $\hat{f}_T\,(\theta)$ is approximately $2 \sin^2\theta$ in the Pfirsch-Schlüter and plateau [10] collisionality regimes where $\mathbf{B} \bullet \nabla \circ \underline{\Pi} \sim (\mathbf{B} \bullet \nabla B)^2$. However, in the banana collisionality regime where the dominant physical effect is the viscous drag on the untrapped particle parallel (poloidal) flow, which is caused by the trapped particles, the shape factor $\hat{f}_T\,(\theta)$, albeit quite complicated, is fairly close in shape to the fractional trapped-particle density distribution $n_T(\theta)\ /\ n_o \cong \left[\varepsilon(1 + \cos\theta)\right]^{1/2}$. This extension to a non-flux-surface averaged parallel viscous force should be quite useful in numerical simulations of neoclassical MHD instabilities, turbulence and transport [11].

Linearized Kinetic Closures In A Sheared Slab. The general Chapman-Enskog procedure has also been used to develop closure relations for linearized drift-type microinstability problems. Neglecting the heat flux evolution equation, an appropriate linearized drift kinetic equation has been solved [12] in a sheared slab geometry for Lorentz-type collision model that includes momentum and heat restoring terms. The linearized closure relations that are obtained include full Landau damping and collisional effects, and reduce to the linearized Braginskii equations with all coefficients accurate to within a factor of two in the fluid, collisional limit. In the collisionless limit they reduce to the usual drift-kinetic Landau damping results. Our results show that Landau damping comes into the fluid equations through both the perturbed viscous stress and heat flux, instead of just the heat flux [13]. Simplified linear and nonlinear forms of these closure relations are presently being developed.

Development of Net Transport Equations. The flux-surface-average of our extended fluid moment equations yield "radial" transport equations that include classical, neoclassical and fluctuation-induced transport effects. It can be directly shown from these equations that while perturbations with $E + V \times B - (1/nq) \nabla p = 0$ cause no net transport (for $\nabla n \times \nabla T \equiv 0$, those which include dissipative effects due to plasma resistivity [14] and viscosity do. The net transport equations reduce to the neoclassical transport equations [3, 4] in the equilibrium ($\partial/\partial t << \nu$) limit where the fluctuation effects (fluidlike or kinetic) are negligible. In particular, they include the neoclassical bootstrap current, poloidal flow damping, irreducible minimum neoclassical ion heat conduction, and other effects which do seem to be observed experimentally in tokamaks. Turbulent fluctuations induce additional, anomalous transport through changes in the (second order and nonlinear) anomalous friction and viscosity in tokamak plasmas.

Summary and Discussion. The work presented above represents a beginning in the development of a comprehensive hybrid fluid/kinetic model for describing tokamak plasmas. The rigorous Chapman-Enskog-like approach which we have outlined has allowed us to add new effects (variation of parallel viscous force within a flux surface, linear Landau damping) to the closure relations. While we are constantly seeking to further expand the effects included through analytic calculations, it will undoubtedly be necessary to calculate many of the effects numerically. In fact, one can imagine a "grand challenge" class computational problem in which the kinetic equation for F is solved through computer simulation (via particle pushing, gyrokinetics or other techniques). Then, such results would be used to calculate the needed closure moments which in turn would be utilized in a fluid moment code that advances time at a very different rate. Alternatively, one could perform a DIA-type renormalization of a Chapman-Enskog-like kinetic equation like Eq. (1) to obtain nonlinear closure moments in the presence of strong turbulence effects. The Chapman-Enskog-like approach outlined here provides a rigorous framework for such future developments.

*Research supported by U.S. DOE grant no. DE-FG02-86ER53218.

[1] S.I. Braginskii, in Reviews of Plasma Physics (Consultants Bureau, NY, 1965), Vol. I, p. 205.

[2] See for example: J.D. Callen, B.V. Waddell, B.A. Carreras et al., Plasma Physics and Controlled Nuclear Fusion Research 1978 (IAEA, Vienna, 1979), Vol. I, p. 415.

[3] F.L. Hinton and R.D. Hazeltine, Rev. Mod. Phys. 48, 239 (1976).

[4] S.P. Hirshman and D.J. Sigmar, Nuclear Fusion 21, 1079 (1981).

[5] J.P. Wang and J.D. Callen, "Fluid-Kinetic Hybrid Moment Description of Plasmas Via A Chapman-Enskog-Like Approach," UW CPTC Report 90-8, (DRAFT: November 9, 1990).

[6] J.D. Callen et al., Plasma Physics and Controlled Nuclear Fusion Research 1986 (IAEA, Vienna, 1987), Vol. II, p. 157.

[7] H.R. Strauss, Phys. Fluids 19, 134 (1976); B.V. Waddell, B. Carreras, H.R. Hicks, J.A. Holmes, Phys. Fluids 22, 896 (1979).

[8] J.D. Callen, Z. Chang and J.P. Wang, "Direct Derivation of Neoclassical Viscosity Coefficients in Tokamaks," paper at EPS Amsterdam meeting, 25-29 June 1990.

[9] S.P. Hirshman and D.J. Sigmar, Phys. Fluids 19, 1532 (1976).

[10] W.M. Stacey, Jr., A.W. Bailey, D.J. Sigmar, K.C. Shaing, Nuclear Fusion 25, 463 (1985).

[11] J.D. Callen et al., Plasma Physics and Controlled Nuclear Fusion Research 1988 (IAEA, Vienna, 1989), Vol. II, p. 53; D.A. Spong et al., ORNL/TM-10947 (1988) and ORNL/TM-10951 (1988).

[12] Z. Chang, J.D. Callen, J.P. Wang, "Fluid/Kinetic Plasma Theory from a Chapman-Enskog Approach, Part II. Application to a Sheared Slab Geometry," Bull. Am. Phys. Soc. 35, 2037 (1990).

[13] G.W. Hammett and F.W. Perkins, Phys. Rev. Lett. 64, 3019 (1990).

[14] B.B. Kadomtsev and O.P. Pogutse, Plasma Physics and Controlled Nuclear Fusion Research 1984 (IAEA, Vienna, 1985), Vol. II, p. 69.

The Theory of Turbulence and Anomalous Transport in Plasmas: Past, Present, and Future

John A. Krommes
Princeton University, P.O. Box 451, Princeton, NJ 08543 U.S.A.

1. INTRODUCTION

The purpose of this lecture is to briefly review the theory of plasma turbulence, describe some recent developments, and comment on future directions. This is a daunting task, made even more difficult by a very severe length constraint. Therefore the discussion cannot possibly be complete, nor can the logic be unbroken. The reader is referred to the references for much more detailed discussion.

It is important to state at the outset what one expects from a "theory." To many people, it may suffice to determine a simple scaling law for a transport coefficient. Others will not be content until they have understood, both qualitatively and quantitatively, the intimate details of the nonlinear dynamics, both for an individual realization as well as on the average. In any event, it must be made clear that once a fundamental primitive nonlinear amplitude equation, such as that of Hasegawa and Mima,[1] has been specified, the remaining problem—of determining the associated transport, spectra, *etc.*—is essentially one of mathematics. A great deal of confusion results when one postulates behavior that, however desirable or intuitive, contradicts the actual mathematical behavior of the given equation.

At the simplest level, one is interested in transport coefficients, here generically called D. The theory of random walk leads to the form $D \sim \Delta x^2/2\Delta t$, where Δx and Δt are characteristic correlation lengths and times. For example, in drift-wave problems $\Delta x \sim \rho_s$ (where $\rho_s \doteq c_s/\omega_{ci}$, $c_s \doteq T_e/m_i$, and $\omega_{ci} \doteq eB/m_i c$) and $\Delta t \sim \omega_*^{-1}$ [where $\omega_*(k_y) \doteq k_y V_d$ and $V_d \doteq c_s \rho_s / L_n$]. Then $D \sim \rho_s^2 \omega_* \sim (\rho_s/L_n)(cT_e/eB) \equiv D_0$ for $k_\perp \rho_s = \mathcal{O}(1)$. This scaling is called "gyro-reduced Bohm." Such useful results do not require elaborate theories; they are simple dimensional consequences of the primitive equations.

On the other hand, the dimensional arguments are by no means complete. More precisely, the diffusion coefficient for a drift-wave problem might be written in the form $D = Cf(\gamma/\omega_*)D_0$, where C is a numerical coefficient, γ is a characterisic linear growth rate, ω_* is evaluated at some characteristic wavenumber, and f is an undetermined function. Detailed theories are needed to determine C and f, as well as more subtle details such as the fluctuation spectrum as a function of k and ω. Note, however, that *all* analytic theories will determine *some* numerical coefficient C. It is useless, then, to perform long analytic calculations based on unjustifiable algorithms, however tractable. A proper theory of turbulence is difficult and subtle; rapid progess must not be expected. However, in this work I report some encouraging advances.

The theory of plasma turbulence has many facets. Historically there were quasilinear theory[2,3] (QLT), weak turbulence theory[3] (WTT), resonance-broadening theory[4–6] (RBT), and clump theory[7,8] (CT), for example. Later, the importance of the direct-interaction approximation[9–13] (DIA) and related theories was recognized. Each of these can be classified as a *statistical closure*. Recently, an alternative procedure has been explored: the theory of *rigorous bounds* on transport.[14,15] Although it is possible to describe detailed logical connections between all of these, I cannot do so here because of limited space. Therefore, in Sec. 2 I shall merely comment briefly on RBT, CT, and the DIA. In Sec. 3 I describe state-of-the-art research on realizable Markovian statistical closures. In Sec. 4 I introduce the theory of rigorous bounds. Finally, in Sec. 5 I very briefly discuss trends for the future.

2. HISTORICAL PERSPECTIVE

In general, we shall be interested in nonlinear equations of the schematic form $\partial_t \psi + \mathcal{L}\psi + \frac{1}{2} U \psi\psi = \widehat{\eta}$. Here $\mathcal{L}$ is a linear operator, U is a coupling coefficient (an operator), and $\widehat{\eta}$ will later be set to 0. In plasma physics, Dupree was the first to go beyond QLT and WTT and to address regimes of strong turbulence, where perturbation theory is inappropriate. His RBT[4–6] provided a simple algorithm to determine transport in steady states. To place that theory in perspective, we introduce two of the fundamental objects in the theory of statistical dynamics[16,13]: the correlation function $C(\boldsymbol{x}, t, \boldsymbol{x}', t') \doteq \langle \delta\psi(\boldsymbol{x}, t)\, \delta\psi(\boldsymbol{x}', t') \rangle$ and the infinitesimal response function $R(\boldsymbol{x}, t; \boldsymbol{x}', t') \doteq \langle \delta\psi(\boldsymbol{x}, t)/\delta\widehat{\eta}(\boldsymbol{x}', t') \rangle_{|\widehat{\eta}=0}$. Here $\delta\psi \doteq \psi - \langle \psi \rangle$, $\langle \ldots \rangle$ denotes an ensemble average, and $\delta/\delta\widehat{\eta}$ denotes a functional derivative. Assume that the turbulence is statistically steady. Then C describes the intensity and correlation properties of finite-size fluctuations in the steady state, whereas R describes the relaxation of infinitesimal fluctuations away from the steady state.

2.1 Resonance-broadening theory

For definiteness, consider the simple drift-kinetic equation $\partial_t f + V_E \cdot \nabla f = 0$. (I temporarily ignore linear terms for simplicity.) The associated unaveraged response function $\widetilde{R}$ obeys $\partial_t \widetilde{R} + V_E \cdot \nabla \widetilde{R} + \left[(\delta V_E / \delta f)\widetilde{R}\right] \cdot \nabla f = \delta(x - x')\delta(t - t')$. The term in $\delta V_E / \delta f$ describes an important effect due to self-consistency, which Dupree ignored—essentially, he considered the problem of *passive advection*. Still following Dupree, now make the strong assumption that $V_E \equiv V$ is spatially uniform. Then upon Fourier-transforming one finds for the passive problem $\partial_t \widetilde{R}_k + i k \cdot V(t) \widetilde{R}_k = \delta(t - t')$. This so-called stochastic oscillator equation[17] can be solved exactly[10,13]; if one furthermore assumes that V is Gaussian, then on the average $R_k(\tau) = H(\tau)\exp(-k_\perp^2 D\tau)$ for time difference $\tau \doteq t - t'$ bigger than the autocorrelation time τ_{ac} of the velocity fluctuations. Here $D \doteq \int_0^\infty d\tau \, \langle \delta V_x(\tau) \, \delta V_x(0) \rangle$ and H is the Heaviside function. The diffusion effect induces a resonance-broadening due to random Doppler shifts, as is evident upon Fourier-transforming: if $\Sigma \doteq k_\perp^2 D$, then $R_{k,\omega} = 1/[-i(\omega + i\Sigma)]$, $\mathrm{Re}\, R_{k,\omega} = \Sigma/(\omega^2 + \Sigma^2)$. Dupree noticed that these forms can be derived from linear theory by replacing $\omega \to \omega + i k_\perp^2 D$. Then, in an unjustifiable leap of logic, he suggested that the true, nonlinear dielectric function $\mathcal{D}$ of the plasma could be simply obtained from the linear dielectric $\mathcal{D}^{(\ell)}$ according to $\mathcal{D}(k, \omega) = \mathcal{D}^{(\ell)}(k, \omega + i k_\perp^2 D)$. If the linear dispersion relation $\mathcal{D}^{(\ell)}(k, \omega) = 0$ leads to $\omega_k = \omega_{\mathrm{r},k}^{(\ell)} + i\gamma_k^{(\ell)}$, then $\mathcal{D}(k, \omega) = 0$ leads to $\omega_{\mathrm{r},k} = \omega_{\mathrm{r},k}^{(\ell)}$ and $\gamma_k = \gamma_k^{(\ell)} - k_\perp^2 D$; this then suggests the saturation criterion $\gamma_k = 0$, or $D = \gamma_k^{(\ell)} / k_\perp^2$. Here k must be interpreted as some characteristic wavenumber $\overline{k}$. Apparently, this algorithm immediately determines a diffusion coefficient!

However, although this result is dimensionally correct, it is impossible to justify the logic in detail. There are many points of concern: (1) Many diffusion coefficients characterize the turbulence; the RBT D may or may not be the particle diffusion coefficient. (2) It is unclear which k to use in the saturation criterion. Typically this is taken to be the most unstable linear mode, but that may not be where most of the energy resides nonlinearly. Furthermore, if the algorithm were taken literally, only one (marginal) mode would remain at saturation; that is not a turbulent state. (3) One began with a *passive* problem, but ended with a saturation level criterion for the velocity fluctuations. (4) The assumption of spatial uniformity of the advecting field is suspect. If the problem is intended to model aspects of self-consistent turbulence and if $\overline{k}$ is an energy-containing wavenumber, then the wavenumbers k of other energy-containing fluctuations satisfy $k \sim \overline{k}$, not $k \ll \overline{k}$. (5) As a consequence of the last point, the theory does not conserve important invariants such as the energy. (6) The nonlinear dispersion relation leads to a line spectrum: $\mathcal{D}(k, \omega)\delta\varphi_{k,\omega} = 0 \to \delta\varphi_{k,\omega} \propto \delta(\omega - \omega_{\mathrm{r},k})$. (The paradox is resolved by noting that R describes relaxation of instantaneous fluctuations *away* from steady state, whereas $\delta\varphi_{k,\omega}$ is a property *of* the steady state.) (7) Most importantly, there is no nonlinear *emission* term in the theory. The RBT is concerned with the behavior of the response function R, which describes nonlinear damping or absorption. However, in addition nonlinear forcing or emission must be present in order to support a steady state with many fluctuating modes.

2.2 Clump theory

RBT is a primitive theory of the nonlinear dielectric. Following Dupree,[8] I shall call the fluctuations associated with dielectric response[(a)] the *coherent* fluctuations $\delta f^{(\mathrm{coh})}$ and everything else the *incoherent* fluctuations $\delta f^{(\mathrm{inc})}$. Then exactly $\delta f = \delta f^{(\mathrm{coh})} + \delta f^{(\mathrm{inc})}$. Dupree further wrote[8] $\delta f^{(\mathrm{inc})} = \delta f^{(\mathrm{mc})} + \delta f^{(\mathrm{cl})}$, neglected without explanation the mode-coupling contribution $\delta f^{(\mathrm{mc})}$, and proposed the so-called *clump algorithm* to describe the effects of localized fluctuations $\delta f^{(\mathrm{cl})}$ on saturated turbulence. This algorithm has been analyzed extensively,[20,19] and fundamental logical flaws have been uncovered. The difficulty[19] is that mode-coupling effects are *everywhere*. Far from being ignorable, they contribute to both $\delta f^{(\mathrm{cl})}$ and $\delta f^{(\mathrm{coh})}$. Dupree's intuitive treatment is not in accord with the dynamics of the actual nonlinear equation or with the conventional definition of the dielectric function. The algorithm, which begins by computing the *clump lifetime* due to stochastic stretching, is a useful way of thinking about the very small scales[20]; however, it cannot be used for describing the mode coupling and saturation of the large, energy-containing scales. Transport coefficients are determined by the energy-containing fluctuations.

[(a)] Detailed discussions of the nonlinear dielectric function are given in Refs. 18 and 13. The proper definition of the coherent response is described in Refs. 13 and 19.

2.3 The direct-interaction approximation

In fact, Kraichnan had already by 1959 gone far beyond the scope of RBT and CT with his DIA.[9,10] This theory has been studied and reviewed extensively[13]; it is a reasonable starting point for discussions of saturation and transport, and it embraces[11] QLT, WTT, RBT, CT, and much more. The DIA equations are

$$\partial_t R_k(t;t')+\int_{t'}^{t} d\bar{t}\,\Sigma_k(t;\bar{t})R_k(\bar{t};t') = \delta(t-t'), \quad \partial_t C_k(t,t')+\int_0^t d\bar{t}\,\Sigma_k(t;\bar{t})C_k(\bar{t},t') = \int_0^{t'} d\bar{t}\,F_k(t,\bar{t})R_k^*(t';\bar{t}),$$

where the "mass operator" Σ and the "nonlinear noise" F are defined by

$$\Sigma_k(t;t') = -\sum_{p,q} M_{k,p,q}M^*_{p,q,k}R^*_p(t;t')C^*_q(t,t'), \quad F_k(t;t') = \tfrac{1}{2}\sum_{p,q}|M_{k,p,q}|^2\, C^*_p(t,t')C^*_q(t,t').$$

Nonlinear emission is described by F. (The operator $RFR^\dagger$ is positive-definite.) The DIA takes into account self-consistency in a reasonable way, conserves quadratic invariants, and leads to broadened spectra.

A further, most important property of the DIA is that it is *realizable*—it is the exact solution of an actual statistical problem. This can be demonstrated in several ways; for our purposes the best is to exhibit an underlying Langevin equation,[21] namely $\partial_t\psi_k + \mathcal{L}\psi_k + \int_0^t d\bar{t}\,\Sigma_k(t;\bar{t})\psi_k(\bar{t}) = \widetilde{f}_k(t)$, where $\widetilde{f}_k(t) \doteq \frac{1}{\sqrt{2}}\sum_{p,q} M_{k,p,q}\xi^*_p(t)\xi^*_q(t)$. Here ξ_k is an auxiliary *Gaussian* field whose covariance is constrained to be that of ψ_k itself. The mere existence of the Langevin equation ensures that solutions of the DIA are well-behaved. For example, it is guaranteed that $C(x,t,x,t) \geq 0$.

3. REALIZABLE MARKOVIAN CLOSURES

In general, it is necessary to solve the DIA numerically.[22] In plasma physics, the earliest work was that of Krommes,[23] who compared direct numerical solutions of a three-mode problem involving a strange attractor with solutions of the DIA; he found excellent agreement for the saturation levels. Unfortunately, the DIA exhibits an unfavorable scaling of computation time with the number of time steps N_T: Since for each t and t' a convolution over $\bar{t}$ must be performed, the run time is $\mathcal{O}(N_T^3)$. This is necessary in order that details of the two-time fluctuation spectrum be computed accurately. However, sometimes one is not interested in those details. For example, transport coefficients are given by one-point correlation functions in time. One therefore attempts to develop *Markovian closures*, which are local in time.

In a Markovian closure, one asserts that $\Sigma(t;t') = \eta(t)\delta(t-t')$, $F(t,t') \propto \delta(t-t')$. In a Langevin sense, this means that one represents the random nonlinear stirring as a *white noise* process in time: $\langle \widetilde{f}_k(t+\tau)\widetilde{f}_k(t)\rangle \propto \delta(\tau/\Theta_{k,p,q})$, where Θ is the *triad interaction time*: $\Theta_{k,p,q} = \int_0^t d\bar{t}\,R_k(t;\bar{t})R_p(t;\bar{t})R_q(t;\bar{t})$. (We are still omitting the linear terms, so Θ is real.) One therefore proposes the Markovian Langevin equation[21] $\partial_t\psi_k(t) + \eta_k(t)\psi_k(t) = \widetilde{f}_k(t)$, where $\widetilde{f}_k(t) = \frac{1}{\sqrt{2}}\sum_{p,q} M_{k,p,q}\left[w(t)\sqrt{\Theta_{k,p,q}}\right]\xi^*_p(t)\xi^*_q(t)$ and $w(t)$ is a Gaussian white noise process of unit intensity. One finds that Θ evolves according to $\partial_t\Theta_{k,p,q} + [\eta_k(t)+\eta_p(t)+\eta_q(t)]\Theta_{k,p,q} = 1$; note that in steady state $\Theta_{k,p,q}(\infty) = (\eta_k+\eta_p+\eta_q)^{-1}$. If one now defines $I_k(t) \doteq C_k(t,t)$, then one finds by proceeding from the DIA that $\eta_k(t) = -\sum_{p,q} M_{k,p,q}M^*_{p,q,k}\Theta^*_{k,p,q}(t)I_q(t)$; one is finally led to the computationally tractable spectral evolution equation $\partial_t I_k(t) + 2\eta_k(t)I_k(t) = \sum_{p,q}|M_{k,p,q}|^2\,\mathrm{Re}\,\Theta_{k,p,q}(t)I_p(t)I_q(t)$.

Unfortunately, severe difficulties emerge when one attempts to admit linear waves or non-Hermitean effects. In this case, one must replace η by $i\Omega + \eta$; Θ and η are now complex, so $\mathrm{Re}\,\Theta$ may no longer make sense as a triad interaction time. As an example, consider the equation $d\Theta/dt + \Delta\eta\,\Theta = 1$ for time-*independent*, complex $\Delta\eta$. The solution is $\Theta(t) = (1-e^{-\Delta\eta t})/\Delta\eta$, so $\mathrm{Re}\,\Theta(t) = |\Delta\eta|^{-2}\left\{\Delta\eta_r\left[1-e^{-\Delta\eta_r t}\cos(\Delta\eta_i t)\right] + \Delta\eta_i e^{-\Delta\eta_r t}\sin(\Delta\eta_i t)\right\}$; this quantity can easily be negative! Because the random force is proportional to $\sqrt{\Theta_{k,p,q}}$, *realizability fails*! Typically, this failure manifests itself by an explosion of the spectral functions $I_k(t)$ to $-\infty$.

Recently, progress has been made in the development of realizable Markovian closures that include the effects of waves. The final form of any such theory is heavily constrained by the desiderata of (1) realizability; (2) conservation of invariants; (3) covariance; (4) achieving a reasonable final state. The method[24] is, briefly, to *modify the transient dynamics* of $\Theta(t)$. As an example, the equation $d\Theta/dt + (\mathrm{Re}\,\Delta\eta)\Theta = \mathrm{Re}\,\Delta\eta/\Delta\eta$ does not exhibit an oscillatory approach to equilibrium, yet has the same final state as before. (This prescription, although quite simple, becomes quite involved when multiple fields are considered. Also, the actual realizable closures under present consideration[24] are more involved; the details cannot be described here.)

These ideas have been tested by careful comparisons between direct simulations and various closures for a forced, dissipative Hasegawa-Mima equation. A realizable closure with wave effects was found[24] to give excellent agreement with the simulations. The detailed results will be presented elsewhere.

4. RIGOROUS BOUNDS

Statistical closures attempt to compute the statistics as accurately as possible. However, since they are approximations, little can be said *a priori* about the relation of the results to the true dynamics. (Realizability does not necessarily imply accuracy.) An intriguing alternative is to determine a *rigorous bound* on the transport. By exploiting the rigorous steady-state balance equation for important energy-like quantities, one can develop nonlinear variational principles whose eigenvalues are upper or lower bounds on the true transport. Space precludes a detailed discussion here. However, the subject, relatively new to plasma physics, has been described in detail in a number of recent publications,[14,15] to which I refer the reader.

5. DISCUSSION

In summary, there have been promising advances in (1) the theory of realizable Markovian closures that include wave effects, and (2) the theory of rigorous bounds on transport. In addition, it is clear that as computing power increases, the already important role of direct simulations will correspondingly increase. However, I must caution that simulation is useless unless the results are interpreted in the light of detailed analytic theory. The theory of statistical dynamics provides the appropriate tools. In the future, I believe simulation and analysis will become ever more intertwined, in ways that we possibly do not presently anticipate. All of these areas pose fascinating, challenging problems for future research.

ACKNOWLEDGEMENTS

I am very grateful for many detailed and stimulating discussions with Dr. Ralph Smith and Dr. Chang–Bae Kim on the subject of rigorous bounds, and with Dr. Maurizio Ottaviani and Mr. John Bowman on the topics of realizability and other facets of plasma turbulence. This work was supported by U.S.D.o.E. Contract No. DE–AC02–76CHO3073.

REFERENCES

[1] A. Hasegawa and K. Mima, *Phys. Fluids* **21**, 87 (1978).
[2] W. E. Drummond and D. Pines, *Nucl. Fusion Suppl.* **Part 3**, 1049 (1962).
[3] R. Z. Sagdeev and A. A. Galeev, *Nonlinear Plasma Theory*, revised and edited by T. M. O'Neil and D. L. Book (Benjamin, New York, 1969).
[4] T. H. Dupree, *Phys. Fluids* **9**, 1773 (1966).
[5] T. H. Dupree, *Phys. Fluids* **10**, 1049 (1967).
[6] T. H. Dupree, *Phys. Fluids* **11**, 2680 (1968).
[7] T. H. Dupree, *Phys. Rev. Lett.* **25**, 789 (1970).
[8] T. H. Dupree, *Phys. Fluids* **15**, 334 (1972).
[9] R. H. Kraichnan, *J. Fluid Mech.* **5**, 497 (1959).
[10] R. H. Kraichnan, *J. Math. Phys.* **2**, 124 (1961).
[11] J. A. Krommes, in *Theoretical and Computational Plasma Physics* (International Atomic Energy Agency, Vienna, 1978), p. 405.
[12] D. F. DuBois and M. Espedal, *Plasma Phys.* **20**, 1209 (1978).
[13] J. A. Krommes, in *Handbook of Plasma Physics*, edited by M. N. Rosenbluth and R. Z. Sagdeev. Vol. 2: *Basic Plasma Physics II*, edited by A. A. Galeev and R. N. Sudan (North-Holland, Amsterdam, 1984), Chap. 5.5.
[14] J. A. Krommes and R. A. Smith, *Ann. Phys.* **177**, 246 (1987).
[15] C.–B. Kim and J. A. Krommes, *J. Stat. Phys.* **53**, 1103 (1988); J. A. Krommes, in *Proc. Int. Conf. on Plasma Physics* (Indian Academy of Sciences, Bangalore, India, 1989), in press; J. A. Kronunes and C.–B. Kim, *Phys. Fluids B* **2**, 1331 (1990).
[16] P. C. Martin, E. D. Siggia, and H. A. Rose, *Phys. Rev. A* **8**, 423 (1973).
[17] R. Kubo, *J. Math. Phys.* **4**, 174 (1963).
[18] J. A. Krommes and R. G. Kleva, *Phys. Fluids* **22**, 2168 (1979).
[19] J. A. Krommes and C.–B. Kim, *Phys. Fluids* **31**, 869 (1988).
[20] J. A. Krommes, *Phys. Fluids* **29**, 2756 (1986); in *Proceedings of the Fifth Statistical Plasma Physics Workshop of U.S.–Japan Joint Institute for Fusion Theory Program* (Nagoya U. P., Nagoya, Japan, 1986), p. 226.
[21] R. H. Kraichnan, *J. Fluid Mech.* **41**, 189 (1970).
[22] R. H. Kraichnan, *Phys. Fluids* **7**, 1163 (1964).
[23] J. A. Krommes, *Phys. Fluids* **25**, 1393 (1982).
[24] M. Ottaviani, *Bull. Am. Phys. Soc.* **35**, 1968 (1990); J. Bowman, M. Ottaviani, and J. A. Krommes, work in progress (1990).

Ion Temperature Gradient Turbulence and Coherent Structures

D.I.Choi, B.G.Hong[a], F.Romanelli[b] and M.Ottaviani[b]
Korea Advanced Institute of Science and Technology
P.O.Box 150 Cheongryang, Seoul, Korea

To study the anomalous transport associated with the ion temperature gradient driven mode, we investigate the effect of magnetic shear on the coherent structure of the toroidal ion temperature gradient driven mode (η_i-mode) turbulence. Recent 2-D numerical simulations[1,2] of the η_i-mode show that long-lived, large scale coherent structures exist and considerably affect the level of magnitude of the anomalous transport. A significant reduction of the turbulent heat flux with respect to the quasilinear estimate and positive dependence on dissipations are indeed observed. We address the question whether the nonlinear equations admit a coherent solution in the presence of the magnetic shear.

The stationary solutions of the nonlinear equations describing the dynamics of η_i-mode are investigated and found to be a dipolar vortex in shearless case. This is a simple generalization of the dipolar vortex solution of the Hasegawa-Mima equation.

In the presence of the magnetic shear, we find a modified dipolar vortex solution through perturbation theory. The circular boundary of shearless modon solution becomes an ellipse and the number of free parameters reduce to one. This solution is self consistent as far as the radius of the vortex is small compared with the position of the ion sound turning points. The vortex dynamics will be as important as the turbulence represented by the wave components in the study of the anomalous transport.

1. B.G.Hong and W.Horton, Phys. Fluids B2, 978 (1990).
2. M.Ottaviani, F.Romanelli, R.Benzi, M.Briscolini, P.Santangelo and S.Succi, Phys. Fluids B2, 67 (1990).

---

a) Korea Atomic Energy Research Institute, P.O.Box 7, DaeDuk-DanJi, TaeJon, Korea

b) Associazione EURATOM-ENEA sulla Fusione, C.R.E. Frascati, 00044 Frascati (Roma), Italy

Three-Dimensional Particle Simulation of Trapped Electron Instabilities in Tokamaks

C. Z. Cheng and H. Okuda
Princeton Plasma Physics Laboratory, Princeton University, Princeton, NJ 08543

Abstract

Anomalous plasma transport due to dissipative trapped electron instabilities in toroidal geometry is studied by means of three-dimensional particle simulations. The electron dynamic is approximated with a guiding center drift-kinetic description, and the full ion dynamic is retained. The electron-ion pitch angle scattering is simulated by a Monte-Carlo collisional model. The collision frequency is chosen such that the bulk of the plasma is in the banana and the plateau regimes corresponding to high temperature tokamak experiments. Initially the particles have Maxwellian velocity distributions with density and temperature nonuniformities. Within an electron-ion collision time the electrons establish a neoclassical distribution, and a bootstrp current is formed consistent with the neoclassical theory. In the linear stage of the dissipative trapped electron instabilities, the growth rates and the radial and poloidal ballooning structures observed in the simulation agree well with linear theory. In the nonlinear stage of the dissipative trapped electron instabilities, the poloidal ballooning effect is reduced because of the generation of strong plasma turbulence due to E×B nonlinearity. The resultant wavenumber and frequency sprectra resemble the experimental observations. Particle and temperature diffusion, which is relatively small in the linear stage of the dissipative trapped electron instabilities, is enhanced rapidly in the nonlinear stage leading to the stabilization of the system. The observed particle diffusion agrees well with the gyro-reduced Bohm diffusion $D_\perp = (\rho_i / L_n)(cT_e / eB)$.

Edge Anomalous Transport in Heliotron/Torsatron

M. Wakatani and K. Watanabe
Plasma Physics Laboratory,
Kyoto University
H. Sugama
National Institute for Fusion Science
M. Yagi
Japan Atomic Energy Research Institute

Abstract

Resistive interchange instabilities (or g modes) destabilized by the pressure gradient in the unfavorable magnetic curvature region are studied to explain the edge anomalous transport which increases in the radial direction. First reduced resistive MHD model is applied to derive the transport coefficient. By extending this model several new effects are investigated for comparison with the Heliotron E experiment: 1) radial electric field effect on the g modes, 2) coupling between the g mode and the resistive drift wave and 3) coupling between the g mode and the η_i mode.

1. Transport driven by the g mode turbulence

Reduced MHD equations for stellarators are useful to study the g mode turbulence and associated anomalous transport$^{1\sim3)}$. Since the edge plasma beta value is assumed extremely low, magnetic fluctuations are negligible. For this situation $\boldsymbol{E} \times \boldsymbol{B}$ motion due to fluctuating electric field becomes a dominant transport process and the diffusion coefficient

$$D_\perp^0 = \frac{\eta c^2}{4\pi}\frac{\kappa\beta_p}{s^2} r \frac{d\Omega}{dr} \tag{1}$$

is obtained by using the mixing length theory or the scale invariance principle. Here η is resistivity, $\kappa = -r d \ln n/dr$, β_p is poloidal beta and $d\Omega/dr$ is averaged curvature due to stellarator field. The numerical coefficient of the expression (1) can be determined by the two-point renormalized theory$^{3)}$ which gives about 4. Although $D_\perp^0$ increases toward the edge of the plasma column, a numerical coefficient of the order of 10 is necessary to be consistent with the experiment.

Other point is that the resistive MHD model assumes 90° degree phase difference between the density fluctuation and the potential fluctuation. This seems different from the fluctuation measurements in Heliotron E$^{4)}$. By using a generalized Ohm's law we may extend the electrostatic resistive MHD model to include the diamagnetic drift effect[5)],

$$(\frac{\partial}{\partial t} + \hat{z} \times \nabla\phi \cdot \nabla)\nabla_{\perp}^{2}\phi = \frac{\omega_{ce}}{\nu_{e}}\nabla_{\parallel}^{2}(n - \phi) + \nabla n \times \nabla\Omega \cdot \hat{z} \tag{2}$$

$$\begin{aligned}\left(\frac{\partial}{\partial t} + \hat{z} \times \nabla\phi \cdot \nabla\right)(n + \bar{n})\\ = \frac{\omega_{ce}}{\nu_{e}}\nabla_{\parallel}^{2}(n - \phi) + \nabla(n - \phi) \times \nabla\Omega \cdot \hat{z},\end{aligned} \tag{3}$$

where $e\phi/Te \equiv \phi$, $\tilde{n}/n_0 = \bar{n} + n$, $\omega_{ci}t \equiv t$, $x/\rho_s \equiv x$, $v/c_s \equiv v$. These two-field model equations for $\{n, \varphi\}$ will be discussed in §3.

2. Radial electric field effect on g mode

Here we use the reduced MHD model in the electrostatic limit,

$$\left(\frac{\partial}{\partial t} + \hat{z} \times \nabla\phi \cdot \nabla\right)\nabla_{\perp}^{2}\phi = -\frac{\omega_{ce}}{\nu_{e}}\nabla_{\parallel}^{2}\phi + \nabla n \times \Omega \cdot \hat{z} \tag{4}$$

$$\left(\frac{\partial}{\partial t} + \hat{z} \times \nabla\phi \cdot \nabla\right) n = 0, \tag{5}$$

to study the radial electric field effect on the linear g mode. In the (x, y, z) coordinates the electrostatic potential is written as $\phi = \phi_0(x) + \tilde{\phi}(x, y, z)$. In the sheared slab magnetic field of $\boldsymbol{B} = B_0[(x/L_s)\hat{y} + \hat{z}]$, $\nabla_{\perp} = \hat{x}\,\partial/\partial x + \hat{y}\,\partial/\partial y$ and $\nabla_{\parallel} = \hat{y}(x/L_s)\partial/\partial y$, where $x = 0$ is the mode resonant surface. The profile of $\phi_0(x)$ is given by to satisfy

$$v_E(x) = \hat{z} \times \nabla\phi_0 \cdot \hat{y} = v_0 \tanh(x/L_E). \tag{6}$$

In the slab model $\nabla\Omega = [d\Omega(x)/dx]\hat{x}$, and two parameters $\kappa = -(dp_0(x)/dx))/p_0(x)$ and $g = [d\Omega(x)/dt](P_0/\rho_0)$ are introduced in the linear stability analysis. The eigenvalue equation is obtained by linearizing (4) and (5),

$$\left[\frac{d^2}{d\xi^2} - k^2 + \frac{\mu^2\alpha u''}{\bar{\omega} - \alpha u} - \frac{1}{(\bar{\omega} - \alpha u)^2} - i\,\frac{\xi^2}{\bar{\omega} - \alpha u}\right]\tilde{\phi} = 0, \tag{7}$$

where $\xi = x/\Delta$, $\Delta^{-1} = [B_0^4 k_y^2/\rho_0^2 g\kappa\eta^2 c^4 L_s^4]^{1/6}, \bar{\omega} = \omega/\gamma_g, \gamma_g = [\rho_0 g^2\kappa^2\eta\, c^2 L_s^2 k_y^2/B_0^2]^{1/3}$,

$k = k_y\Delta$, $\alpha = k_y v_0/\gamma_g$, $\mu = \Delta/L_E$, $u = \tan h(\mu\xi)$, $u'' = -2u(1 - u)$.

Here it should be noted that γ_g and Δ correspond to the linear growth rate and the characteristic mode width of g mode without the poloidal shear flow, respectively. Figure 1 shows the growth rate of the g mode modified by the flow $v_E(x)$ as a function of α for different μ in the small $k_y\Delta$ limit. The conditions, $k_y v_0 > \gamma_g L_E/\Delta$ and $\Delta < L_E$, are required for decreasing the growth rate. If we consider $k_y \simeq 0.2(\text{cm}^{-1})$ and $\gamma_g \simeq 10^5\text{sec}^{-1}$, $\alpha \sim 3$ requires $v_o \sim 1.5 \times 10^6 cm/sec$. At present $v_0 \gtrsim 10^6$cm/sec is not realized in the Heliotron E.

3. Drift resistive interchange turbulence driven transport

Linear stability analysis of the drift resistive interchange mode described by eqs.(2) and (3) gives

$$\omega = \frac{\pi}{2}\frac{a}{\rho_s \varepsilon \left|k_{\parallel}'\right|}\frac{\omega_g \omega_*}{\left|\omega_g - \omega_*\right|^{1/2}}\nu_e^{1/2}\frac{(1+i)}{\sqrt{2}} \tag{8}$$

for $\omega_g = m/r(d\Omega/dr) < \omega_* = -m/r(1/n_0 \cdot dn_0/dr)$ in the sheared cylindrical plasma model, where $\varepsilon = a/R_o$. The eigenvalue is valid in the semi-collisional regime. The important parameter for eqs.(2) and (3) are $A = |\omega_{ce}\nabla_{\parallel}^2/\nu_e|$. When $A \gg 1$ or adiabatic care, the Boltzmann relation $\tilde{n} \simeq \tilde{\varphi}$ is realized and transport rate decreases. On the other hand, for $A \ll 1$ or non-adiabatic case, deviation from the Boltzmann relation becomes large and the growth rate given by (8) also increases. The left figure of Fig.2 shows the poloidal mode number spectra of $\sum_n |n_{mn}|^2$ and $\sum_n |\phi_{mn}|^2$ for $A \ll 1$ case, where m and n are poloidal and toroidal mode number; respectively. It is clearly seen that the density fluctuation spectrum has a larger m component than the potential fluctuation. This means that the real space density fluctuation structure has a finer scale than that of the potential fluctuation. The right figure of Fig.2 shows the poloidal mode number spectra for $A \gg 1$ case, which shows that $\tilde{n} \simeq \tilde{\varphi}$ is approximately valid. The both potential fluctuation spectra in Fig.2 are similar. Thus the density fluctuation of $A \gg 1$ becomes smoother than that of $A \ll 1$ and the resultant particle flux decreases.

Since ν_e increases radially for $r/a \gtrsim 0.8$ in the Heliotron E experiment, this result may be consistent with the increase of $D_\perp$ in the radial direction. When the density fluctuation spectra are observed in various positions, we can compare the above result with experiment.

4. g mode coupled to η_i mode

Here we show that the g mode couples to the η_i mode driven by the ion pressure gradient linearly in the presence of the unfavorable magnetic curvature. The η_i mode appears for $\tilde{n} \simeq \tilde{\phi}$ in the regime of $k_{\parallel}^2 v_{Te}^2 > \omega\nu_e$. The condition for the g mode is that the electrons behave adiabatically in the regime of $k_{\parallel}^2 v_{Te}^2 < \omega\nu_e$. Hence the mode structure in a collisional plasma in the sheared magnetic field with the unfavorable curvature will be strongly affected by the mechanism driving the g mode near the resonant surface and the η_i mode in the finite $k_{\parallel}$ regime around the resonant surface for $\eta_i \equiv d\ell n T_i/d\ell n n_o \gtrsim 1$. We have derived the following four-filed equations including the coupling between the η_i mode and the g mode$^{6)}$,

$$\frac{n_o m_i c}{B_o}\left(\frac{\partial}{\partial t}\nabla_{\perp}^2\phi + \frac{c}{B_o}[\phi, \nabla_{\perp}^2\phi]\right) - \frac{1}{\omega_{ci}}\frac{c}{B_o}\nabla_{\perp}\cdot[P_i,\ \nabla_{\perp}\phi] = -\frac{B_o}{c\eta}\nabla_{\parallel}^2\left(\phi - \frac{nTe}{en_o}\right) + [P_i + nTe, \Omega] \tag{9}$$

$$n_o m_i\left(\frac{\partial}{\partial t}v_{\parallel i} + \frac{c}{B_o}[\phi,\ v_{\parallel i}]\right) = -\nabla_{\parallel}P_i - en_o\nabla_{\parallel}\phi, \tag{10}$$

$$(11)\quad \left(\frac{\partial}{\partial t}n + \frac{c}{B_o}[\phi,\ n]\right) = -\frac{cn_o}{B_o}\left[\phi - \frac{nTe}{en_o}, \Omega\right] - n_o\nabla_{\|}v_{\|i} - \frac{1}{en_o\eta}\nabla_{\|}^2\left(\phi - \frac{nTe}{en_o}\right),$$

$$(12)\quad \frac{\partial}{\partial t}P_i + \frac{c}{B_o}[\psi,\ P_i] = 0,$$

where $[f,\ g] = \nabla f \times \nabla g \cdot \hat{z}$ is a Poisson bracket. From eqs.(9)-(12) the eigen-value equation is written as

$$(13)\quad \left(\frac{d^2}{d\zeta} + \Gamma - \frac{\zeta^2}{4} - \frac{\Lambda}{\zeta^2 + \zeta_R^{*2}}\right)\tilde{\phi} = 0,$$

where $\Gamma = i\frac{\bar{\omega}}{2|s|}\left(k_y^2 + \frac{\bar{\omega_g}}{\bar{\omega}} + \frac{\bar{\omega} - 1}{\bar{\omega} + K}\right) + \frac{\tau_R^2}{4}$, $\Lambda = i\frac{\bar{\omega}\tau_R^2}{2|s|}\frac{\bar{\omega} - 1}{\bar{\omega} + K} + \frac{\tau_R^2}{4}\frac{\bar{\omega} - \bar{\omega_g}}{\bar{\omega}}$,

and $\bar{\omega} = \omega/\omega_{*e}$, $s = Ln/Ls$, $K = (1 + \eta_i)/\tau$, $\tau = Te/Ti, \bar{\omega_g} = Ln\ d\Omega/dr$,

$$\tau_R^2|s| = 2\nu_e\ m_e/\omega_{*e}m_i, \zeta_R^{*2} = \tau_R^2(\bar{\omega} - \bar{\omega g})/\bar{\omega}.$$

Figure 4 shows the growth rate of the mode with a radial mode number of $\ell = 0$ as a function of $\nu_* \equiv \nu_e/\omega_{*e}$ for $K = 2, k_y = 2.74 \times 10^{-2}$ and $s = 7.35 \times 10^2$ corresponding to $q = 1$ surface of Heliotron E. Here $\bar{\omega_g} = 0$ case (curve b) corresponds to the slab η_i mode. The unfavorable average curvature case of $\bar{\omega_g} = 0.181$ enhances growth rate compared to curve b). Both curves a) and b) show a destabilizing dependence on the collision frequency. When ν_* increases, the radial mode structure expands, as shown in Fig.4, due to the coupling to the g mode.

In Heliotron E the new type of η_i mode coupled to the g mode is destabilized strongly for $\eta_i \gtrsim 1$, which may produce the ion anomalous thermal transport in the edge region.

5. Summary

Theoretical results of the g modes may be promising for understanding the edge turbulence and the anomalous transport in Heliotron E. When the wave number spectrum of the density and the potential fluctuations at various radial positions and the particle transport driven by the edge turbulence are obtained like in the TEXT tokamak, we may compare the details of the g mode theory with the data. We also expect that the radial electric field improves the energy confinement of Heliotron E.

References

1) M.Yagi, M.Wakatani and A.Hasegawa, J.Phys.Soc.Jpn 56(1987)973.
2) M.Yagi, M.Wakatani and K.C.Shaing, J.Phys.Soc.Jpn 57(1988)117.
3) H.Sugama and M.Wakatani, J.Phys.Soc.Jpn 57(1988)995.
4) H.Zushi et al., Nucl. Fusion 28(1988)433.
5) A.Hasegawa and M.Wakatani, Phys.Rev.Letters 59(1987)1581.
6) M.Yagi et al., J.Phys. Soc. Jpn 58(1989)4265.

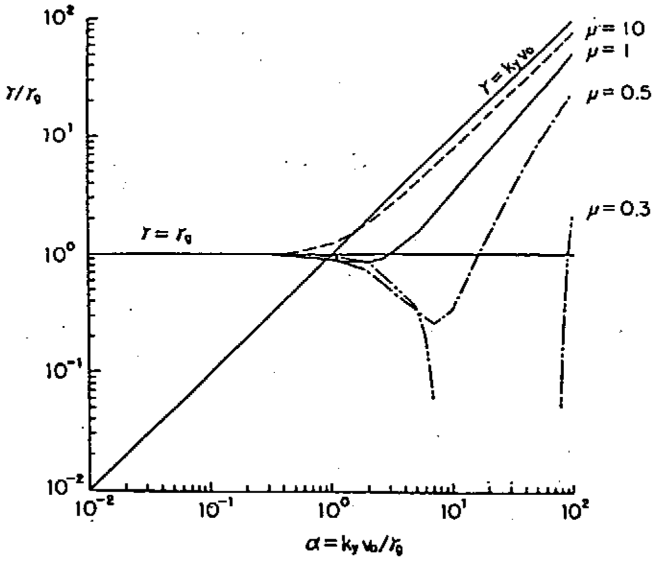

Fig.1 Growth rate of g mode in the presence of sheared poloidal flow.

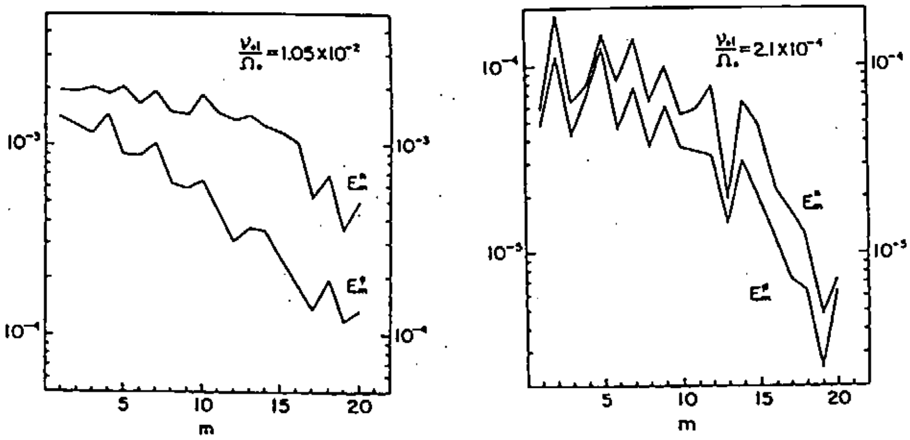

Fig.2 Poloidal mode number spectra of density fluctuation (E_m^n) and potential fluctuation (E_m^ϕ) for $\nu_e/\omega_{ce} = 1.0 \times 10^{-2}$ (left) and $\nu_e/\omega_{ce} = 2.1 \times 10^{-4}$ (right).

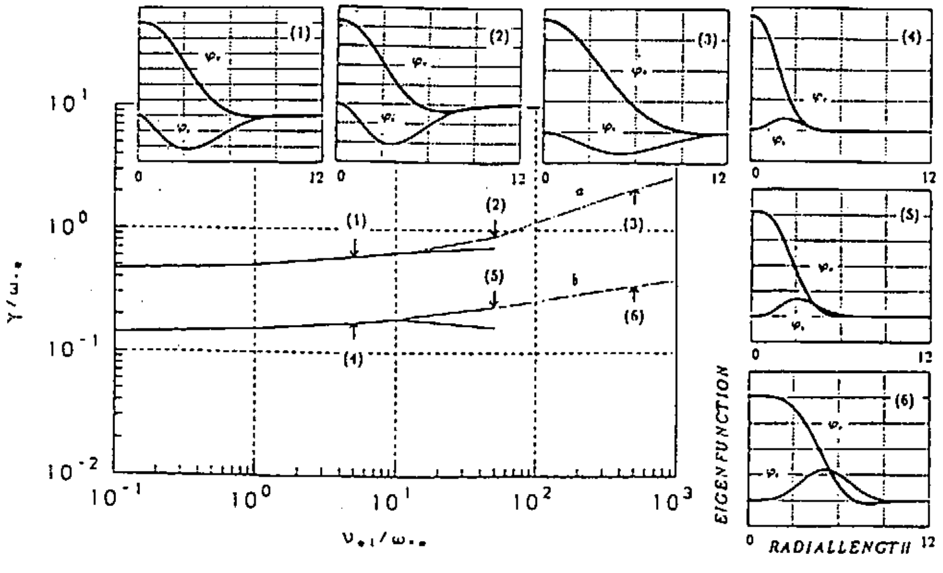

Fig.3 Growth rate ν/ω_{*e} versus ν_{ei}/ω_{*e} for a) $\bar{\omega}_g = 0.181$ and b) $\bar{\omega}_g = 0$. Radial eigenfunctions, ϕ_{real} and ϕ_{imag}, of $\ell = 0$ mode are shown for three ν_{ei} cases. Thick lines show analytic growth rate for both cases.

Sec. Int. Toki Conf.,1990

OPTIMIZATION, NON-LOCAL MHD-MODE, AND α-PARTICLE CONFINEMENT BEHAVIOUR OF HELIAS EQUILIBRIA

W. LOTZ, J. NÜHRENBERG, C. SCHWAB
IPP-Euratom Association,
Max-Planck-Institut für Plasmaphysik,
Garching, Federal Republic of Germany

Stellarators need optimization because classical physics issues seriously limit their viability as fusion devices. Such issues are for example their magnetic surfaces, their MHD and neoclassical properties, and their realization by coils. On the other hand, stellarators can really be optimized. An example for their optimization potential are quasi-helically symmetric toroidal magnetic fields [1] which show that the magnetic geometry of a stellarator can be decoupled from its real space geometry. Thus, stellarator optimization does not only mean an improvement of some given basic concept but primarily the selection of basic physics properties.

Stellarator optimization naturally divides into a set of general guidelines and a set of specific physics objectives.

The plasma behaviour in the confinement region can be optimized by noting that the geometry of the confinement boundary within the last closed flux surface completely determines the properties of the confinement region. Thus, boundary value problems may be solved during optimization, the parameters of the boundary being the optimization variables. Boundary value problems are the basic steps of the optimization procedure employed here, which allows large steps to be taken in the stellarator configurational space. The boundary representation used for Helias [2] equilibria appears to provide a suitable configuration space.

In this paper, the objectives of the optimization and its result as well as aspects of the MHD stability and the collisionless α-particle confinement behaviour of the optimized configuration are described.

1. OPTIMIZATION OF HELIAS CONFIGURATIONS

For the optimization of Helias configurations for W VII-X the following set of criteria has been used [3]:

1. high quality of vacuum field magnetic surfaces (sufficiently small relative thickness Δ_{is} of islands),
2. good finite-β equilibrium properties (sufficiently high β_{eq}),
3. good MHD stability properties (sufficiently high β_{stab}),
4. small neoclassical transport in the $\frac{1}{\nu}$-regime (small equivalent ripple δ_{e}),
5. small bootstrap current in the lmfp-regime ($J_{\mathrm{BS,stell}}/J_{\mathrm{BS,tok}}$ sufficiently small),
6. good collisionless α-particle containment (fraction of prompt loss f_α sufficiently small),
7. good modular coil feasibility (sufficiently large distances Δ_{c} and radii of curvature R_{c} of the coils).

The constructiveness of this set of classical physics goals in connection with an optimization procedure results from the dimensionless goodness parameters indicated above.

Criteria 1 and 7 are taken into account by solving Helias boundary value problems with side conditions on the shaping parameters. Criteria 2 and 3 are satisfied by maintaining resistive-interchange and ballooning stability at $\langle\beta\rangle \approx 0.05$ for configurations with 5 periods and aspect ratio of approximately 10. Maintaining resistive-interchange stability is directly incorporated into the optimization, while ballooning stability is taken into account through its driving terms [4]. Criteria 4, 5, and 6 are taken into account by optimizing the structure of $B(\theta, \phi)$ in magnetic coordinates. This optimization procedure constitutes an inner optimization loop.

The evaluation of ballooning stability and of the three neoclassical properties 4, 5, and 6 leads to an iteration of this inner loop until satisfactory properties are found. Goodness parameters $\Delta_{\rm is}$, $\beta_{\rm eq}$, $\beta_{\rm stab}$, $\delta_{\rm e}$, $J_{\rm BS,stell}/J_{\rm BS,tok}$, f_α which can simultaneously be achieved appear to be 0.1, 0.05, 0.05, 0.01, 0.1, 0.1 [5].

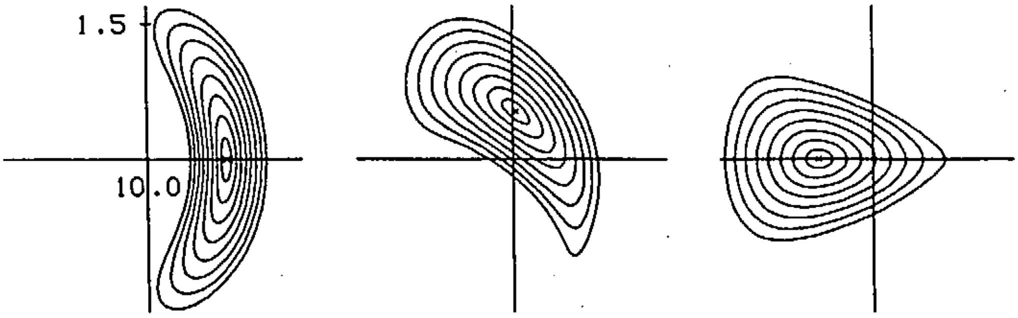

Fig. 1: Flux surface cross-sections of a configuration obtained by the optimization prescription described below. Shown are sections at the beginning of a period, after quarter of a period, and after half a period.

An explanation for the compatibility of the seven criteria listed above can be obtained in terms of a unified optimization procedure. Key ingredients are:

i) it suffices to consider the structure of $B(\theta,\phi)$; the real space geometry is a result of the optimization;

ii) the spectrum of $B(\theta,\phi)$ can be optimized;

iii) a unified optimization procedure simply consists in keeping the spectrum pure and in minimizing the helical and toroidal curvature terms under the constraints of small bootstrap current and location of trapped particles in the weak-curvature region.

Indeed, optimization in a large (approximately 20 dimensional) space of boundary variables [6], in which only an ellipticity and a triangularity parameter are kept fixed, with the above prescription yields the configuration in Fig. 1, which is nearly identical with the one obtained by optimization according to the seven criteria listed above. Ingredient iii) of the optimization procedure described above elucidates the degree of unambiguity of the optimization result. The major type of a qualitatively different result would be obtained by requiring the principle toroidal curvature term to be zero; this would result in quasi-helically symmetric equilibria with a finite bootstrap current. The solution chosen here essentially eliminates the bootstrap current as an alien element of stellarators proper and, on the other hand, achieves the other neoclassical physics requirements (see sec. 1.1, principles 4 and 6); here it has to be noted that the good collisionless α-particle confinement requires a non-vanishing β-value, see Sec. 3.

2. MHD-MODE BEHAVIOUR

Global mode calculations made with the Finite-Element Fourier code CAS3D [7] (Code for the Analysis of the MHD Stability of 3D Equilibria) concentrated on applications to unstable and stable Helias configurations with 5 equilibrium periods, aspect ratio 10, $\langle j_\parallel^2/j_\perp^2\rangle \approx 0.7$ and a small-shear ι-profile including the rational $\iota = {}^3\!/_4$. Parameter studies in a set of configurations of this type show that, though the low-poloidal-node-number non-local modes are less restrictive than the Mercier criterion, the two stability limits are so close that, in practice, low-shear stellarators have to be Mercier stable. The results obtained from CAS3D demonstrate various critical aspects of the 3D linear stability analysis. For optimal convergence the calculation has to be based on a large number L (up to $L = 60$ has been considered) of Fourier components in the perturbation functions. For this purpose CAS3D provides an automatic selection process. Discussion of the various contributions to the energy functional shows that energy minimization occurs simultaneously with the annihilation of the field line compression term. Near the Mercier stability limit the mode localizes radially. These and other aspects were successfully embedded into the code development (CAS3D1, which only employs the perturbation component $\vec{\xi}\cdot\nabla s$ in the eigenvalue problem). Furthermore, the dominating poloidal mode number M of the perturbations enters the code as an input parameter which is not connected with the spatial resolution of the stability calculation so that high-M unstable modes could be obtained.

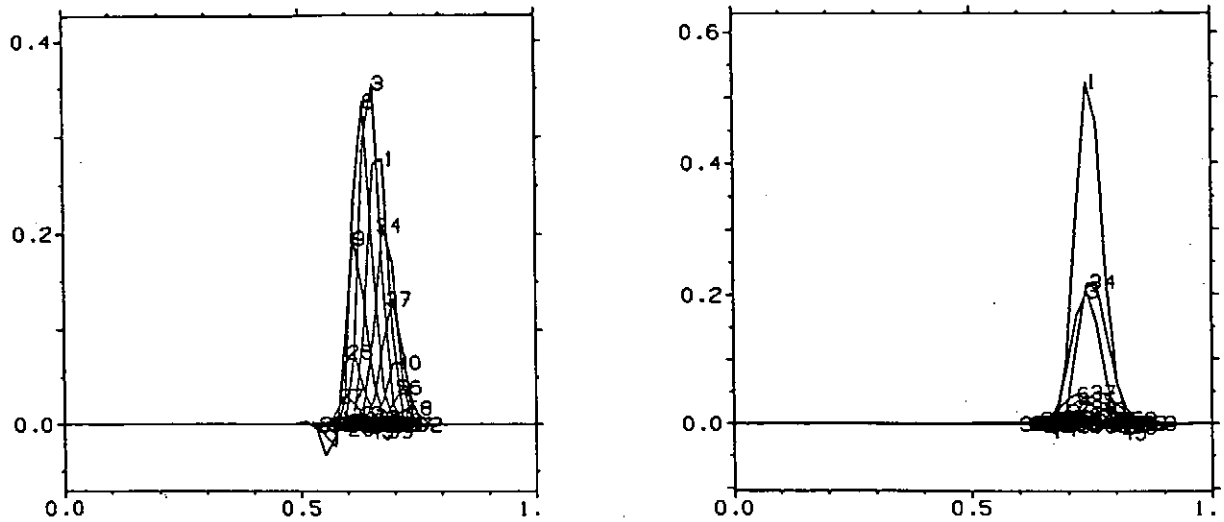

Fig. 2: Fourier coefficients of $\vec{\xi} \cdot \nabla s$ as obtained from CAS3D1MNint for a strongly-negative-shear Mercier stable 3D stellarator (left) and for a weakly-positive-shear Helias equilibrium. The toroidal node number is 72.

With a further modification concerning the numerical stability of the discretized eigenvalue problem [8], the code (CAS3D1MNint) has also been used to investigate modes with ballooning character in tokamaks and stellarators. Ballooning modes in Mercier stable stellarators with significant negative shear (i.e. a rotational transform decreasing towards the plasma edge) have been obtained. Fig. 2 shows the transition of high-node-number ballooning mode behaviour in such a case to the structure of these modes in the weakly-positive-shear situation of Helias equilibria.

As results of these investigations the following statements can be made. In Helias stellarators Mercier mode stability has to be satisfied to avoid global modes and low-poloidal-node-number ballooning modes then do not exist.

3. COLLISIONLESS α-PARTICLE CONFINEMENT

The collisionless α-particle confinement is assessed by guiding centre orbits of a sample of α-particles started at aspect ratio $A = 40$ (which corresponds to $1/4$ of the plasma radius a) with random values in the angular-like magnetic coordinates θ and ϕ and the pitch angle $\eta = v_{\|}/v$. In W VII-AS all α-particles that undergo reflections are quickly lost, but no passing particle is lost. In a quasi-helically symmetric stellarator all particles are completely confined. A particular characteristic of the optimized configuration of Sec. 1 is that the β-effect at $\langle\beta\rangle \approx 5\%$ is sufficient to improve the α-particle confinement in such a way that the fraction of prompt losses is reduced to approximately 0.1 [9], see Fig. 3.

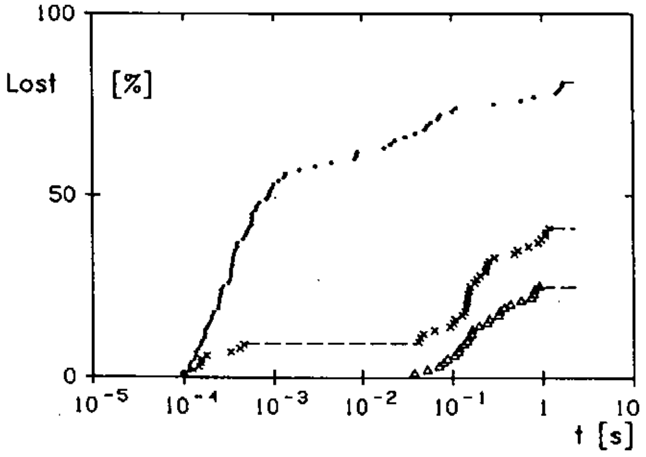

Fig. 3: α-particle losses in Helias50B with $\langle\beta\rangle = 0(\circ)$, 0.024 ($\times$), and 0.049 ($\triangle$); as a function of collisionless time of flight. A random sample of α-particles (ratio of plasma to gyroradius 30) is started at aspect ratio 40. Shown is the fraction of reflected particles which is lost. Number of reflected particles is 100 in all cases. Altogether there are 260 particles, i.e. 160 passing particles. Each symbol indicates the loss of one particle.

A significant improvement of the fast particle losses already occurs at the modest value of $\langle\beta\rangle = 0.024$, which may also be of importance for NBI- and ICR-heating.

The favourable collisionless particle confinement result can be understood in terms of the creation of a maximum-$\mathcal{J}$ configuration, with $\mathcal{J}$ the second adiabatic invariant. Figure 4 shows the formation of poloidally closed $\mathcal{J}$-contours as β is increased. Another way of characterizing the favourable orbit behaviour is shown in Fig. 5.

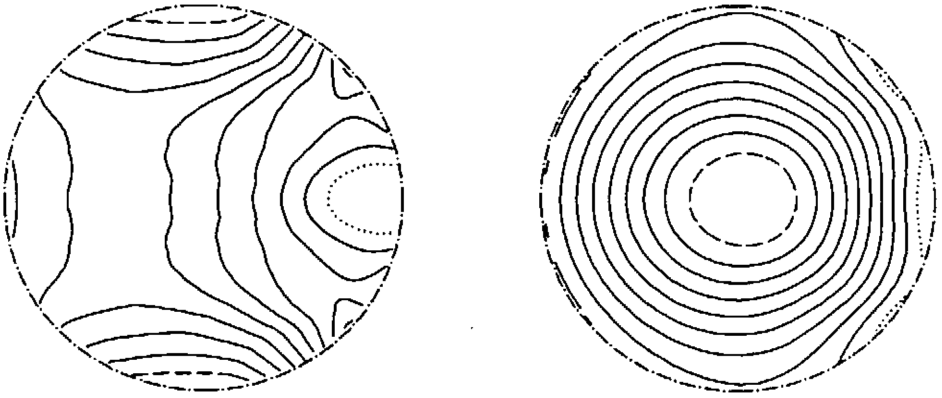

Fig. 4: Constant $\mathcal{J}$-contours in Helias50B with $\langle\beta\rangle = 0.0$ and $\langle\beta\rangle = 0.049$. Shown is a $\sqrt{s}$, θ-plane with s the flux label and θ the poloidal magnetic coordinate. Dashed lines indicate regions close to maxima, dotted lines those close to minima. The reflection value of B is a constant and defines the reflected particles considered as moderate-deeply trapped.

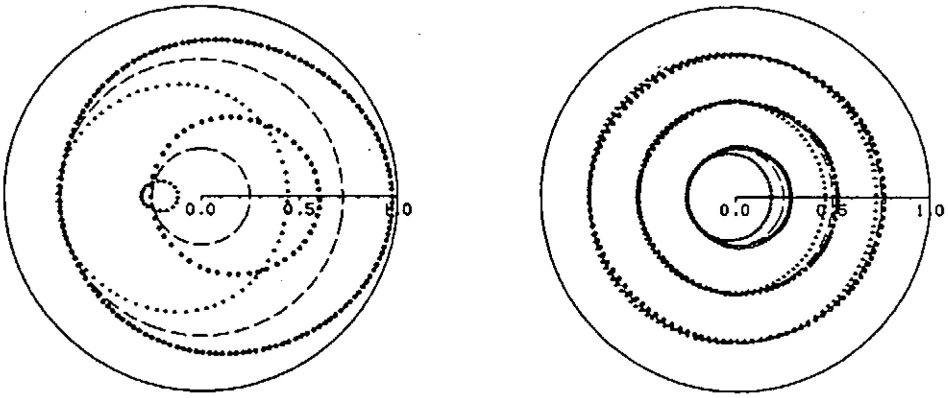

Fig. 5: Drift surfaces of barely passing α-particles in W7-AS (left) and the optimized Helias stellarator (plasma- to gyro-radius ratio 30). Start values for $\sqrt{s}$: 0.25, (0.5), 0.75; (+ positive $v_{\|}$; o negative $v_{\|}$).

REFERENCES

[1] NÜHRENBERG, J., ZILLE, R., Phys. Letters **129A** (1988) 113.

[2] NÜHRENBERG, J., ZILLE, R., Phys. Letters **114A** (1986) 129.

[3] GRIEGER, G. et al., Proc. 12th Conf. on Plasma Physics and Contr. Nuclear Fusion Research, Nice (FR) 1988, STI/PUB/787 (1989) 369.

[4] NÜHRENBERG, J., Zille, R., Int. Sherwood Theory Conf., San Antonio (US) 1989 (1989) 1D4.

[5] LOTZ, W., MERKEL, P., NÜHRENBERG, J., SCHLÜTER, A., ZILLE, R., IPP-Rep. 2/302 (1989) 8.

[6] NÜHRENBERG, J., Proc. First Int. Toki Conference 1989, Toki, Japan, NIFS-PROC-3 (1990) 29.

[7] SCHWAB, C., In: Theory of Fusion Plasmas (Bologna 1989) 85.

[8] SCHWAB, C., In: Theory of Fusion Plasmas, 1990.

[9] LOTZ, W., IPP-Rep. 2/302 (1989) 31.

EQUILIBRIUM BETA LIMIT OF HELICAL SYSTEMS

T.HAYASHI, A.TAKEI, N.OHYABU, T.SATO
National Institute for Fusion Science, Furocho, Nagoya, Japan

ABSTRACT

The equilibrium beta limit, which is defined by the breaking of magnetic surfaces due to the finite beta effect, is investigated for two types of helical systems. The results indicate that the breaking often imposes severer limitation on beta than the Shafranov shift. However, if we properly choose controllable parameters, such as the vertical field B_v, we can obtain a high beta equilibrium, such as $\bar{\beta} \geq 5\%$. Furthermore, a simple method is proposed, by which the breaking can be actively suppressed and fairly high beta equilibria with clearly nested magnetic surfaces can be realized.

1.Introduction

The equilibrium beta limit of a helical system is conventionally defined by the amount of the Shafranov shift, such as $\Delta_s(\beta) < \frac{\bar{a}_p}{2}$. However, we must care about the breaking of magnetic surfaces due to the finite pressure effect, since it is well known that a non-axisymmetric toroidal finite beta equilibrium does not necessarily regularly nest magnetic surfaces. The boundary region of a helical system is ergodic even in a vacuum field. Therefore, the physical issue in this paper is to investigate how large the boundary ergodic region expands in a finite beta equilibrium, as is shown in Fig.1, and to look for methods to suppress it. In spite of several works thus far, numerical evaluation of the breaking of magnetic surfaces due to the finite pressure effect remains unclarified,

The origin of the appearance of magnetic islands in a finite beta equilibrium of toroidal helical systems is attributed to the plasma current which is induced to satisfy the equilibrium force balance condition $\mathrm{j} \times \mathbf{B} = \nabla p$. The resonant field, which can be produced by the plasma current for the case of nonaxisymmetric torus, causes the appearance of magnetic islands inside the plasma. When an island is induced, the pressure profile is significantly modified near the island. Thus, a consistent analysis between the $\mathrm{j} \times \mathbf{B} = \nabla p$ condition and the island formation is required.

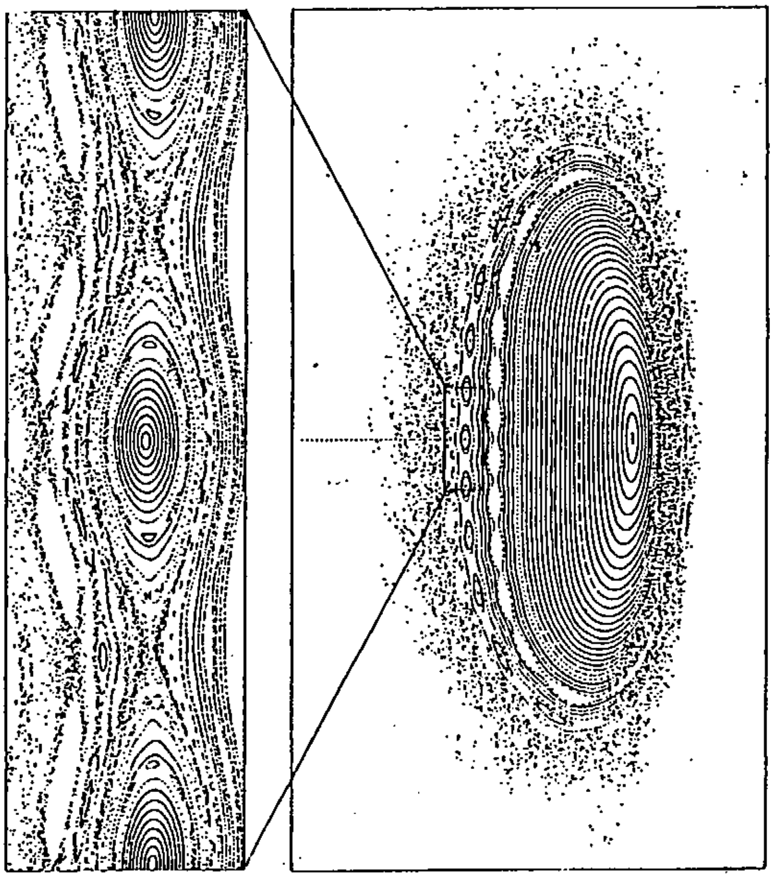

Fig.1 Magnetic surfaces of an $l = 2$ heliotron equilibrium with $\bar{\beta} \sim 4\%$, where islands are induced on the boundary due to the finite pressure effect. The induced islands area is expanded on the left.

In order to analyze quantitatively the total 3D effect of the plasma current on rational surfaces, we have developed a 3D equilibrium code (HINT).[1][2] In the following, we show results of HINT on Heliotron/Torsatron and Helias configurations and propose a simple method to suppress the breaking.

2. l=2 Heliotron/Torsatron

In order to understand the general tendency of the "fragility" of magnetic surfaces in a finite beta equilibrium, we have executed parameter survey for several kinds of physical parameters. The M (pitch period number) dependency of the breaking of magnetic surfaces is shown in Fig.2(a) for the l=2 heliotron configuration. This survey was made under conditions that the pitch parameter $\gamma_c \equiv \frac{M}{l}\frac{a_c}{R_c}$ is fixed to be 1.3, the vacuum magnetic axis is at the helical coil center, external quadrupole component $B_q = 0$, and the helical coil has no modulation. The broken line in Fig.2 indicates a tentative beta limit at which the outer region of about 30 % of the minor radius becomes ergodic. In general, the breaking has a tendency to be suppressed as M increases. For low M (low aspect ratio) configurations, however, we find that the breaking can be improved by properly choosing several free parameters.[2]

Figure 2(b) shows the effect of the external vertical field B_v, which controls the radial position of the vacuum magnetic axis. As is shown in Fig.2(b), the inward shift of the magnetic axis is favorable to suppress the breaking, and in fact, we can obtain the high beta equilibrium (such as $\bar{\beta} \geq 5\%$) keeping clearly nested surfaces by a small inward shift for the $M = 10$ configuration. As for the effect of B_q, vertically elliptic shaping of the surfaces is favorable to suppress the breaking. Another survey indicates that the breaking is significantly improved by decreasing $\gamma_c(= 1.2)$, or is also improved by making the helical coils positively modulated.

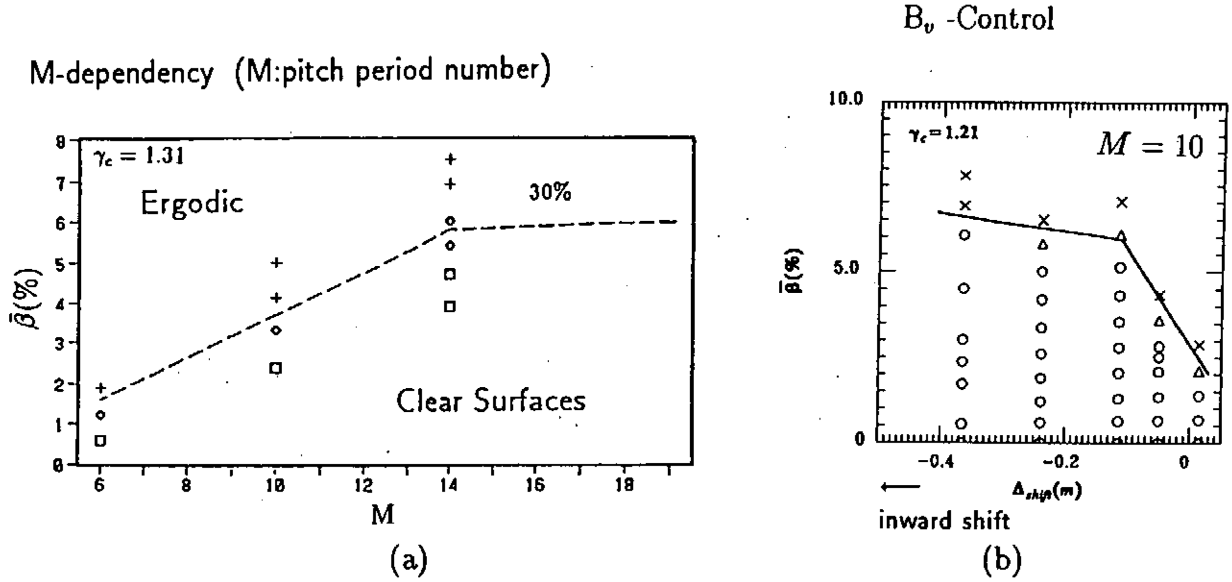

M-dependency (M:pitch period number)

B_v -Control

(a)

(b)

Fig.2 (a) M dependency and (b) B_v control of the breaking of magnetic surfaces for $l = 2$ heliotron configuration. Lines indicate a tentative beta limit at which the outer region of about 30 % of the minor radius becomes ergodic.

3. Helias

The Helias configuration [3], in contrast with the heliotron configuration, has a very low shear, but the Pfirsch-Schlüter current is optimized to be small. The island size induced by the finite pressure effect is determined by the competition between these effects. The way islands appear for the Helias is different from that for the heliotron case; the number of relevant dangerous rational surfaces is much smaller, but the size of islands is much bigger when they appear. The results indicate that the dangerous rational surface, that is the $\iota = 5/6$ surface, comes into the plasma region as beta increases, and m=6 islands are formed on the surface. However, the size of the island is not so serious as to destroy the whole plasma. When we further increase beta, the 5/6 surface is again removed away from the plasma region, and a high beta equilibrium with clear surfaces can be achieved. In this process, it turns out that the pressure profile plays an important role: A broader profile is favorable. This is because the magnetic axis shift becomes smaller and the change of iota profile is smaller, whereby the number of relevant dangerous rational surfaces can be suppressed.

4. Suppression of breaking by adding a simple extra coil

As is stated above, the axisymmetric external poloidal fields, such as B_v, can be used to suppress the breaking of surfaces. One problem of this method, however, is that such an external field significantly changes the physical properties of the configuration, such as the well depth. Here we propose another way to suppress the breaking. Islands which appear on a rational surface either in a vacuum field or in a finite beta field of a heliotron configuration have the following empirical properties; 1) the island size is noticeably larger on the outer side of the torus, and 2) islands appear in phase at the outside of the torus. By taking advantage of these properties, we can come up with a set of simple extra coils enough to suppress induced islands. This method is studied by using the Cary-Hanson technique [4] to measure the island size. Results indicate that islands which appear in a finite beta equilibrium of a $l = 2$ heliotron configuration are clearly suppressed by adding an extra coil. It is interesting to note that the required extra coil current is only about 3% of the helical coil current. One important advantage of this method is that the physical properties, such as the well depth and the ι profile, are very slightly changed when the extra coil field is imposed. Thus, this method can provide an efficient and powerful way to remedy magnetic islands for any reasonable beta value.

REFERENCES

[1] HARAFUJI, K., HAYASHI, T., SATO, T., *J. Comput. Phys.* 81 (1989) 169.

[2] HAYASHI, T., SATO, T., TAKEI, A., *Phys. Fluids B* 2 (1990) 329.

[3] NÜHRENBERG, J., MERKEL, P., *private communication.*

[4] CARY, J.R., HANSON, J.D., *Phys. Fluids* 29 (1986) 2464.

SUPPRESSION AND CONTROL OF MAGNETIC ISLANDS IN TOROIDAL PLASMAS

C. C. HEGNA and A. BHATTACHARJEE
Department of Applied Physics
Columbia University
New York, New York
United States of America

Y. NAKAMURA and M. WAKATANI
Plasma Physics Laboratory
Kyoto University
Kyoto, Japan

Abstract

In this paper, some recent theoretical developments on the formation and dynamics of magnetic islands in toroidal plasmas are reported. It is shown that an energetic ion population can have a significant effect on the nonlinear stability of a single-helicity tearing mode. A dynamical equation for the magnetic island width is derived from kinetic theory. It is shown that island growth can be suppressed in tokamak plasmas by injecting an energetic ion beam with a density profile which peaks just outside the rational surface. This technique can be used for suppressing major disruptions caused by the nonlinear growth of m = 2, n = 1 islands in a tokamak. The formation of magnetic islands as a result of plasma pressure in three-dimensional equilibria is also studied. The width of the equilibrium islands is shown to depend on the resistive interchange properties of the plasma.. This analytical theory is applied to the Heliotron-E configuration. Equilibrium beta limits due to the criterion of island overlap are investigated. It is suggested that experimental observations of internal disruptions on Heliotron-E can be interpreted as a loss of equilibrium due to island overlap. Energetic ions can also be used to modify magnetic islands in three-dimensional equilibria. It is shown that energetic ions can be used to reduce the size of equilibrium islands in a stellarator due to vacuum field errors.

1. INTRODUCTION

The formation of magnetic islands in toroidal magnetic configurations generally has a detrimental effect on the confinement properties of plasmas. Islands caused by resistive tearing instabilities [1,2] are believed to play a role in a variety of relaxation phenomena in toroidal discharges. In particular, the nonlinear growth of the m = 2, n = 1 tearing mode can trigger major disruptions. For confinement systems without a continuous symmetry, such as stellarators, magnetic islands exist in equilibrium. If the magnetic islands are large and overlap with each other, magnetic confinement is lost since stochastic magnetic fields cannot sustain a plasma pressure gradient.

In this paper, we examine two problems involving the formation of magnetic islands. In Section 2, we propose a method for drastically reducing the size of nonlinear $m \geq 2$ tearing modes by introducing a population of energetic ions in the vicinity of the magnetic island [3,4]. This technique can be used for disruption control in tokamaks by suppressing the growth of m = 2, n = 1 magnetic islands. In Section 3, we calculate the widths of magnetic islands induced by plasma pressure in stellarator equilibria [5] which extends earlier work on this subject [6]. When neighboring magnetic islands overlap, magnetic confinement is lost. This island overlap condition can then set an equilibrium beta limit in stellarators. The theory is applied to the Heliotron-E device in Section 4. It is demonstrated that experimental observations of internal disruptions on Heliotron-E are consistent with the interpretation of an equilibrium beta limit [7]. Finally, we apply the method introduced in Section 2 to show that an injected beam of energetic ions can be used to control the size of islands in stellarator equilibria [4].

2. SUPPRESSION OF TEARING MODES BY ENERGETIC IONS

In this section we present a method which can be used to suppress the nonlinear growth of $m \geq 2$ tearing modes. In order to understand the underlying physics of the calculation, we first give a simplified heuristic interpretation of the results in slab geometry [3,4]. Consider the equilibrium magnetic field given by $\mathbf{B} = B_0 \hat{\mathbf{z}} + B_y (x/L_s) \hat{\mathbf{y}}$ where $x = 0$ is the location of the rational surface, L_s is the local shear length, and B_0 is a large constant magnetic field in the $\hat{\mathbf{z}}$-direction. If a coherent symmetry-breaking perturbation $\mathbf{B}_1 = b_0 \sin(ky) \hat{\mathbf{x}}$ is imposed, magnetic islands of half-width $w = 2(b_0 L_s/kB_y)^{1/2}$ form at the rational surface. Fig. 1a shows the projection of the magnetic field in the $\hat{\mathbf{x}}$-$\hat{\mathbf{y}}$ plane.

The guiding center motion of an energetic ion is given by $\mathbf{v} = v_{\parallel}\mathbf{b} + \mathbf{v}_d$, where $\mathbf{b} = \mathbf{B}/B$, $B = |\mathbf{B}|$, and $\mathbf{v}_d = [(v_{\parallel}^2 + v_{\perp}^2/2)/\Omega_i]\, \mathbf{b} \times \nabla \ln B$ is the magnetic drift. For $B = B(x)$ and $B' > 0$, the drift velocity is predominantly in the $\hat{\mathbf{y}}$-direction. If the drift velocity is added to the field aligned velocity of the equilibrium field, the null line of the velocity of the equilibrium field is shifted by an amount

$$x_* = -\frac{(v_{\parallel} + v_{\perp}^2/2v_{\parallel})}{\Omega_i} \frac{L_s B_0}{L_B B_y},$$

from the null line of B_y, where $L_B = (d\ln B/dx)^{-1}$ and Ω_i is the hot-ion cyclotron frequency. (For toroidal geometry, $|x_*| \equiv \varepsilon q v_{\parallel}/\Omega_i$, where ε is the inverse aspect ratio and q, the safety factor .) In the presence of the perturbation, the spatial contours of the hot-ion velocity field show islands similar to the magnetic islands of Fig. 1a. This is shown in Fig. 1b, where the assumption $|x_*| > w$ is used. Note that the sign of $v_{\parallel}$ determines whether the islands form above or below $x = 0$. The contours of Fig. 1b represent constant-density contours of the hot ions.

If untrapped energetic ions have a net fluid velocity, they produce an electrical current. The plasma electrons tend to follow the ions in order to cancel this current; however, since the electrons scatter into the trapping loss cone faster than the ions, a net current in the direction of the ion flow results [8,9].

In the vicinity of the island, as shown in Fig. 1c, the effect of the perturbing field is to slightly deform the constant energetic ion contours from horizontal lines, as long as the inequality $|x_*| > w$ holds. We now allow for an energetic ion density gradient. For $n_h' > 0$, there are more ions at the top of Fig. 1c than at the bottom. For this density gradient, the energetic ions produce a current profile as one passes from the X-point of the island to the O-point with $j_{\parallel}(X) > j_{\parallel}(O)$. This spatial dependence of the current produces a magnetic field that is stabilizing. If the sign of the density gradient or the magnetic drift is reversed (given by B'), the energetic ions causes a field that enhances the perturbation. Note that the stabilizing effect is independent of the direction of injection of the energetic ions and depends only on the sign of $n_h' B'$.

The details of the calculation in toroidal geometry are carried out using a kinetic theory in the long mean-free-path regime [4], along with the usual Rutherford analysis [10]. Effects due to resistive interchanges [11], and bootstrap currents [12,13] are included in the calculation. The injected energetic ions are assumed to be circulating, so that the effects due to magnetic trapping of the energetic ions can be ignored.

The dynamical equation for the magnetic island half-width w of a nonlinear tearing mode is given by

$$\frac{1}{\eta_n}\frac{dw}{dt} = k_o\Delta' - Nw + \frac{Q}{w}, \tag{1}$$

where η_n is the neoclassical resistivity,

$$k_o = c^2\,|\Phi|^2/4\pi\ , \qquad N = 1.46\sqrt{\varepsilon}\,k_v\,\omega_{ph}^2\,d_\Phi \ln n_h / 4\pi\, d_\Phi \ln B\ ,$$

$$Q = 0.75\,(E+F)\,c^2\,|\Phi|^2 - 0.5\sqrt{\varepsilon}\,p'\,R^2\,c^2\,q_o/q_o'\ ,$$

where Φ is the toroidal flux function that labels magnetic surfaces, k_v is a numerical coefficient that is approximately one, ω_{ph} is the hot-ion plasma frequency, R is the major radius, and q_o and q_o' the safety factor and its derivative evaluated at the rational surface. The first term on the right-hand-side of equation (1) describes the magnetic free energy (measured by Δ') available to the tearing mode [10]. The term Q contains the effects due to resistive interchanges, described by the quantity E + F [14], and bootstrap currents. The new result of this analysis is the term Nw in equation (1). As mentioned above, this term is stabilizing if $n_h'\,B' > 0$. For discharges with $\Delta' > 0$, it is possible to control the island width by tailoring the hot-ion density profile. The saturated island-width is given by

$$w_s = k_o\Delta'/2N + \sqrt{(k_o\Delta'/2N)^2 + Q/N}\ . \tag{2}$$

Numerical estimates of w_s consistent with the inequality $|x_*| > w_s$ indicate that by using energetic ions, the saturated island width can be made much smaller than the usual quasilinear saturated island width [15]. The energy requirements for this scheme appear to be quite modest, and involve a small fraction of the energy expended on Ohmic or neutral-beam heating. Thus, our analysis suggests that it is possible to suppress the m = 2, n = 1 island in tokamaks by having the energetic-ion profile peak just outside the q = 2 surface.

3. MAGNETIC ISLAND FORMATION IN THREE-DIMENSIONAL PLASMA EQUILIBRIA

Well-defined magnetic surfaces do not generally exist for three-dimensional equilibria [16]. However, if one postulates the existence of magnetic surfaces, it can be shown that the general solution of the equilibrium equations contains singularities in the plasma current. To see this, assume that the magnetic field can be written

$$\mathbf{B} = \nabla\Phi \times \nabla(\theta - \iota\!\!\!-\phi)\ , \tag{3}$$

where Φ, θ, and ϕ are magnetic coordinates, where Φ is the toroidal flux function, θ and ϕ are the poloidal and toroidal angles, respectively, and $\iota\!\!\!-$ is the rotational transform. The magnetic field-lines lie on surfaces of constant Φ. The Jacobian, $\mathcal{J} = (\nabla\Phi\cdot\nabla\theta\times\nabla\phi)^{-1}$ and the parallel current profile $Q = \mathbf{J}\cdot\mathbf{B}/B^2$ are represented by a Fourier series

$$\mathcal{J} = \sum_{mn} \mathcal{J}_{mn}\, e^{im\theta - in\phi}, \quad Q = \sum_{mn} Q_{mn}\, e^{im\theta - in\phi}, \tag{4}$$

for equilibria with no symmetry. Using the force balance equation $\mathbf{J} \times \mathbf{B} = \nabla p$, and the quasineutrality condition $\nabla\cdot\mathbf{J} = 0$, we find $p = p(\Phi)$ and the current amplitude Q_{mn} has the general solution

$$Q_{mn} = -p'[\mathcal{J}_{mn}/(\iota - n/m)] + \hat{Q}_{mn}\, \delta(\Phi - \Phi_r), \tag{5}$$

where $\hat{Q}_{mn}$ is an undetermined amplitude of a current sheet at the rational surface $\iota(\Phi_r) = n/m$.

The singularity is resolved by allowing for the formation of a magnetic island at the rational surface. The magnetostatic equations are then solved for self-consistently. The detailed calculation [5] leads to an equation for the magnetic island half-width. Written in terms of the extent of the magnetic island as measured by the rotational transform, $\delta\iota$, the half-width of the magnetic island is given by the expression

$$\delta\iota = \frac{\rho}{2} + \sqrt{\left(\frac{\rho}{2}\right)^2 + |C|}, \tag{6}$$

where

$$\rho = \frac{(E + F)Z}{m_r} |\iota(a) - \iota(0)|, \tag{7}$$

$$C = \frac{\beta}{m_r^2 \varepsilon_t^2} \left(\frac{\mathcal{J}_{m_r n_r}}{\mathcal{J}_{00}}\right), \tag{8}$$

$E + F$ is the resistive interchange instability criteria [14], Z is a numerical constant $\cong 0.5$, $|\iota(a) - \iota(0)|$ is the total shear, and m is the poloidal mode number of the island. If $E + F$ is negative (indicating resistive interchange stability), equation (6) predicts a small island since the term $|C|$ is usually made small by design. However, if $E + F$ is positive (resistive interchange instability), magnetic islands may by large. Furthermore, if $E + F > 0$, it can be demonstrated that island overlap is inevitable [6]. The island overlap criterion establishes an equilibrium beta-limit that is generally more stringent than the ad hoc limit obtained by assuming that the flux surfaces are perfect, and then identifying the plasma beta at which the Shafarnov shift exceeds one-half of the plasma radius.

The present calculation assumes that the vacuum magnetic field has well-defined magnetic surfaces. If vacuum magnetic islands exists, equation (6) is modified by letting $|C| \rightarrow |C| + (\delta\iota_v)^2$, where $\delta\iota_v$ is the amplitude of the vacuum magnetic island. Notice that equation (6) predicts that devices with favorable resistive interchange properties can reduce the size of magnetic islands as plasma pressure is introduced [17].

To understand the physics of this result, it is useful to draw an analogy between 2-D axisymmetric systems with saturated 3- D instabilities, and intrinsically 3-D configurations [6]. In the 2-D case, the perturbations grow from the axisymmetric equilibrium until some nonlinear process saturates the mode. A 3-D equilibrium can then be thought of as a 2-D equilibrium with intrinsic symmetry-breaking perturbations. If the stellarator has unfavorable resistive interchange properties, the equilibrium has the same island structure as the axisymmetric device with saturated instabilities [11].

4. EQUILIBRIUM BETA LIMITS IN HELIOTRON-E

The theory of the previous section is now applied to the Heliotron-E experiment [7]. The island widths, given by equation (6) in the previous section, are evaluated numerically using a modified version of the STEP code [18]. Since Heliotron-E has unfavorable resistive interchange properties over a large part of the plasma, substantial magnetic island formation is predicted for Heliotron-E equilibria. Figure 2 plots the magnetic island half-width $\delta\iota_I$ computed for plasmas with $\beta(0) = 2\%$ and mode numbers m = 10–29. Also plotted is the width computed from the Chirikov criteria (given by $\delta\iota_c = |\iota_1 - \iota_2|/2$ where ι_1 and ι_2 are neighboring resonant surfaces). Notice that for $0.65 < \iota < 1.0$, island overlap is predicted since $\delta\iota_I > \delta\iota_c$. Although the analytical calculation breaks down when magnetic stochasticity occurs, this result is suggestive of an equilibrium beta-limit due to the onset of island overlap.

These results motivate us to revisit experimental observations of internal disruptions in Heliotron-E [19]. It is observed that as β increases for discharges with peaked pressure profiles, internal disruptions occur at $\beta \sim 2\%$ that lead to the flattening of the pressure profile. A possible explanation of this phenomena is that as the Heliotron-E plasma relaxes through a series of quasistatic, 3-D equilibria, magnetic islands form and increase in size with beta. When low-order islands become sufficiently large that they overlap with each other, magnetic stochasticity occurs and the pressure relaxes to a flat profile. The computation suggests that this occurs at $\beta \gtrsim 2\%$.

5. SUPPRESSION OF MAGNETIC ISLANDS IN STELLARATOR EQUILIBRIA WITH ENERGETIC IONS

An extension of the technique to suppress nonlinear tearing modes with energetic ions can be used to control island sizes in stellarator equilibria as well [4]. For this problem, we consider island widths that satisfy the inequality $|x_*| < w < a$, where a is the minor radius and the length $|x_*|$ is introduced in Section 2. (For the limit $|x_*| > w$, the physical picture given in Section 2 applies.) When w exceeds $|x_*|$, the energetic ions near the rational surface are trapped in the magnetic island at the rational surface. For this problem, Fig. 1a also represent constant density surfaces for the energetic ion population. In this limit, the direction of the net ion current and the sign of the shear determine whether the ions enhance or reduce the island size. If the islands are injected parallel to the magnetic field, with $\iota' > 0$, the ions produce a magnetic field with the same helicity as the perturbation and the island size increases; however, if the ions are injected antiparallel to the magnetic field, the magnetic island is suppressed.

In the detailed calculation, we assume that the source of the magnetic island is a vacuum field error. In the presence of a plasma and the injected ions, the island half-width is computed self-consistently. The island equation is given by

$$\delta\iota = \frac{S}{2} + \sqrt{\left(\frac{S}{2}\right)^2 + (\delta\iota_v)^2}, \tag{9}$$

where

$$S = \frac{8\pi}{c}\frac{k_s}{m_r}\frac{R\, f_t\, j_0}{B}\,\kappa \ , \tag{10}$$

$\delta \text{ƚ}_v$ is the vacuum magnetic island half-width, k_s is a numerical factor of order unity, m is the poloidal number of the rational surface, R is the major radius, f_t is the electron trapping fraction, $\kappa = \mathrm{sign}(\text{ƚ}')$ and j_0 is the injected energetic ion current. The sign of S is determined by the sign of $j_0\kappa$, so that if $j_0\kappa < 0$, the magnetic island width is smaller in the presence of the energetic ions than in the vacuum configuration.

ACKNOWLEDGEMENTS

This work is supported by the United States Department of Energy Contract No. DE-FG02-86ER-53222.

REFERENCES

[1] FURTH, H. P., KILLEEN, J., ROSENBLUTH, M. N., Phys. Fluids **6** (1963) 459.

[2] COPPI, B., GREENE, J. M., JOHNSON, J. L., Nucl. Fusion **6** (1966) 101.

[3] HEGNA, C. C., BHATTACHARJEE, A., Phys. Rev. Lett. **63** (1989) 2056.

[4] HEGNA, C. C., BHATTACHARJEE, A., Phys. Fluids B **2** (1990) 1804.

[5] HEGNA, C. C., BHATTACHARJEE, A., Phys. Fluids B **1** (1989) 392.

[6] CARY, J. R., KOTSCHENREUTHER, M., Phys. Fluids **28** (1985) 1392.

[7] NAKAMURA, Y., WAKATANI, M., HEGNA, C. C., BHATTACHARJEE, A., to appear in Phys. Fluids B.

[8] CONNOR, J. W., CORDEY, J. G., Nucl. Fusion **14** (1974) 185.

[9] FISCH, N. J., Rev. Mod. Phys. **59** (1987) 173.

[10] RUTHERFORD, P. H., Phys. Fluids **16** (1973) 1903.

[11] KOTSCHENREUTHER, M., HAZELTINE, R. D., MORRISON, P. J., Phys. Fluids **28** (1985) 294.

[12] CARRERA, R., HAZELTINE, R. D., KOTSCHENREUTHER, M., Phys. Fluids **29** (1986) 899.

[13] CALLEN, J. D., QU, W. X., SIEBERT, K. D., CARRERAS, B. A., SHAING, K. C., SPONG, D. A., "Neoclassical MHD equations, instabilities and transport in tokamaks", Plasma Physics and Controlled Nuclear Fusion Research 1986 (Proc. 11th Int. Conf. Kyoto, 1986), Vol. 2, IAEA, Vienna (1987) 157-166.

[14] GLASSER, A. H., GREENE, J. M., JOHNSON, J. L., Phys. Fluids **18** (1975) 875.

[15] WHITE, R. B., MONTICELLO, D. A., ROSENBLUTH, M. N., WADDELL, B. V., Phys. Fluids **20** (1977) 800.

[16] GRAD, H., Phys. Fluids **10** (1967) 137.

[17] TALMADGE, J., private communication, 1990.

[18] NAKAMURA, Y., ICHIGUCHI, K., WAKATANI, M., JOHNSON, J. L., J. Phys. Soc. Jpn. **58** (1989) 3157.

[19] HARRIS, J. H., et al., Phys. Rev. Lett. **53** (1984) 2242.
ZUSHI, H., et al., Nucl. Fusion **27** (1987) 895.

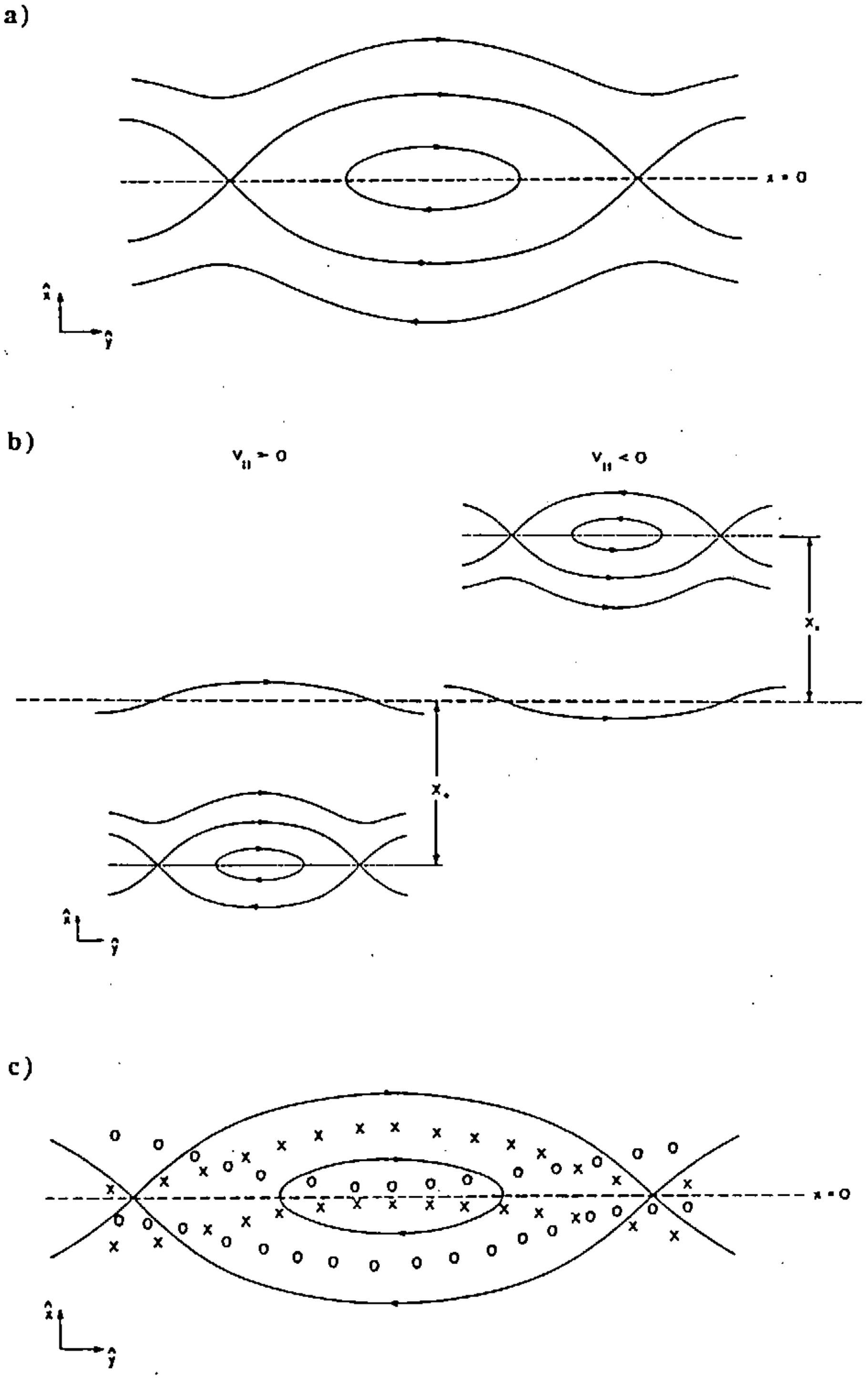

Figure 1

Fig. 1. (a) The projection of the magnetic field in the **x**-**y** plane. (b) The projection of the guiding-center velocity field for $v_{\|} = \mathbf{v}\cdot\mathbf{b} > 0$ and $v_{\|} < 0$. (c) The effect of the energetic ions with $|x_*| > w$. The solid lines are the magnetic field lines, with the X's representing constant-density contours for ions with $v_{\|} > 0$ and O's the constant-density contours for ions with $v_{\|} < 0$.

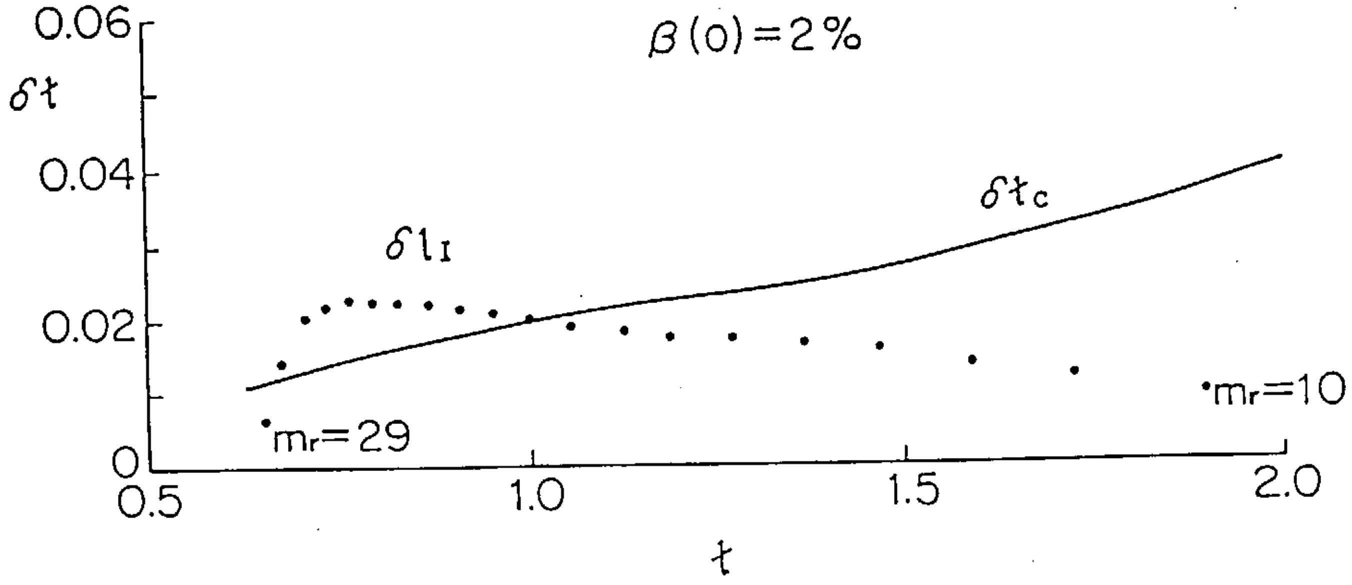

Figure 2

Fig. 2. Magnetic island widths $\delta ⱡ_I$ for $\beta = 2\%$ and pressure profile $p = p_0(1-\psi)^2$, where ψ is the poloidal flux function. The abscissae is the rotational transform which is used as a radial label. The Chirikov criterion for island overlap is also shown, and represented by $\delta ⱡ_c$. The region $\delta ⱡ_I > \delta ⱡ_c$ is assumed stochastic.

Theoretical Studies of Nonlinear Sheath Dynamics

Jae Koo Lee and Sang June Hahn

Department of Physics
Pohang Institute of Science and Technology
Pohang 790-600, KOREA

Abstract

Kinetic particle simulation of the system consisting of plasma, sheath, material, and an external driving circuit is carried out. The nonlinear sheath dynamics on the plasma ion implantation is studied in a series of simple simulations. Other similar applications include the dc and rf glow discharges for electronic material processing such as etching or doping. The unsteady acceleration and the polarity-dependent behaviors in the pulsed plasma accelerator are also studied in view of transient sheath dynamics.

I. Introduction

The plasma ion implantation[1] relies on the ion acceleration in the charge-nonneutral sheath region to a necessary energy ($10-50\ keV$), alleviating the cumbersome system of conventional ion implantor. The dynamic evolution of the sheath characteristics is highly nonlinear and complex especially when the applied negative voltage at the target material is modulated at a finite frequency to contain the sheath expansion to a manageable size. To have enough informations about the ion flux and energy distribution, the understanding of time-dependent sheath evolution is important. By using a kinetic particle code[2] in modest computing facilities, we calculate the average and peak currents together with the sheath size and the implanted ion energy distribution.

Capacitive rf discharges are widely used for matreial processing in the electronic industry. The discharges are usually asymmetric in the cylindrical and spherical shell geometries. The rf-powered electrode and the grounded electrode have different areas A_0 and A_1, with A_0 typically less than A_1. This asymmetry determines the magnitude of the self-bias voltage V_0 at the powered electrode.

We also apply the nonlinear sheath dynamics to the pulsed plasma accelerator, which might be of use for the injector to the fusion machine and the space propulsion system. The evolution of current sheets can be understood in terms of fluid dynamics. However, the unsteady acceleration and the behavior of the current sheet which are strongly dependent on the polarity of the electrode can not be explained by the fluid theory.

II. Simulation Results

1) Plasma Ion Implantation

Most simulations are carried out with a collisionless nitrogen plasma whose gas pressure is 0.1 $mTorr$. The typical parameters used in our simulation are given in Table 1. The time varying sheath thickness can be determined by monitoring the temporal profiles of electric field and potential. The ion matrix sheath extent as the function of applied voltage and plasma density, and the temporal evolution of the sheath potential at the specific positions in the sheath are also calculated. All current densities at the target electrode are measured by monitoring the accumulated wall charge of implanted ions (Fig. 1(a)). These results agree very well with two previous fluid calculations[1]. To determine the effective total ion dose at the target we calculate the ion energy distribution (Fig. 1(b)), which is one of the unique properties in the kinetic simulations.

Plasma density	$n = 10^9 cm^{-3}$
Plasma temperature	$T_e = 3eV, T_i \simeq 0$
Target bias voltage	$-V_o = 10 - 50kV$
Pulse length	$10\mu sec$
Plasma frequency	$\omega_{pe} = 1.8 \times 10^9 sec^{-1}$ $\omega_{pi} = 7.9 \times 10^6 sec^{-1}$
Gas pressure	$0.1 mTorr$

Table 1

2) Asymmetric dc and rf Discharges

For capacitive discharges, almost all the applied rf voltage is dropped across thin sheaths, having thickness s_0 and s_1. The sheath properties play an important role in determining the self-bias voltage at the powered electrode. Typical discharge parameters are pressure $p = 10 - 300$ $mTorr$, $f = 13.56$ MHz, voltage $V = 50 - 1000$ V and the typical output is shown in Fig. 2. In a simple collisionless discharge model, the sheath scaling for the dependence of the powered-to-grounded voltage ratio V_0/V_1 on the area ratio A_1/A_0 is given by $V_0/V_1 = (A_1/A_0)^4$. When we consider the additional effects of secondary electron emission in the glow and local ionization near the sheath, the scaling exponent can be varied between 1 and 4 [3].

3) Pulsed Plasma Accelerator

Many parallel plate or coaxial plasma accelerator experiments[4] have shown that the acceleration is unsteady, showing a pronounced tipping with a leading edge near the positive electrode. These polarity dependent behaviors are strongly dependent on the radius ratio of electrodes and the mass of neutral gas material. Existing analyses on the current sheet, mostly fluid model, mainly deal with the case where polarity of center electrode is positive and no successful result has been obtained for the negative polarity. Futhermore they fail to explain the tipping of current sheet[5]. Thus the microscopic kinetic approach is needed. It is the major goal of our study to provide the mechanism of the tipping of current sheet near the positive electrode. From the profile of sheath electric field we estimate the additional $\mathbf{E} \times \mathbf{B}$ component of the sheet velocity, which may be the cause of the tipping (Fig. 3). The expanded detailed study will be made in a near future.

III. Conclusion

Many of our simulation results agree with previous calculations. The important roles of nonlinear sheath in the bounded plasma system are elucidated. We are in the progress of including the effects of collision and secondary electron emission.

Since the pulsed plasma accelerator involves the self-generated magnetic field, it must be considered as a fully electromagnetic problem, which makes the sheath dynamics more complicated. The 2-dimensional sheath dynamics with a finite time-varying magnetic field is an interesting subject of future study.

References

1. M.A.Lieberman, J. Appl. Phys. **66**, 2926 (1989);
   M.M.Widner et al., Phys. Fluids **13**, 2532 (1970).
2. W.S.Lawson, J. Comp. Phys. **80**, 253 (1988);
   V.Vahedi and C.K.Birdsall (private communications).
3. M.A.Lieberman, J. Appl. Phys. **65**, 4186 (1989)
4. T.N.Lee, AIAA Journal **8**, 206 (1970)
5. T.D.Butler et al., Phys. Fluids **12**, 1204 (1969)

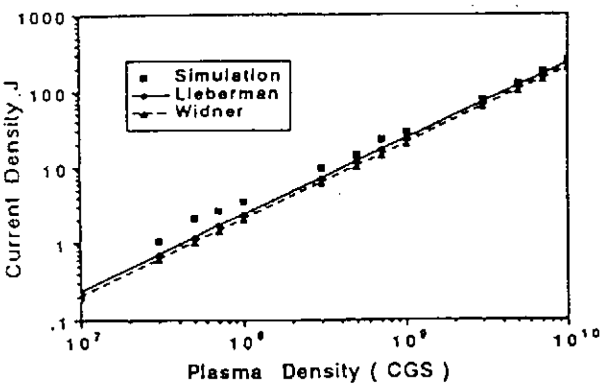

Figure 1(a)

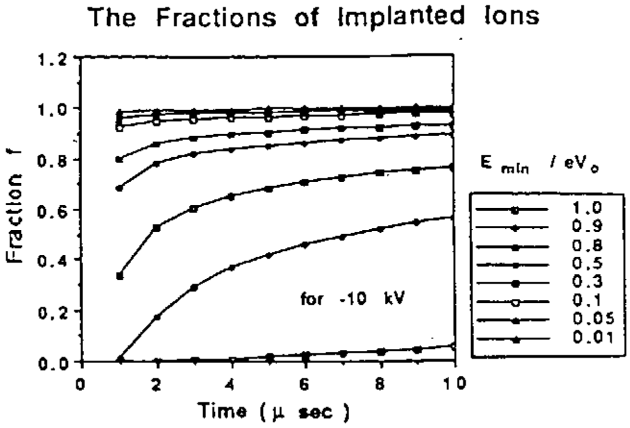

Figure 1(b)

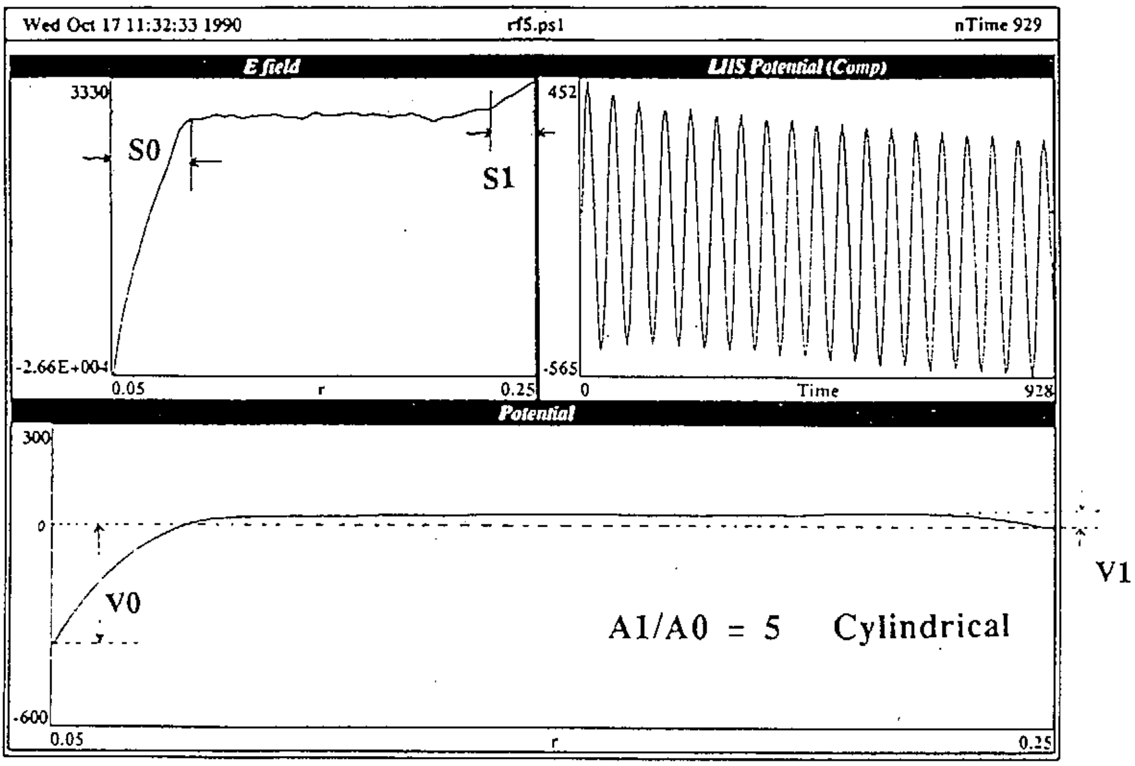

Figure 2

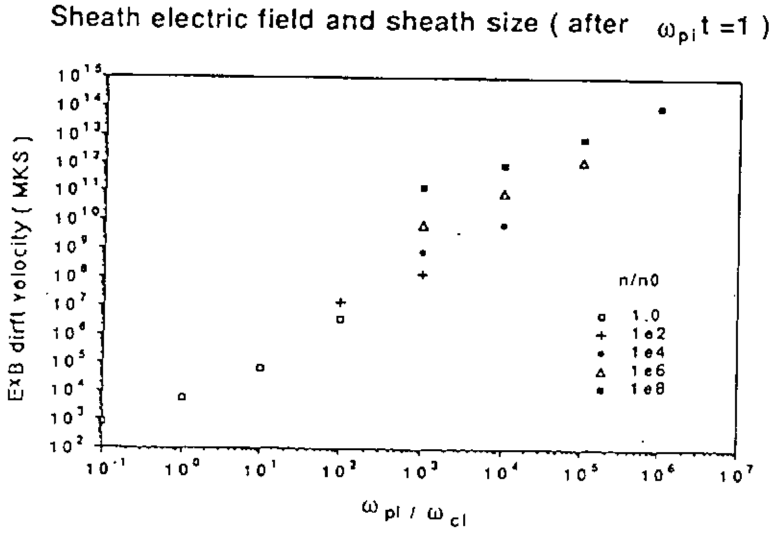

Figure 3

Hydrodynamic Instabilities in Laser Driven Implosion

K. Mima, S. Kato, A. Nishiguchi and H. Takabe

Institute of Laser Engineering, Osaka University
2-6 Yamada-oka, Suita, Japan

(Abstract)

Recently, high density plasmas with a density higher than 600 times solid density have been produced by laser implosion. This compressed density agrees reasonably well with one dimensional simulation. However, the neutron yield is less than $10^{-2} \sim 10^{-3}$ times 1D simulation result for the high density compression. These results indicate that the outside surface of the compressed plasma is stable, but the internal hot dense plasma surface is not stable.

In this presentation, the instabilities driven by the internal temperature and pressure gradients will be discussed. By using the quasi linear approximation we estimated the saturation level of the fluctuations to determine the convective heat flux. The self-consistent temperature profile is then found to evaluate the reduction of neutron yield.

§1. Introduction

In laser fusion, a hot dense plasma whose temperature is higher than 5 keV is required to be formed at the center of the compressed DT plasmas, which is called 'hot spark'. The hot spark is heated by both shock waves and the following adiabatic compression, when a cold high density plasma layer stagnates as shown in Fig. 1. In the recent CDT shell target compression experiments, the neutron yield is less than $10^{-2} \sim 10^{-3}$ times neutron yield which is predicted by the 1D implosion simulation, although the compressed plasma density which is several hundred solid density agrees fairly well with the simulation result. The main subject of this paper is to investigate the mechanisms of the reduction of the neutron yield.

As shown in Fig. 1, the interface between cold and hot plasmas is unstable with respect to the interchange mode. This Rayleigh-Bénard instability may cause mixing of hot and cold plasmas. As a result, the hot spark temperature decreases due to the convective heat flux and the neutron yield may be lowered.

§2. Instability and Cooling of a Hot Spark

We solve numerically the following quasi-linear equation for the Rayleigh-Bénard modes.

$$\frac{\partial}{\partial t} v_k (r, t) = \Gamma_k (r, t)\, v_k (r, t) \quad ,$$

and

$$\frac{\partial \langle T \rangle}{\partial t} = \frac{\partial}{\partial x} X_{NL} \frac{\partial}{\partial x} \langle T \rangle \quad ,$$

where

$$\Gamma_k (r, t) = -\frac{\mu + \kappa}{2} k^2 + \left| g \frac{d \ln \langle T \rangle}{dr} \right|^{1/2}$$

and

$$X_{NL} = \int_0^\infty d\tau \sum_k (2k+1)\, v_k (t)\, v_k^* (t - \tau) \quad .$$

Here, v_k is a Fourier amplitude of velocity fluctuations at a radial position r, μ and κ are the shear viscosity and the thermal diffusivity and g is the gravity. Note here that a local dispersion relation is applied to evaluate the growth rate Γ_k.

In the numerical integration, we assumed that the initial wavenumber spectrum of v_k is given by Fig. 2-(a). This initial wavenumber spectrum is evaluated by using Fourier components of laser intensity irregularity. The amplitude is normalized by the imploding shell velocity. We normalized the time by $\sqrt{R_0 / g}$, where R_0 is the initial target radius. The plasma reaches the maximum compression state at $t = \tilde{t} / (R_0 / g)^{1/2} = \sqrt{2}$.

The velocity fluctuation wavenumber spectrum at $\tilde{t}$=1.8 is shown in Fig. 2-(b). The temporal evolution of the temperature profile is simultaneously determined as shown in Figs. 3. Since the plasma density is the order of 100 g / cm^3, the electron mean free path is shorter than 0.1 μm even for $T_e > 1$ keV. Therefore, the classical electron thermal conduction can be neglected when the temperature scale length $L_T >$ 1 μm and the stagnation time duration is less than 100 psec. The relaxation of the temperature profile is due to the turbulent convection. At the maximum compression, the hot spark temperature decreases to be half of the stable case.

§3. Summary

Because of the convective heat transport, the present irradiation nonuniformity reduces the hot spark temperature to be half. The hot spark temperature of the 1D simulation is about 1 keV. Therefore, the spark temperature will be less than 500 eV in the experiment. Since the neutron yield is proportional to $T^4 \sim T^5$ in this temperature range, the neutron yield will reduce to be 1/20 ~ 1/40 of the 1D neutron yield. This partially explains the experimental results. Further investigation of the reduction mechanism is required.

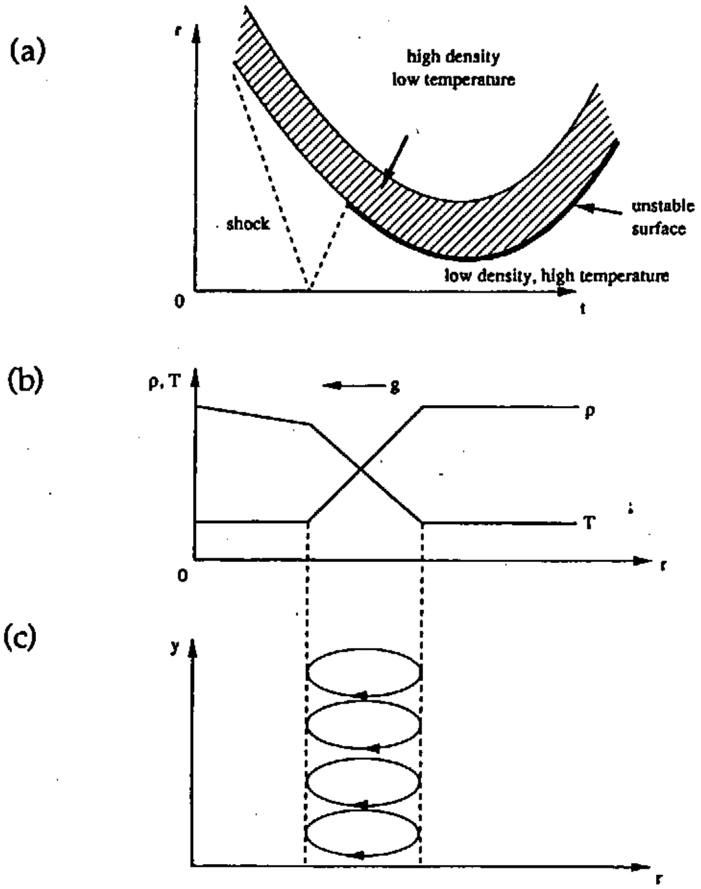

Fig. 1. (a) Radial motions of stagnating plasma layer, shock front and the contact surface.
(b) Density and temperature profiles.
(c) Convective flows in the unstable layer.

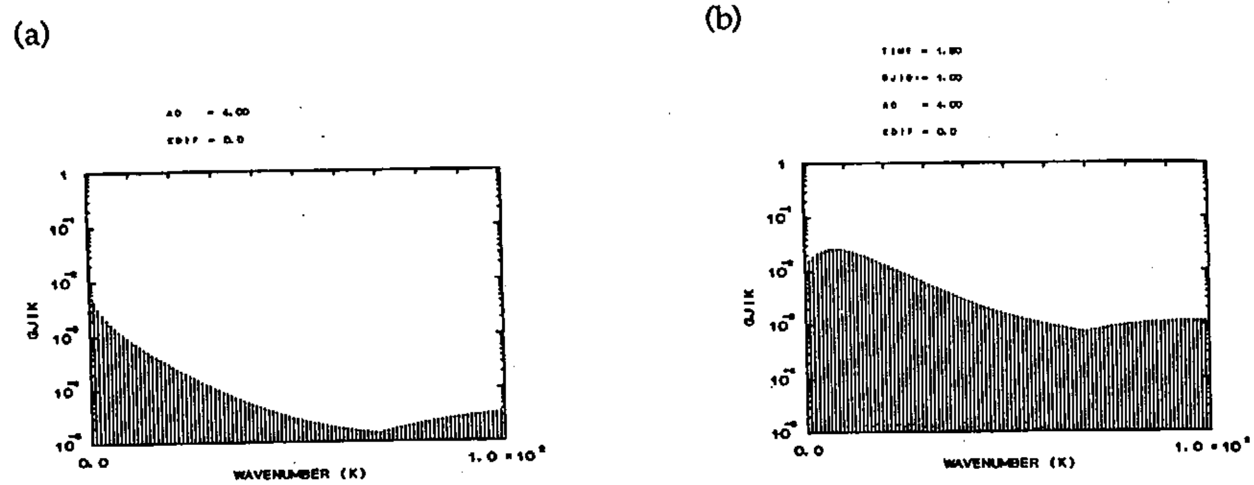

Fig. 2. (a) Initial wave number spectrum of fluid velocity fluctuation.
(b) The spectrum at t = 1.8.

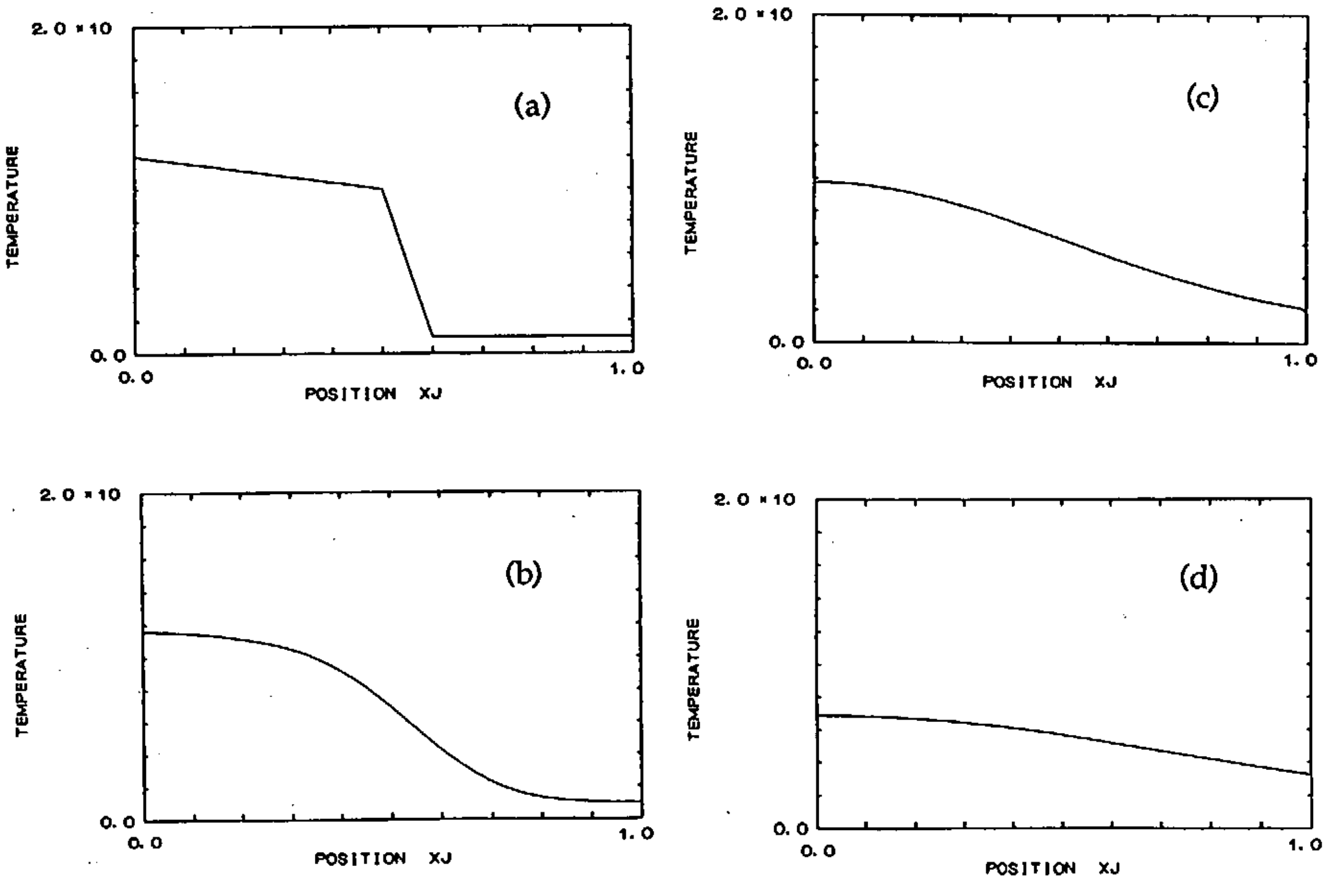

Fig. 3. Temporal revolution of temperature profile; (a) t = 0, (b) t = 0.2, (c) t = 1.0, (d) t = 2.0.

"Solitons and Chaos in Laser-Plasma Interaction"

C.S. Liu, W. Shyu, P. Guzdar, H.H. Chen and Y.C. Lee
University of Maryland

Transitions from soliton to chaos in laser irradiated inhomogeneous plasmas are studied for (1) Resonance absorption (2) Raman backscattering. To model resonance absorption, both driven nonlinear Schrodinger equation and Zakharov equations with inhomogenuity term added were solved to show that the final states of (a) steady state of modified Airy function (b) periodic solutions -representing regular soliton emission and (c) chaos through period doubling, 2nd frequency appearance (breather emission) and breaking of two-frequency torus through the generation of broad bands of harmonic at $n\omega_1 + m\omega_2$. Conditions for these transitions were obtained.

In Raman scattering, we found that coupled scattered light soliton and Langmuir soliton adequately describe the saturation at low laser intensity just above the inhomogeneity threshold. At higher laser intensity, transient, intermittent turbulence results. At a critical laser intensity, the interval for the turbulent transient became infinite - transition to chaos by *Crisis* from a stable attractor to chaotic attractor much like a phase transition. Thus these numerical solutions of nonlinear partial differential equations give two interesting routes to turbulence. Space-time turbulence also will be discussed.

Nonlinear Evolution of 2d and 3d Rayleigh-Taylor Instability at Stagnation Phase in Laser Implosion

Katsunobu Nishihara and Hitoshi Sakagami*

Institute of Laser Engineering, Osaka University
2-6, Yamada-oka, Suita, Osaka 565
* Institute for Supercomputing Research, Recruit Co. Ltd.
1-13-1, Kachidoki, Chuo-ku, Tokyo 104

Abstract

Two and three dimensional Rayleigh-Taylor instabilities of the fuel-pusher contact surface in a cylindrically or spherically stagnating system are investigated using of 2d and 3d fluid codes, IMPACT-2D and 3D. Geometrical difference of the free-fall speeds following the saturation of the exponential growth is studied for planer, cylindrical and spherical geometries. Nonlinear made coupling of unstable surface waves is also investigated for a 2d planer geometry.

I. Introduction

In the stagnation phase of imploding targets in inertial-confinement fusion, a perturbation at the fuel-pusher contact surface is Rayleigh-Taylor unstable. It is important to investigate this instability since the R-T instability causes the pusher-fuel mixing[1] and thus reduces the fusion yield. We have investigated the linear growth and the saturation of the linear growth of the R-T instability in the cylindrically[2] and spherically[3] stagnating systems. In this paper, the free-fall speeds following the saturation of the exponential growth are studied for various geometries.

Since the short wavelength modes have large growth rates, high modes grow initially and mode coupling of those modes may generates low modes. Nonlinear mode coupling of the unstable surface waves is also studied for a 2d planer geometry.

II. Geometrical Difference of Free-Fall Speeds

To study the R-T instability in the stagnation system, the pusher and ablator are initially assumed to have constant velocity toward the center of a target, with the fuel at rest. The shock wave then propagates through the fuel and is accelerated to the center of the target until it collides at the origin. After the collision the shock wave is reflected and collides at the contact surface which is also accelerated to the center and the stagnation phase begins at this time. A single-mode perturbation is applied to the density profile near the contact surface at this time with a trigonometrical function for the 2d cylindrical case and a spherical-harmonic function for the 3d spherical case. The details of the simulation conditions are found in Ref. 2 and 3. In the fluid codes, IMPACT-2D and-3D, the basic conservation equations are solved with an explicit total variation diminishing (TVD) scheme.

The saturation of the exponential linear growth is followed by the free-fall phase, in which the time evolution of the amplitudes is described by $\delta=\eta gt^2$. The saturation amplitudes and free-fall speeds for the spherical geometry are found to be, respectively, the largest and fastest among the planer, cylindrical and spherical geometries as summarized in Table 1, in which the wavelength λ_o is defined as $2\pi r/n$ using the radius of the contact surface at the saturation and the polar mode number for the cylindrical and spherical geometries. The free-fall coefficient of $\eta=0.08$ for the planer case agrees quite well with the expriments.[4]

It is noted that the free-fall speed exceeds 1/2 for the spherical geometry. This fast speed is due to the fact that in 3d spherical case bubbles are surrounded by spikes and strong vortex rings are developed to feed the bubbles by blowing off the fuel into them, especially around the bases of bubbles. The free-fall speeds have weak dependence on the polar and azimuthal mode numbers as shown in Fig. 1. As increasing the polar mode number n and for the azimuthal mode number m ~ n/2,the size of the bubble bases becomes small and the strong vortex rings are formed and thus they lead to fast free-fall speeds. On the other hand, the large bubble structures make this feeding mechanism ambiguous and lead to slow free-fall speeds for such as small n and m ~ 0 or m ~n cases.

III. Mode Coupling of Unstable Surface Waves

In an incompressible fluid in a planer geometry, the linear growth rate of the R-T instability is given by $\gamma_k{}^2=kgA$, where k is the wave number, g the gravity and A the Atwood number, $A=(\rho_H-\rho_L)/(\rho_H+\rho_L)$, where ρ_H and ρ_L are heavy and light fluid mass densities. The high modes have larger growth rates and they may grow initially. The mode coupling of high modes generates low and high modes due to the mode coupling. We have developed a theory of the mode coupling by a perturbation method. The second order solution is found to be given as

$$\xi_k=\xi_{ok}e^{\gamma_k t}+\gamma_k^2 A\sum_{k'}\frac{|k'|+|k-k'|}{(\gamma_{k'}+\gamma_{k-k'})^2-\gamma_k^2}\xi_{ok'}\xi_{ok-k'}\exp[(\gamma_{k'}+\gamma_{k-k'})t].$$

The first term represents the linear growth and the second term dose the nonlinear mode coupling between the modes k' and k-k'.

As an example, 2-modes k_1 and k_2 are initially excited, the mode coupling of these two modes excites the modes $k_\pm=k_1\pm k_2$ with the exponents of $\gamma_{k\pm}=\gamma_{k1}+\gamma_{k2}$. Since $\gamma_{k1}+\gamma_{k2}$ is proportional to $\sqrt{k_1}+\sqrt{k_2}$, while γ_{k-} proportional to $\sqrt{|k_1-k_2|}$, the excitation of the low modes by the mode coupling of high modes can be important compared with the linear growth.

When the two modes of 20 and 30 are excited initially, the mode of 10 is found to grow with the exponent of $\gamma_{20}+\gamma_{30}$ as expected from the theory. When the single mode of 10 is excited initially, the higher harmonics of 20 and 30 also grow. The phases of the modes excited by the mode coupling are locked to satisfy $\phi_k=\phi_{k'}+\phi_{k-k'}$. The phase lock prevents the growth of the second harmonics compared with the third harmonics, and thus it is observed in the simulation that the third harmonics becomes larger than the second harmonics.

The theory varied only for small amplitudes. The simulation results of the mode coupling with the two modes of 20 and 30 excited initially are compared with the single mode 10 excited initially in Fig.2, at the time when their amplitudes become very large. In Fig.2, the horizontal scale is reduced to 1/5. It is clearly seen that the mode of 10 is excited by the mode coupling of the modes 20 and 30, especially in the spikes. The latter time, the mode of 10 in the bubbles also appears clearly. In the bubble-spike structure for the case of the external gravity force, the spikes grow faster than the bubbles. It is also noted that the mode coupling of the modes 20 and 30 generates larger amplitude of the mode 10 than the case of the single mode 10 excited initially.

IV. Conclusion

Geometrical dependence of the free-fall speeds following the saturation of the exponential growth is studied. The fast speeds of $\eta \sim 1$ in 3d spherical case is found to be due to the feeding mechanism of the bubbles by strong vortex ring surrounding them. Low modes are excited very rapidly by the mode coupling of high modes initially excited.

References

1. Yu. F. A fanasev et. at al., Pisma Zh. Eksp. Teor. Fig. 23, 617 (1976)
   [JETP Lett. 23, 566 (1976)].
2. H. Sakagami and K. Nishihara, Phys. Fluids B2, 2715 (1990).
3. H. Sakagami and K. Nishihara, Phys. Rev. Lett. 65, 432 (1990).
4. K. I. Read, Physica 12D, 45 (1984).

(dim)	saturations amplitude	free-fall coefficient
plane (2d)		$\eta \sim 0.08$
cylinder (2d)	$\delta \sim 0.35\,\lambda_0$	$\eta \sim 0.2$
sphere (3d)	$\delta \sim \lambda_0$	$\eta \sim 1$

Table.1 Geometrical dependence of saturation amplitudes of exponential linear growth and free-fall coefficients following the saturation, where $\lambda_0=2\pi r/n$ and $\delta=\eta g t^2$.

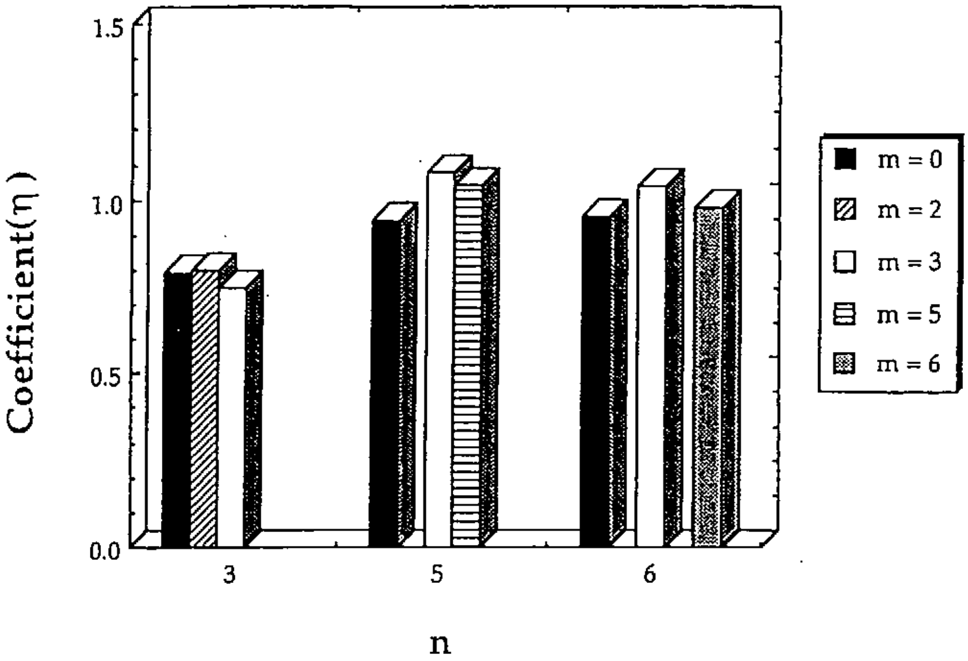

Fig. 1　Free-fall coefficients for various polar and azimuthal mode numbers, n and m.

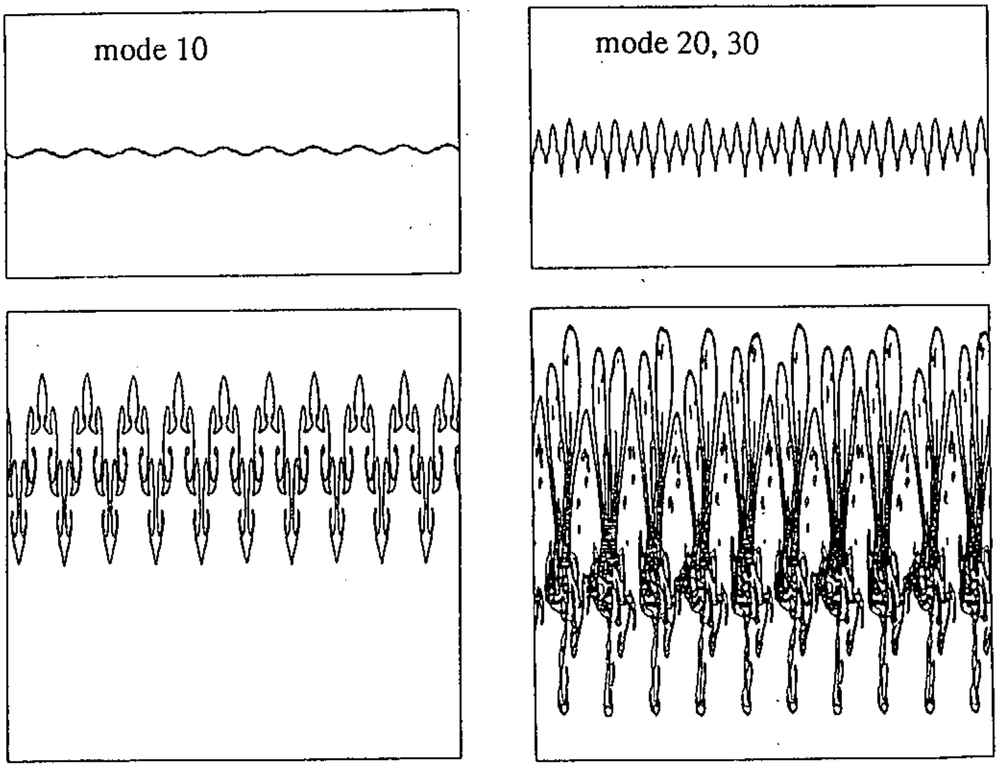

Fig. 2　Iso-density contours for a single mode excited case m = 10, and two modes excited case m = 20 and 30.

MODELS OF COLLISIONNAL TRANSPORT ACROSSS A MAGNETIC FIELD WITH DESTROYED SURFACES

G. Laval
Centre de Physique Theorique
Ecole Polytechnique
91128 Palaiseau Cedex, France

In this work, we study diffusion and heat transport of a collisionnal plasma across a confinement magnetic field with destroyed surfaces. We consider only the case where, at the lowest order, the particles diffuse along the field lines, i.e. we asssume that the mean free path is shorter than the field lines length. It is well known that, in such conditions, theories starting from linearized particle motions do not provide the right answer. In this work we try another method by using exactly soluble simple models in which the full non-linearized motion is kept.

In the first part, we introduce the field and collision models. These models are not self-consistent and electric fields are entirely neglected. The diffusion coefficient is obtained from a variationnal form from which convergent approximate solutions can be obttained. In the second part, we introduce self-consistent electric fields and we estimate their effect on the transport.

I-Field and collision models

We describe the electrons by a simple model which keeps the main physical features of the collisionnal diffusion. We assume that electrons move along the field lines with constant and opposite velocities ±v and with densities respectively N_+ and N_-. The transition probability per unit time from one species to the other is $\nu/2$ and models the effect of collision on the parallel motion. Moreover both species diffuse across the field lines with a diffusion coefficient $\chi_\perp$. We assume that the unit vector along the magnetic field $\vec{b}$ is divergence free and can be written

$$\vec{b} = \vec{b}_0 + \vec{b}\,(\vec{r})$$

where $\vec{b}_0$ is the unit vector along the average equilibrium field, $\vec{b}(r)$ being a small correction related to fluctuations. Then we have :

$$\frac{\partial N_+}{\partial t} + v\,(b.\nabla)\,N_+ - \chi_\perp \Delta_\perp N_+ = -\frac{v}{2}(N_+ - N_-)$$

$$\frac{\partial N_-}{\partial t} - v\,(b.\nabla)\,N_- - \chi_\perp \Delta_\perp N_- = -\frac{v}{2}(N_- - N_+)$$

It makes it possible to write D under the variational form D=minW where

$$W = 2 < v\,\phi^2 + \chi_\perp (\vec{\nabla}_\perp \phi)^2 + \chi_\perp (\vec{\nabla}_\perp n)^2 >$$

the functions ϕ and n being related by the constraint

$$v\,\phi - \chi_\perp \Delta_\perp \phi + v(\vec{b}\,.\,\vec{\nabla} n + b_x) = 0$$

where it has been assumed that the averaged density depends only on x.

We consider a simple magnetic field model in which b_x is taken under the form :

$$b_x = \sum_{n=-\infty}^{n=+\infty} g(y)\,L\,\delta(z - nL)$$

where g(y) is a periodic function of y such that $g(y + L_y) = g(y)$ and L is a constant.

Thus we choose, for $0 \leq y < Ly$

$$g(y) = 2\pi\,\overline{K}\left[y - \frac{L_y}{2}\right] / L_y$$

For such a confinement field, the successive crossings of magnetic field lines with planes z=nL define a sawtooth map. The corresponding Lyapunof exponent is L/Ln(λ) where λ is a solution of the equation: $\lambda^2 - \lambda\,(K + 2) + 1 = 0$ where $K = \frac{\overline{K}\,kL^2}{L_s}$

For these models and for integer K, the diffusion coefficient can be computed explicitely in terms of continued fractions. It shows that the inhibition of the diffusion by collisions is strongly weakened by the amplification of the collisionnal transverse diffusion in the chaotic field lines as predicted by Rechester and Rosenbluth.

However, this very precise computation of the diffusion coefficient makes it possible to understand all the details of this mechanism. It is found that, at least in these simple models, the amplification process is somewhat different from the picture given by Rechester and Rosenbluth, leading to dicrepancies in the values of the diffusion coefficients.

II-Self consistent electric fields.

As a first attempt to introduce self-consistency, we take into account the radial electric field which is necessary to inhibit the particle flux when ion diffusion can be considered as negligible. Again in this case it is possible to write a heat diffusion coefficient in terms of continued fractions. It is found that there is a parameter domain where the electric drift velocity has a dominant effect on the transport and where the transverse collisionnal diffusion can be neglected.

Finally, we introduce a fluctuating potential which is chosen to cancel the electron density fluctuations; it would correspond to a case where the ions may be considered as motionless.

Then it is argued that this fluctuating electric field introduce an additionnal anomalous diffusion which is itself amplified by the stochastic diffusion of the field lines. The new diffusion coefficient resulting from this process is estimated.

Issues in Direct Numerical Simulation of Plasma Turbulence and Transport

A. Thyagaraja, W. Arter and F.A. Haas

AEA Fusion/Euratom Assoc. Culham Lab. Abingdon, OX14 3DB, UK.

1. Introduction: The problem of direct numerical simulation of plasma turbulence in magnetic confinement systems such as the tokamak is as formidable as it is important in gaining a fundamental theoretical understanding of anomalous transport of particles, energy, momentum and impurities in such systems. At Culham, we are engaged in developing two complementary but distinct approaches to this question. The present paper will first outline the design philosophy and the basic numerical problems encountered and solved in the construction of a two-fluid, three-dimensional, electro-magnetic, finite-difference, time evolution code CUTIE. In particular, the importance of qualitative consistency, time-reversal, conservation properties, "phase mixing", and boundary conditions will be illustrated in the context of both passive and active electrostatic turbulence.

A quite separate study has been undertaken to enhance the understanding of drift-wave turbulence in tokamak plasmas. In this connection, we have written a three-dimensional, time-dependent, electrostatic drift wave code called DRIFT. This has features which take account of toroidicity, non-adiabaticity and magnetic shear. The resulting code is very flexible, and has been used to solve the Hasegawa-Mima equation efficiently in 2-d. Results from time-dependent, 3-d calculations run on a Cray-2 will be presented.

The ultimate aim of these studies is to obtain a proper physical understanding of plasma turbulence in typical tokamak conditions by calculating the power spectra of the turbulent fluctuations and their transport consequences. It is believed that this can only be achieved by a step-by-step approach to the numerics, making sure that the calculated effects represent genuine physics and are not mere artefacts of the numerical simulation.

2. CUTIE: In the first instance, we have made the following assumptions: (1) The code solves two-fluid equations in the usual periodic cylindrical geometry. Effects of toroidal geometry will be considered in later versions. (2) The quasi-neutral, low-β approximation will be used, with the usual low-frequency drift approximations. (4) Nonlinear, local equations of the Braginskii type are used with appropriate corrections for parallel coefficients[1].

From the above equations, we get a system of coupled equations for 7 fields: n, T_i, T_e, $v_{\|}$, $\varpi_{\|}$, Φ, and $A_{\|}$. The last three variables are respectively the parallel vorticity, electrostatic potential and the parallel vector potential. All of these variables are functions of position and time and all except Φ satisfy conservation equations of the same general form derived from the equations of continuity, energy and momentum. The quasi-neutrality condition (equivalently, Ampère's law) relates Φ and $\varpi_{\|}$ by an elliptic equation of the Poisson type. The field Φ is self-consistently time-evolved by solving this equation.

The code is required to meet the stringent conditions imposed by 'qualitative consistency'. Thus, whatever the grid sizes and time-steps, positive physical quantities must always be maintained positive[2]. In addition, if the boundary conditions allow it, global conservation of particles, energy and momentum must be 'automatic'. The numerical dissipation must be controlled in such a manner that in the absence of dissipation in the conservation equations and the boundary conditions, 'time-reversibility' of the differential equations must be mirrored by the numerical scheme. As spectral techniques are not effective in strongly nonlinear systems, especially as regards positivity preservation properties (they are inevitably subject to the Gibbs phenomenon leading to overshoots and undershoots near the boundaries) a fully three-dimensional, explicit, finite-difference scheme was chosen. Such a scheme has proved very effective in modelling very complex multiphase flows which occur in fission reactor safety analyses[2,3]. The two-fluid Braginskii-like equations in three spatial dimensions represent a formidable challenge to these techniques. Provision is made for mesh resolutions $\frac{\Delta r}{a}$, $\frac{\Delta z}{2\pi R}$ to be such that $\rho_i \simeq 0.1\Delta r$. This corresponds to mode numbers m, n upto about 20. The time step is of order 10^{-7} secs, clearly sufficient to model frequencies upto 100 khz. The code runs both on the Cray-2 at Harwell and the 'Hitech' workstation in only three times the Cray cpu time.

The highlights of the code development so far will now be summarised. If $F(r, \theta, z, t)$ is any function satisfying the conservation equation,

$$\frac{\partial F}{\partial t} + \nabla.\mathrm{v}F = S_F \tag{1}$$

the problem is one of *passive* transport if the field v is prescribed together with the source function. Choosing the source to be zero and suitable boundary conditions, we have verified for a variety of 'turbulent' velocity fields expected in tokamaks that the code evolves Eq.(1) in a consistent way. Thus, initially non-negative F's are maintained non-negative for all times. The integral $\int_{vol} F dv$ is kept constant to sufficient accuracy for time-scales long compared with typical variations of F. The numerical diffusivity of the scheme in its primitive form is of order $\mid \mathrm{v} \mid_{max} \Delta r$. This is clearly smaller than the 'Bohm' value, $v_{th_i}\rho_i$. In fact, by a special device, the numerical diffusivity has been lowered sufficiently for the finite-difference form of Eq.(1) to exhibit 'reconstruction' to the initial state when the velocity field is reversed after a certain period of evolution 'forward' in time.

It has also been checked that the code leads to real transport losses of the expected size when the boundaries are made 'absorbing' even though the equation is fully reversible. This is an example of 'dissipationless phase mixing' in the confinement zone leading to transport losses due to irreversible boundary conditions at the edge. Longitudinal sound waves and drift waves have been found to be calculated in accordance with existing linear theories. The treatment of sound waves showed that the energy equation should be solved in the 'entropy' formulation to get the best results for the given level of finite-difference approximation. At the moment, the code works with only electrostatic modes, the electron physics being treated adiabatically. After exploring this regime somewhat further nonlinearly, it is proposed to investigate the full electromagnetic capabilities of the code. The ultimate aim is the direct simulation of the relatively long wavelength, low frequency drift and tearing modes in cylindrical geometry. The resultant power spectra and transport properties will be studied with realistic applications in mind.

3. DRIFT:

3.1 Choice of Scheme: Of the many drift wave turbulence models [4], we have chosen the system derived by Biskamp and Walter[5] for electrostatic drift waves in a sheared magnetic field that also includes non-adiabatic effects. Accurate computation of this system in the appropriate limit is known to be difficult, due to the appearance of small-scale features.

Previous authors have mostly used spectral schemes to study nonlinear drift wave interactions. We should like to be able to study the effects of varying boundary conditions which is not easy for any method which employs global basis functions. Moreover, such functions are invariably smooth, and do not represent solutions with strong gradients well. The work of Morton[6] provides an approximate theoretical argument for preferring Lagrangian-coordinate-based methods. Their use when advection dominates is, in any event, very compelling from a physical point-of-view.

We have chosen to employ the extended PIC or EPIC method proposed by Eastwood[7]. In brief, the mass density ρ and the parallel canonical ion momentum g become attributes of particles distributed initially uniformly throughout the computational domain. These particles move following the lines of constant electric potential Φ, where Φ is calculated from ρ by introducing a uniform mesh using the 'dual basis' method. The variables ρ and g change due to the effects of diffusion, shear, etc.

3.2 Practicalities: Although the basic scheme is very elegant and simple, its actual implementation was a lengthy business. Preliminary investigations showed the importance of considering a difficult test case, where the coherent part of the numerical error dominates the fluctuations. Early calculations supported the elementary inference that accurate tracking of the particle trajectories is crucial. The trapezoidal rule was found to be superior to schemes of the same formal accuracy because it has the property that, if Φ is independent of the time t, particles remain on lines of constant Φ. Although this is technically an implicit scheme, if the dual basis consists of piece-wise linear ('chapeau') functions, explicit formulas are easily obtained, at least within each computational cell.

The non-adiabatic drift wave equations take the form (Biskamp and Walter[5]):

$$\frac{d}{dt}(\Phi - \nabla^2\Phi + \delta_n y) = (\mathrm{b}.\nabla)v_{\|}, \tag{2}$$

$$\frac{dv_{\|}}{dt} = (\mathrm{b}.\nabla)\Phi, \tag{3}$$

where, $\mathrm{b} = (\delta_s y, 0, 1)$. The first test problem is in 2-D and sets $v_{\|} \equiv 0$, i.e, concerns the diffusionless Charney-Hasegawa-Mima equation. We solve in the unit box with periodic boundaries for $\delta_n = 100$ and initial conditions $\Phi = \sin 10\pi x \sin 8\pi y$.

Numerous runs indicate the importance of defining energy as $E = \frac{1}{2}\sum_i \rho_i \Phi_{\mathbf{P}}(\mathrm{x}_i)$, where i is a particle index and $\mathbf{P}$ a mesh label. The inferiority of other schemes is then plainer and the use of three time-levels in the particle integration is seen to be advantageous. The energy error ΔE increases linearly with time at a rate $\frac{\Delta E}{t} = \frac{2}{3}\alpha \frac{E|\overline{\Phi}_{xy}|^3 \Delta t^3}{(\Delta x)^2 n_{pn}}$.

This formula was derived assuming correlated fluctuations, at the level of truncation error enhanced by feed-back. Empirically $\alpha \simeq 7$. The high power of Δt is unfortunate, since it negates a possible asset of EPIC, namely no restriction on the Courant number c. $\Delta E/t \simeq 20$ may seem large for $c = \frac{1}{2}$, $\Delta x = \frac{1}{32}$ and number of particles per node, $n_{pn} = 4$, but our results show that for the Lax-Wendroff-Taylor-Galerkin scheme (Löhner *et al.*[8]), the error is an order of magnitude larger at equivalent parameters and computational cost. For EPIC at $c = \frac{1}{4}$, ΔE is down at the fluctuation level.

We have also checked the growth rates for the sheared system in 3-D ($\delta_s = 100$). The linearized solution given by Biskamp and Walter[5] grows in energy at a rate $\gamma = \frac{2k\delta_s}{(1+k^2)} =$ 31.04, where $k = 2\pi$ is the wave number. Runs with $h = \frac{1}{8}, \frac{1}{16}$ and $\frac{1}{32}$ gave $\gamma = 48.0$, 34.7 and 31.8 respectively. This rate of convergence appears slow because the problem is driven by the boundary conditions.

4. Conclusions

In conclusion, CUTIE has been developed to the point where a number of interesting electromagnetic turbulence investigations can be made. We have designed and written a qualitatively consistent, stable, time-evolution code for the two-fluid equations in cylindrical tokamak geometry with suitable conservation properties. In parallel, fundamental studies of drift wave turbulence are being made with DRIFT. Indeed, DRIFT is the first large code to employ the EPIC scheme. EPIC's good stability and accuracy properties will be a considerable asset in the planned investigation of electrostatic drift wave turbulence. The two approaches are together expected to lead to a better understanding of the difficult problems involved in the direct numerical simulation of tokamak turbulence.

5. References

[1] *A. Thyagaraja, I.L. Robertson and F.A. Haas*, Plasma Phys. & Contr. Fusion, **27**, 1217, (1985).

[2] *A. Thyagaraja and D.F. Fletcher*, Comp. Phys. Communs. **56**, 291, (1989).

[3] *A. Thyagaraja and D.F. Fletcher*, Computers & Fluids, **16**, 59, (1988).

[4] *W. Horton*, Physics Reports, **192**, 1, (1990).

[5] *D. Biskamp and M. Walter*, Phys. Letts. A, **109**, 34, (1985).

[6] *K.W. Morton*, in The State of the Art in Numerical Analysis, (Eds. A. Iserles and M.J.D. Powell), Clarendon, 645, (1987).

[7] *J.W. Eastwood*, Comp. Phys. Communs. **43**, 89, (1986).

[8] *R. Löhner, K. Morgan, and O.C. Zienkiewicz* , Computer Meths. Appl. Mech. Eng. **51**, 441, (1985).

ANOMALOUS TRANSPORT DUE TO THE SKIN SIZE ELECTROMAGNETIC DRIFT MODE IN TOKAMAKS

Akira Hirose

Department of Physics, University of Saskatchewan
Saskatoon, Saskatchewan S7N 0W0, Canada

The presence of skin size ($k_\perp \simeq \omega_{pe}/c$) electromagnetic turbulence in tokamaks has originally been speculated by Ohkawa (1) who has proposed the well known formula for the anomalous electron thermal diffusivity given by

$$\chi_e \simeq (c/\omega_{pe})^2 \omega_{Te}$$

Here, $\omega_{Te} = v_{Te}/qR$ is the electron transit frequency. Subsequent attempts to identify linear electromagnetic instabilities in the region $k_\perp \simeq \omega_{pe}/c$ have not been very successful.(2) The nonlinear down cascade of the electrostatic shorter wavelength η_e mode (3,4,5) is unlikely because a recent electromagnetic analysis of the η_e mode (6) has revealed that the critical β (or α, the balloning parameter) is not too much different from that of the ideal MHD balloning mode.

In a low β tokamak discharge, the skin depth c/ω_{pe} and the ion Larmour radius are comparable. Therefore, a fully kinetic (rather than adiabatic) ion response should be employed for more satisfactory stability analysis in the regime $k_\perp \simeq \omega_{pe}/c$. Electron dynamics should also be treated kinetically incorporating kinetic resonances (magnetic drift and Landau resonances). The ion response for modes having $\omega \gg \omega_{bi}$ (the ion bounce frequency) is

$$f_i = -\frac{e\phi}{T_i} f_{Mi} + \frac{\omega + \bar{\omega}_{*i}}{\omega + \bar{\omega}_{Di} - k_\parallel v_\parallel} J_o^2(\Lambda_i)\left(\phi - \frac{v_\parallel}{c} A_\parallel\right) \frac{e}{T_i} f_{Mi} \tag{1}$$

while the electron response for $\omega < \omega_{be}$ is approximately

$$f_e = \frac{e\phi}{T_e} f_{Me} - \frac{\omega - \bar{\omega}_{*e}}{\omega - \bar{\omega}_{De} - k_\parallel v_\parallel \delta_{Uj}} J_o^2(\Lambda_{ej})\left(\phi - \frac{v_\parallel}{c} A_\parallel \delta_{Uj}\right) \frac{e}{T_e} f_{Me} \tag{2}$$

where $j = U$ (untrapped electrons) is for $|v_\parallel| > \sqrt{\varepsilon}\, v_\perp$, $j = T$ (trapped electrons) for $|v_\parallel| < \sqrt{\varepsilon}\, v_\perp$, $\Lambda_{eT} \simeq q\, k_\perp v_\perp/\sqrt{\varepsilon}\, \Omega_e$, $\bar{\omega}_*$ is the energy dependent diamagnetic frequency with a temperature gradient, and $\bar{\omega}_D$ is the velocity dependent magnetic drift frequency. (Remaining notation is standard.) The charge neutrality $\int (f_i - f_e) d\vec{v} = 0$ and Ampere's law $\nabla^2 A_\parallel = -(4\pi e/c)\int v_\parallel (f_i - f_e) d\vec{v}$ yield the following dispersion relation

$$\left\{k^2 + 2\left(\frac{\omega_{pe}}{c}\right)^2 F_{eU2} + 2\left(\frac{\omega_{pi}}{c}\right)^2 F_{i2}\right\}\left(F_{eU0} + F_{eT0} - 1 - \tau(1 - F_{io})\right)$$

$$= 2\left(\frac{\omega_{pe}}{c}\right)^2 \left(F_{eU1} + \sqrt{\tau m/M}\, F_{i1}\right)^2 \tag{3}$$

where

$$F_{in} = \left\langle \left(\frac{v_{\parallel}}{v_{Ti}}\right)^n \frac{\omega + \bar{\omega}_{*i}}{\omega + \bar{\omega}_{Di} - k_{\parallel} v_{\parallel}} J_o^2(\Lambda_i) \right\rangle \tag{4}$$

$$F_{ejn} = \left\langle \left(\frac{v_{\parallel}}{v_{Te}}\right)^n \frac{\omega - \bar{\omega}_{*e}}{\omega - \bar{\omega}_{De} - k_{\parallel} v_{\parallel} \delta_{Uj}} J_o^2(\Lambda_{ej}) \right\rangle_j \tag{5}$$

with < > for averaging with a Maxwellian weighting. The norms of the operators $k_{\perp}$, ω_{Dj}, $k_{\parallel}$ for a strongly ballooning eigenfunction are (7)

$$\langle k_{\perp}^2 \rangle = k_{\theta}^2 \left(1 + (\pi^2/3 - 7.5)s^2 - 10s\alpha/9 + 5\alpha^2/12\right) \tag{6}$$

$$\langle \omega_{Dj} \rangle = 2\varepsilon_n \omega_{*j} (2/3 + 5s/9 - 5\alpha/12) \tag{7}$$

$$\langle k_{\parallel}^2 \rangle = \frac{1}{3(qR)^2} \frac{1 + (\pi^2/3 - 0.5)s^2 - 8s\alpha/3 + 3\alpha^2/4}{1 + (\pi^2/3 - 2.5)s^2 - 10s\alpha/9 + 5\alpha^2/12} \tag{8}$$

where $s = rd\ell nq/dr$ is the shear parameter, $\alpha = -q^2 R d\beta/dr$ is the ballooning parameter, and < > here indicates the norm of an operator in the ballooning space.

Figure 1 shows the growth rate normalized by the ion transit frequency $k_{\parallel} v_{Ti}$ when $\beta = 0.2$ and 1%, $\tau = 1$, $\varepsilon_n = 0.3$, $\varepsilon = 0.25$, $\eta_e = \eta_i = 2$, $s = 1$, $q = 2$. The growth rate peaks at $k_{\theta} \simeq \omega_{pe}/c$ relatively insensitive to β, which is weakly destabilizing. The maximum growth rate is of the order of the acoustic transit frequency. Stabilization at short wavelengths is due to the finite banana orbit of trapped electrons. The mode frequency is approximately given by $\omega_r \simeq 2\varepsilon_n \omega_{*e}$. The instability persists even when trapped electrons are artifically suppressed, although the growth rate is reduced. In this case, the source of the instability is in the inverse Landau damping of untrapped electrons, as for the electrostatic toroidal drift mode.

The quasilinear particle and electron thermal fluxes are given, respectively, by

$$\Gamma = -\sum_k \mathrm{Im}\, F_{io} \frac{cT_i k_{\theta}}{eB} \left(\frac{e\phi_k}{T_i}\right)^2 n_o \tag{9}$$

$$Q_e = \sum_k \mathrm{Im}\, F_{eq} \frac{cT_e k_{\theta}}{eB} \left(\frac{e\phi_k}{T_e}\right)^2 n_o T_e \tag{10}$$

where

$$F_{eq} = \left\langle \frac{mv^2}{2T_e} \frac{\omega - \bar{\omega}_{*e}}{\omega - \bar{\omega}_{De} - k_{\parallel} v_{\parallel}} J_o^2(\Lambda_{eU}) \left| 1 - \frac{v_{\parallel} D_{es}}{v_{Te} F_{eU1}} \right|^2 \right\rangle_U + \left\langle \frac{mv^2}{2T_e} \frac{\omega - \bar{\omega}_{*e}}{\omega - \bar{\omega}_{De}} J_o^2(\Lambda_{eT}) \right\rangle_T \tag{11}$$

with $D_{es} = F_{eUO} + F_{eTO} - 1 - \tau(1 - F_{io})$ being the electrostatic dispersion relation when equated to 0. Fig. 2 shows the imaginary part of F_{io} and F_{eq} for the mode shown in Fig. 1 ($\beta = 0.2\%$). Im F_{io} is predominantly positive. Therefore, Γ is predominantly negative (anomalous pinch, $\Gamma < 0$). Im F_{eq} is positive, indicating $Q_e > 0$.

Nonlinear saturation of the instability is a challenging theoretical problem. For a qualitative estimate of the electron thermal diffusivity, we resort to the mixing length theory (8)

$$\chi_e = \frac{\gamma}{k_\perp^2} (1 + Aq^2) \frac{1 + \eta_e}{\eta_e} \tag{12}$$

where the factor $1 + Aq^2$ is to take into account a possible enhancement due to the toroidal geometry, and the factor $(1 + \eta_e)/\eta_e$ is due to the disparity between D and χ_e ($D << \chi_e$). (9) Since $\gamma \simeq k_\parallel c_s \simeq c_s/qR$, and $k_\perp \simeq \omega_{pe}/c$, we obtain

$$\chi_e \simeq \left(\frac{c}{\omega_{pe}}\right)^2 \frac{c_s}{qR} (1 + Aq^2) \frac{1 + \eta_e}{\eta_e} \tag{13}$$

This formula has been tested against the χ_e profiles deduced from JET discharges. (10) Fig. 3 shows experimental χ_e profiles in (a) ohmic, (b) ohmic + ICRH, (c) ohmic + NBI, and corresponding χ_e with A = 2 in Eq. (13). Agreements within a factor 2 can be seen. It is noted that the parameter A is the only adjustable unknown. The formula has also been compared with the TFTR ohmic data (11) by Hiroe (12) with a favorable agreement.

The thermal diffusivity given in Eq. (13) is proportional to

$$\chi_e \propto \frac{1}{n_e} \sqrt{T_e/M_i} \frac{q}{R} \frac{1 + \eta_e}{\eta_e} \tag{14}$$

A heavier ion mass is favorable (the isotope effect). A larger plasma current also improves energy confinement. Both features have been observed experimentally.

In summary, it is shown that a low β (below the MHD limit) tokamak discharge is unstable against skin size electromagnetic "drift" mode with a maximum growth rate of the order of the ion acoustic transit frequency. The proposed anomalous electron thermal diffusivity satisfactorily recovers the χ_e profiles in three different types of JET discharges and that in TFTR ohmic discharges.

This research has been sponsored by the Natural Sciences and Engineering Research Council of Canada.

REFERENCES

1. T. Ohkawa, Phys. Lett. **67A**, 35 (1978).
2. Y.Z. Zhang and S.W. Mahajan, Comm. Plasma Phys. Cont. Fusion 21, 243 (1988).
3. W. Horton et al., Phys. Fluids 31, 2971 (1988).
4. B.B. Kadomtsev and O.P. Pogutse, *Reviews of Plasma Physics*, Vol. 5, p.309.
5. P.N. Guzdar et al., Phys. Rev. Lett. 57, 2818 (1986).
6. A. Hirose, Univ. of Sask. PPL-117 (1990) (to be published).
7. A. Hirose, Nucl. Fusion (in press).
8. B.B. Kadomtsev, *Plasma Turbulence*, p. 106.
9. A. Hirose et al., IAEA Washington, D.C. (1990), paper CN-53/I-2-1.
10. D.F. Düchs et al., IAEA Kyoto (1986), Vol. 1, p. 325.
11. TFTR ohmic database prepared by D.W. Johnson (PPPL).
12. S. Hiroe (ORNL) (private communication).

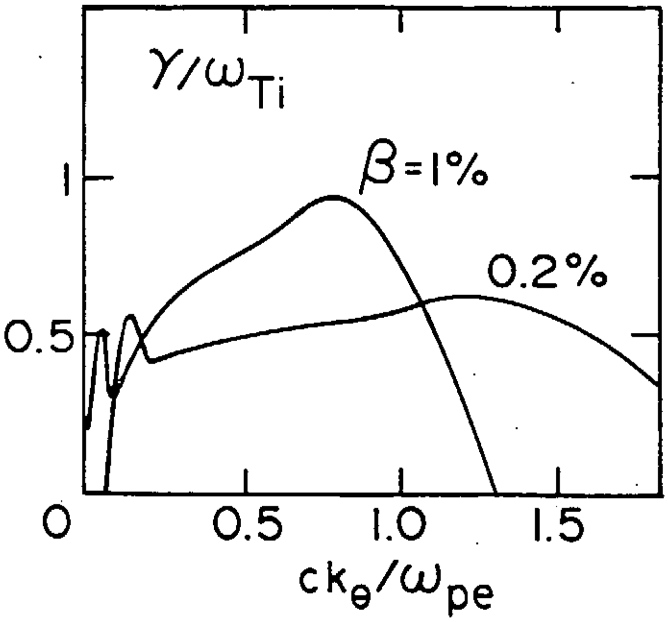

Fig. 1 Growth rates (normalized by $k_{\parallel}v_{Ti}$) $\tau = 1$, $\varepsilon_n = 0.3$, $\varepsilon = 0.25$, $\eta = 2$ $s = 1$, $q = 2$.

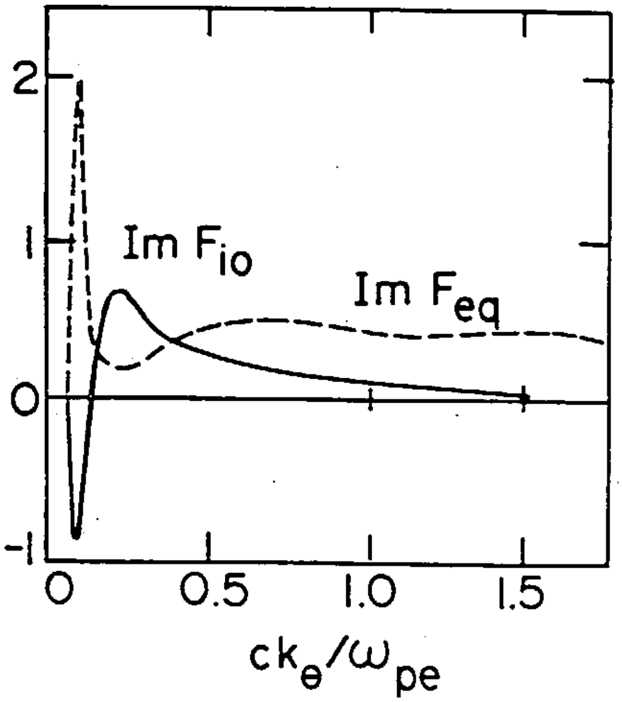

Fig. 2 Imaginary parts of F_{io} and F_{eq}. $\beta = 0.2\%$ case in Fig. 1.

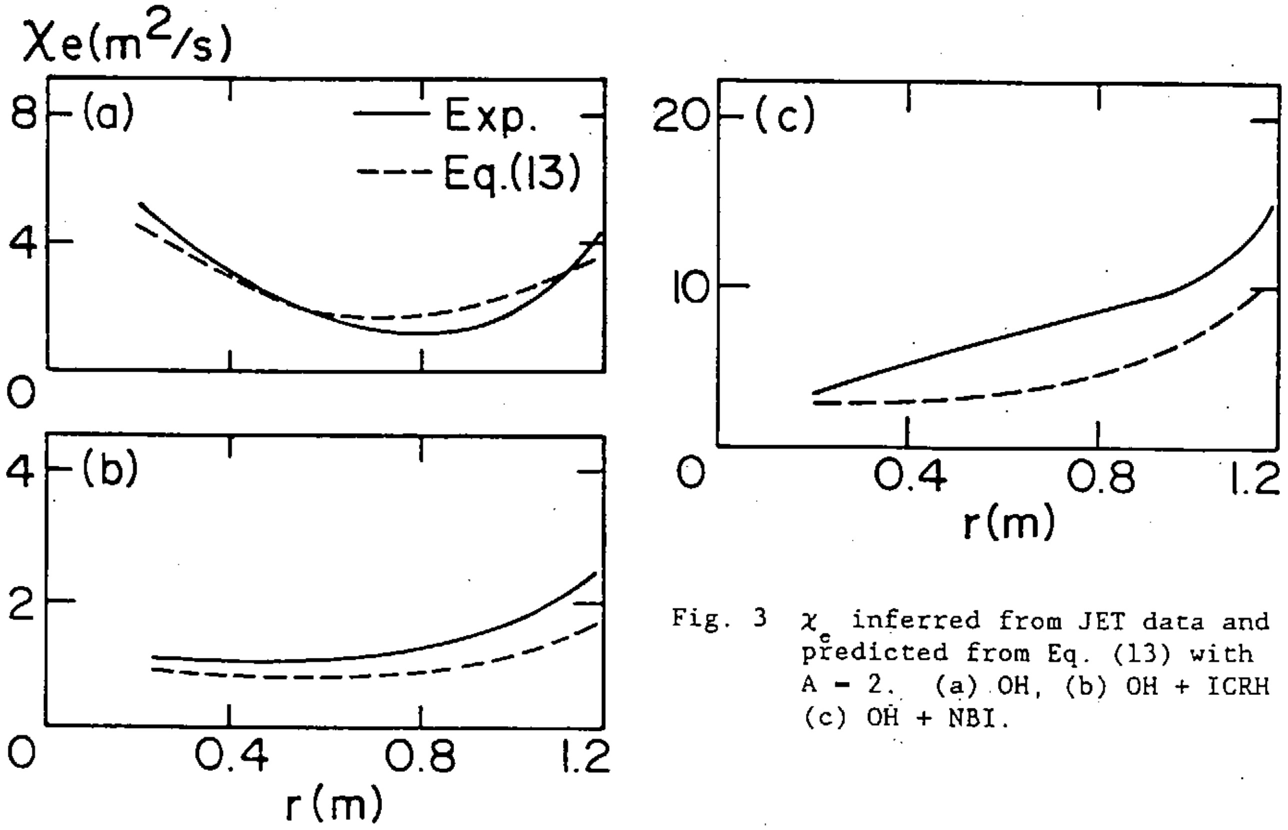

Fig. 3 χ_e inferred from JET data and predicted from Eq. (13) with $A = 2$. (a) OH, (b) OH + ICRH (c) OH + NBI.

Magnetohydrodynamical Formation of Astrophysical Jets from Gravitationally Collapsing Objects

Yutaka UCHIDA
Department of Astronomy, University of Tokyo
and
National Institute for Fusion Studies

Abstract

It is well known that there are jet-like phenomena in a wide variety of astronomical hierarchies, ranging from substellar to galatic, with scales of 10^9 cm in the case of stellar spicule jets, 10^{18}cm in the case of star-formation bipolar jets, and 10^{23}cm in the case of radio jets and lobes from active galactic nucleui and quasers. These are usually seen to be related with large scale magnetic field in a characteristic way.

In the present paper, we take up the case of the bipolar jets in the star formation as an example, and demonstrate that a magnetohydrodynamic mechanism proposed by the present author by noting that the central active objects are the gravitationally collapsing objects which brought a part of the large scale magnetic flux with their mass. The central object consisted of the accreting disk with angular momentum rotating around the forming star at the center twists up that part of the magnetic field through the differential rotation in the disk. When the thus-generated large amplitude torsional Alfven wavepackets relaxing through the atmospheric part of the accretion disk into bipolar directions, the packets drive the atmospheric mass into helical bipolar flows whose axis lie in the direction of the large scale magnetic field. The production of such non-linear torsional Alfven wavepackets by the rotating disk causes a continuous draining of the angular momentum from the disk. This allows further accretion of the disk mass towards the central object, liberating the gravitational energy from the inner part of the disk, and the magnetic field transports a part of this to bipolar directions through magnetic stresses.

The model predicts that the Jets will be spinning inherent to the magnetic stress involved. This 'dynamically sweeping pinch' character causing spinning jets makes a good contrast with the models proposed thus far: based on the 'wind from the central object' having a negligibly small angular momentum, the jets in the previous models will not show any spinning. Therefore, recent detection of the spinning velocity field in some of the bipolar flows gave a strong support to our magnetic model.

The model has been extended to the case of large scale radio jets and emanated from the central object of active galactic nuclei and quasars. In this case, the central object we assume is a giant blackhole at their center surrounded by a compact disk with high density and strong magnetic field, and the process physically similar to the star formation case but with much larger energy will be taking place. We report the detail of the model and the results of our 2.5D MHD simulations we have performed for these cases.

Computer Simulation of Solar Wind-Magnetosphere Interaction

K. Watanabe and T. Sato
National Institute for Fusion Science Nagoya, 464-01 Japan

A. Kageyama and A. Usadi
Faculty of Science, Hiroshima Univ. Hiroshima, 730 Japan

A three-dimensional high accuracy magnetohydrodynamic (MHD) simulation code was developed, in which the 4-th order Runge-Kutta-Gill method and the direct finite difference method were adopted. We have performed a global 3-D MHD simulation of the magnetosphere involving the distant tail (to 100 R_E) using the new simulation code.

Initially, the geomagnetic field is given as the superposition of a dipole field placed at the center of the earth and its mirror image dipole outside the solar boundary, so that the magnetic field has no component perpendicular to the solar boundary. As the solar wind flows from the solar boundary into the simulation box, the initial dipole field is deformed to the magnetosphere configuration, forming the bow shock, magnetopause, polar cusp, plasma sheet, etc. within 1.5 hours. The features of the formed magnetosphere is shown in the left top panel of the Figure 1, where magnetic field lines and solar wind streamlines are drawn for the meridian cross section.

The magnetosphere formed in this simulation is not in a stationary state. The plasma sheet in the region x = -15 to -30 R_E continues to thin and finally, at t = 1.62 hours, magnetic field reconnection occurs in the plasma sheet at x = -16 R_E in the equatorial plane (the x axis is along the sun/earth line with the positive direction pointing towards the sun). As a result of this near-earth reconnection, a plasmoid is produced and ejected tailward which is shown in Figure 1. Its size grows to more than 80 R_E and its speed is about 80 $\sim$ 100 km/sec. This plasmoid leaves the simulation box at t = 6.59 hours. After this plasmoid ejection, the width of the magnetosphere reduces by about 5 R_E. The ejecting plasmoid takes flux from the lobe field out the system with it, thus causing this reduction in magnetosphere width. The ejection of the first plasmoid was followed by a second reconnection and plasmoid ejection.

Though a small constant resistivity is assumed in the plasma sheet (magnetic Reynolds number 1000), no artificial methods are imposed to trigger the reconnection. Since the magnetic reconnection on the nightside is triggered by the cross tail current in the plasma sheet, the reconnection is considered to occur at the place where the tail current has its maximum value. In fact, the reconnection point is at x = -14 $\sim$ -18 RE in our simulations which is roughly at the demarcation region between the hard core of the dipole-like field and the tail configuration. This is the most fragile region in the magnetosphere. The intensity of the tail current as well as the magnetic field lines in the meridian plane are drawn in Figure 2, where the region of the strongest current is indicated in white.

The neutral point in the plasma sheet is located at about x $\sim$ -20 R_E throughout the ejection processes of the plasmoid. The point on the surface of the earth that is connected to the neutral point by a magnetic field line is at about 64.1 ° to 64.5 ° in latitude.

It can be easily imagined that the existence of the Interplanetary Magnetic Field (IMF) will enhance or suppress the reconnection rate on the nightside due to compression or decompression of the plasma sheet. Next, we performed global simulations in which the solar wind with a southward or northward IMF is injected into the simulation box after the magnetosphere is almost completely formed (about 1 hour after a nonmagnetized solar wind is introduced).

Figure 3 shows the time development of the magnetospheric structure when there is a southward IMF. The IMF reconnects with the geomagnetic field on the dayside, thus carrying it towards the nightside of the Earth. The IMF connected to the geomagnetic field piles up on the nightside magnetosphere and compresses the plasma sheet, increasing the temperature and pressure. In this case, the reconnection rate in the plasma sheet is enhanced and the size of the resultant plasmoid becomes large in a time short compared to the case without an IMF. The speed of the plasmoid is almost the same or a little higher than the previous case. It is noticed that the reconnection point in the plasma sheet is the same place as the case without an IMF. This fact suppoorts the above mentioned idea that the tail current peaking, hence reconnection, occurs at the demarcation region between the hard core of dipole-like field and the tail configuration. The current peaking at this point is seen more clearly than the case with no IMF. In this simulation the nightside reconnection starts about 20 minutes after a southward IMF arrives at the dayside geomagnetic field. This shows a good agreement with the fact that magnetospheric substorms are often observed tens of minutes after a southward turning of the IMF.

In Figure 4, the simulation results of the case with a northward IMF are shown. In this case, the northward IMF reconnects not on the dayside closed field line region but on the shoulder of the geomagnetic field lines which are blown off toward the tail by the solar wind. Consequently, the reconnected shoulder geomagnetic field lines are stripped off from the nigthtside magnetopause, decreasing the temperature and pressure. As can be seen in Figure 4, reconnection in the plasma sheet does not occur and hence, no plasmoids can be observed. It is interesting to note that as a result of the stripping of the geomagnetic field, the structure of the geomagnetic field returns to its initial dipole-like field.

References

Watanabe, K., and T. Sato, Global Simulation of the Solar Wind-Magnetosphere Interaction : The Importance of Its Numerical Validity, J. Geophys. Res., 95, 75-88, 1990.

Kageyama, A., K. Watanabe, and T. Sato, A Global Simulation of the Magnetosphere with a Long Tail : no IMF, to be published in J. Geophys. Res.

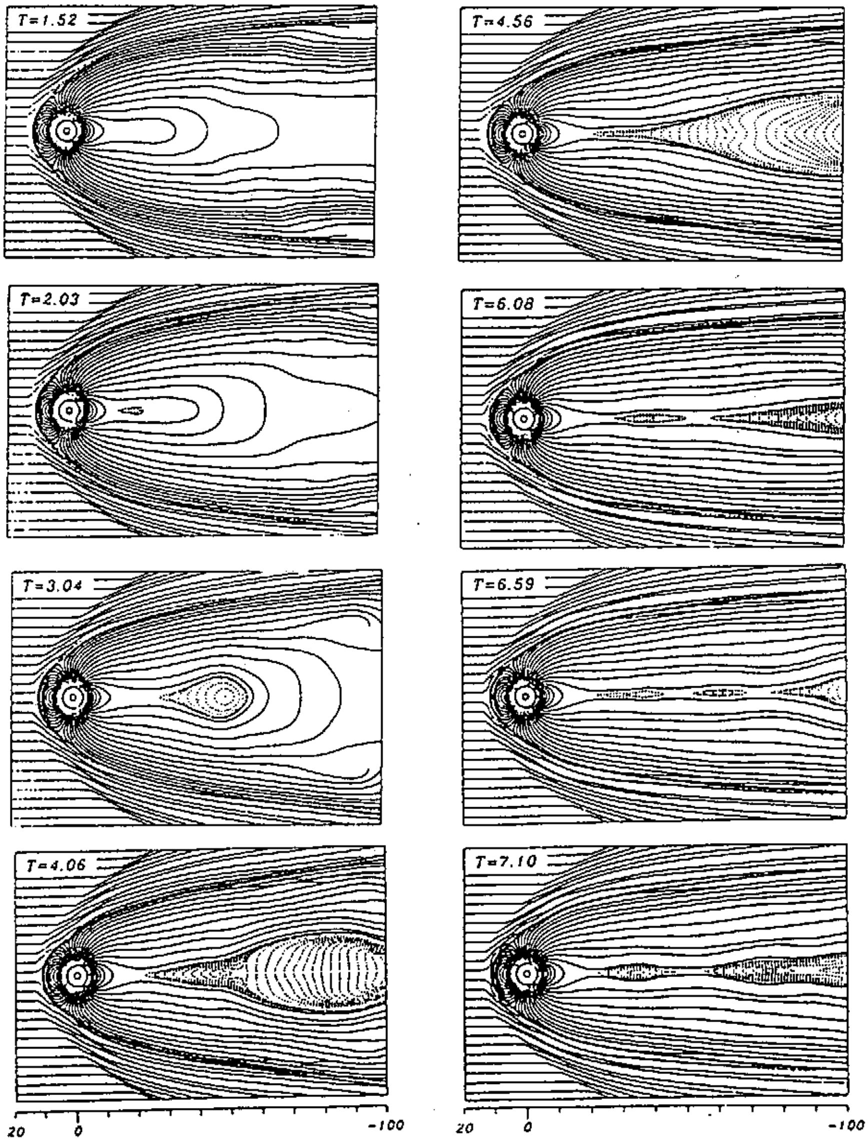

Figure 1

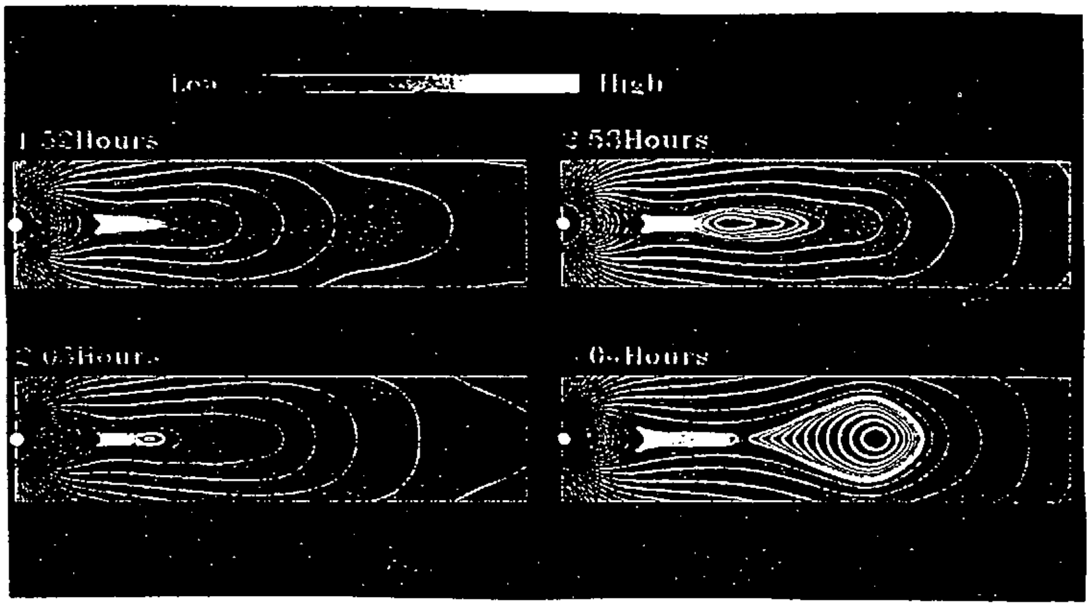

Figure 2

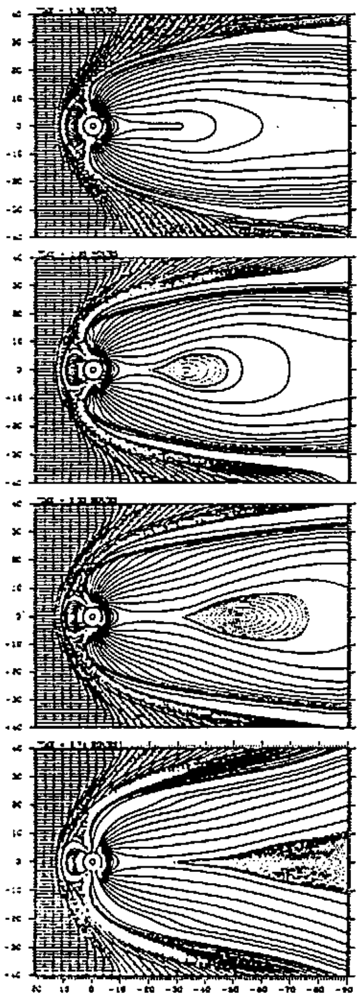

Figure 3

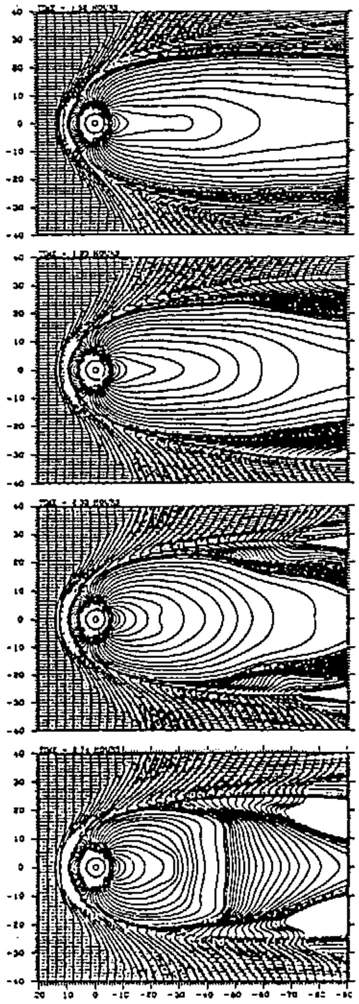

Figure 4

Rapid Acceleration of Protons in a Nonlinear Magnetosonic Wave and Their Energy Spectrum

Y. OHSAWA and Y. TERASHIMA

Plasma Science Center, Nagoya University, Nagoya 464-01, Japan

Abstract

This paper describes the prompt proton acceleration to relativistic energies in a large-amplitude magnetosonic wave which can take place in a rather strong magnetic field such that the electron cyclotron frequency is greater than the electron plasma frequency. The acceleration time is of the order of the ion cyclotron period. A fully electromagnetic, relativistic particle simulation shows that the differential energy spectrum of those accelerated protons can be very hard; it can have a truncated power-law form with the spectral index about unity. Using these energy spectra of protons, the energy spectra of gamma rays from the decay of neutral pions are calculated. These results indicate that this mechanism can explain the rapid proton acceleration in solar flares.

§1. Introduction

It has been recently found (Nakajima et al. 1983; Forrest et al. 1983; Kane et al. 1986) that solar flares can accelerate particles to relativistic energies very promptly ($\lesssim 1$ s). Among those flares, the 1982 June 3 flare was especially energetic event and was studied by many authors (McDonald and Van Hollebeke 1985; Forrest et al., 1986; Chupp et al. 1987). McDonald and Hollebeke (1985) observed the interplanetary proton spectrum associated with this flare and found that the proton differential energy spectrum for this event is a well-defined power law over the energy range 3 MeV - 200 MeV with a spectral index of 1.2. Observations of gamma rays and neutrons also showed that relativistic protons with energies a few GeV are promptly produced in this flare. (Gamma rays with energies greater than ~10 MeV are emitted from the electron bremssstrahlung and/or the decay of pions, which are generated from collisions of high-energy protons ($\gtrsim 300$ MeV) with background ions.) The energy spectrum of gamma rays is so flat and can be fit quite well if the parent ion spectrum has the same shape as the interpalnetary proton spectrum. A stochastic acceleration model can not explain either the prompt acceleration or the hard energy spectrum extending beyond 1 GeV.

On the other hand, it has been recently recognized (Ohsawa 1985; Tokar et al. 1987) that a large-amplitude magnetosonic wave can promptly accelerate some ions to high-energies through one or multiple reflections of ions by the large potential jump in the wave front; the acceleration time is of the order of the ion cyclotron period. In particular, when the electron cyclotron frequency is greater than the electron plasma frequency ($\omega_{ce} \gtrsim \omega_{pe}$), protons with relativistic energies can be produced (Ohsawa 1986ab; Lembege and Dawson 1989). The condition $\omega_{ce} \gtrsim \omega_{pe}$ can be satisfied in some coronal magnetic loops. Therefore, it is expected (Ohsawa and Sakai 1988) that relativistic protons can be promptly produced in solar flares if large-amplitude magnetosonic waves are excited in coronal magnetic loops in association with solar flares.

In this paper we briefly describe our theory and particle simulation of a large-amplitude magnetosonic wave and associated proton acceleration. We also discuss resultant energy spectra of protons and gamma rays from the decay of neutral pions.

§2. Ion Acceleration and Spectrum

We may classify ion orbits in a perpendicular nonlinear magnetosonic wave into three basic patterns. In the first type, ions pass through the wave without strong interactions. Most of ions belong to this type. In the second type, ions are reflected only once by the wave and gain a great amount of energy; after the reflection, they return to the wave front by the Lorentz force and pass through the wave. The final maximum speed of these ions is $v \simeq M v_A + (2e\varphi_m/m_i)^{1/2}$, where v_A is the Alfvén speed, M the Alfvén Mach number, φ_m the maximum value of the potential; for a stationary solitary wave, it is given by $e\varphi_m \simeq 2m_i v_A^2 (M-1)$. In the third type, ions are reflected several times by the wave front. The final maximum speed of this type of ions is limited by the value $v \sim v_A (m_i/m_e)^{1/2}(M-1)^{3/2}$.

We show in Fig.1 the ion orbits of the second (Fig.1a) and third (Fig.1b) types. (We have carried out numerical calculation of single particle orbits in stationary electric and magnetic fields of a stationary solitary wave.) The third type reflection can take place when the wave propagation velocity and the ion velocity in the direction of the wave normal are very close in the wave front. When the gyration speed is much smaller than the wave propagation speed, the third type reflection does not occur. Hence, the second type reflection is important when the Alfvén speed is much larger than the ion thermal speed.

Next we show results of a relativistic electromagnetic particle simulation of a perpendicular magnetosonic shock wave. The particle simulation follows the evolution of the wave and particle motion in a totally self-consistent manner. The plasma parameters in the simulation were $\omega_{ce}/\omega_{pe}=3.0$ in the far upstream region, the plasma beta value $\beta=0.02$, and the electron inertial length $c/\omega_{pe}=4$. The mass ratio was $m_i/m_e=100$. The Alfvén Mach number was 2.7. Figure 2 shows ion phase space plots (x,p_x) and (x,p_y) for this shock. A number of ions are rapidly accelerated to relativistic energies in the shock front. We plot in Fig.3 ion energy spectra at $\omega_{pe}t=0$ and at $\omega_{pe}t=408$. It indicates that a large-amplitude magnetosonic wave can produce flat energy spectrum such as observed in association with the 1982 June 3 flare.

In order to make more detailed comparisons with observations, we are also studying gamma-ray spectra emitted from the decay of pions. Figure 4 shows energy spectra of gamma rays from the decay of neutral pions which are generated from collisions of high-energy protons with background protons. The power-law forms of the ion spectra produce much harder photon energy-spectra than do the modified Bessel function forms (for more details, see Ohsawa and Terashima 1990). The calculation of energy spectra of photons arising from charged pions is under way.

References

Chupp, E.L., Debrunner, H., Fluckiger, E., Forrest, D.J., Golliez, F.,

Kanbach, G., Vestrand, W.T., Cooper, J., and Share, G. 1987, *Astrophys. J.*, 318, 913.
Forrest, D.J., and Chupp, E.L. 1983, *Nature*, 305, 291.
Forrest, D.J., Vestrand, W., Chupp, E.L., Rieger, E., Cooper, J., and Share, G. 1986, *Adv. Space Res.*, 6, 115.
Kane, S.R., Chupp, E.L., Forrest, D.J., Share, G.H., and Rieger, E. 1986, *Astrophys. J. letters*, 300, L95.
Lembege, B., and Dawson, J.M. 1989, *Phys. Fluids*, B1, 1001.
McDonald, F.B., and Van Hollebeke, M.A.I. 1985, *Astrophys. J.*, 290, L67.
Nakajima, H., Kosugi, T., Kai, K., and Enome, S. 1983, *Nature*, 305, 292.
Ohsawa, Y. 19865, *Phys. Fluids*, 28, 2130.
Ohsawa, Y. 1986a, *J. Phys. Soc. Japan*, 55, 1047.
Ohsawa, Y.. 1986b, *Phys. Fluids*, 29, 2474.
Ohsawa, Y., and Sakai, J-I. 1988, *Ap. J.*, 332, 439.
Ohsawa, Y., and Terashima, Y. 1990, *Publ. Astron. Soc. Jpn.*, 42, 551.
Tokar, R.L., Gary, S.P., and Quest, K.B. 1987, *Phys. Fluids*, 30, 2569.

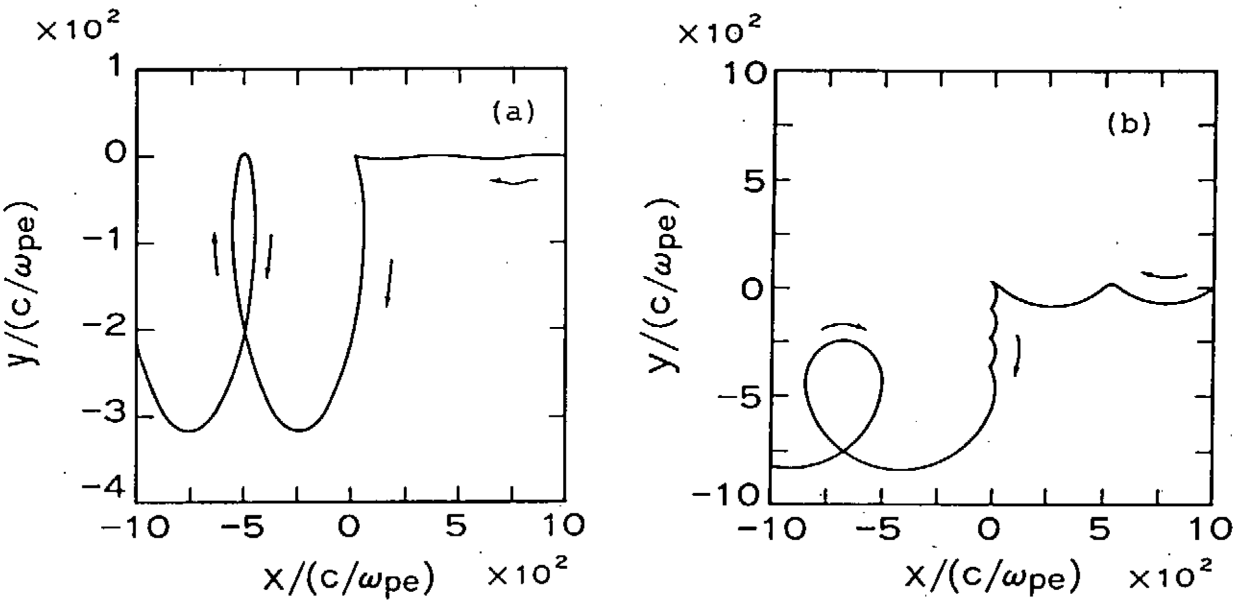

Fig.1. Ion orbits of the second (Fig.1a) and third (Fig.1b) types in a stationary solitary wave propagating in the x direction in a magnetic field in the z direction. The orbits are drawn in the wave frame.

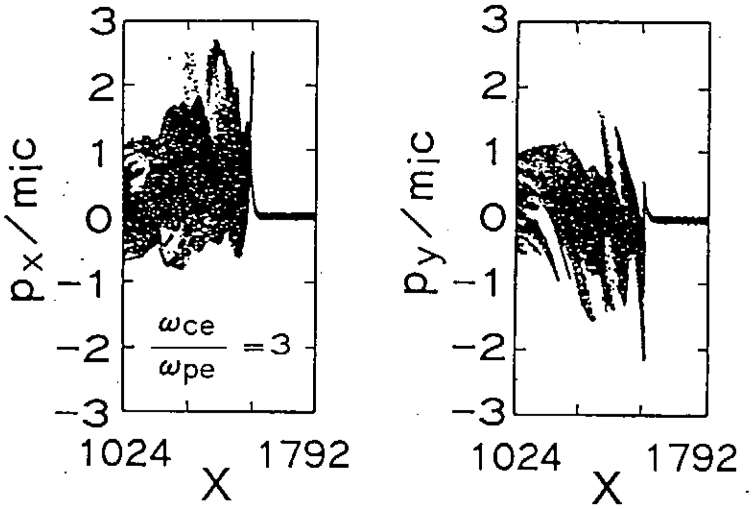

Fig.2. Snapshot of ion phase-space, $(x, p_x/m_ic)$ and $(x, p_y/m_ic)$.

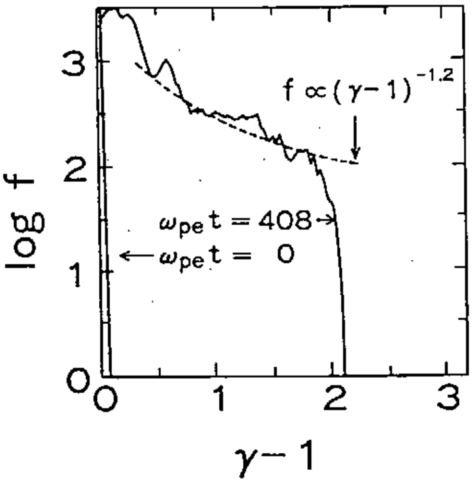

Fig.3. Ion energy spectra at $\omega_{pe}t=0$ and at $\omega_{pe}t=408$. The dashed line shows a power-law form $\propto(\gamma-1)^{-1.2}$, where γ is the Lorentz factor.

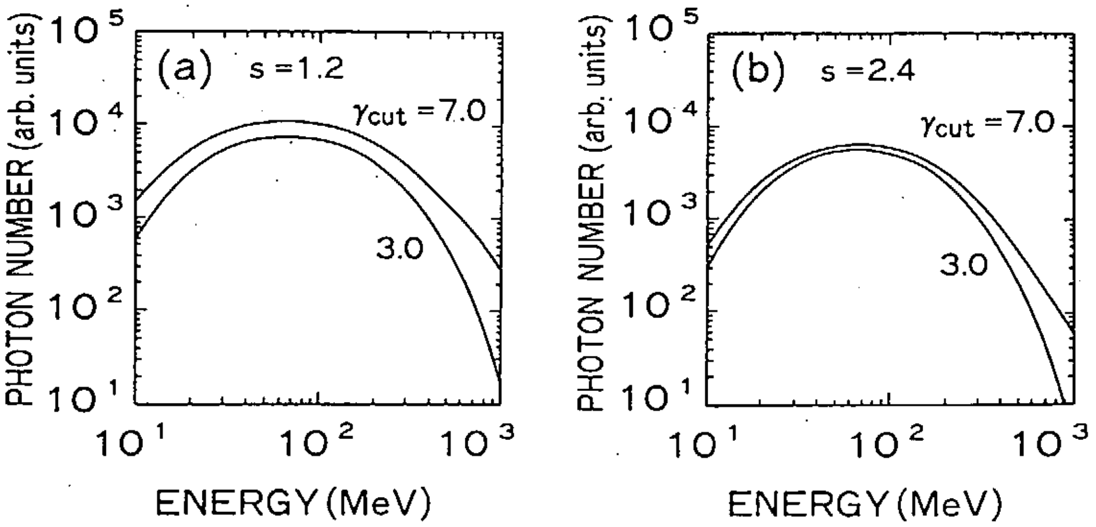

Fig.4. Photon energy-spectra for the truncated power-law spectra of protons with a spectral index $s=1.2$ (a) and with $s=2.4$ (b).

Effect of Pressure on Mode Transition Point of Partially Relaxed States with Peripheral Loss

Yoshiomi KONDOH

Department of Electronic Engineering, Gunma University,
Kiryu, Gunma 376, Japan

The well-known $\beta = 0$ Bessel function model configuration (BFM) was given more fundamental significance by Taylor who used it to explain the relaxation and the production of the reversed field pinch (RFP) configuration.[1,2] The mode transition point from the cylindrical state to the mixed helical one for the $\beta = 0$ BFM of the force-free equilibria, $\mu_0 j = \lambda B$, was studied by Taylor with use of analytical solutions giving minimum magnetic energy[1,2] and by Jensen and Chu with the use of an eigenvalue analysis.[3] The deviation of the experimental data[4] from the theoretical result by the BFM is considered to be connected with the deviation of the experimental profile of λ from the constant λ profile in the theory by Taylor, because of the high plasma resistivity near the wall by the plasma-wall interaction as was pointed out by Taylor himself.[2] The energy principle including the effect of the peripheral loss has been developed by the present author.[5,6] The effect of the λ profile on the mode transition point has been investigated in detail in Refs.6 and 7.

The equilibrium equation of the partially relaxed state plasma is given as follows in the orthogonal magnetic coordinate system $(-\psi, \omega, \zeta)$,[6]

$$j = \lambda_0 \Lambda(\psi) B/\mu_0 + p_0 (dP/d\psi)(\nabla\zeta / |\nabla\zeta|^2), \qquad (1)$$

where λ_0 and p_0 are the current density ratio ($\mu_0 j/B$) and the pressure at the magnetic axis, respectively, and $\Lambda(\psi)$ and $P(\psi)$ denote respectively the normalized profiles of λ and p by λ_0 and p_0. The relaxed states are characterized by having their own unique profiles of $\Lambda(\psi)$ and $P(\psi)$. Using two different processes of formulation, the energy integral for the nonideal MHD plasma (in the sence of the increment of the potential energy $\delta^2 F$ in the second order associated with the perturbed vector potential and the perturbed current density) is derived in the following form, as was reported in ref.6,

$$\delta^2 F = \int_{v_0} \delta A \cdot \delta [j - (\lambda B/\mu_0) - (dp/d\psi)(\nabla\zeta / |\nabla\zeta|^2)] dV$$

$$+ (1/\mu_0)\{\sum_i \oint_{s_i} [\delta A \times \delta B]_+^- \cdot dS + \oint_{s_w} (\delta A \times \delta B) \cdot dS\} > 0, \qquad (2)$$

where δA and δB are the variations of A and B, respectively. Here, $\delta [\ \ ]$ in the integrand is the first variation of the quantities in [ ], S_w is the boundary wall surface, S_i is the singular surface where δB is singular, and $\oint [\ \ ]_+^- \cdot dS$ denotes the difference of surface integral between the inside and the outside surface on the singular surface S_i.[6] The energy integral $\delta^2 F(\delta A, \delta A)$ has the symmetric quadratic form with respect to arbitrary δA that satisfies $\delta^2 F(\delta A^*, \delta A) = \delta^2 F(\delta A, \delta A^*)$.[6]

Reminimizing $\delta^2 F$ with respect to the variation of δA itself to find the most dangerous perturbation against stability, we obtain the following three Euler equations for the reminimization of $\delta^2 F$,[6]

$$\delta [\ \mathbf{j} - (\lambda \mathbf{B} / \mu_0) - (dp/d\psi)(\nabla \zeta / |\nabla \zeta|^2)\ ] = 0$$
$$(\text{ inside the regions where } \delta \mathbf{B} \text{ has no singularity }). \qquad (3)$$

$$\delta \mathbf{j}_s = [\ \mathbf{n} \times \delta \mathbf{B}\ ]^{+}_{-} = 0 \ (\text{ at the singular surfaces } S_i\ ). \qquad (4)$$

$$\mathbf{n} \times \delta \mathbf{B} = 0 \ (\text{ at the wall surface } S_w\ ). \qquad (5)$$

Here, $\mathbf{n}$ is the unit normal vector defined by $\mathbf{n} \equiv d\mathbf{S}/dS$ at S_i or at S_w. Since eq.(4) indicates that the marginally stable perturbations for singular mode, such as the tearing mode, must have no singularity at S_i, the overall stability limit for both the non-singular and the singular perturbations is determined by the solutions of the Euler equation (3).[6] The mode transition points of relaxed states are given by the eigenvalues of the following associated eigenvalue problem for the Euler equation (3), as was shown in ref.6,

$$\nabla \times \nabla \times \delta \mathbf{A}_i - \lambda_i \delta [\ \Lambda(\psi) \nabla \times \mathbf{A}\ ]_i$$
$$- \mu_0 p_i (\ d^2 P/d\psi^2)(\ \delta A_{i\zeta}\, \mathbf{e}_\zeta / |\nabla \zeta|^2\ ) = 0, \qquad (6)$$

with a given boundary condition at the wall, where λ_i and p_i are the eigenvalues and the subscript i denotes the eigensolution, $\delta A_{i\zeta}\, \mathbf{e}_\zeta$ is the ζ component of $\delta \mathbf{A}_i$, and the relations of $\mu_0 \mathbf{j} = \nabla \times \nabla \times \mathbf{A}$ and $\delta \mathbf{A} = \delta \psi \nabla \zeta + \delta \phi \nabla \omega - \delta \omega \nabla \phi$ are used.[6] When we use the ideally conducting wall, the boundary condition is $\delta \mathbf{A} \times d\mathbf{S} = 0$. The mode transition takes place at the point where

$$\lambda_0 = \lambda_i, \quad \text{and} \quad p_0 = p_i. \qquad (7)$$

The mode transition points given by eq.(7) also represent the bifurcation points of the equilibrium configuration determined by the equilibrium equation (1), which is generally equivalent to the Grad-Shafranov equation for the axisymmetric toroidal equilibria with the relation of $\lambda(\psi) = \mu_0\, dI(\psi)/d\psi$, where $I(\psi)$ is the current flux function.[8] In the case of the idealized model for relaxation by Taylor without net loss of helicity,[1,2] the relaxed state, so called " the fully relaxed state ", is given by $\Lambda(\psi) \equiv 1$ and $dP/d\psi \equiv 0$, and the associated eigenvalue problem, eq.(6), is written as $\nabla \times \nabla \times \mathbf{a}_i - \lambda_i^{(0)} \nabla \times \mathbf{a}_i = 0$, where $\lambda_i^{(0)}$ denotes the eigenvalue for the case of the fully relaxed state. Following Jensen and Chu,[3] we note that the eigenfunctions, $\mathbf{a}_i$, form a complete set.

Since it is difficult to solve eq.(6) directly, we have solved it to the first-order approximation by the perturbation method with the assumption of the ideally conducting wall, in the same way as was used in ref.6. We represent $\Lambda(\psi)$ and $d^2P/d\psi^2$ as $\Lambda(\psi) = 1 - \varepsilon E(\psi)$, and $d^2P/d\psi^2 \rightarrow \varepsilon\, d^2P/d\psi^2$, where ε is an artificial small parameter. We expand $\delta \mathbf{A}_i$ and λ_i as $\delta \mathbf{A}_i = \delta \mathbf{A}_i^{(0)} + \varepsilon \delta \mathbf{A}_i^{(1)} + \dots$, and $\lambda_i = \lambda_i^{(0)} + \varepsilon \lambda_i^{(1)} + \dots$, where $\delta \mathbf{A}_i^{(0)}$ and $\delta \mathbf{A}_i^{(1)}$ are the 0th and the 1st order solutions respectively, and $\lambda_i^{(0)}$ and $\lambda_i^{(1)}$ are the 0th and the 1st order eigenvalues, respectively. Using the same procedure used in ref.6, we obtain the following form of the smallest positive eigenvalues λ_1 and p_1 in the 1st order approximation,

$$\lambda_1 + \varepsilon \mu_0 p_1 H_{11} = \lambda_1^{(0)} (1 + \varepsilon G_{11}), \tag{8}$$

where $G_{ik} \equiv \int [(a_i \cdot \nabla \times a_k)E + (a_{i\zeta} a_k \cdot B / |\nabla \zeta|) dE/d\psi]dv$, and $H_{ik} \equiv \int (d^2 P/d\psi^2)(a_{i\zeta} a_{k\zeta} / |\nabla \zeta|^2)dv$.

Taking account of the experimental RFP plasma which has the finite pressure gradient and satisfies the boundary condition that the current density $j = 0$ at the wall, the present author had introduced the partially relaxed state model (PRSM) and developed numerical codes for the RFP equilibria and for the mode transition point of the relaxed state.[8,9,6] In the PRSM, various trial functions are used for the $\lambda(\psi)$ profile, and the pressure profile is determined numerically by using the Suydam criterion with the Suydam parameter S, where the stable region is $S \leq 1$.[8,9] We use here one of the simplest trial functions for the $\lambda(\psi)$ profile, which is given by

$$\lambda(\psi) = \lambda_0 \Lambda(\psi) = \lambda_0 \{1-[(\psi - \psi_{ax})/(\psi_w - \psi_{ax})]^m\}^n, \tag{9}$$

where the subscripts ax and w denote the values at the magnetic axis and the wall, respectively. Changing the four parameters of S, λ_0, m, and n, we obtain numerically various configurations of the PRSM for the RFP equilibria which satisfy the Suydam criterion. Using an iteration method, we obtain the mode transition point given by eq.(8). Numerical result of the pressure term in eq.(8) for the case of $S = 1$ and $n = 0$ is $3.72 \times 10^{-2}/r_w$ which is quite small compared with $\lambda_1^{(0)} = 3.11/r_w$. This result indicates that the effect of the pressure on the value of λ_1 is not strong for the Suydam stable pressure profiles. However, when we further calculate the pinch parameter θ at the mode transition point, we notice the strong effect of the pressure on the mode transition point in the F-θ diagram. Figure 1 shows the typical numerical results of the mode transition points (●) in the F-θ diagram for various values of S in the case of $\Lambda \equiv 1$. The Taylor curve and the mode transition point by Taylor ($\theta \sim 1.56$ and $F \sim -1.54$) are also shown for comparison. It is recognized from Fig.1 that the transition points of mode deviate fairly far from the point of $\theta \sim 1.56$ on the Taylor curve, especially in the case of $S = 1$. In Figs.2 and 3, we respectively show typical numerical results of the $\Lambda(\psi)$ profile and those of the transition points of mode for the case with $n = 1$, various values of m, and $S = 0$ [force-free fields and hence $H_{11} = 0$ in eq.(8)]. It is seen from Figs.2 and 3 that the deviation of the $\Lambda(\psi)$ profile from $\Lambda \equiv 1$ of the BFM leads to the move of the transition point of mode in the F-θ diagram. More detailed discussion on this force-free field case was reported in ref.7. When we include the pressure effect into the case of Fig.3, by using $S = 1$ (the marginally Suydam stable case), we obtain numerical results of the mode transition point in the F-θ diagram as shown in Fig.4, where the Taylor curve and the mode transition point for the BFM are also shown for comparison. It is recognized from Fig.4 that the effect of the pressure leads to fairly large shifts of the transition points of mode to the higher θ region and makes them closer to the experimental operating region reported so far.[4]

[1] J.B. Taylor, Phys. Rev. Lett. 33 (1974) 1139.
[2] J.B. Taylor, Rev. Mod. Phys. 58 (1986) 741.

[3] T.H. Jensen, M.S. Chu, Phys. Fluids 27 (1984) 2881.
[4] H.A.B. Bodin, A.A. Newton, Nucl. Fusion 20 (1980) 1255.
[5] Y. Kondoh, J. Phys. Soc. Jpn. 54 (1985) 1813.
[6] Y. Kondoh, J. Phys. Soc. Jpn. 58 (1989) 489.
[7] Y. Kondoh, N.Takeuchi, et al., J.Phys.Soc.Jpn. 58 (1989) 887.
[8] Y. Kondoh, Nucl. Fusion 21 (1981) 1607.
[9] Y. Kondoh, Nucl. Fusion 22 (1982) 1372.

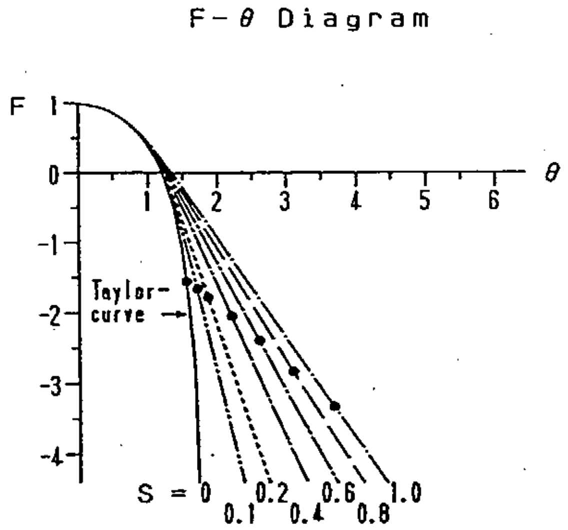

Fig.1 (n = 0, Λ (ψ)≡ 1)
mode transition points (●)

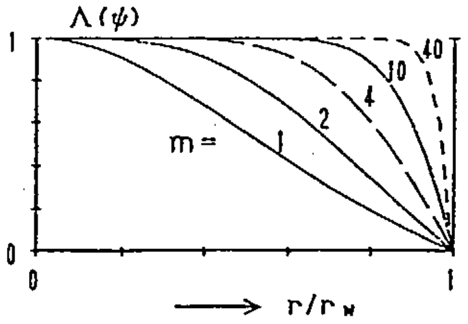

Fig.2 (S = 0, n = 1)

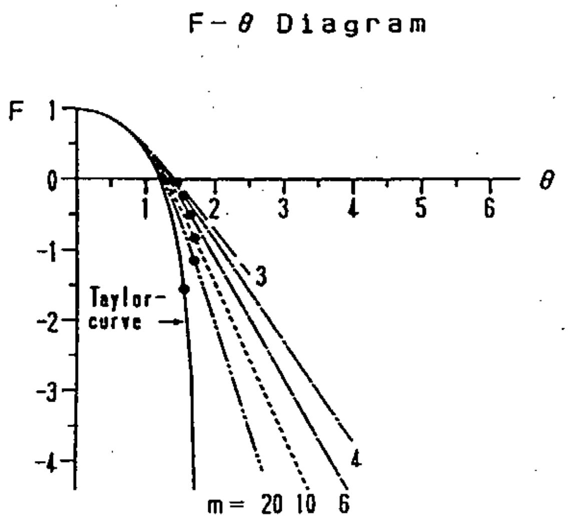

Fig.3 (S = 0, n = 1)

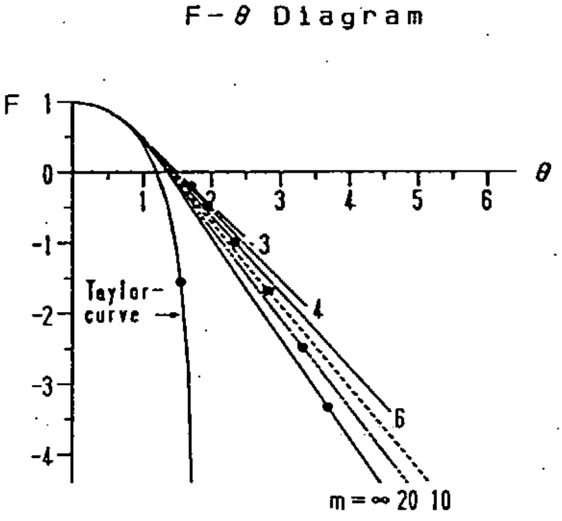

Fig.4 (S = 1, n = 1)

Relaxed state and entropy production

T. Kato and T. Furusawa

Department of Applied Physics, Waseda University,Tokyo,169

The relaxed states in RFP which are quiescent states and have been discovered in the experimental results of the large toroidal device ZETA were beautifully analysed by J.B.Taylor(1974). He assumed the single invariant helicity K_0 in the derivation of the relaxed state. Although the assumption on the invariance of the helicity integrated over the all magnetic field lines seems to be reasonable, one can only verify the invariance of helicity integrated along each line of magnetic flux. The validity of the ergodic property of magentic field line necessitates the finite electric resistivity of the MHD fluid.

To understand the relaxed states in RFP, We try introducing the thermodynamics of irreversible processes. Instead of the magnetic enery $W = \int B^2 d\tau/(2\mu_0)$, we must use the entropy production in the plasma. The entropy production due to the electric resistivity η of the plasma is expressed by $\sigma_{res} = \frac{1}{2}\int \eta J^2 d\tau$. The state of the minimum entropy production subject to the invariant K_0 is determined after the variational calculus with respect to the vector potential $\mathbf{A}$. The resultant differential equations which determine the relaxed state are given by

$$\nabla \times \nabla \times \nabla \times \mathbf{B} = \gamma^3 \mathbf{B} \tag{1}$$

with the following boundary condition on the surface

$$\delta \mathbf{A} \ = \ 0 \text{ and } \delta \mathbf{B} \cdot (\mathbf{J} \times \mathbf{B}) \ = \ 0, \tag{2}$$

where $\mathbf{B} = \nabla \times \mathbf{A}$, $\gamma^3 = 2\lambda\mu_0^2/\eta$ and λ is Lagrange's multiplier. Solutions of eqs.(1) satisfy the lower order differential eqs.

$$\nabla \times \mathbf{B}_j \ = \ \gamma\omega^j \mathbf{B}_j, \qquad (j = 0, 1, 2) \tag{3}$$

where ω and ω^2 denote the cube root of the unity. Eq.(3) with j=0 expresses the force free condition and coincides with Taylor's relaxed state. Although the other two solutions of eq.(3) with j=1 and 2 also express formally the force free condition, their proportional constants $\gamma\omega$ and $\gamma\omega^2$ are complex numbers and the real and imaginary parts of these solutions do not satisfy the force free condition, respectively.

The general solution of eq.(1) is given by a linear combination of three solutions of eq.(3) as,

$$\mathbf{B} \;=\; c_0\mathbf{B}_0 \;+\; c_1\mathbf{B}_1 \;+\; c_2\mathbf{B}_2. \tag{4}$$

The ratio of three constsnts c_j 's are uniquely determined by the boundary conditions (2) and magnitudes of c_1 and c_2 are found to be far smaller than that of c_0 .

[Cylindrical limit]

It is well known that the analytical solutions of eq.(3) with j=0 in cylindrical coordinates are given by the Bessel function $J_0(\gamma r)$ and $J_1(\gamma r)$ .Obviously the solutions of the rest equations are expressed by the Bessel function with complex argument $\gamma\omega$ and $\gamma\omega^2$. The Kelvin function ber and bei are the well known example of the functions. We define new real functions $L_\nu^\pm(r)$ by the aid of the modified Bessel function $I_\nu(r)$

$$L_\nu^\pm(r) \;=\; \Re\frac{1}{2}\{i^\nu[I_\nu(re^{i\frac{\pi}{6}}) \pm I_\nu(re^{-i\frac{\pi}{6}})]\}, \tag{5}$$

which can be evaluated by the numerical calculation by using the integral representation of the modified Bessel function.

The boundary condition (2) on the cylindrical suface of radius a is reduced to the condition on the components of the current J as

$$J_z \;=\; J_r \;=\; 0 \quad \text{on } r = a. \tag{6}$$

The resulting components of the magnetic field are expressed as

$$B_\theta(r) = J_1(\gamma r) - [J_1 B_z^r - J_0 B_\theta^r B_\theta^i(r) - \{[J_1 B_z^i - J_0 B_\theta^i] B_\theta^r(r)\}/(\gamma\Delta), \tag{7}$$

$$B_z(r) = J_0(\gamma r) - \{[J_1 B_z^r - J_0 B_\theta^r] B_z^i(r) - [J_1 B_z^i - J_0 B_\theta^i] B_z^r(r)\}/(\gamma\Delta), \tag{8}$$

where $\Delta = B_\theta^r B_z^i - B_z^r B_\theta^i$ and $B_\theta^r(r) = L_1^+(r)$,$B_\theta^i(r) = L_1^-(r)$, $B_z^r(r) = L_0^+(r)$, and $B_z^i(r) = L_0^-(r)$. The values of the component of magnetic field on the boundary surface are denoted by capital letters without argument.

The relation between the values of the helicity and energy W is given by Taylor. We obtain the relation between the entropy production σ_{res} and helicity K_0 .

$$\sigma_{res} - \mu\eta K_0 = \int_s \mathbf{n} \cdot (\mathbf{B} \times \mathbf{J} + \mathbf{A} \times \nabla \times \mathbf{J}) ds, \tag{9}$$

The right hand side of eq.(9) can be evaluated when the model is specified.

[$F - \theta$ diagram]

Using these components of the magnetic field, we can draw $F-\theta$ diagram whose coordinates are determined by the following formula

$$\theta = \frac{B_\theta(wall)}{< B_z >} \quad \text{and} \quad F = \frac{B_z(wall)}{< B_z >}, \tag{10}$$

where

$$< B_z > = \frac{\int B_z(r,z) r dr d\theta}{\pi a^2}. \tag{11}$$

Some of the numerical example are shown in figure 1. For small η , the $F - \theta$ curve coincides with that of the Bessel function model. The curves shift outwards and cross the θ -axis at the points $\theta > 1.2$ as η increase and finally shows erratic behaviors.

[Viscosity]

From the view point of the thermodynamics of irreversible processes the entropy production due to the viscosity and thermal conductivity of the plasma are available for discussion of the relaxed state in RFP. The problem of the thermal conduction is substantially nonlinear and the present analysis are greatly simplified by assuming uniform temperature distribution. The enrtopy production due to the viscosity ζ is given by,

$$\sigma = \frac{1}{2} \int \zeta \left(\frac{\partial v_i}{\partial x_k} + \frac{\partial v_k}{\partial x_i} \right)^2 d\tau. \tag{12}$$

The viscosity of plasma in a magnetic field depends on the angle between the velocity gradient and magnetic field. We consider the stress is parallel to the magnetic field and incompressible plasma.

The state of minimum entropy production subject to constant kinetic energy is similarly discussed. In cylindrical coordinates, the resulting differential equations are reduced to

$$\nabla^2 v_\theta + \beta v_\theta = 0 \text{ and } \nabla^2 v_z + \frac{1}{r}\cdot\frac{\partial v_z}{\partial r} = 0. \qquad (13)$$

It is assumed that the components of the velocity depend on r only and $v_r(r) = 0$. The magnetic field B and velocity v coulpe through the viscosity coefficients ζ. But analysis of the mutual relation through the viscosity coefficient is seemed to be difficult. Another coupling is possible through the some invariants other than helicity.

[References]
1)J.B.Taylor:Phys.Rev.Lett.33,1139(1974), Rev.Mod.Phys.58,741,(1986)
2)R.N.Sudan:Phys.Rev.Lett.42,1277,(1977)

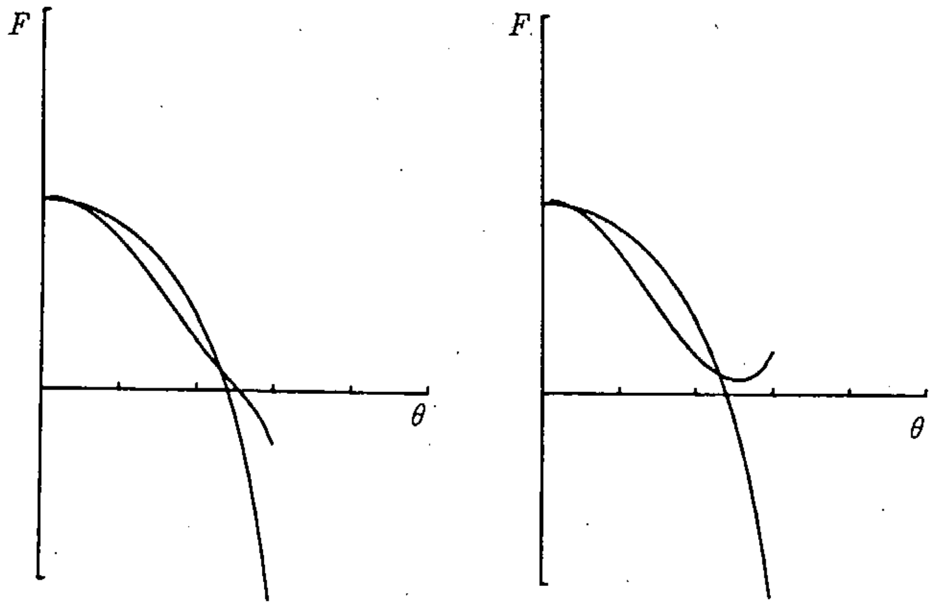

(a) (b)

Fig.1 $F-\theta$ Diagram : $F-\theta$ curves of present theory shift outwards comparing to B.F.M. , (a)κ=0.5 and (b)κ=0.8

SIMULATION STUDY OF MHD RELAXATION AND RECONNECTION PROCESSES

Kanya KUSANO, Kaito KUNIMOTO, Mami KUMANO,
Teruo TAMANO[1] and Tetsuya SATO[2]

Faculty of Science, Hiroshima University, Hiroshima 730, Japan
[1] *General Atomics, San Diego, California 92138-5608, U.S.A.*
[2] *National Institute for Fusion Science, Nagoya 464-01, Japan*

We have studied several nonlinear processes in fusion plasmas through the use of 3D MHD simulations. In particular, we have shed light on: 1) dynamo and self-sustainment in reversed-field pinch (RFP), 2) sawtooth activity in tokamak, and 3) the heating and acceleration in magnetic reconnection process.

dynamo and self-sustainment in RFP: First, we investigate the detail of the dynamo mechanism in RFP. Although it is widely believed that the $m = 1$ kink mode instabilities lead to a dynamo process like self-reversal, the role of nonlinear coupling between different kink modes in the dynamo is still in dispute [1,2]. The contributions of the kink ($m = 1$) mode (linearly unstable) and of the $m = 0$ mode (driven by nonlinear coupling) to the dynamo are qualitatively evaluated by observing the amount of dynamo electric field on the reversal surface. It is found that the contribution of the $m = 0$ mode is affected by the amount of the free energy driving the linear instability. If the free energy for kink instabilities is smaller than 7% of Taylor's minimum energy, the $m = 0$ modes, driven nonlinearly, play a more important role in the flux generation process than the kink modes. If not, (*i.e.* there are extremely unstable kink modes), the contribution of the $m = 0$ modes decreases. It suggests that in the experimental plasma, where the stored free energy is at most several percent of Taylor's minimum energy, the $m = 0$ modes actually play an important role for dynamo.

Secondly, numerical simulations of the self-sustainment process in a RFP are performed. It is confirmed that the self-sustainment process is a coherent oscillating process composed of the MHD relaxation and the resistive diffusion processes. The excess magnetic energy, which appears as result of the resistive diffusion, is quickly released by the MHD relaxation process. As this process is repeated, the RFP configuration stays in the neighborhood of Taylor's minimum energy state. We find that the MHD relaxation is triggered when at least two ideal kink modes become unstable. This is due to the fact that two unstable kink modes nonlinearly drive the $m = 0$ modes, which can effectively generate dynamo electric field. Therefore, in order to trigger the relaxation the unstable region in the toroidal wavelength space must be so wide as to include two different kink modes. The difference of the toroidal wave lengths between the neighboring kink modes is given by a decreasing function of the major radius,

$$\Delta\lambda \equiv \lambda_n - \lambda_{n+1} = \lambda_n^2(2\pi R + \lambda_n)^{-1}.$$

Because the wider unstable region requires the larger free energy, it is predicted that the critical free energy for the relaxation process decreases with the increase of the aspect ratio. This prediction is numerically confirmed. Figure 1(a) and (b) show the history of the free energy for the aspect ratio $R/a = 1.6$ and 4.8, respectively. We can see that the free energy just before the relaxations in Fig.1(b) is smaller about 1 or 2% of Taylor's minimum energy compared with those in Fig.1(a). These results strongly support the nonlinear reconnection model for the $m = 0$ mode [3].

Thirdly, phase locking of kink modes is numerically observed in simulations of self-reversal and self-sustainment processes. It has characteristics similar to the 'slinky mode' observed in the OHTE experiment [4]. We have in detail considered a question of what determines the location where the phase locking takes place. Figure 2 shows the relation between two toroidal locations $z_{p.l.}$ and $z_{4/5}$ for the 27 different simulations, those have different phase distributions in the initial state. The location $z_{p.l.}$ is where the phase locking takes place, but the location z_{n_1/n_2} is the location where the two kink modes, $(m;n) = (1, n_1)$ and $(1, n_2)$, initially have the same phase. We can see that there is a good correlation between the locations $z_{p.l.}$ and $z_{4/5}$. However, for the other modes except (1;4) and (1;5) we can not observe a correlation with the $z_{p.l.}$. In fact, the modes (1;4) and (1;5) are the most unstable modes in the initial perturbation. These results mean that the most dominant two kink modes rule the other modes through the nonlinear coupling between them, and introduce the phase locking. We also confirm that if the most dominant mode (1;5) is excluded from the system, the phase locking process becomes more obscure.

sawtooth activity in tokamak: Sawtooth activity in tokamak plasma is numerically investigated. Although the employed numerical model is rather simple (cylindrical geometry, scalar heat conductivity, and uniform density), we can find that two different types of sawtooth oscillations appear depending on the amount of heat conductivity. One of them is similar to the conventional Kadomtsev's type sawtooth [5], where the internal disruption is triggered by the reconnection for the resistive kink ($m = n = 1$) mode. On the other hand, the another type sawtooth does not involve any reconnection processes. In whole sawtooth period, the q-value nowhere goes down to less than unity. The fast crush of the central temperature is triggered by the growth of a pressure driven instability. It is much similar to Wesson's interchange model of sawtooth [6]. The quantitative relation of these sawteeth on the heat conductivity is investigated and it is found that the sawtooth mechanism is changed from the Kadomtsev's type to the Wesson's type as the heat conductivity decreases. Figure 3 shows the typical sawtooth oscillation (the history of the central temperature) of the latter case.

heating and acceleration in magnetic reconnection: We investigate the magnetic reconnection process as the heating and the acceleration mechanism of plasma. We find that reconnection can accelerate plasma over an local magnetosonic speed under a certain condition. This is a result of the fact that the magnetic field in the downstream area plays a similar role to *de Laval nozzle*, if the direction of the electric current in the downstream area is opposite to the current at the reconnection point. We also investigate the viscous heating of the super-magnetosonic plasma as a possible mechanism of the effective ion heating, which is observed in many RFP experiments.

[1] K.Kusano and T.Sato, *Nuclear Fusion* **27** (1987) 821.
[2] R.A.Nebel, E.J.Caramana and D.D.Schnack, *Phys. Fluids B* **1** (1989) 1671.
[3] K.Kusano and T.Sato, *Nuclear Fusion* **30** No.11 or 12 (1990).
[4] T.Tamano, W.D.Bard, C.Chu, Y.Kondoh, R.J.L.Haye, P.S.Lee, M.Saito, M.J.Schaffer, and P.L.Taylor, *Phys. Rev. Lett.* **59** (1987) 1444.
[5] B.B.Kadomtsev, *Sov. J. Plasma Phys.* 1 (1975) 389.
[6] J.A.Wesson, *Plasma Physics and Controlled Fusion* 28 (1986) 243.

FIG.1. Time History of the free magnetic energy in the cases of (a) the small aspect ratio (1.6) and of (b) the large aspect ratio (4.8). The free energy is normalized by a Taylor's minimum energy.

FIG. 2. The phase locking points $z_{p.l.}$ are plotted as a function of the location $z_{4/5}$ where the modes $(m;n) = (1;4)$ and (1;5) initially have a same phase. The solid circles show the 27 different simulation results, in which the different phase distribution in the initial perturbation is adopted, respectively.

FIG. 3. Time history of the central temperature in the tokamak sawtooth simulation.

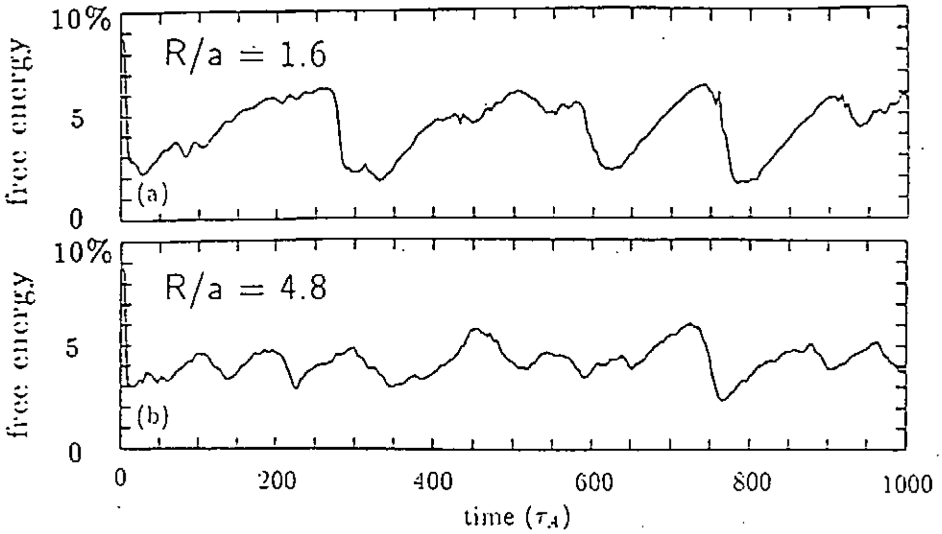

Fig.1

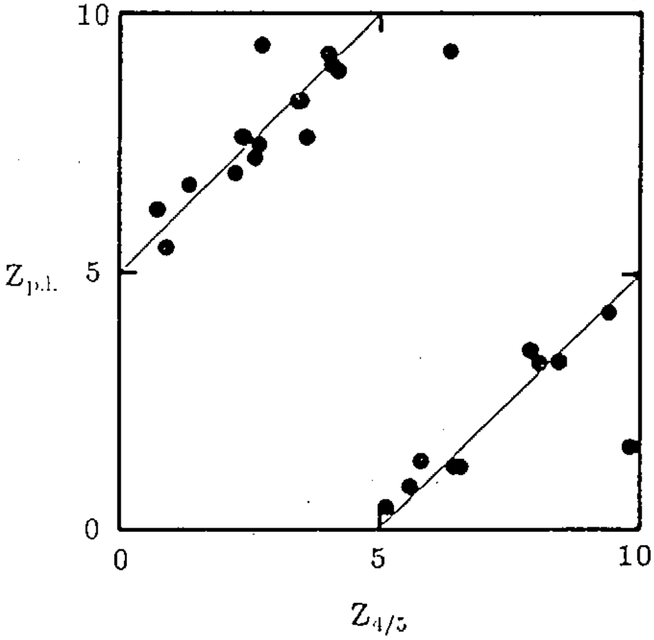

Fig.2

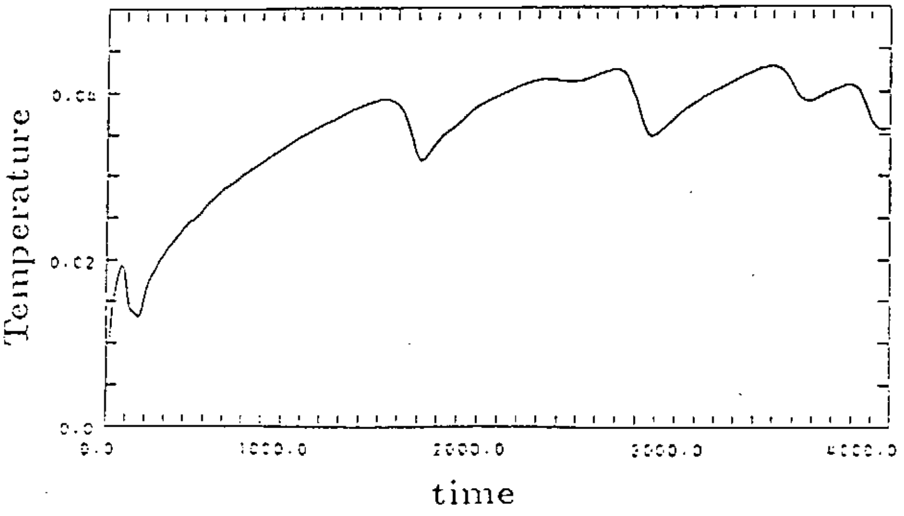

Fig.3

Finite β Equilibirum for A Pressure Configuration

Shinsaku Kajita
Department of Electronics and Computer Engineering
Faculty of Engineering, Gifu University
Yanagido, Gifu 500, Japan

Abstract

The equilibrium on the toroidal plasma with a configuration of parabolically increasing pressure is investigated. The critical pressure, affection of uniform transverse field and flux surfaces are investigated and compared to the linearly increasing one.

1. Introduction

The value of β which the shift of plasma owing to the curvature gets infinite is instructive(1) but practically could not realize because if the pressure got up the shift of the plasma would become very high. The pressure fluctuation of the steady plasma causes the shift of the plasma surface. The pressure increasing gets the plasma to shift outwards in the torus. The lowest shift of the plasma surface owing to the pressure increasing will probably occur at the extreme slope on the curve for β vs the plasma shift on the plasma surface : $\xi(a)$. The highest shift will occur at the moderate slope. The plasma shift $\xi(r)$ is concerned with the flux function which gives the pressure configuration, the rotational transform and the others through the following equation

$$B^0 r \iota_j \xi(r)\cos\theta = -\kappa\Psi_\kappa$$

where $\kappa\Psi_\kappa$: small flux function in κ order. ι_j: the lowest order rotational tranform of the helical field per unit length.
The κ order small flux function $\kappa\Psi_\kappa$ is obtained through the small-curvature expansion.

In the present report we investigate the equilibrium of a pressure configuration parabolically increasing ; $p^* = (1-\Psi_j(r)/\Psi_j(a))^2$. The linearly increasing pressure and the free boundary case is reported in the previous reference(1). The equilibrium of a parabolic configuration with r and a fixed boundary case is chiefly reported about the toroidal shift of the magnetic axis.(2)

2. Calculating Process

The equation of the κ order flux surface with the plasma confined through the helical field in a torus of a small curvature is given.(3) The equation is expanded through a small parameter κ and the κ order equation of the flux surface is solved. The equation is reduced to a convenient form in numerical work.(1) It has the usual singularity at the origin. We analytically solved the equation near by the origin and obtained the exact solution at the origin. These are as follows:

$$\xi(0) = C\frac{\gamma_1}{2} + 10\beta\frac{\kappa}{h^2}\frac{z_0}{1.6I_2'(z_0)I_2(z_0) + \beta z_0}, \qquad \xi'(0) = 0,$$

for our linear standard case.

$$\xi(0) = C\frac{\gamma_2}{2} + 20\beta\frac{\kappa}{h^2}\frac{z_0}{1.6I_2'(z_0)I_2(z_0) + 2\beta z_0}, \qquad \xi'(0) = 0,$$

for our parabolic standard case.

where

$$\gamma_1=[2.5(1.6+\beta\frac{z_0}{I_2'(z_0)I_2(z_0)})]^{1/2}, \qquad \gamma_2=[2.5(1.6+2\beta\frac{z_0}{I_2'(z_0)I_2(z_0)})]^{1/2},$$

$z_0=2ha$,
a denotes the plasma radius, C is the integral constant. $\xi(0)$ should be bounded, C also should be bounded. The other boundary condition is

$$\xi'(a) = -\frac{1}{a}[\frac{a\iota_l'(a)-2\iota_e(a)}{\iota_0(a)}+\frac{2S^2}{S^2-a^2}]\xi(a) + \frac{2B_x S^2}{aB^{(0)}\iota_0(a)(S^2-a^2)},$$

where $\iota_0(a)\fallingdotseq\iota_l(a)+\iota_e(a)$. This equation is given in reference(1). We consider $\iota_e=0$.

We prodceed to calculate from the origin for the various integral constant C. At the plasma boundary $\xi'(a)$ should agree with the boundary value fixed through substituting $\xi(a)$ into the equation. This is our process of calculation. We solve the equation for the various parameters as follows, (1) the helical field itensity changes, (2) the location of the conducting boundary outside the plasma changes, (3) the uniform transverse field changes. The case of linear pressure configuration to compare with the parabolic case is calculated on each case. We calculate the plasma boundary $\Psi_0+\varepsilon\Psi_1=C$ concerning $\varepsilon\Psi_1$ properly small.

We solved the equation changing β and C with the other fixed parameters. If the calculated results are expressed through β vs. the shift of plasma ; $\xi(a)$ on the plasma surface, we can obtain the critical value of $\beta;\beta_c$. The curve for β vs. $\xi(a)$ is indirectly concerned with the instability.

3. Calculated Results

Fig.(1) shows the results for the various fields. $H_\phi=1$ is standard for the comparative field intensity. The critical value of β is approximately 0.44 for the parabolic pressure configuration (P^2). Fig.(2) is for the linear one (P^1). The latter has a critical β somewhat large compared to the former.

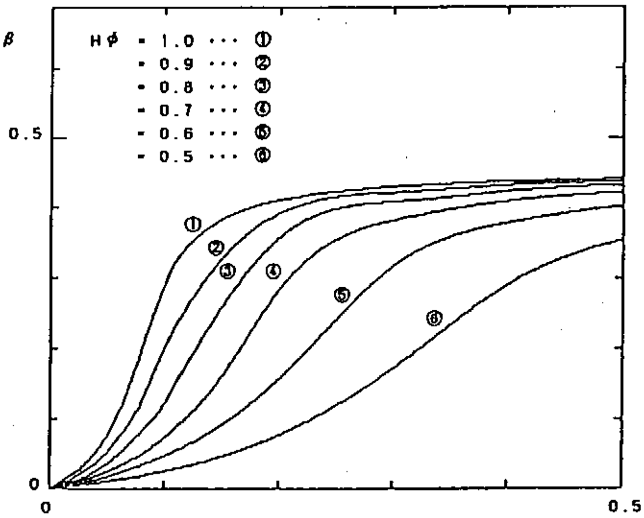

Fig.1 The original pressure curves vs. the shift of plasma on the plasma surface showing a critical pressure. (p^2)

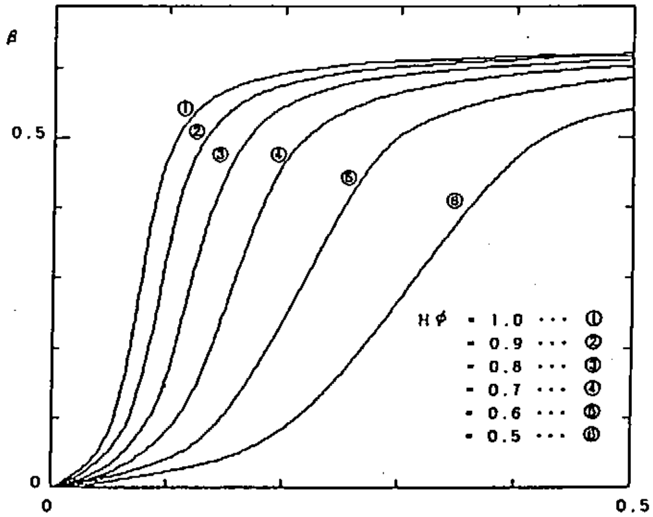

Fig.2 The original pressure curves vs. the shift of plasma on the plasma surface showing a critical pressure. (p^1)

Fig.(3) shows the shift of plasma; $\xi(0)$ at the origin. These are of course bounded. These for the linear one is also bounded. Fig.(4) shows the curves of β vs. the shift of the plasma ; $\xi(a)$ on the plasma surface for two different locations of the conducting boundary. V=0 is the infinitely far location. The location of the surface of plasma is unchanged. This shows that access to the plama surface gets β_c up.

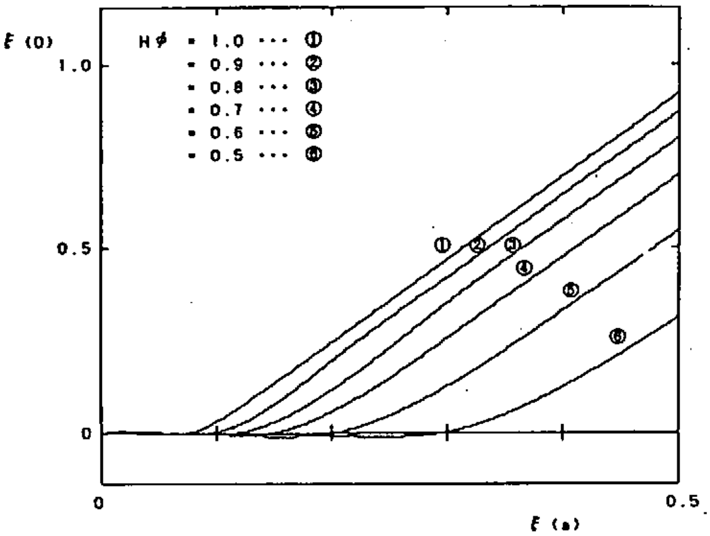

Fig.3 The curves of the shift of plasma at the origin vs. the shift of plasma on the plasma surface. (p^2)

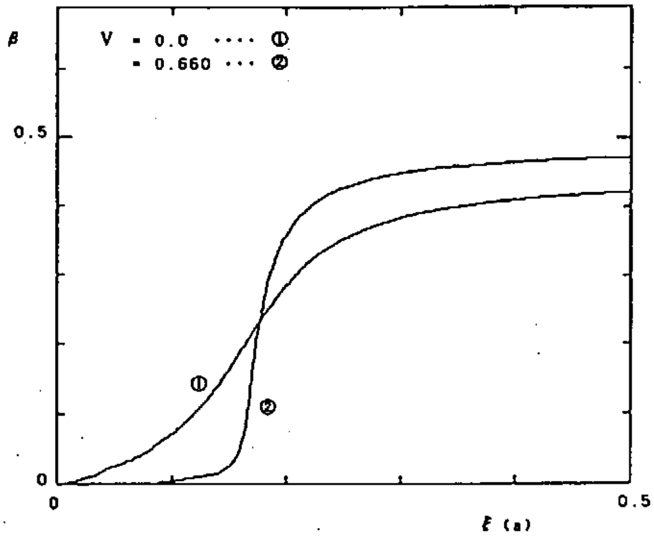

Fig.4 The pressure curves vs. the shift of plasma on the plasma surface for the different locations of the conducting surface. (p^2)

Fig.(5) shows the curves of β v. ξ(a) for two small uniform transverse fields applied. The curves shift towards the negative direction. It means that the transverse field makes the plasma on the plasma surface move outwards or inwards in the torus. The linear case is shown in Fig.(6). It also shows the transverse field makes the plasnma on the plasma surface move outwards or inwards in the torus.

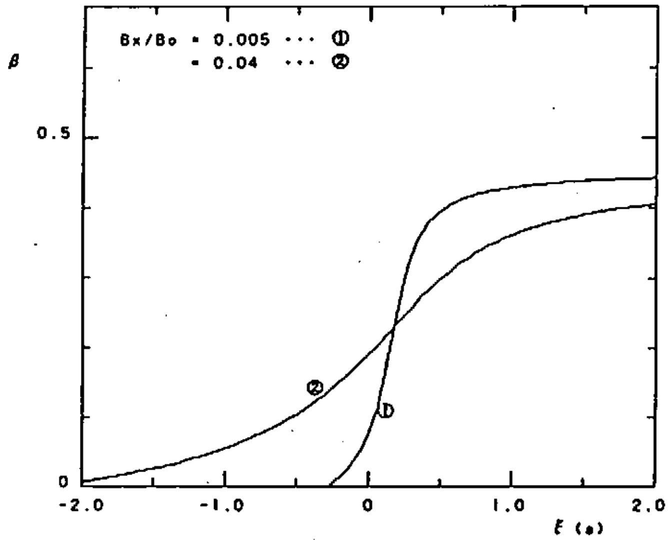

Fig.5 The pressure curves vs. the shift of plasma on the plasma surface for the different uniform transverse fields. (p^2)

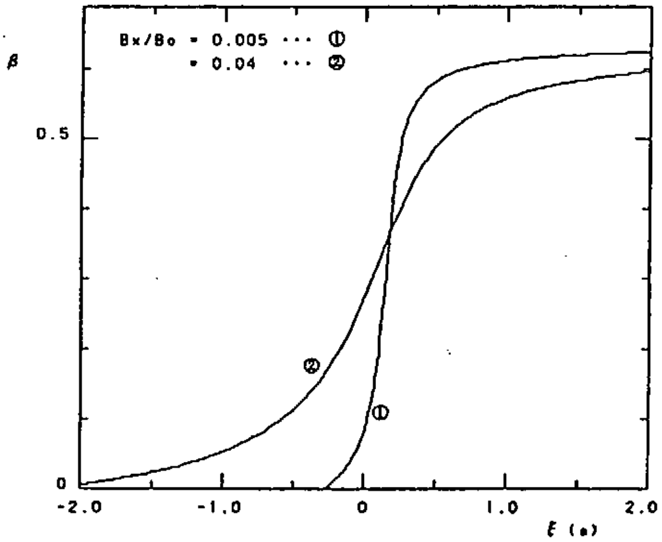

Fig.6 The pressure curves vs. the shift of plasma on the plasma surface for the different uniform transverse fields. (p')

Fig.(7) shows the shift of the plasma boundary with a small transverse field. The solid line shows the plasma boundary of the leading order and the dashed line shows the plasma boundary considering the flux function of the ε order. It shows the outward shift of the plasma boundary occurring in the torus. The linear case also shifts outwards for the same transverse field as shown in

Fig.(8).

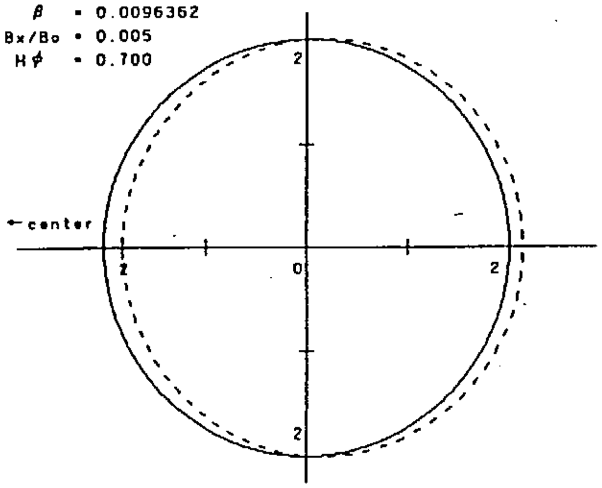

Fig.7 The section of the plasma surface for a transverse fields.(p^2)

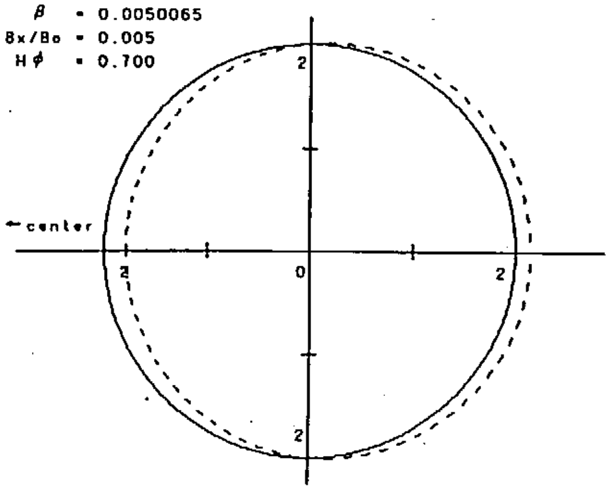

Fig.8 The section of the plasma surface for a transverse fields.(p')

4. Summary

We solved the ι order differential equation concerning the plsma shift;$\xi(r)$ by obtaining $\xi(0)$,$\xi'(0)$. Our main purpose motivated was to obtain the critical β for the configuration of the parabolically increasing pressure. Howerever, it seems that the critical pressure is not so much important to realize the steady plasma. The plasma shift near β_c is too high to keep the plasma steady. There would be the low pressure to overcome before arriving near at the critical pressure because the curves explain that the pressure at the starting point getting it up takes the considerably high plasma shift on the surface of the plasma (Fig(4)).

Our parabolic one is the similar characteristic as the linear one, though β_c of the former is smaller than the latter's. The critical value β_c does not change through changing the field intensity (Fig.(1),(2)), however,the location of the conducting boundary changes β_c (Fig.(4)). A small transverse field causes the plasma surface to shift large enough (Fig.(5),(6)). It would seem useful for not only the shift of the plasma surface but the realization of the stability. However, first of all, it is necessary to be stable that β of the plasma is smaller than β_c as J.L.Johnson pointed out.[4]

References

1) John M. Greene, John L. Johnson and Katherine E. Weimer, Plasma Phys (J. Nucl .Energy Part C) 8 (1966) 145.
2) M. Wakatani, IEEE PS-9 (1981) 243.
3) John M.Greene and John L.Johnson, Phys. Fluids 4 (1961) 875.
4) John L.Johnson, IPP 6/162 (1977).

Application of Mathematica to Energy Principle

T. Yamagishi
Fukui Institute of Technology, Gakuen, Fukui 910 Japan

Magnetohydrodynamic(MHD) equilibrium and stability analysis need laborious analytical works particuraly in nonlinear problems and in non-symmetric systems. Most of such analytical works are substitutions of equations, performing the dot and cross products, elimination of variables, differentitations and integrations, which may be carried out by computer. We here present applications of Mathematica[1)] to the derivation of nonlinear perturbations and evaluation of the plasma energy.

Formal Theory

By applying Mathematica, we first solve the system of MHD equations: the equation of motion, induction equation, continuity equation and equation of state, respectively written as follows,

$$\rho\frac{d\boldsymbol{v}}{dt}=\boldsymbol{J}\times\boldsymbol{B}-\nabla p\,, \tag{1}$$

$$\frac{\partial \boldsymbol{B}}{\partial t}=\mathrm{rot}(\boldsymbol{v}\times\boldsymbol{B})\,, \tag{2}$$

$$\frac{\partial \rho}{\partial t}+\boldsymbol{v}.\nabla\rho=-\rho\,\mathrm{div}\,\boldsymbol{v}\,, \tag{3}$$

$$\frac{\partial p}{\partial t}+\boldsymbol{v}.\nabla\rho=-\gamma p\,\mathrm{div}\,\boldsymbol{v}\,. \tag{4}$$

where all notations are standard. We solve these equations order by order by expanding in terms of the smallness parameter ε of the forms

$$\boldsymbol{B}=\boldsymbol{B}_o+\varepsilon\boldsymbol{B}_1+\varepsilon^2\boldsymbol{B}_2+\varepsilon^3\boldsymbol{B}_3+\cdots, \tag{5}$$

$$\boldsymbol{v}=\boldsymbol{v}_1+\varepsilon\boldsymbol{v}_1+\varepsilon^2\boldsymbol{v}_2+\varepsilon^3\boldsymbol{v}_3+\cdots, \tag{6}$$

The equilibrium quantities which are expressed by the subscript o, are assumed to be given. To have formal solution by Mathematica, the mathematical operators grad, div and rot are defined notationally which do not excecute anything.

The fluid velocity $\boldsymbol{v}$ is related to the plasma displacement ξ by

$$\boldsymbol{v}=\frac{\partial\xi}{\partial t}+(\boldsymbol{v}.\nabla)\xi\,. \tag{7}$$

Introducing eq.(6) into eq.(7), we have an iteration scheme $\boldsymbol{v}_{i+1}=(\boldsymbol{v}_i,\nabla)\xi$, where $\boldsymbol{v}_i=\partial\xi_i/\partial t$ with $\xi_{i+1}=(\xi_i.\nabla)\xi$ for i > 1. Introducing eqs.(5) and (6) into eq.(2), and solving each order of equation, we have for the i-th order magnetic field in the form

$$\mathrm{B}_i=\mathrm{rot}(\xi_1\times\boldsymbol{B}_{i-1}+\xi_2\times\boldsymbol{B}_{i-2}+\cdots+\xi_i\times\boldsymbol{B}_0)\,. \tag{8}$$

For i=1 in particular, eq.(8) reduces to the familiar result: $\mathrm{B}_1=\mathrm{rot}(\xi_1\times\boldsymbol{B}_0)$. Corresponding to B_i, the i-th order of plasma current is given by $\boldsymbol{J}_i=\mathrm{rot}\boldsymbol{B}_i$. By the same manner, from eq.(4), we have the i-th order of plasma pressure perturbation

$$p_i=-[\xi_1\nabla p_{i-1}+\cdots+\xi_i\nabla p_0+\gamma(p_0\mathrm{div}\xi_i+\cdots+p_{i-1}\mathrm{div}\xi_i)] \tag{9}$$

In eqs.(8) and (9), higher order quantities are determined iteratiely making use of lower order quantities. By useing these perturbations, the i-th order of plasma energy may be defined for i ≥ 1 by

$$W_{i+1}=-\int d^3r\,\xi^*.(\boldsymbol{J}_0\times\boldsymbol{B}_{i-1}+\boldsymbol{J}_1\times\boldsymbol{B}_{i-2}+\cdots+\boldsymbol{J}_{i-1}\times\boldsymbol{B}_0-\nabla p_i\ )\,. \tag{10}$$

Energy Principle

We now apply Mathematica to the derivation of the eigen mode equation by executing mathematical operators, grad, div and rot in the cylindrical coordinate system $(r,\theta,z)^{2)}$. In the linear theory, i=1, eq.(10) reduces to

$$W_2=\int d^3r\,\left(|B_1|^2-\xi^*\cdot J_0\times B_1+\gamma p_0|\mathrm{div}\xi|^2+\mathrm{div}\xi^*\xi\cdot\nabla p_0\right). \qquad (11)$$

We expand all perturbations in Fourier series of the form

$$B_1=\sum_{k,m}B_{km}(r)e^{im\theta+ikz}. \qquad (12)$$

By Mathematica commands, the perturbed magnetic field B_1 is easily obtained in term of ξ and B_0 by

```
B1=Expand[Exp[-I m phi-I k z]Curl[o[ξ,BO],Cylindrical]
```

where o[ξ,B_O] means the cross product $\xi\times B_0$. All perturbations are expressed in terms of $\xi=(\xi,\xi_p,\xi_z)$. By imposing the incompressibility condition $\mathrm{div}\xi=0$, one variable can be eliminated. Since ξ_p and ξ_z appear frequently in the form $\xi_p B_z-\xi_z B_p$, we expess all perturbations by ξ and $A=\xi_p B_z-\xi_z B_p$$^{3)}$. By solving simultaneous equations, $\mathrm{div}\xi=0$ and $A=\xi_p B_z-\xi_z B_p$, ξ_p and ξ_z can also be expressed by ξ and A, which can easily be done by Mathematica commands:

```
Solve[{divξ==0,yBz-zBp==A},{y,z}],
```

where y and z stand for ξ_p and ξ_z, respectively.

Introducing B_1 and ξ which are expressed in terms of ξ and A into eq.(11), the energy is now the quadratic form with respect to ξ, ξ' and A. The quantity A must be eliminated by an optimization condition of the energy. By Mathematica commands, this is done by Solve[D[E_1,A]==0,A] in which E_1 stands for the integrand of eq.(11) and D[E_1,A] means the partial derivative of E_1 with respect to A. By introducing A thus determined into E_1, E_1 becomes a quadratic form of ξ and ξ'. After factorizations for each coefficient of ξ^2, $\xi\xi'$ and ξ'^2 by using the command Factor, the energy is finally written in the familiar form

$$W_2=\int_0^a dr[f_m\xi_m'^2+g_m\xi_m^2]+((kaB_z)^2-(mB_p)^2)/(m^2+(ka)^2), \qquad (13)$$

where the coefficients f_m and g_m are given as follows

$$f_m=r(mB_p+krB_z)^2/(m^2+(kr)^2),$$

$$g_m=(mB_p+krB_z)^2-2B_p(rB_p)'/r+(mB_p-krB_z)^2/(m^2+(kr)^2)-$$
$$(((mB_p)^2-(krB_z)^2)/(m^2+(kr)^2))'$$

From eq.(13), the Euler equation is derived in the form

$$(f_m\xi_m')'-g_m\xi_m=0.$$

Nonlinear Theory

We now proceed to derivation of higher order perturbations. For the sake of simplicity, we neglect the nonlinearity due to the convection, i.e., $\xi_i=0$ for $i\geq 2$. In this case, eq.(8) reduces to $B_i=\mathrm{rot}(\xi_1\times B_{i-1})$ for $i\geq 1$. If we apply the same A as obtained in the linear theory, the second order magnetic field is given by the mode coupling form

$$\boldsymbol{B}_{2m} = \sum_{m_1+m_2=m} (\psi_1 \xi_{m1} \xi_{m2} + \psi_2 \xi_{m1} \xi'_{m2} + \psi_3 \xi'_{m1} \xi'_{m2}) \qquad (14)$$

where the mode number k has been dropped. The vector coefficient ψ_i involves $\boldsymbol{B}_0$, mode numbers (k.m), (k_1,m_1) and shear $(k\boldsymbol{B}_0)'$, which can be determined by applying Mathematica. The third order magnetic field given by $\boldsymbol{B}_3 = \mathrm{rot}(\xi \times \boldsymbol{B}_2)$ must have k=0 and m=0 mode number, i.e., the sum of mode numbers of ξ_1 and $\boldsymbol{B}_2$ must cancel. In this case, each comporment of $\boldsymbol{B}_3$ is written by $B_{3r}=0$, $B_{3p}=(\xi B_{2p}-\xi_p B_{2p})'$ and $B_{3z}=(r(\xi_z B_{2r}-\xi B_{2z}))'/r$.

The third order plasma energy W_3 is given by

$$W_3 = \int d^3r\, (\boldsymbol{B}_1^* \boldsymbol{B}_2 + \boldsymbol{B}_1 \boldsymbol{B}_2^* + \boldsymbol{B}_0 \boldsymbol{B}_3 + \left|\mathrm{div}\xi_1\right|^2 \gamma p_1 + \mathrm{div}\xi_1^* \xi_1 \nabla p_1) . \qquad (15)$$

For the case of incompressible force free plasma, the magnetic energy may be written in the form

$$W_3 = \int dr\, (\xi Q_{1m} + \xi'_m Q_{2m} + \xi''_m Q_{3m}) \qquad (16)$$

where Q_{im} is the quadratic form of ξ_{m1}, ξ_{m2}' and ξ_{m3}'', i.e., the mode coupling of other perturbations with different mode numbers. Combining eq.(13) and eq.(16), the Euler equation may be modified in the inhomogeneous form

$$(f_m \xi'_m)' - g_m \xi_m - \frac{1}{2}(Q_{1m} - Q'_{2m} + Q''_{3m}) = 0 , \qquad (17)$$

where all nonlinear terms come from the mode coupling of other pertubations with different mode numbers.

Although the Euler equation can determine the profile of eigenfunction, it does not determine the amplitude of eigen function. We introduce the amplitude perameter λ for the displacement: $\xi=\lambda\hat{\xi}(r)$. Then the i-th order of plasma energy may be written as $W_i=\lambda^i \hat{W}_i$. If we consider up to third order of energy, the plasma energy may be written as $W_p=\lambda^2\hat{W}_2+\lambda^3\hat{W}_3$. In the linear theory, the equilibium state $\lambda=0$ is stable when $\hat{W}_2>0$, otherwise the state is unstable. When the third order energy is taken into account, the stability criterion changes. As seen in Fig.1, when $\hat{W}_2>0$ and $\hat{W}_3<0$, the energy Wp has a peak at $\lambda=\lambda^*=-2\hat{W}_2/(3\hat{W}_3)$. The linearly stable state $\lambda=0$ is nonlinearly stable only when the kinetic energy W_k is less than the 'potential barrior' $\Delta=W_p(\lambda^*)$, otherwise $(W_k>\Delta)$ the linearly stable state becomes nonlinearly unstable.

On the other hand, when $\hat{W}_2<0$ and $\hat{W}_3>0$, the linealy unstable state $\lambda=0$ suffers transition to a nonlinearly stable state $\lambda=\lambda^*$. When $\hat{W}_2<0$ and $\hat{W}_3<0$ or $\hat{W}_2>0$ and $\hat{W}_3>0$, i.e., $\lambda^*<0$, the linear stability criterion does not change, i.e., the linearly stable (unstable) state is nonlinearly stable(unstable).

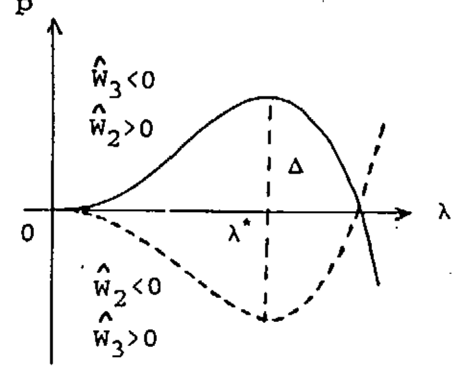

Fig.1

In the above case, W_3 is produced

by mode couplings of other perturbations with different mode numbers, which may be possible when many modes exist. Let us now consider a nonlinear problem due to single mode with the mode number (k,m). In this case, the second order magnetic field becomes (0,0) mode, which is given by eq.(14) with k=0 and m=0. The third order magnetic field B_3 in this case has the same phase as B_1, and the forth order field B_4 becomes (0,0) mode. The third order energy W_3 vanishes on the volume integral. The fourth order plasma energy can be written in the form

$$W_4 = \int d^3r\, (B_o B_4 + B_1^* B_3 + B_3^* B_1 + |B_2|^2 + |\mathrm{div}\xi_1|^2 \gamma p_2 + \mathrm{div}\xi_1^* \xi_1 \nabla p_2) \qquad (18)$$

Taking into account up to the fourth order, the plasma energy may be expressed by $W_p = \lambda^2 \hat{W}_2 + \lambda^4 \hat{W}_4$. The change of stability criterion due to W_4 is similar to the above mode coupling case. When $\hat{W}_2 > 0$ and $\hat{W}_4 < 0$, W_p has a peak at $\lambda = \lambda^* = (-\hat{W}_2/(2\hat{W}_4))^{1/2}$. The linearly stable state $\lambda=0$ is nonlinearly stable when $W_k < \Delta$, otherwise $(W_k > \Delta)$, the state becomes nonlinearly unstable. On the other hand, when $\hat{W}_2 < 0$ and $\hat{W}_4 > 0$, the linearly unstable state suffers transition to a new equilibrium state at $\lambda = \lambda^*$. This transition may be interpreted from the view point of synergetics$^{4)}$, i.e., the linearly unstable mode may form a spatial pattern (self organization), and tends to the nonlinearly stable state. When $\hat{W}_2 > 0$ and $\hat{W}_4 > 0$ or $\hat{W}_2 < 0$ and $\hat{W}_4 < 0$, λ^* becomes imaginary, and the linearly stable (unstable) state is also nonlinearly stable (unstable).

We can calculate W_3 and W_4 by applying Mathematica. The analytical expression becomes in general too long to write down even in the single mode case. If we assume a particular simple mode structure, for example, the m=1 kink mode with uniform displacement, $\xi' = \xi'' = 0$, near the plasma center $kr \ll 1$, then W_4 becomes calculable form.

In summary, Mathematica is useful both for nonlinear formal theory and complicated analytical calculations.

Acknowledgement
The author would like to thank Prof. T. Amano for providing information about Mathematica.

References

1) S.Wolfram, *Mathematica, A system for Doing Mathematics by Computer*, Addison-Wesely Publishing Co., New York, 1988.
2) T. Yamagishi, Memoir of Fukui Institute of Technology, No.21 (1991) to be published.
3) K.Mayamoto, *Plasma Physics for Nuclear Fusion*, Iwanami, Tokyo, 1976.
4) H. Haken, *Advanced Synergetics*, Springer, Tokyo, p.53, 1983.

DIRECT ION HEATING IN MHD RELAXATION

Z. YOSHIDA

Department of Nuclear Engineering,
The University of Tokyo,
Hongo, Tokyo 113, JAPAN

Dissipative power depositions through MHD relaxation into electrons and ions have been studied using classical resistivity and viscosity coefficients. In the reconnection process, perturbation currents (electron flow) and perturbation vortices (ion flow) are dissipated by resistivity and viscosity, respectively. An excess of electromagnetic energy is released through the MHD relaxation process. In this paper, we show that the energy dissipation in the MHD relaxation process is dominated by the ion viscosity.

Assuming a slab plasma model and Braginskii's viscosity, we obtain the ratio of the viscosity dissipation power P_D^i and the resistivity dissipation power P^e;

$$P_D^i/P^e = 0.3\beta_i(m_i/m_e)^{1/2}[1+(\omega_i\tau_i)^2](\gamma/\omega_A)^2(\lambda/k_{//})^2,$$

where $\beta_i = 2n_iT_i\mu_0/B_0{}^2$ is the ion beta ratio, ω_A is the Alfven frequency, and γ is the growth rate of the instability. Here we assumed hydrogen plasma, and used relations

$$B^* \sim \varepsilon(dB^*/dx) \sim \varepsilon\mu_0 j_{0z} \sim \varepsilon\lambda B_0,$$

where B* is the sheared component of magnetic field, $\lambda = \mu_0 j_{//}/B_0$, and $j_{//}$ is the parallel current of the mean field. To obtain numerical example, let us take $T_i = 100$ eV, $n_e = n_i = 10^{20}$ m^{-3}, and $B_0 = 0.3$ T. Then we have $\beta_i \sim 0.04$, $\omega_i\tau_i \sim 2\times10^2$. Both λ^{-1} and $k_y{}^{-1}$ are in the order of the minor radius a. For driven reconnections (γ/ω_A) is estimated to be typically in the order of 10^{-1}. Then we obtain $P_D^i/P^e \sim 10^2$. We thus see that MHD relaxation process driven by instabilities with a large growth rate results in ion viscosity heating.

Helical Field Effect in Solar/Stellar Wind

Haruichi Washimi

Solar-Terrestrial Environment Laboratory, Nagoya University, Toyokawa 442, Japan

Summary. Structure of the solar/stellar wind plasma and the helical magnetic field B_ϕ are studied by means of MHD simulation in an axisymmetric system. It is shown that, when the stellar rotation is much faster than the solar rotation, the magnetic pressure force $-\nabla B_\phi^2$ works and the interplanetary current is pinched along the rotation axis and the equatorial plane.

1. Introduction

Helical magnetic field B_ϕ is formed in solar/stellar wind plasma due to the solar/stellar rotation. One of the important parameters in the study of the wind is the Alfven Mach number of the flow, $M_A (= V/V_A)$, where V is the wind velocity in the meridional plane (poloidal component) and V_A is the Alfven speed. Weber and Davis (1967) showed in their 1-dimensional model that the total angular momentum, i.e., the summation of the magnetic torque and the plasma angular momentum, is given by the critical condition at $M_A = 1$. Their theory means that the line $M_A = 1$ should be included in the simulation box for a multi-dimensional computer simulation. In this paper an axisymmetric solar wind structure is studied by the method of MHD computer simulation including the solar rotation effect.

Wind from a rapid rotating star provides quite an efficien process to extract the angular momentum from the central body. If the wind is driven centrifugally, the angular momentum is transferred outwardly. It is shown that the magnetic pressure force $-\nabla B_\phi^2$ works on the wind plasma and that the losses of the mass, energy and angular momentum are enhanced for rapid rotating stars where the helical magnetic field B_ϕ is large.

2. Method of Simulation

We assume that the solar/stellar wind plasma obeys the coupled MHD and Maxwell equations. The energy equation is assumed to be described by a polytropic relation, and the polytropic index is 1.05 in our simulation. The cylindrical coordinates (r, ϕ, z) are used, and axial symmetry is assumed. The plasma density N and the pressure P, at 1 R_s (solar radius) from the sun, are taken as $N_0 = 10^8\ cm^{-3}$ and $P_0 = 3.8 \times 10^{-2} dyne \cdot cm^{-2}$, respectively. The temperature is 1.38×10^6 K at $1 R_s$. The sun is assumed to be rigidly rotating with the angular frequency $\Omega_s = 2.902 \times 10^{-6}$ rad/s. Starting with an appropriate initial condition, our aim is to obtain a steady or quasi-steady solution. For our initial condition of ρ, v_r, v_z and P, the spherically symmetric transonic solution is adopted.

Our simulation box includes the lines $M_A = 1$ and $M = 1$, where $M (= V/V_s)$ is the Mach number and V_s the sound velocity. Under these initial and boundary conditions, the computation is performed to obtain a quasi-steady state using the two-step Lax-Wendroff scheme.

3. Results and Discussion

The global structures of the solar wind are studied by numerical simulation for the case of the dipole magnetic field configuration. The global pattern in the meridional plane is shown in Fig. 1, and the latitudinal dependences of the physical quantities are shown in Fig. 2. N is large and V is slow in the closed field region (low latitudes), whereas N is small and V is large in the open field region (high latitudes). The azimuthal velocity v_ϕ in the closed field region shows an almost rigid corotation with the sun. But v_ϕ in the open field region is almost free of corotation. The azimuth magnetic field B_ϕ in the closed region is found to be almost zero, which means the plasma corotation creates no azimuth magnetic field. On the other hand, B_ϕ becomes maximum at the region just outside of the boundary and decreases again to zero at the rotation axis. This latitudinal dependence of B_ϕ is consitent with the inward poloidal current in the open region and sharp outgoing current just inside of the boundary shown in Fig. 1.

Sicnce magnetic pressure of the helical field has its maximum in middle latitudes for dipole field configuration, the stellar wind is pressed to the equator as well as deflected toward the rotation axis due to the magnetic pressure force $-\nabla B_\phi^2$ when B_ϕ is large (Fig. 3). As a result the centrifugal acceleration takes place most efficiently in the middle latitudes, and the mass flux has its peaks both on the rotational axis and on the equator. Loss rates of the mass, energy and angular momentum are shown in Fig. 4.

More detailed discussions have been given in papers (Washimi(1990), Washimi and Sakurai(1990), Washimi and Shibata(1990)).

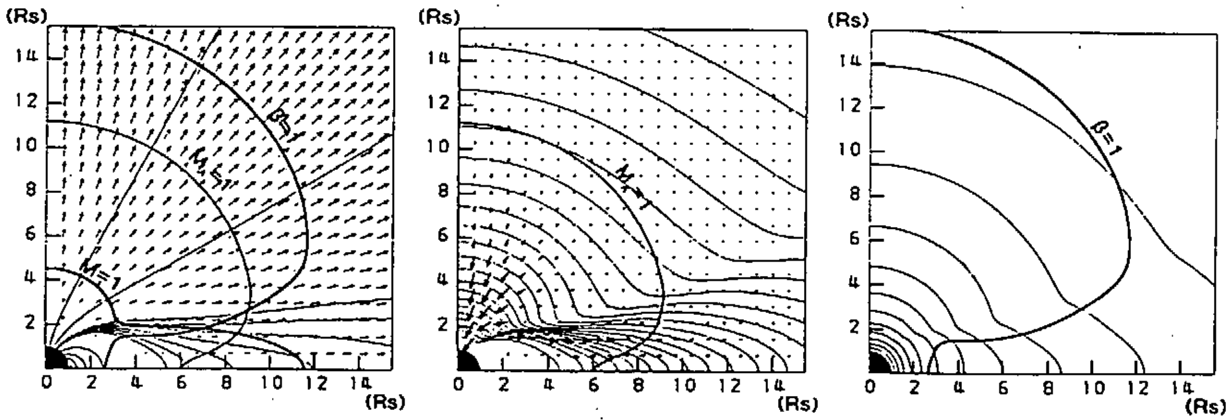

(a)

(b)

(c)

Fig. 1. Global patterns of the magnetic field lines and velocity vectors (a), equi-velocity contours and poloidal current vectors (b), and equi-density contours (c), when the magnetic field has a dipole configuration.

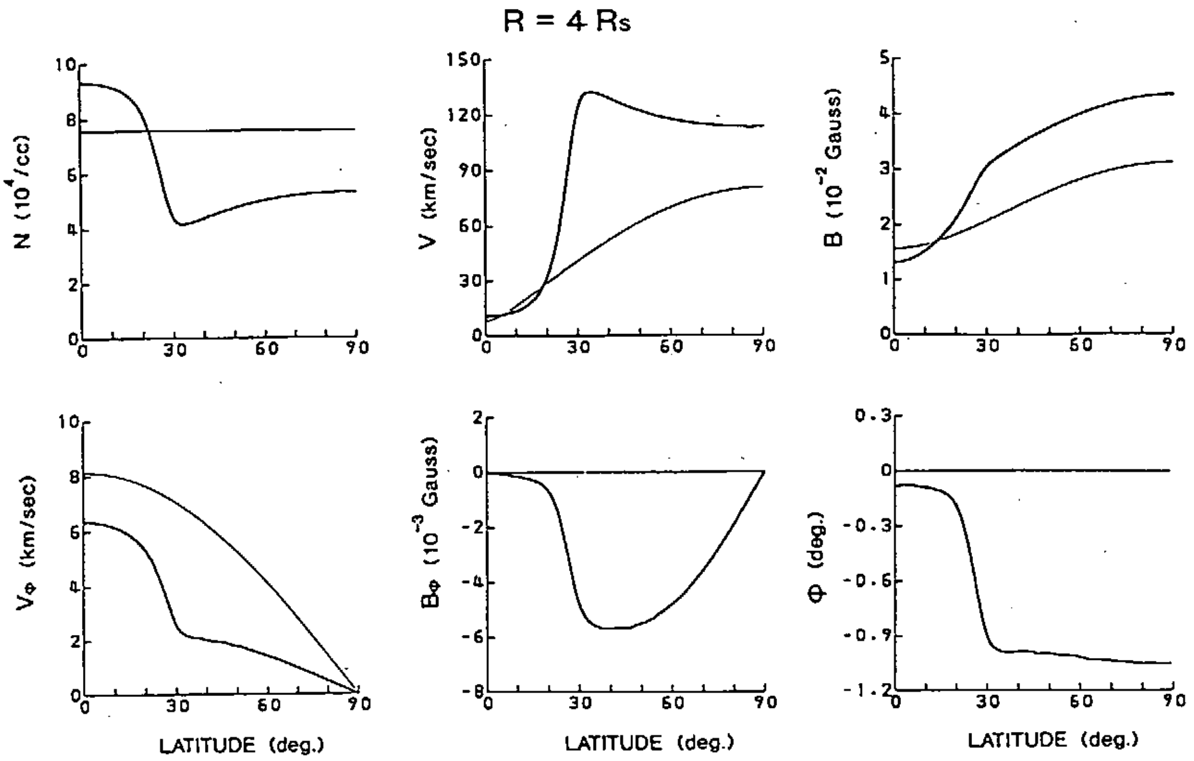

Fig. 2. Latitudinal variation of N, V, B, v_ϕ, B_ϕ and the direction angle of the magnetic field, Φ, for $R = 4R_s$. The thin line in each figure means initial state, while the thick line represents the final state.

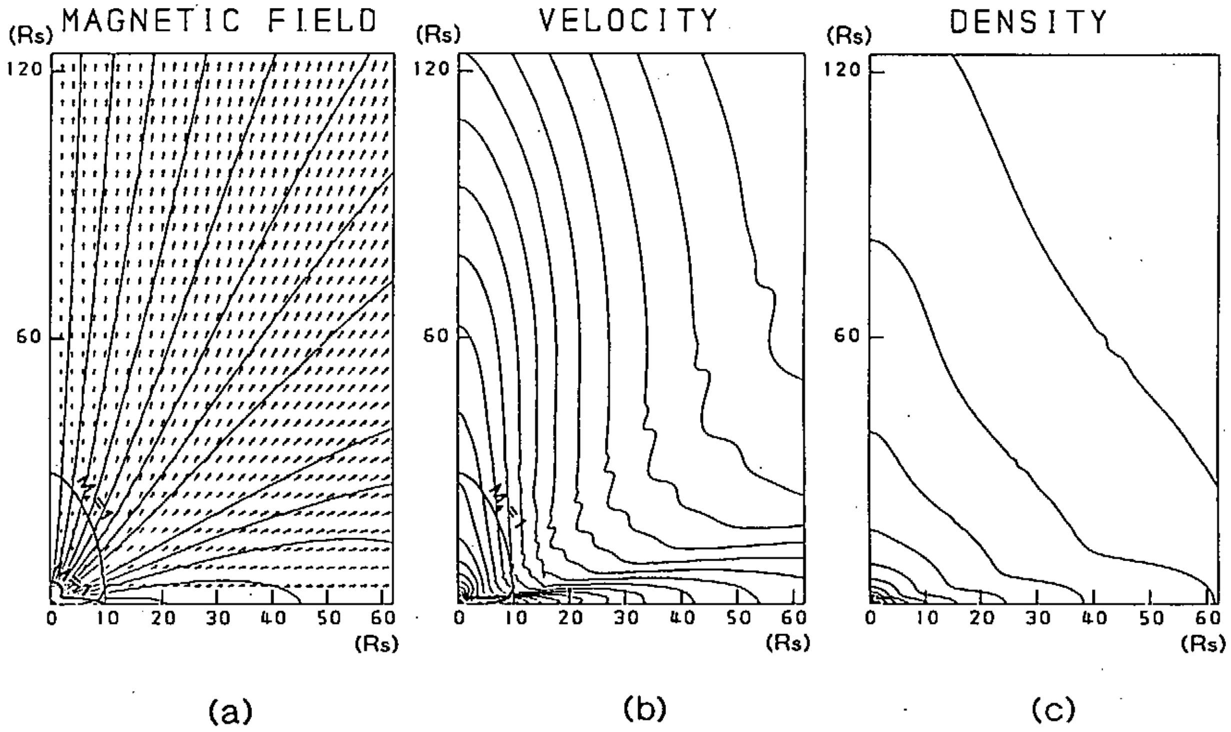

Fig. 3. Global patterns of the magnetic field lines and velocity vectors(a), eqi-velocity (b), and equi-density (c) contours for the rotation speed of $50\Omega_s$.

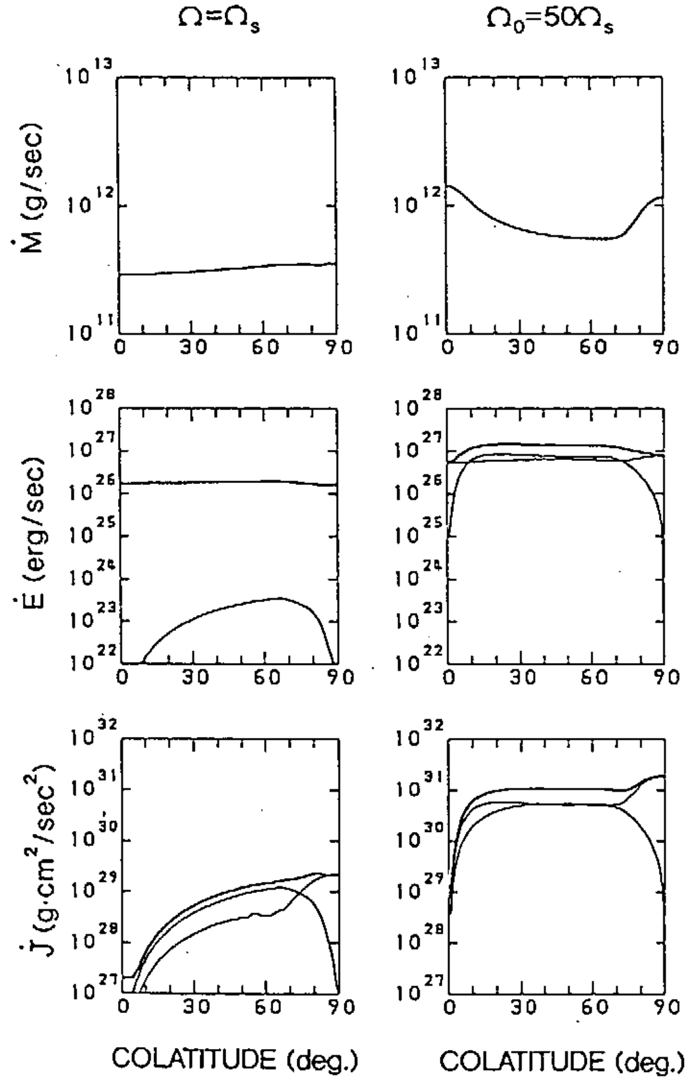

Fig. 4. Colatitude dependence of loss rates of the mass, energy, and angular momentum on the surface $R = 60R_s$. The left-hand panels are for Ω_s while the right-hand ones are for $50\Omega_s$.

Acknowledgements. The author would like to express his thanks to T. Ogino for his consent to use his two-step Lax-Wendroff scheme and to T. Sakurai and S. Shibata for their discussions. Computation was performed with Facom VP-200 and VP-200E at the Computer Center of the Institute of Nuclear Fusion.

References

Washimi, H.: 1990, *Geophys. Res. Letters*, **17**, 33.
Washimi, H. and T. Sakurai: in submission.
Washimi, H. and S. Shibata: in submission.
Weber, E.J. and Davis, L.: 1967, *Astrophys. J.*, **148**, 217.

Self-Similar Evolution of Nonlinear Magnetic Buoyancy Instability

K. Shibata[1], T. Tajima[2], and R. Matsumoto[3]

[1] Department of Earth Sciences, Aichi University of Education, Kariya, Aichi 448, Japan
[2] Institute for Fusion Studies, University of Texas, Austin, USA
[3] College of Arts and Sciences, Chiba University, Chiba 260, Japan

Abstract: A new type of self-similar solution of ideal magnetohydrodynamics in the nonlinear stage of undular mode (k $\parallel$ **B**) of magnetic buoyancy instability (Parker instability or ballooning instability) is found through MHD simulation and theory. The solution has the characteristics of nonlinear instability in Lagrangian coordinates; the fluid velocity and the Alfven speed on each magnetic loop increases exponentially with time, because the loop is evacuated by the field aligned motion of matter due to gravitational acceleration.

A plasma that is supported by a magnetic field under the gravitation is known to be subject to the Kruskal-Schwartzschild (or magnetic Rayleigh-Taylor) instability. Similar instability results in a gravitationally stratified plasma with non-uniform magnetic field, called magnetic buoyancy instability. The magnetic curvature can play a role similar to gravity. The undular mode (k $\parallel$ **B**) of the magnetic buoyancy instability, where k and **B** are the wavenumber and magnetic field vectors, is believed to be important in various physical phenomena ranging from astrophysical plasmas to fusion plasmas, because this mode can be unstable even when the plasma layer is stable against the interchange mode (k $\perp$ **B**). For example, for an isothermal case the former is unstable when $dB/dz < 0$, while the latter is unstable only when $d/dz(B/\rho) < 0$, where ρ is the density and the gravitation is in the negative z direction. Parker[1] applied the undular instability to the disk of Galaxy. Hence, this instability is called the Parker instability in some astrophysical literatures. The ballooning instability[2] in fusion plasmas has essentially the same physical characteristics as that of the Parker instability with general orientation of k with respect to **B**. In spite of many linear theory investigations, however, the physics of nonlinear stages of this instability is much less known. Here, we report the discovery of a self-similar solution in the nonlinear stage of the undular instability, which has a characteristics of the *nonlinear instability* (exponential growth in time) in a Lagrangian frame. A full discussion of this study is found in Ref. 3.

A self-similar solution has been found by using nonlinear simulations,[3] which are carried out with assumptions that (1) two-dimension (2D) [$V_y = B_y = \partial/\partial y = 0$ in Cartesian coordinate (x, y, z)], (2) ideal magnetohydrodynamics, (3) a constant gravitational acceleration (g) in the negative z-direction. A full set of compressible ideal MHD equations with the adibatic index γ (=1.05) are solved by using modified Lax-Wendroff scheme with artificial viscosity. The initial gas layer is in magneto-static equilibrium and consists of a cold isothermal plasma layer, which is partly permeated by horizontal isolated magnetic flux sheet with $\beta = 1$ in $z_0 < z < z_0 + D$, and a hot isothermal, non-magnetized plasma layer above the cold layer, where $D = 4H$. Hereafter, the units of length, velocity, and time are H, C_s, and H/C_s, where H is the pressure scale height and C_s is the sound speed in the cold layer. We initially give the system small-amplitude perturbations having the same spatial distributions as those of linear eigenfunctions in the most unstable mode with $\lambda = 20H$ in the finite horizontal domain.

Fig. 1 shows the time evolution of magnetic lines of force, the velocity field, and the density distribution. As the magnetic loop rises, the gas slides down along the loop. Spikes of dense regions are created on the valleys of the undulating field lines, whereas the rarefied regions are produced around the top of magnetic loops. The most significant character in the nonlinear stage ($t > 40$) is the approximate *self-similar pattern* of magnetic loop expansion; the rise velocity of the magnetic loop and the velocity of downflow along the loop increase with height as the loop expands and ascends. Fig. 2 shows some physical quantities at $x = X_{max}/2$ (midpoint of the magnetic loops), indicating approximate self-similar behavior as a function of height. We also find

$$V_z = a_1 z; \quad V_A = a_2 z, \tag{1}$$

where $a_1 \simeq 0.06 C_s/H \simeq 0.5\omega_l$ (for $t < 60$), $a_2 \simeq 0.3 C_s/H$, z is the height measured from $z_0 (= 4)$, and ω_l is the linear growth rate. On the other hand, we find the density and magnetic field strength have the power-law distribution;

$$\rho \propto z^{-4}; \quad B_x \propto z^{-1}. \tag{2}$$

We shall now look for a self-similar solution of the problem by analytical method. We have the following relation from Eq. (1); $\partial V_z/\partial\tau = \partial V_z/\partial t + V_z \partial V_z/\partial z = a_1 V_z$, where τ is the time in Lagrangian coordinates, while t and z are the Eulerian coordinates. This leads to

$$V_z(\xi, \tau) = a_1 \xi \exp(a_1 \tau), \tag{3}$$

where $\xi = z \exp(-a_1 \tau)$ is the Lagrangian coordinate. We assume the quasi one-dimension (1D) for the problem, i.e. we consider only vertical (z) variation of the physical quantities at the midpoint of the loop. Under this assumption, a particular self-similar solution, that satisfies our empirical velocity functions (1) and (3) and quasi-1D MHD equations, is found;

$$\rho = r_1 \xi^{-4} \exp(-4a_1\tau) = r_1 z^{-4}; \qquad B_x = b_1 \xi^{-1} \exp(-a_1\tau) = b_1 z^{-1}, \tag{4}$$

where r_1 and b_1 are constants. This solution agrees very well with the numerical solution (2).

Fig. 3 shows the time evolution of the Lagrangian displacement of a test particle at the midpoint of the loop in the simulation results. In the initial stage, the growth rate of the perturbation amplitude agrees well with linear theoretical values ($\omega_l = 0.121$). The amplitude increases exponentially with time even in the nonlinear stage ($t > 40$); $z \propto \exp(\omega_n t)$ and $\omega_n \simeq a_1 \simeq 0.06 \simeq \omega_l/2$.

It is known that the rise velocity V_b of the bubble observed in the laboratory and in the ionosphere tend to be steady in the Lagrangian frame and is in proportion to the

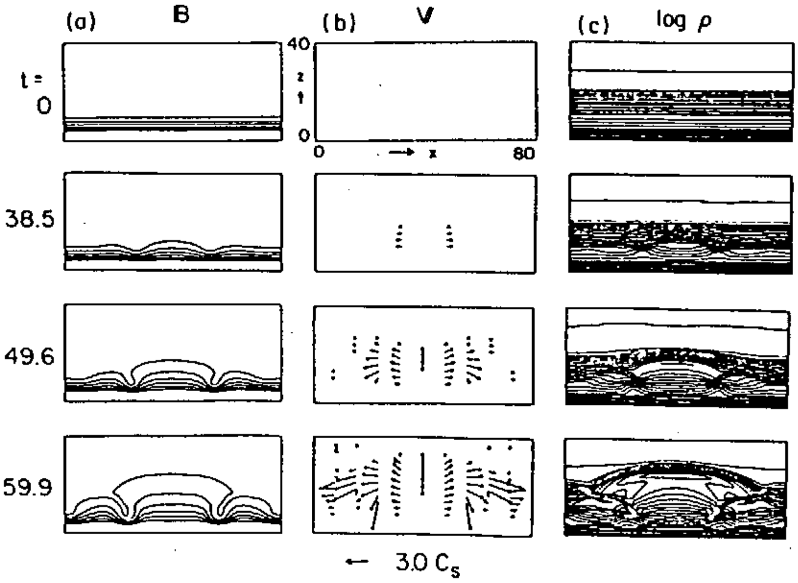

Fig. 1 Simulations results; (a) the magnetic field lines $\mathbf{B} = (B_x, B_z)$, (b) the velocity vector $\mathbf{V} = (V_x, V_z)$, (c) density contours $(\log \rho)$.

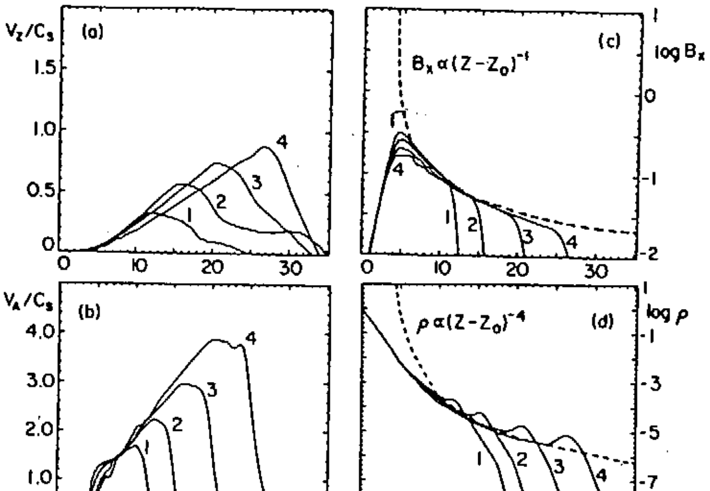

Fig. 2 The distributions in z of (a) the vertical velocity V_z, (b) the local Alfven speed V_A, (c) the horizontal magnetic field $(\log B_x)$, (d) the density $(\log \rho)$ at $x = X_{max}/2 = 40$. The numbers attached to the curves correspond to the following time (in unit of H/C_s); (1) $t=$ 42.1, (2) 49.6, (3) 57.6, (4) 64.6.

radius R_b of the bubble; $V_b = a_3 R_b$, where $a_3 \simeq (1/3 - 1/2) \times (g/R_b)^{1/2}$ is of the order of the linear growth rate of the Rayleigh-Taylor instability. This is similar to our results that $V_z = a_1 z \simeq a_1 R$, where R is the curvature radius of the magnetic loop, $a_1 \simeq \omega_l/2$ and ω_l is the linear growth rate. However, the rise velocity of our magnetic loop is not steady in the Lagrangian frame, but increases exponentially with time. This *nonlinear instability* in the Lagrangian frame is also observed in the exact solution found by Ott[4] for the Rayleigh-Taylor instability of a thin, cold gas layer, which is supported against gravity by a hot gas, with a second hot gas above the thin layer. In this case, the growth rate in the nonlinear stage is exactly the same as that in the linear stage. Physically, this is because cold gas in the thin layer freely falls along the curved interface between two hot gases, and mathematically, because the nonlinear basic equations become linear ones in the Lagrangian frame. Although the nonlinear growth rate is not exactly equal to the linear growth rate in our case, the involved physics is common between ours and Ott's problem; the exponential growth in the nonlinear stage is due to the gravitational free fall *along* the magnetic loop. That is, the equation of motion along magnetic loop in our problem is written as $d^2\theta/dt^2 = (g/R)\theta$, where $\theta = x/R$ and x is the horizontal distance from the midpoint of the loop.[3] This equation has the exponential solution with the growth rate of $(g/R)^{1/2}$. In addition to this character of *nonlinear instability*, our solution has the *self-similar* property, which is not in Ott's solution.

[1] E. N. Parker, Astrophys. J. 145, 811 (1966).

[2] B. Coppi and M. N. Rosenbluth, in *Plasma Phys.and Cont. Nucl. Fus. Res. vol. 1*, (IAEA, Vienna, 1966), p. 617.

[3] K. Shibata, T. Tajima, and R. Matsumoto, Phys. Fluids B, 2, 1989 (1990).

[4] E. Ott, Phys. Rev. Lett. 29, 1429 (1972).

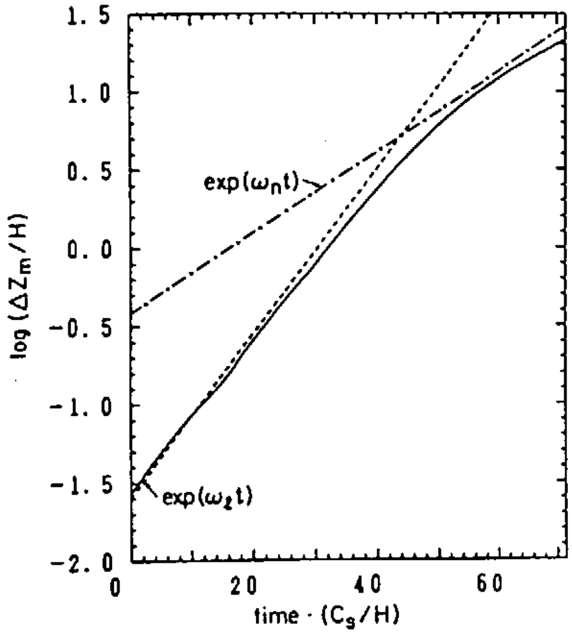

Fig. 3 The time evolution of Lagrangian displacement ($\Delta z_m = z_m(t) - z_m(0)$; solid curve) of a test particle. The dashed line shows the linear growth with $\omega_l = 0.121 C_s/H$, and the dash-dotted line shows the nonlinear growth with $\omega_n = 0.06 C_s/H$.

Turbulent Mixing due to Rayleigh-Taylor Instatability in Laser Driven Implosion

H. Takabe and A. Yamamoto

Institute of Laser Engineering Osaka University
2-6 Yamada-oka Suita, Osaka 565 Japan

A simple, nonlinear diffusion model is proposed to describe the turbulent mixing generated in the laser driven implosion through the Rayleigh-Taylor instability. The model is applied to simulate the recent high density implosion experiment done at Osaka . It is demonstrated that the introduction of mixing model into the implosion code can well reproduce the experimental results as for neutron yields and maximum ρR.

I. Introduction

Hydrodynamic stability is a key element for achieving inertial confinement fusion with a realistic driven energy. The Rayleigh-Taylor and Richtmyer-Meshkov instabilities triggered by non-uniformity in laser irradiation and target structure potentially degrade the performance in target implosion. A variety of implosion experiments have been carried out and compared with implosion codes.[1,2,3] However, for example, the neutron yields can not be accurately predicted and in most of cases the numerical yields are higher by two or three orders of magnitude than the experimental ones. Two dimensional implosion codes have been used to explain the discrepancy by including relatively longer wavelength nonuniformities [$l \leq 24$ of $Y_l^m(\theta,\phi)$-mode][4]. It is, however, difficult to reproduce the reduction of 2~3 orders of magnitude in the neutron yields from the one dimensional simulation with reasonable nonuniformity due to the finiteness in the number of beams. Therefore, our attention is focused on the contribution of perturbations with relatively shorter wavelength. In dealing with multi-mode, higher *l*-mode phenomena, conventional two-dimensional codes are not useful and we need to develop some theoretical model describing the dynamics of such turbulent mixing phenomena.[4]

In the present note, we assume a weakly nonlinear stage for the multi-mode Rayleigh-Taylor instability and the quasi-linear theory is used to describe the development of the turbulent mixing layer. A diffusion model is introduced and is installed in the one-dimensional fluid code ILESTA as an mixing model The recent 600xLD (600 times solid density implosion done with deuterized polyethylene shell target at Osaka[3]) experiment is simulated with the code. It is demonstrated that the turbulent mixing in the stagnation phase does not allow the formation of a spark region at the center of compressed core which is always seen in the conventional one dimensional simulation without such mixing model. As the result, the neutron yield as well as the compressed density measured in the experiment can be reproduced.

II. Turbulent Mixing

The turbulent mixing and inverse-cascading phenomena in the Rayleigh-Taylor instability have been observed in a model experiment by Read.[5] (Fig.1) In the experiment, no initial perturbations are imposed. The instability grows from the natural noise with predominant growth of shorter wavelength mode in the initial stage, while the longer wavelength modes (large size eddies) are generated in the later time as the mixing layer grows.

Now, let as assume that ξ represents the displacement due to the instability and f_0 is some physical quantity in case of no perturbation. Then, the perturbation f_1 is roughly given to be

$$f_1 = -\xi \nabla f_0 \qquad (1)$$

The convection term in the 0-th order is given to be

$$u\nabla f = u_0 \cdot \nabla f_0 + \langle u_1 \nabla f_1 \rangle \qquad (2)$$

where u is the flow velocity and u_0 and u_1 are its 0-th and 1-st order quantities. In Eq.(2), < > means to take average over a macroscopic scale. Then the time variation of f_0 is governed by the form;

$$\frac{df_0}{dt} = \nabla D \nabla f_0 + (\text{other} \quad \text{source} \quad \text{terms}). \qquad (3)$$

where

$$D = \langle \xi \cdot \dot{\xi} \rangle \qquad (4)$$

In driving Eq.(3), we have assumed the incompressibility to the perturbed motion $\nabla u_1=0$ and used the relation $\dot{\xi}=u_1$. If the displacement ξ is given, Eq.(3) can predict the evolution of the mixing layer as a diffusion model.

Let us briefly study the properties of the diffusion term. If f_0 varies in th x-direction in the planner geometry, the diffusion distance Δx is roughly predicted in the form

$$\Delta x \cong (2Dt)^{1/2} \qquad (5)$$

$$\cong \left(2 \int_0^t D dt\right)^{1/2}$$

Since the diffusion is in x-direction, the diffusion coefficient is approximately given to be

$$D \cong \xi_x \cdot \dot{\xi}_x \qquad (6)$$

where ξ_x is the displacement in the x-direction. Inserting Eq.(6) into Eq.(5) yields the relation

$$\Delta_x \cong |\xi_x| \qquad (7)$$

Namely, the diffusion distance is almost equal to the amplitude of the dominant mode of the instability. On the other hand Eq.(6) is rewritten to be $D=\gamma\xi_x^2$ with the growth rate γ and in the diffused structure the growth rate of the Rayleigh-Taylor instability is given to be

$$\gamma=(\alpha_A g / \Delta x)^{1/2} \qquad (8)$$

where α_A the Atwood number. By the use of Eq.(8), Eq.(5) reduces to the form;

$$\frac{d}{dt}(\Delta x)^2 \cong 2(\alpha_A g)^{1/2} \Delta x^{3/2} \qquad (9)$$

Eq.(9) is easily solved to reduce

$$\Delta x=\eta\alpha_A g t^2 \qquad (10)$$

where $\eta=1/4$. It should be noted that Eq.(10) explains qualitatively the scaling law to the mixing layer observed experimentally by Read. Numerical constant $\eta=0.07$ obtained by Read could be reproduced with more detail calculation.

In applying the above idea to the mixing model coupled with a consistent implosion dynamics, we have to determine the dynamics of the displacement ξ in space and time. for this purpose, we developed a perturbation code and coupled it with the one-dimensional implosion code ILESTA. In the perturbation code, all the perturbations are expanded with the spherical harmonics, for example,

$$\xi(r,t) = \sum \xi_{l,m}(r,t) Y_{l,m}(\theta,\phi) \qquad (11)$$

and time developments of the coefficients of the spherical harmonics are solved by the finite difference method, simultaneously with the implosion code at each time step. Then the turbulent diffusion coefficient

$$D = \sum_{l,m} \xi_{l,m} \dot{\xi}_{l,m} \qquad (12)$$

is used to solve the diffusion model in the implosion code.

III. Application to Target Implosion by Gekko XII Laser System.

For achieving high density, a hollow shell target made of deuterized polyethylene has been used.[3] The density of 600 times solid density has been achieved by Gekko XII laser system.

A typical target the simulation of which will be shown here is of the parameters: outer diameter ϕ=494μm, thickness 8.71μm, made of C(42.8%), D(53.5%), T(1.3%), and Si(2.4%) in number fraction. The laser of 8.14k Joule in 0.53μm wavelength is irradiated in the form of two Gaussians with 1.3 and 1.0 nsec FHWM's with the separation of 760 psec from peak to peak. Since the random phase plates are used, about 60% of the irradiated energy are focused on target.

In simulating the implosion, additional key points are (1) equation of state and (2) radiation preheat due to silicon K-line radiation. A simple fitting formula for the equation of state of matter described in Ref.6 has been used in the code. The radiation transport has been treated with the multi-group flux-limitted model and a non LTE atomic model shown in Ref.7 has been used. The amount of silicon K-line emission has been checked with a model experiment done in planer and spherical targets.[8]

In Fig.2, the r-t diagram near the maximum compression is shown for the case without the mixing. In this case, a hot spot of the radius about 5μm with the density 100g/cc and temperature 2-3keV is generated. The hot spot is surrounded by high density (~500g/cc, ρR~0.3g/cm^2) and low temperature (~300eV) region. This is a typical structure seen in a hollow shell implosion without mixing phenomena. The inclusion of the mixing model alters the structure drastically. The r-t diagram for this case is shown in Fig.3. By comparing with Fig.2, it is clear that the mixing is not help the stagnation of the high density part and this part collides directly near the center, consequently no spark region being generated.

Both of the simulation results are compared with the experimental results. The resultant neutron yields due to D-T reactions are $Y_N=6\times10^7$(w/o mixing) and 8×10^5(w/ mixing). The experimental one is $Y_N=1\times10^6$. The ρR values obtained in the experiment is 0.37~0.65 g/cm^2, while the simulation results are ρR=0.33 (w/o mixing) and 0.6(w/mixing). The one-dimensional simulation with the mixing model can predict the experimental result well, and it suggests that the hot-and cold structure is not generated due to the mixing process in the stagnation phase. This is due to the explosive growth of the Rayleigh-Taylor instability in the stagnation phase as already pointed out in Refs.9.10.11.

IV. Conclusion

The nonlinear mixing model has been introduced in the framework of the week turbulence theory and applied to the simulation of the recent high density compression with hollow CD shell targets. It is demonstrated that the turbulent mixing in the stagnation phase do not allow the formation of a speak region at the center of the compressed core, which is always seen in the conventional 1-D code without any mixing model. As the results, the neutron yield is reduced by roughly two orders of magnitude than that in the case without the mixing. It is found that the resultant neutron yield and maximum ρR well coincide with the experimental ones.

References.

1. H. Takabe, etal, Phys. Fluids 31, 2884 (1988).
2. F. J. Marshall etal, Phys. Rev. A40, 2547 (1989).
3. S. Nakai etal, IAEA Conference, Oct. Washington (1990).
4. H. Takabe etal, Laser and Particle Beams 7, 175 (1989).
5. K. I. Read, Physica 12D, 45 (1984).
6. K. Takami and H. Takabe, Tech. Rep. Osaka Univ. 40, 159 (1990).
7. H. Takabe, "Radiation Transport and Atomic Modeling for Laser Produced Plasmas", ILE Research Report 9008P, Sep. 10, 1990.

8. N. Miyanaga, Private communication .
9. J. R. Freeman etal, Nucl. Fusion 17, 223 (1977).
10. F. Hattori etal, Phys. Fluids 29, 1719 (1986).
11. H. Sakagami and K. Nishihara, Phys. Rev. Lett. 65, 432 (1990); Phys. Fluids B2, 2715 (1990).

Figure Captions

Fig.1 Turbulent mixing observed in a tank accelerated by a rocket. The experiment has been done by K. I. Read (Ref.5). The contact surface is unstable to the Rayleigh-Taylor instability.

Fig.2 Detail r-t diagram of an implosion of a hollow shell target. The turbulent mixing is not treated in the simulation.

Fig.3 The same as Fig.2 but the turbulent mixing is treated in the one dimension simulation. No spork formation is seen.

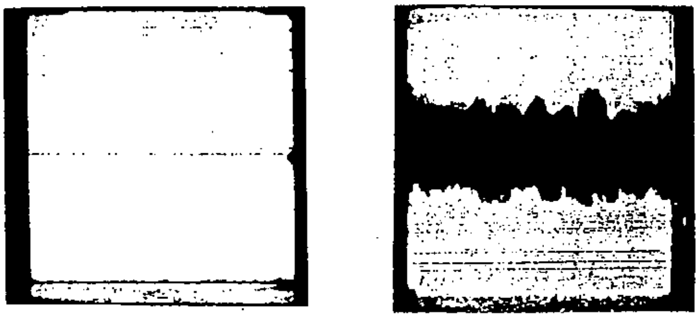

0ms

45·9ms

Fig.1

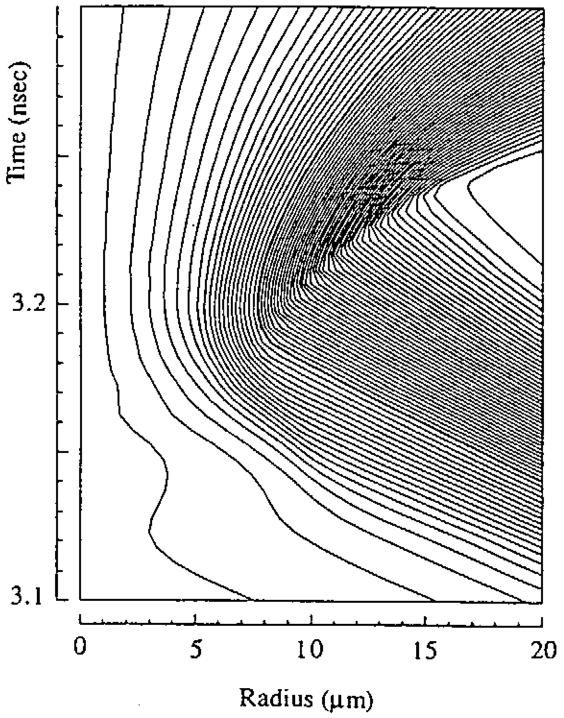

Fig.2

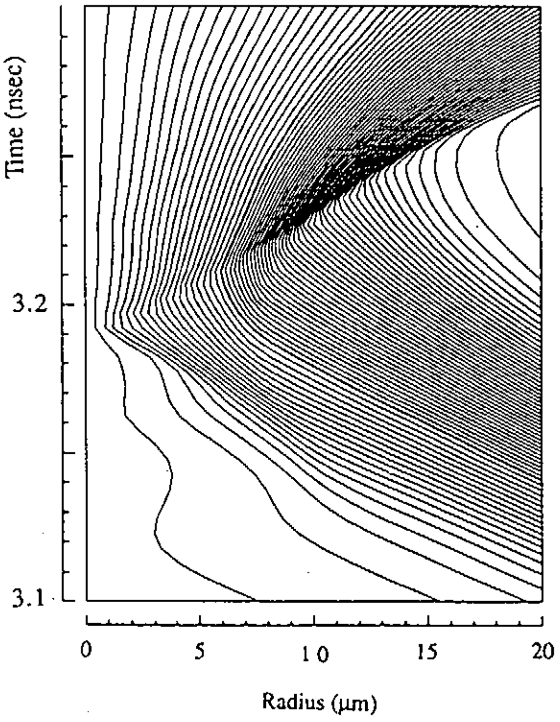

Fig.3

Electrostatic Particle Simulations of Density and Temperature Driven Modes in a Toroidal Plasma

M. J. LeBrun
JAERI

G. Furnish, T. Tajima
Institute for Fusion Studies
The University of Texas at Austin

Simulation runs of the toroidal plasma in the presence of density and temperature profiles have been performed with the toroidal particle code [1] (TPC) developed at the IFS. These calculations are fully self-consistent (electrostatic) and nonlinear, using drift dynamics electrons and full dynamics ions in a toroidal metric. We present results from runs with $\eta_i = 0, 1$ using kinetic electrons, which show strong (marginally stable or unstable) modes with frequencies well below ω_*. In the case of $\eta_i = 1$, substantial particle and heat transport for both species is seen. By contrast, the cylindrical geometry (control) run shows a weak response and negligible transport. Runs with $\eta_i = 1, 4$ using a Bolzmann electron response are also performed, and these are compared to the kinetic electron runs.

By pursuing kinetic simulation, we seek a fundamental description of the plasma confinement, with the hopes of unraveling the long-standing problem of anomalous transport. We use a coordinate system well-suited for confinement studies — with the radial coordinate everywhere perpendicular to the magnetic field. Thus the rapid variation across field lines may be resolved more easily than with codes that employ e.g. a rectangular cross section approximation. Further, a modular programming style in a structured programming language (MPPL, a preprocessor to Fortran) is used to enable "drop-in" replacement of various components such as field solvers, dynamics types, graphics, and so on.

The simulation runs considered here generally utilized a single toroidal Fourier harmonic ($n = 9$) and multiple poloidal harmonics ($m = 5$–15)

in a tokamak magnetic field. The rationale for this choice is that toroidal coupling between modes at neighboring rational surfaces gives rise to the formation of marginally stable or unstable radially extended, ballooning-type modes[2]. An actual plasma supports these "quasimodes" for each toroidal mode number n, each linearly independent of the others; information gained through study of a single mode may thus shed much light on overall transport.

The first run with $\eta_e = \eta_i = 0$ shows instability in the vicinity of the m = 7–9 rational surfaces with growth rate $\gamma/\omega^* \sim 0.12$, close to the theoretical value [3]. This was accompanied by weak profile flattening in the same radial region, which diminished after saturation of the mode. The waveforms of the active modes were found to display the oscillatory, radially-extended character expected of a ballooning-type mode. Direct evidence of ballooning (primarily to the outside, in one or two lobes) was also seen. A similar run in a cylindrical metric, by contrast, showed sharp localization of the wave function around the rational surface and no evidence of ballooning, as expected.

The real frequency response was seen to be dominated by relatively active vs inactive "bands". The lowest frequency band occured at roughly $\omega/\omega^* = 0.4$, in good agreement with theory[4]. Note that the theory eliminates the radial variation through the assumption of translational invariance, and is thus only partly applicable to the situation in a realistic plasma, even when nonlinearities are mild. We show several diagnostics on the frequency response in Fig. 1. In 1(a) is the spatially averaged spectral density as a function of frequency. Note the rather broad spectrum similar to that observed in confined plasmas, although the peaks from the linear mode spectrum are still apparent. The spectrum decays as $S(\omega) \sim \omega^{-1}$. In 1(b) we plot maximum power as a function of ω/Ω_i for the $m = 7$ mode, and in 1(c) we plot ω/Ω_i as a function of radius for the $m = 7$ through $m = 11$ poloidal modes (the arrows mark the rational surfaces). This diagnostic eliminates the spectral widths in order to see the linear physics aspects more clearly. We see a preference for certain discrete frequencies, as one would expect for strongly coupled toroidal modes. Some variation of the dominant frequency between different mode numbers occurs due to nonlinear splitting.

For this parameter regime, the diamagnetic frequency for a given poloidal mode is constant with radius, varying only with m. However, the diamagnetic frequency for the mode ensemble increases as $w^*_{\text{eff}} \propto nq(r)$.

This effect can be seen in the spectrum as an increase in frequency with radius, with transitions occuring from one frequency to the next. Not shown is a higher frequency mode which appears at $r/a \gtrsim 0.5$ for the higher mode numbers ($m = 12$–15).

The next run employs temperature profiles with $\eta_i = \eta_e = 1$, other parameters were the same as previously. A strong, low frequency mode ($\omega/\omega^* \sim 0.4$) is observed, spanning an appreciable radial extent ($0.2 \lesssim r/a \lesssim 0.6$). Here the toroidal coupling induces the formation of a single frequency mode. In this case the temperature gradient causes a strong variation of the diamagnetic frequency with radius for a given m, with $\omega^*/\Omega_i = 0.0031\, m \exp(-0.5\,(3.168\, r/a)^2)$ which tends to localize individual m modes much more than in the $\eta = 0$ case. However, the ensemble value of ω^* (obtained by replacing m by $n\, q(r)$ in the above expression) is roughly constant with radius, promoting strong coupling between modes and consistent with the observed mode strength.

In spite of the observed mode strength, there were no modes which were clearly growing in this case, as expected since at marginal stability Nevertheless strong ion heat transport was observed, as well as significant electron heat transport, primarily in the tail region ($r \gtrsim 0.5a$). Substantial particle transport occured, in the $0.1 \lesssim r/a \lesssim 0.6$ region, which coincides with the region of greatest mode activity. A run in cylindrical geometry, on the other hand, showed no similar spectral feature (with power a factor of 3–5 less) and negligible transport.

Additional runs were made using Boltzmann electrons. For $\eta_i = 1$, the absence of the kinetic electron drive results in a much weaker response at positive frequency (electron diamagnetic direction) than previously, and little transport. Otherwise, the plasma response is similar to that of the kinetic electron case, having rougly the same radial extent ($0.05 \lesssim r/a \lesssim 0.55$), but somewhat higher in frequency ($\omega/\omega^* \sim 0.7$). A relatively strong ion feature appears for small r ($r/a \sim 0.15$), this appeared in the previous run but was weak compared to the electron feature. For the $\eta_i = 4$ Boltzmann electron run, both particle and heat transport were observed, much higher than $\eta = 1$ Boltzmann electron run. The heat transport still less than that observed in $\eta = 1$ kinetic electron run.

To summarize, the simulation runs performed thus far with TPC appear to agree well with the theoretical predictions in regimes where the linear effects dominate and the radial inhomogeneities not too severe. In other regimes (where the physics is much less well understood), we see evidence of the importance of mode strength and the presence of a kinetic electron drive in determining overall transport. Several improvements to the algorithm are currently underway (e.g. gyrokinetic or δf). These will improve the applicability of simulation runs to different parameter regimes, as well as enabling direct comparison between models.

References

[1] M. J. LeBrun and T. Tajima. *Particle Simulation in Curvilinear Coordinate Systems.* Technical Report 374, Institute for Fusion Studies, University of Texas at Austin, 1989.

[2] C. Z. Cheng and Liu Chen. *Unstable universal drift eigenmodes in toroidal plasmas.* Phys Fl, **23**, 1770 (1980).

[3] A. Hirose (University of Saskatchewan). Private communication.

[4] T. J. Schep and M. Venema. *Collisionless Drift Modes in a Toroidal Configuration.* Plasma Phys and Contr Fus, **27**, 653 (1985).

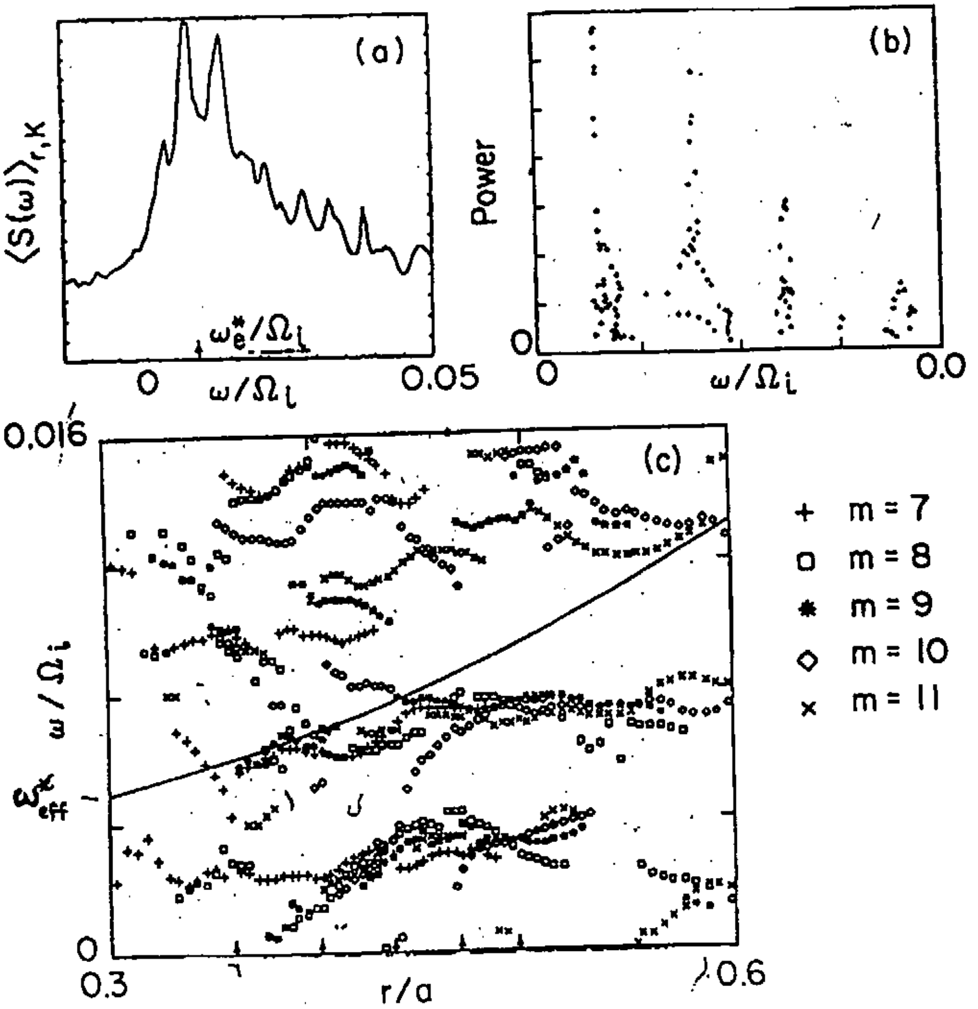

Fig. 1

"Internal Kink Mode Simulation by 3-D Gyrokinetic Code"

H. Naitou and O. Fukumasa
Yamaguchi University
R.D. Sydora
University of California, Los Angeles
W.W. Lee
Plasma Physics Laboratory, Princeton University

3-D ideal MHD simulations with kinetic modifications are now possible by the use of the 3-D gyrokinetic particle code which follows a self-consistent and energy conserving set of nonlinear gyrokinetic equations given by Hahm et al.[1]. Nonlinear evolutions of internal kink modes in a straight tokamak were simulated by this code. An outline of the code is as follows. The model we used is a rectangular tokamak ($L_x \times L_y \times L_z$) being periodic in the z-direction and surrounded by a perfectly conducting wall. Strong and uniform (toroidal) magnetic field is assumed in the z-direction. Poloidal magnetic field (B_x and B_y) is produced by the electron drift current in the z-direction. Compressional component of the magnetic field (perturbed B_z) is neglected in the low beta approximation. Electron and ion dynamics parallel to the magnetic field are followed as well as the E×B drifts perpendicular to the magnetic field. Generally electron gyroradius is assumed to be zero (drift kinetic) whereas ion finite gyroradius effects are properly included (gyrokinetic). For saving of CPU time, ion gyroradius can be set to be zero at will. The electrostatic potential is calculated from a gyrokinetic Poisson equation which includes ion polarization shielding effects. The z-component of the vector potential (A_z) is calculated by Ampere's law. Because a formulation using a canonical momentum (p_z) is used, inductive electric field is not appear explicitly in the code.

The moment equations of the gyrokinetic equations reduce to the Strauss's two fluid model [2] in the longwavelength limit when the electron inertia and pressure terms are neglected [3]. Therefore, in order to excite a internal kink mode, elongation effects of the plasma cross-section ($L_x/L_y = 2$) was employed. If the equilibrium safety factor at the magnetic axis (q_0)is less than unity, unstable internal kink mode was observed. The q_0 dependence of the growth rate, nonlinear evolutions of current, electrostatic potential, and A_z profiles were examined and compared with the results of the reduced MHD simulation in Ref.[2].

[1] T.S. Hahm, et al., Phys. Fluids 31 (1988) 1940.
[2] H.R. Strauss, Phys. Fluids 19 (1976) 134.
[3] W.W. Lee, "Gyrokinetic particle simulation of MHD modes"

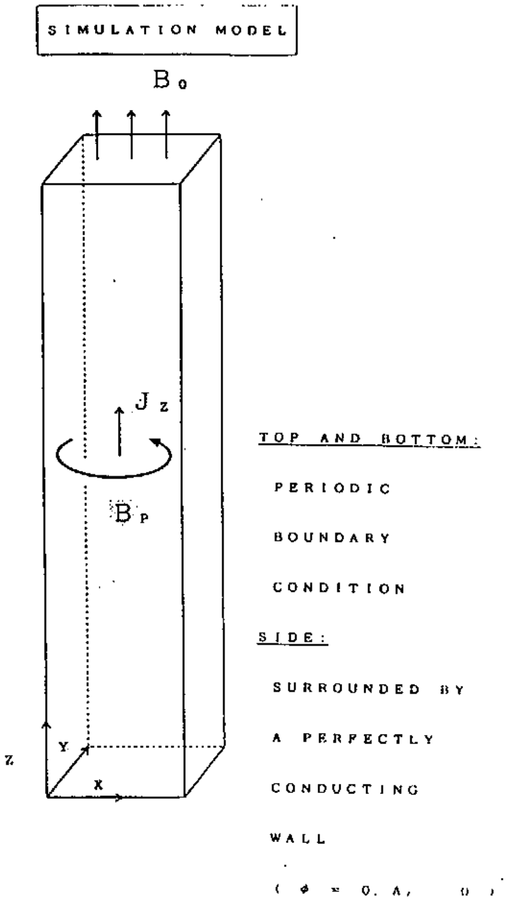

Fig. 1

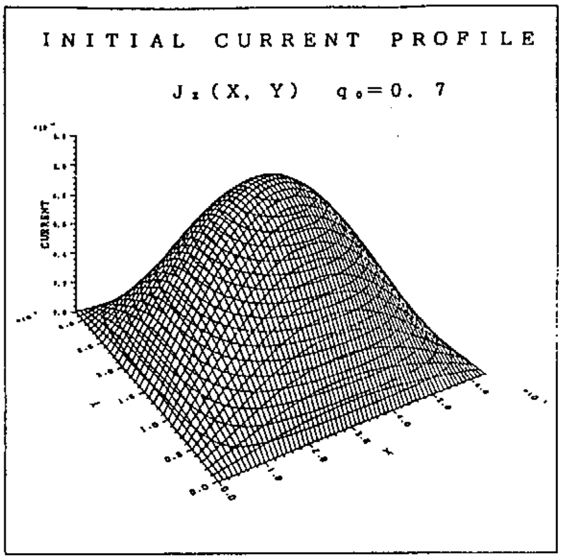

Fig. 2

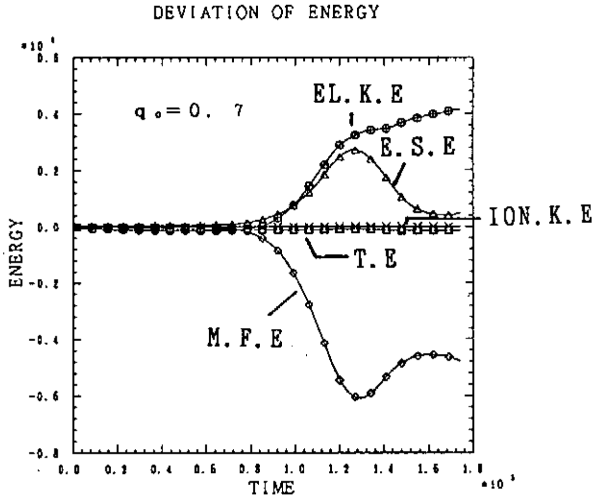

Fig. 3

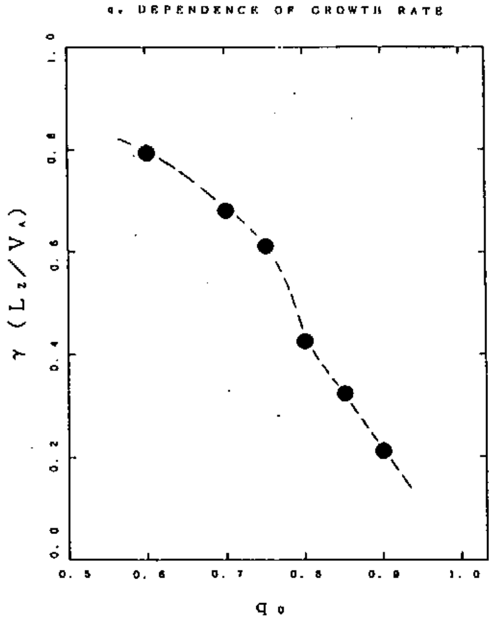

Fig. 4

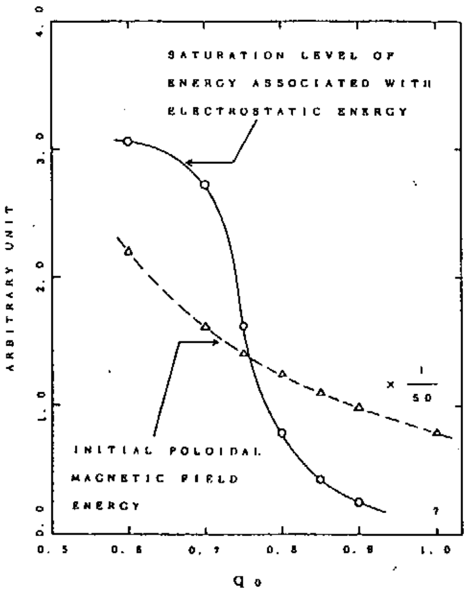

Fig. 5

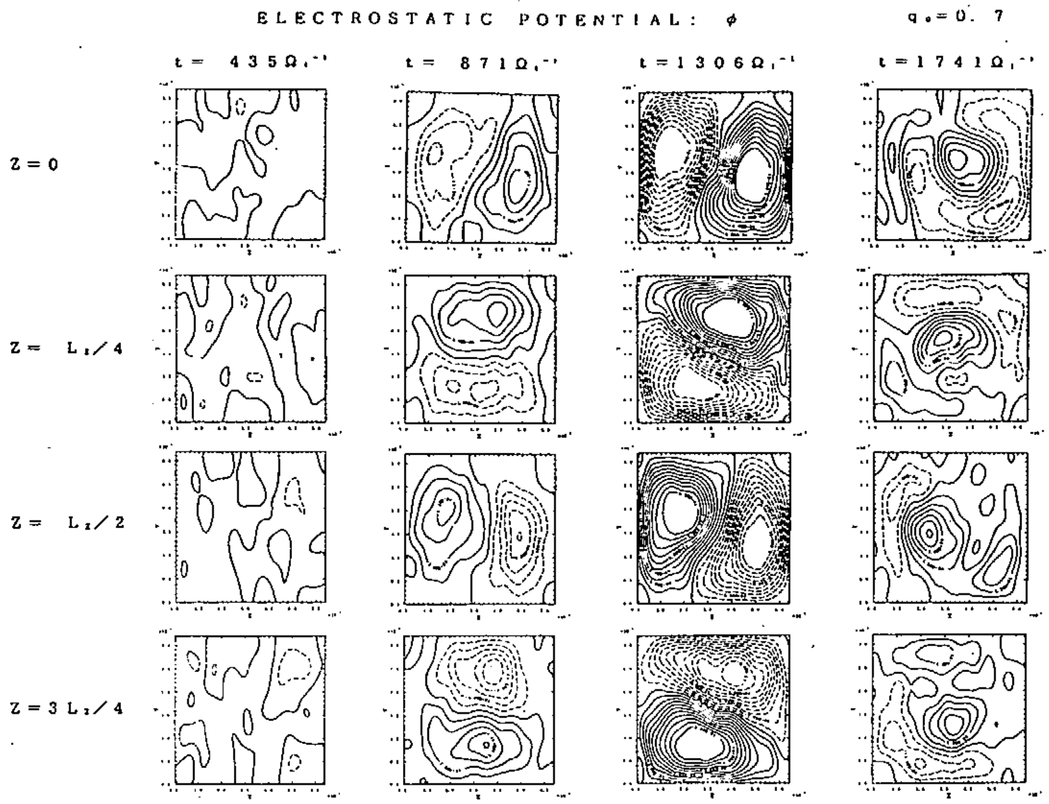
ELECTROSTATIC POTENTIAL: ϕ
$q_0=0.7$
$t=435\Omega_i^{-1}$
$t=871\Omega_i^{-1}$
$t=1306\Omega_i^{-1}$
$t=1741\Omega_i^{-1}$
Z = 0
Z = $L_z/4$
Z = $L_z/2$
Z = $3L_z/4$

Fig. 6

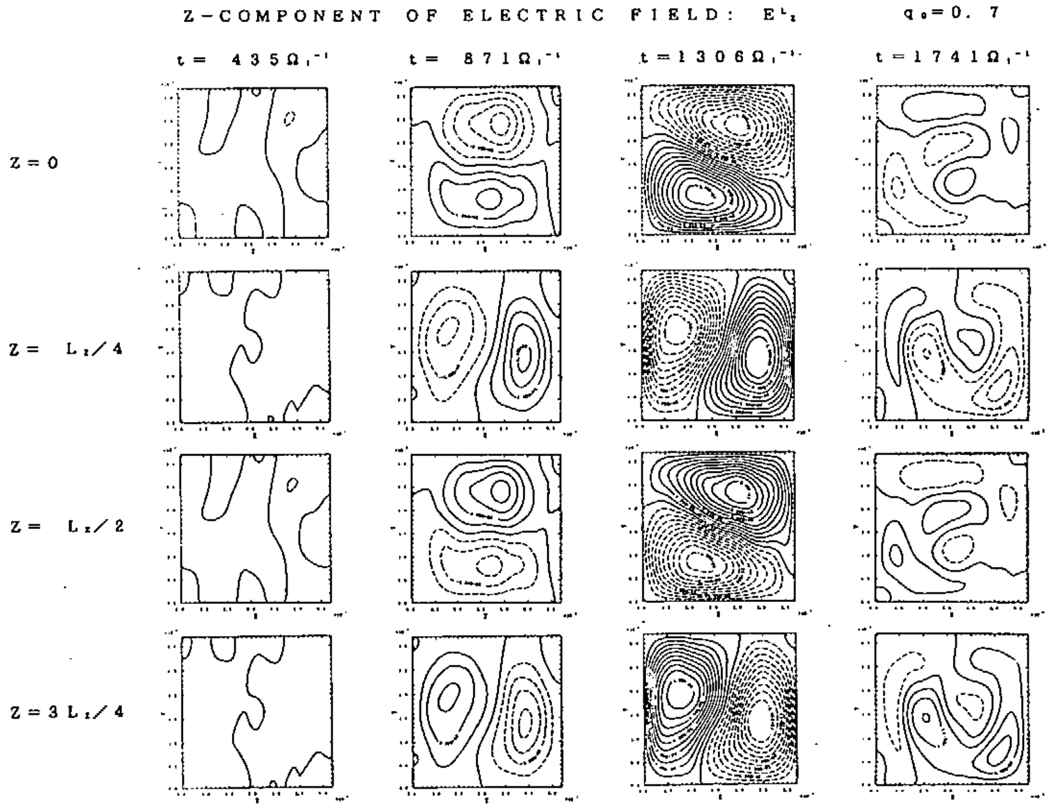
Z-COMPONENT OF ELECTRIC FIELD: E^L_z
$q_0=0.7$
$t=435\Omega_i^{-1}$
$t=871\Omega_i^{-1}$
$t=1306\Omega_i^{-1}$
$t=1741\Omega_i^{-1}$
Z = 0
Z = $L_z/4$
Z = $L_z/2$
Z = $3L_z/4$

Fig. 7

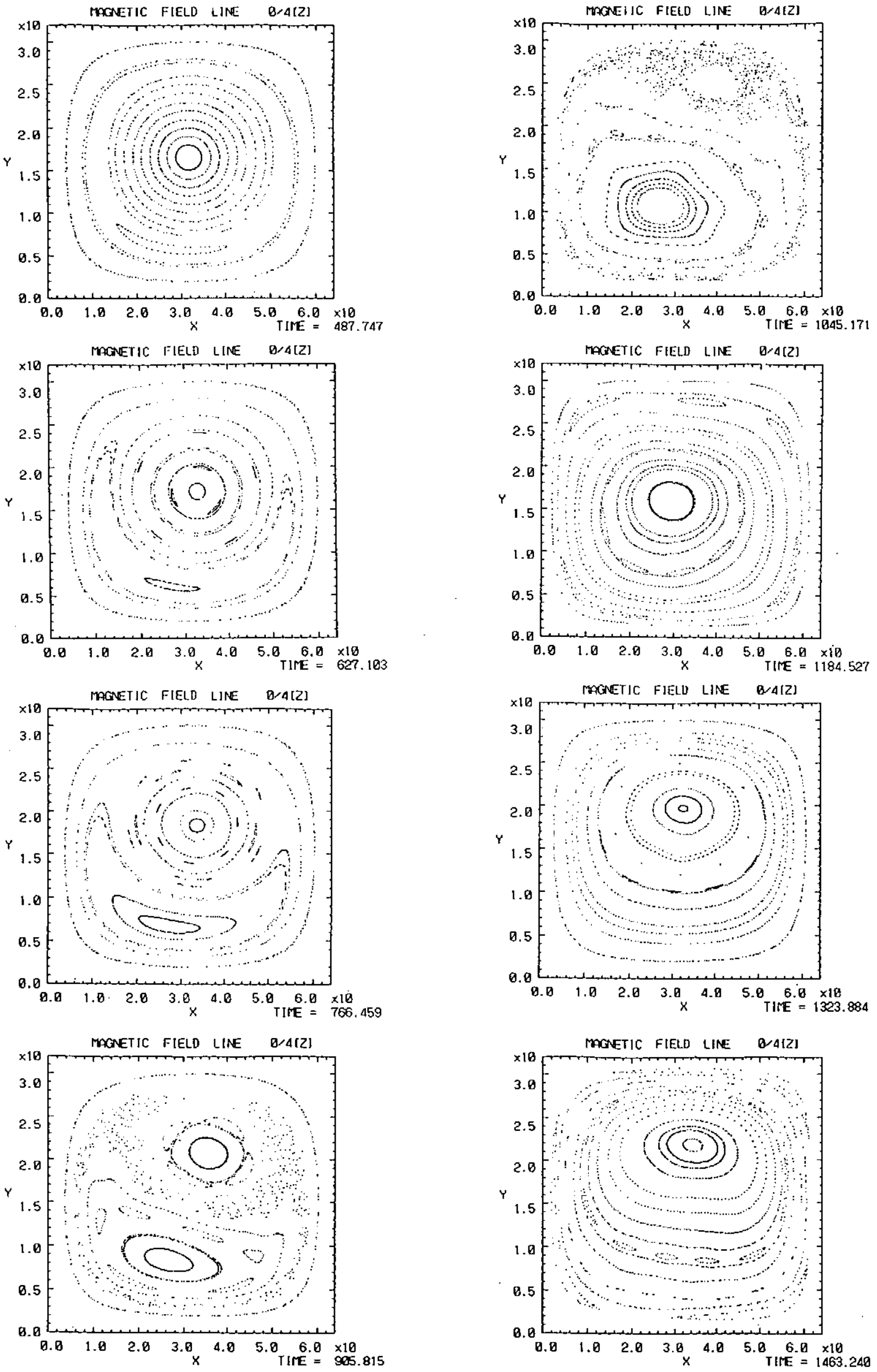
MAGNETIC FIELD LINE 0/4[Z]
x10
3.0
2.5
2.0
1.5
1.0
0.5
0.0
Y
0.0
1.0
2.0
3.0
4.0
5.0
6.0
x10
X
TIME = 487.747
TIME = 1045.171
TIME = 627.103
TIME = 1184.527
TIME = 766.459
TIME = 1323.884
TIME = 905.815
TIME = 1463.240

Fig.8

Particle Simulation Study on the Tilt Stabilization of the FRC Plasma

Ritoku Horiuchi and Tetsuya Sato

National Institute for Fusion Science, Nagoya 464-01, Japan

Abstract

Ion kinetic stabilization of the FRC tilt disruption is investigated by means of three dimensional particle simulation. The growth rate of the tilting instability decreases as the parameter $\bar{s}$ decreases and the instability is completely suppressed when $\bar{s} \approx 1$, where $\bar{s}$ measures the number of ion gyroradii between the magnetic separatrix line and the field-null line. It is found that this kinetic stabilization is attributed to the characteristics of the meandering ions which execute an oscillatory motion with a large amplitude around the field-null point and carry most of the ion toroidal current.

1. Introduction

The field-reversed configuration (FRC) is an attractive device because of the character that a high-beta plasma is confined by a simple magnetic geometry with no toroidal field. A field-null point appears in the plasma center due to the strong diamagnetic field. The existence of a field-null makes a particle motion in the FRC complex, i.e., a particle does not gyrate but executes a meandering motion in the vicinity of the field-null point [1]. Since the ion Larmor radius becomes infinite there, we define the useful parameter $\bar{s}$ as

$$\bar{s} = \int_{r_a}^{r_s} r dr/(r_s \lambda_i), \tag{1}$$

where r_s is the separatrix radius, r_a is the radius of the field-null, and λ_i is the local ion gyroradius. The value of $\bar{s}$ is around a unit in the currently existing devices. This means that the plasma in the FRC device is fairly kinetic.

The magnetohydrodynamic(MHD) theory [2,3] predicts that the FRC plasma is unstable against the tilting instability, while no experimental evidence has so far been reported on the tilt disruption. The discrepancy between the MHD theory and the experiment is thought to be explained by taking into account the stabilization effect due to the ion finite-Larmor radius (FLR) because the plasma confinement scale is comparable to the ion Larmor radius in the currently exsisting device ($\bar{s} \approx 1$). Barnes et al. [4] derived the linear growth rate from the Vlasov-fluid dispersion equations by assuming that an ion is a large orbit, nonrotating Vlasov plasma and an electron is a cold, massless fluid.

The purpose of this paper is to investigate the FLR stabilization effect against the tilting instability by making use of a macro-scale particle simulation code that can describe both the electron and ion FLR effects and the global behavior over the device scale simultaneously [1,5].

2. Simulation model

Let us consider the FRC plasma in a cylindrical conducting vessel in which plasma is confined by a uniform external field. In order to investigate the kinetic effect we solve the equations of motion and the Maxwell equations in the cylindrical coordinates (r, ϕ, z). A two-fluid MHD equilibrium is adopted as an initial condition. The boundary condition is such that the physical quantities are periodic at two axial edges of the cylindrical vessel and a particle is completely elastically reflected on the conducting wall. Numerical scheme used for the three-dimensional particle simulation relies on a semi-implicit method in which both ions and electrons are treated as particles [1,5]. The time step Δt and the grid separation Δx are assigned to satisfy the relations $\Delta t = 2/\omega_{pe}$ and $\Delta x \gg \lambda_{Debye}$, where ω_{pe} is the electron plasma frequency and λ_{Debye} is the ion Debye radius. Four simulation runs with different values of $\bar{s}$ are carried out by using a hundred thousand particles. The simulation runs are terminated after one Alfven transit time t_A where t_A is defined by r_0/v_A ; r_0 and v_A are the device radius and the average Alfven velocity in the plasma region.

3. Simulation results

For $\bar{s} \approx 1$ most of ions move on an orbit with a large amplitude and no self-intersection around the filed-null line, as is seen in Figure 1. This motion is called a meandering motion. The average drift direction of the meandering ions is the same as that of the diamagnetic drift. The number of meandering ions decreases and the oscillation amplitude of meandering motion becomes smaller as $\bar{s}$ increases. Figure 2 shows the profile of the ion distribution in the (v_ϕ, v_z)-plane (right) and in the (v_r, v_z)-plane (left) for the case of $\bar{s} = 1$. A meandering motion has larger oscillation amplitudes along the z direction and nonzero average velocity along the ϕ direction in the prolate FRC plasma. The anisotropy of the meandering motion directly leads to an anisotropic ion temperature of $T_z > T_r$ and $T_z > T_\phi$. On the other hand, the electron distribution is almost isotropic because the number of meandering electrons is very small. The degree of the anisotropy decreases as the number of meandering ions decreases.

Figure 3 shows the $\bar{s}$-dependence of the average growth rate of the tilt mode, where the open circle represents the value obtained by the simulation, and the closed triangles show the results of a linear theory [4]. The evolution of the tilt mode is completely suppressed when $\bar{s} \approx 1$. As $\bar{s}$ increases, the tilt mode tends to be more unstable and the growth rate approaches the MHD value. The behavior of the kinetic growth rate is in good agreement with the result of a linear theory. It can be concluded therefore that the stabilization effect due to the finiteness of the ion Larmor radius is very efficient for the FRC tilt mode.

4. Discussion

By carrying out the macroscale particle simulation we have derived the important result that the FRC tilt disruption can be stabilized for the kinetic plasma of $\bar{s} \approx 1$. In this section we give the stabilization mechanism of the FRC tilt disruption in connection with the characteristic of a meandering motion. For the kinetic plasma of $\bar{s} \approx 1$ most of ions are free from the constraint of the magnetic field and oscillate around the field-null point with a large amplitude [1]. If a perturbation of the tilt mode is added to the velocity field of the meandering ions in a two-dimensional (axially symmetric) equilibrium, the oscillation amplitude and the oscillation period change dependent on the phase difference between the meandering oscillation and the perturbation. However, the oscillation center of a new orbit remains the same. When the orbit is averaged over one oscillation period, the tilt modification of the current profile does not appear in the toroidal current carried by the meandering ions in the average. In other words, the ion executing a meandering motion does not contribute to the growth of the perturbation of the tilt mode. We thus conclude that the ion with a meandering orbit plays a key role in keeping the system stable against the tilting instability, and that the evolution of tilt mode can be completely suppressed when most of the ions move on the stable meandering orbits, i.e., when $\bar{s} \approx 1$.

References

1. R. Horiuchi and T. Sato, Phys. Fluids B2, 2652(1990).
2. W. N. Rosenbluth, M. N. Bussac, Nucl. Fusion 19, 489(1979).
3. R. Horiuchi and T. Sato, Phys. Fluids B1, 581(1989).
4. D. C. Barnes, et al., Phys. Fluids 29, 2616(1986).
5. M. Tanaka and T. Sato, Phys. Fluids 29, 3823(1986).

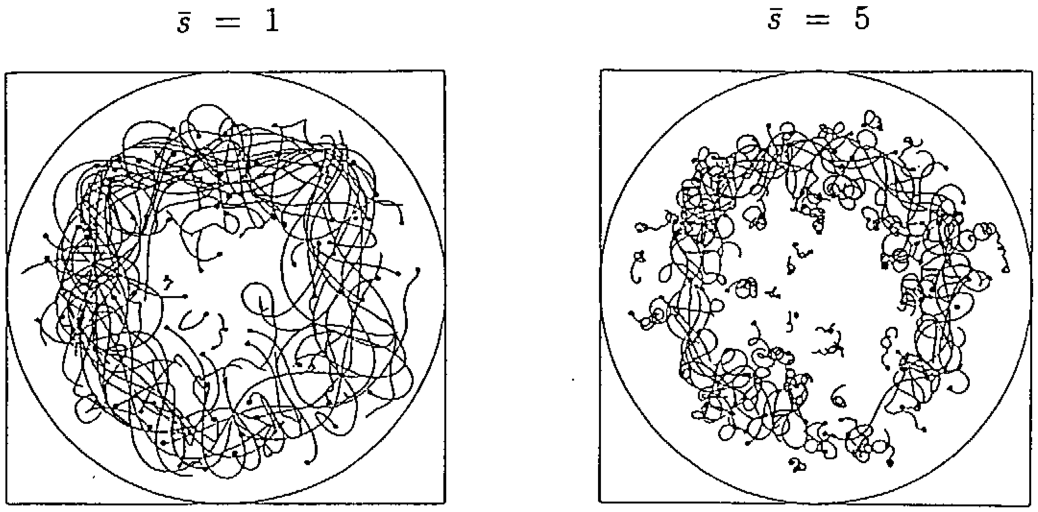

Fig. 1. Top view of the orbits of one hundred ions for the cases of $\bar{s} = 1$ (left) and $\bar{s} = 5$ (right).

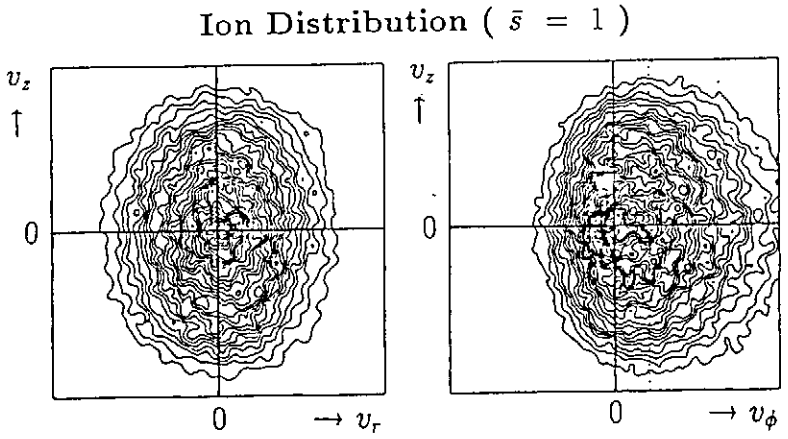

Fig. 2. The ion distribution in the (v_ϕ, v_z)-plane (right) and in the (v_r, v_z)-plane (left) for the case of $\bar{s} = 1$.

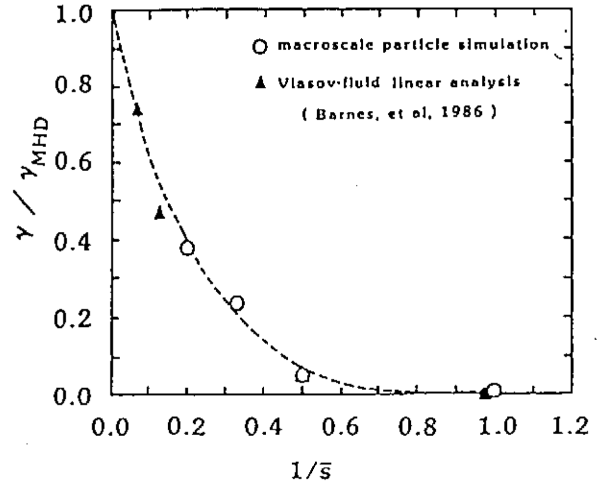

Fig. 3. Dependence of the average growth rate of the tilt mode on the parameter $1/\bar{s}$, where the open circle represents the value obtained by the particle simulation, and the closed triangles show the results of a linear theory [Ref. 4].

3-D Electromagnetic Macroscale Particle Simulation of Inhomogeneous, Magnetized Plasmas

Motohiko Tanaka
National Institute for Fusion Science, Nagoya 464-01, Japan

1. Introduction

For the study of kinetic transport in "macro" (MHD)-scale plasmas, there are several requirements to be satisfied by a simulation code. First, the time and spatial scales are not microscopic, *i.e.*, $\omega_{pe}\Delta t \gg 1$ and $\Delta x \geq c/\omega_{pe}$. Second, confinement plasmas are highly inhomogeneous in density and magnetic field. Moreover, the diamagnetic current must be included for finite temperature plasmas. This leads to an inevitable use of the drift approximation for the electron perpendicular motion since the relation $\omega_{ce} \sim \omega_{pe}$ holds for magnetic fusion plasmas.

For the above purpose, an electromagnetic "kinetic-MHD" simulation technique - Macroscale Particle Code (MACROS) - has been developed[1]. The macroscale particle code is essentially an implicit particle code. The characteristics of the MACROS code is summarized in Table 1. Important feature here is that the MACROS code properly treats low frequency electromagnetic (electrostatic, of course) waves and structures with $\omega\Delta t < 1$. Hence Landau and cyclotron resonances are retained on top of the particle orbit effects. Moreover, the code is numerically stable in nonlinear regimes and energy conservation is acceptably good. These characteristics make this code suitable for the study of large-scale kinetic plasma problems.

Table 1: Characteristics of Macroscale Particle Simulation Code.

- Large time and spatial scales:
  $\omega_{pe}\Delta t \gg 1$, $\omega_{ce}\Delta t \gg 1$, and $\Delta x/(c/\omega_{pe}) \geq 1$ (however, $\omega_{ci}\Delta t \leq 0.4$).
- Fully electromagnetic.
- Multi-dimensions in any geometry (Cartesian, cylinder, torus).
- Inhomogeneous density profile and magnetic field used.
- Fully kinetic:
  - ions: 3-D motion
  - electrons: parallel direction → 1-D motion with $(-\mu\nabla_{\parallel}B)$ force.
    perpendicular direction → guiding-center approximation
    ($\mathbf{E} \times \mathbf{B}$, $\mathbf{B} \times \nabla B$ drifts)

→ Resonance effects (Landau, cyclotron resonances)
Orbit effects: finite Larmor radius effects
diamagnetic current
banana orbit...
Longitudinal particle transport
included.

2. Algorithm of Macroscale Particle Code

The foregoing characteristics of the MACROS code have been achieved by introducing a slightly backward time-differencing method both into the Maxwell equations and the equations of motion of particles[1]. The Maxwell equations with time level suffices are,

$$\frac{1}{c}\left(\frac{\partial \mathbf{E}}{\partial t}\right)^{n+1/2} = \nabla \times \mathbf{B}^{n+\alpha} - \frac{4\pi}{c}\mathbf{j}^{n+\gamma}, \tag{1}$$

$$\frac{1}{c}\left(\frac{\partial \mathbf{B}}{\partial t}\right)^{n+1/2} = -\nabla \times \mathbf{E}^{n+\alpha}, \tag{2}$$

$$\nabla \cdot \mathbf{E}^{n+1} = 4\pi\rho^{n+1}, \tag{3}$$

$$\nabla \cdot \mathbf{B}^{n+1} = 0. \tag{4}$$

The equations of motion for ions are,

$$\frac{d\mathbf{v}_j^{n+1/2}}{dt} = \frac{e_i}{m_i}\left[\mathbf{E}^{n+\alpha}(\mathbf{x}_j) + \frac{\mathbf{v}_j^{n+1/2}}{c} \times \mathbf{B}^{n+\alpha}(\mathbf{x}_j)\right], \tag{5}$$

$$\frac{d\mathbf{x}_j^{n+1/2}}{dt} = \mathbf{v}_j^{n+1/2}, \tag{6}$$

and the equations of motion for electrons are,

$$\frac{dv_{\parallel j}^{n+1/2}}{dt} = \frac{(-e)}{m_e}E_{\parallel}^{n+\alpha}(\mathbf{x}_j) - \frac{\mu_j}{m_e}\nabla_{\parallel}B^{n+\alpha}, \tag{7}$$

$$\mathbf{v}_{\parallel j}^{n+1/2} = v_{\parallel j}^{n+1/2}\mathbf{b}^{n+1/2}(\mathbf{x}_j), \tag{8}$$

$$\mathbf{v}_{\perp j}^{n+\gamma} = c\left(\frac{\mathbf{E}\times\mathbf{B}}{B^2}\right)^{n+\gamma}(\mathbf{x}_j) - \frac{m_e c}{eB^3}\left(\frac{\mu_j}{m_e}B + v_{\parallel}^2\right)^{n+\gamma}\mathbf{B}^{n+\gamma}\times\nabla B^{n+\gamma}, \tag{9}$$

$$\frac{d\mathbf{x}_j^{n+1/2}}{dt} = \left(\mathbf{v}_{\parallel j}^{n+1/2} + \mathbf{v}_{\perp j}^{n+\gamma}\right). \tag{10}$$

The parameters α and γ are the implicitness parameters that are slightly larger than $\frac{1}{2}$. The decentering of the time level for the curl terms in Eqs.(1)(2) results in damping of the high frequency light wave and that for the current density results in damping of high frequency plasma waves. Damping of high frequency electrostatic waves with $\omega \sim \omega_{pe}$ is caused by the decentering of the field in the equations of motion. It should be noted that the guiding-center approximation is used just for the "perpendicular" motion of the electrons to eliminate the electron time scale ω_{ce}. By contrast, the ion and electron parallel motions are exactly traced as particles, making this code suitable for the study of kinetic plasma transport in fusion plasmas ($\omega_{ce} \sim \omega_{pe} \gg \omega_{ci}$). It is also a natural extension of this MACROS code to introduce the guiding center approximation to the ions which enables us simulations with yet a larger time scale $\omega_{ci}\Delta t > 1$.

The technique that makes the implicit algorithm practical is the following: The Maxwell equations in the finite-difference form assume

$$\begin{aligned} \mathbf{E}^{n+1} - \mathbf{E}^{n} &= c\Delta t \nabla \times \mathbf{B}^{n+\alpha} - 4\pi\Delta t\, \mathbf{j}^{n+\gamma}, & (11) \\ \mathbf{B}^{n+1} - \mathbf{B}^{n} &= -c\Delta t \nabla \times \mathbf{E}^{n+\alpha}. & (12) \end{aligned}$$

To avoid the Courant condition which severely restricts the size of the time step Δt, we eliminate $\mathbf{B}^{n+1}$ from Eqs.(11)(12) using the linear interpolation to the non-integer time level:

$$\mathbf{E}^{n+\alpha} = \alpha \mathbf{E}^{n+1} + (1-\alpha)\mathbf{E}^{n}, \tag{13}$$

to yield an equation governing the electric field

$$\begin{aligned} [\, 1 + (\alpha c\Delta t)^2 \nabla \times \nabla \times \,]\, \mathbf{E}^{n+1} &= [\, 1 - \alpha(1-\alpha)(c\Delta t)^2 \nabla \times \nabla \times \,]\, \mathbf{E}^{n} \\ &\quad + c\Delta t \nabla \times \mathbf{B}^{n} - 4\pi\Delta t\, \mathbf{j}^{n+\gamma}. \end{aligned} \tag{14}$$

Since the implicitness parameters are so chosen as $\alpha, \gamma > \frac{1}{2}$, the current density in the above equation must be predicted by some ways. This is done by expressing the current density in terms of the electromagnetic field,

$$\begin{aligned} \mathbf{j}^{n+\gamma}(\mathbf{x}) &= \sum_j e_j \mathbf{v}_j^{n+\gamma} S(\mathbf{x} - \tilde{\mathbf{x}}_j^{n+\gamma}) & (15) \\ &= \sum_i e_i [\mathbf{v}_j^{n} + \gamma\Delta t \frac{e_i}{m_i} \{\mathbf{E}^{n+\alpha}(\tilde{\mathbf{x}}_j^{n+\gamma}) & (16) \\ &\qquad + \frac{\mathbf{v}_j^{n+1/2}}{c} \times \mathbf{B}^{n+\alpha}(\tilde{\mathbf{x}}_j^{n+\gamma})\}]\, S(\mathbf{x} - \tilde{\mathbf{x}}_j^{n+\gamma}) & (17) \\ &+ \sum_e (-e)[\{v_\parallel^{n} + \gamma\Delta t (\frac{(-e)}{m_e} E_\parallel^{n+\alpha}(\tilde{\mathbf{x}}_j^{n+\gamma}) - \frac{\mu_j}{m_e} \nabla_\parallel B^{n+\alpha})\}\, \mathbf{b}^{n+1/2} & (18) \\ &\qquad + \mathbf{v}_\perp^{n+\gamma}(\tilde{\mathbf{x}}_j^{n+\gamma})]\, S(\mathbf{x} - \tilde{\mathbf{x}}_j^{n+\gamma}). & (19) \end{aligned}$$

Substitution of this expression into Eq.(14) with Eqs.(5)(10) and (12) forms a closed set of the Courant-condition-free, implicit equations which are named "field-particle-coupled (FPC)" equations.

3. Applications of Macroscale Particle Code

Physical accuracy of the MACROS code is demonstrated in Fig.1 where the kinetic Alfven wave (KAW) of a finite amplitude is initially loaded in a two-dimensional bi-periodic magnetized plasma[1]. The KAW has both the MHD and kinetic natures accompanied by the density perturbation since its perpendicular wavelength is comparable to the ion gyroradius. It is seen that the wave pattern is fairly well preserved as it propagates obliquely to the ambient magnetic field $k_\perp \gg k_\parallel$. The amplitude of this wave is found to decrease in time. The phase speed and the damping rate of this wave agree very well with the linear theory of the kinetic Alfven wave. As a result of the wave damping, heating of electrons along the ambient magnetic field is observed. The flattening occurs at the resonance velocity $v_\parallel \cong \omega/k_\parallel$ which is an evidence of occurrence of the Landau resonance with the wave.

The intermediate version of MACROS code was completed by 1986. This adopts the predictor-corrector method to obtain the current density term in Eq.(14). This version of the code has been applied to variety of plasmas including a current generation /kink instability[2] and excitation of the kinetic Alfven wave /plasma heating[3]. These studies are virtually the first works that have ever done by kinetic-MHD simulation code of general purposes. A simulation of m/n=1/1 kink instability is shown in Fig.2. For this simulation a drag term is included in the equations of motion. The current carrying beam is seen to be helically distorted by the kink instability. As the result of this instability, the safety factor before the instability $q(0) < 1$ is found to pop up to $q \geq 2$ after the instability.

References
1. M.Tanaka, J.Comput.Phys., vol.79, 209 (1988).
2. M.Tanaka and T.Sato, Physics of Fluids, 29, 3823 (1986).
3. M.Tanaka, T.Sato and A.Hasegawa, Physics of Fluids, B1, 325 (1989).

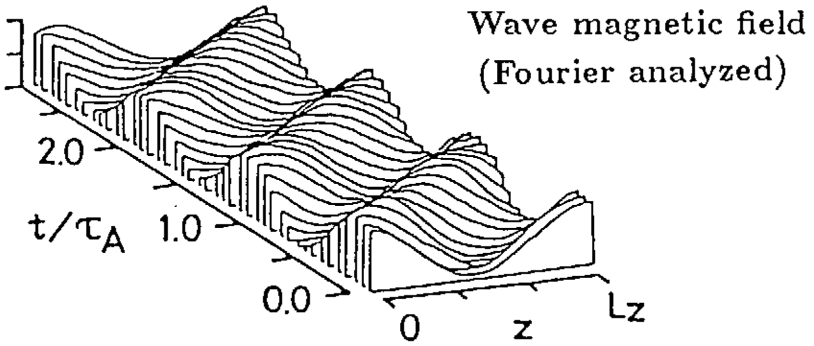

Fig.1 Propagation of the kinetic Alfven wave in a bi-periodic magnetized plasma.

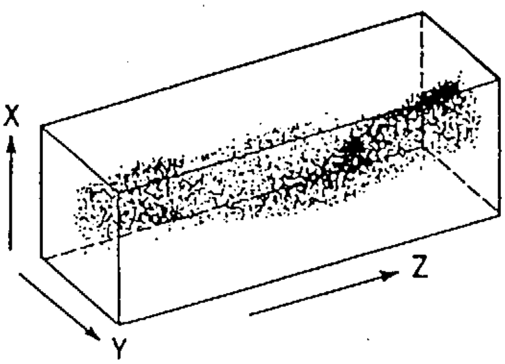

Fig.2 Occurrence of m/n= 1/1 helical kink instability in a three-dimensional magnetized plasma.

Study of kink instability and current relaxation by three dimensional macroscale particle simulation

H. Takamaru [†],
Faculty of Science, Hiroshima Univ., Japan
M. Tanaka and T. Sato,
Theory and Computer Simulation Center
National Institute for Fusion Science, Japan

Abstract

Using the macroscale particle simulation code (MACROS code), we have been able to study nonlinear particle transport on the MHD (large time and space) scales. We apply a semi-implicit version of the MACROS code to problems with a change in the magnetic field structure. We first study qualitatively and quantitatively a pure MHD phenomenon, an ideal kink instability ($m/n = 1/1$). A simple tokamak system with no toroidal effect is used to simulate the time evolution of the instability starting from a typical initial configuration. We observe an occurrence of the kink instability whose growth rate γ_{MACROS} given by the MACROS code takes a value up to, but not greater than twice the linear-analytical value of γ_{linear}. Secondly, we study a current relaxation process from an initial non-equilibrium to a force-free like equilibrium configuration. We have found that kinetic effects may contribute to the relaxation process of the magnetic field - current system.

1. Introduction

Particle transport is a new and old problem in plasma confinement. Though it is a fundamental problem, its mechanism has never been solved self-consistently. The leading factor which has made it hard to solve this problem is the fact that one must deal simultaneously with nonlinear interactions between MHD (large time and space) scale field fluctuations and microscale field-particle nonlinear couplings. The macroscale particle simulation code (MACROS code) has been developed to overcome this difficulty.

We show two applications in this paper. First, in order to demonstrate the applicability of this code to problems with a change in the magnetic field structure, we study qualitatively and quantitatively a pure MHD instability, that is an ideal kink instability

---

[†] Current address is National Institute for Fusion Science, Japan

($m = 1/n = 1$), starting from unstable equilibrium state to stable equilibrium state. Second, we apply the MACROS code to the current relaxation process in tokamak plasmas starting from an initial non-equilibrium state to an equilibrium state.

We consider a simple tokamak system with no toroidal effects and make a simulation using a semi-implicit (predictor-corrector scheme) version of the MACROS code. The simulation box is rectangular with the longitudinal axis and square cross section corresponding to the toroidal axis and a poloidal cross section, respectively. The initial temperature profile and external magnetic field are homogeneous.

2. Kink Instability

The initial configuration is such that the plasma is in the MHD (Grad-Shafranov) equilibrium including a vacuum region between the plasma and the wall. An initial perturbation is given by thermal noise. Initial q (safety factor) and plasma density profiles are shown in Fig.1, where the on-axis q value is 0.56.

Three dimensional scatter plots of Fig.2 shows the appearance of the $m/n = 1/1$ kink mode. Figure a) and b) correspond to t = 0 and t = $12\tau_{PA}$, where τ_{PA} is a poloidal Alfvén time. The points in the figures show plasma particles (ions and electrons) within a region inside the q=1 surface at the initial state.

A time-history of the kink instability is shown in Fig.3 where the plasma column is found to shift radially (ξ). This result shows that the growth rate $(\tau_{MACROS})^{-1}$ given by the simulation takes a value up to, but not greater than twice the linear-analytical value of $(\tau_{linear})^{-1}$. Here the MHD analytical value is calculated in cylinder coordinates under an incompressible approximation.

3. Current Relaxation Process

The initial configuration of the tokamak plasma consists of an external toroidal magnetic field, induced toroidal current, and poloidal magnetic field which is induced by the toroidal current. This initial non-equilibrium configuration may change to the state close to a force-free like equilibrium state ($\boldsymbol{J} \times \boldsymbol{B} \approx 0$) where plasma current runs parallel with magnetic field. It is difficult to measure or theoretically analyze this relaxation process toward the force-free like configuration. The purpose of the present research is to investigate whether this current configuration can be realized or not, and to clarify this mechanism using a three dimensional particle simulation.

Fig.4 shows the time evolution of pitch angle between the current and the magnetic field line from 0 to 20 τ_{PA}. The small panel in the figure shows an enlargement of the time evolution from 0 to 7 τ_{PA}. This pitch angle decreases in the time scale (τ_{relax}) that is longer than a small vibration near the MHD equilibrium point ($\sim 1/2\tau_{PA}$) and shorter than a resistive diffusion time scale. The poloidal current grows from 0 to some finite value in certain time scale ($\sim 1/2\tau_{PA}$ or $1\tau_{PA}$) and is maintained in the time scale (τ_{relax}) as in Fig.5. These results show occurrence of a current relaxation process in tokamak plasmas. This current relaxation process has the time scale (τ_{relax}) and seems to be caused by a kinetic effect rather than MHD effects. However we have not yet found the mechanism for this process, since we simulated in the region ($\boldsymbol{V}_{Alfvén} \sim \boldsymbol{V}_{e(thermal)} > \boldsymbol{V}_{i(thermal)}$) due to the limit of the computer performance. Thus we can not distinguish MHD from kinetic phenomena.

4. Conclusion

1) Simulation results for the kink instability are :
    - i) We have observed the occurrence of the m=1/n=1 ideal kink mode using a three dimensional particle simulation.
    - ii) The growth rate of the kink mode takes a value up to, but not greater than twice the MHD, linear-analytical value.
2) Simulation results for the current relaxation process are :
    - i) We have observed the relaxation of the magnetic field - current system from the initial non-equilibrium to the "force-free like" equilibrium state.
    - ii) Although a conclusive description of this relaxation process has not been obtained yet, we have found that kinetic effects may act as the relaxation mechanism.

References

[1] V.D.Shafranov, *SPTP*, 15, 175 (1970)

[2] M.Tanaka and T.Sato, *Phys.Fluids.*, 29, 3823 (1986)

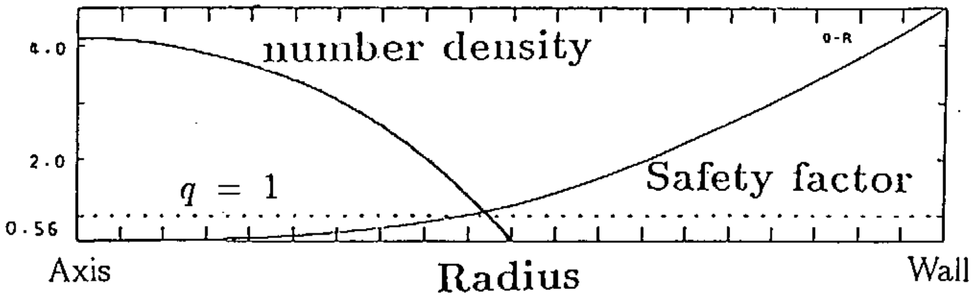

Fig.1

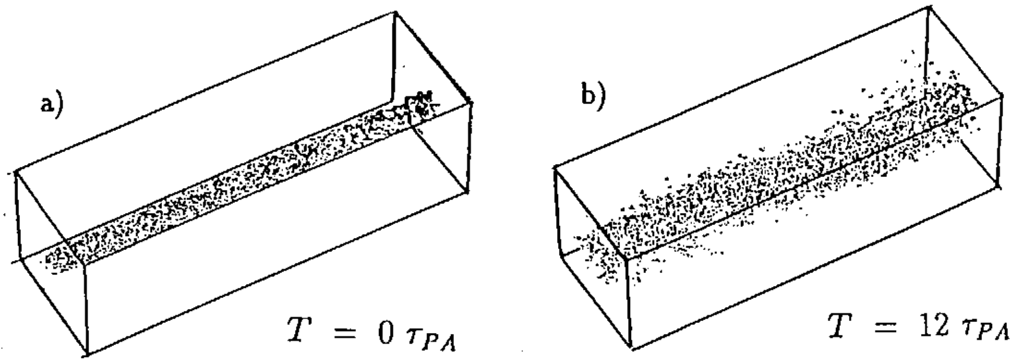

Fig.2

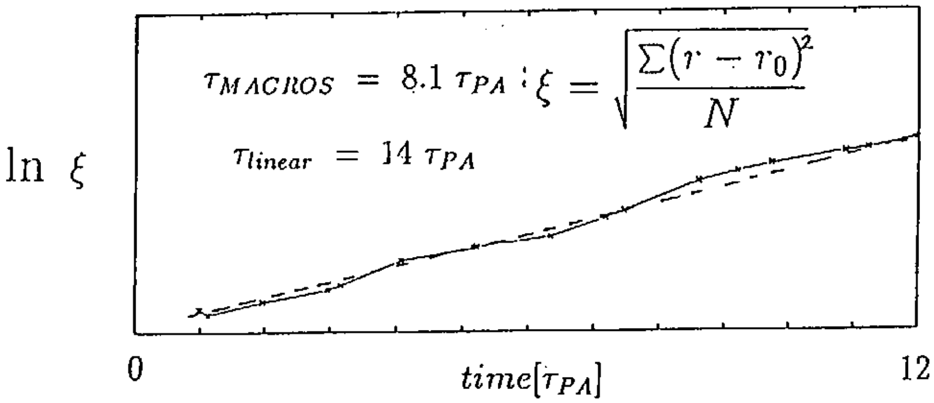

Fig.3

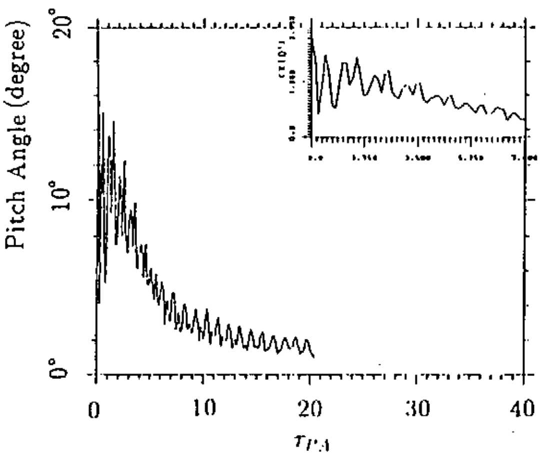

Fig.4

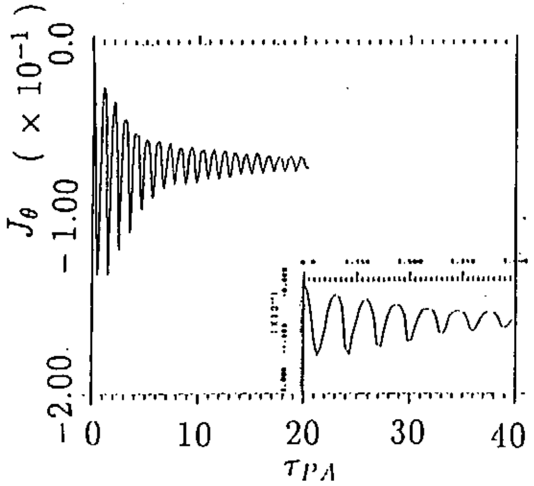

Fig.5

Nonadiabatic behavior of the magnetic moment of a charged particle in a dipole magnetic field[1]

S. Murakami*
Faculty of Science, Hiroshima University, Hiroshima 730
T. Sato
National Institute for Fusion Science, Nagoya 464-01
A. Hasegawa
AT&T Bell Laboratories, Murray Hill, New Jersey 07974, USA

ABSTRACT

Non-adiabatic behavior of the magnetic moment of a charged particle in a dipole magnetic field is studied both numerically and analytically in the presence of a low frequency electrostatic wave with azimuthal component. We obtained numerically two characteristic conditions for the breakdown of μ; one is independent of the wave frequency, and the other forms a spike-like structure in the wave frequency-particle energy space. We showed analytically that the former is caused by the direct interaction between the particle and the electrostatic wave during the gyromotion and that the latter is caused by two kinds of resonances, i.e., the bounce-$E \times B$ drift resonance and the wave-drift resonance. The unstable conditions obtained by theoretical consideration showed good agreements with those of numerical results.

---

*Present address: National Institute for Fusion Science, Nagoya 464-01

The motion of particles which are trapped in a dipole magnetic field consists basically of three periodicities[2]. One is the gyromotion caused by the Lorentz force. The second is the bounce motion along the magnetic field line and the third is the drift motion in the azimuthal direction. We can then define three adiabatic invariants[3,4] as actions associated with these three periodic motions: the magnetic moment μ related to the gyromotion, the action integral J of the bounce motion along the magnetic field line, and the magnetic flux Ψ penetrating the area surrounded by the drift orbit of the particle. We study the motion of a single particle in a dipole magnetic field in the presence of an electrostatic wave which has an azimuthal filed component. The frequency of the ambient electrostatic wave is comparable to the drift frequencies. In the presence of an azimuthal electrostatic wave, the resonances between the particle motion and the wave or the $E \times B$ drift oscillation can violate the adiabaticity. We show two kinds of resonances by which the adiabaticity of the magnetic moment is broken and give the critical condition for magnetic moment conservation in the resonant and nonresonant cases.

First, we numerically study the dynamic behavior of the magnetic moment in the absence of the electrostatic wave. In this case the nonlinear resonance betwen the bounce motion and the gyromotion[5,6] can be a cause of the violation of the adiabaticity of the invariants. The numerical calculations are obtained for various initial velocities and pitch angles. As a result, we found the critical condition for the μ conservation,

$$\bar{v} = \epsilon^* \sin\theta_0 + c, \tag{1}$$

where $\bar{v}$ and θ_0 are the particle velocity and pitch angle, respectively.

Next, we numerically study the case in the presence of a wave. Since the propagating direction of the wave depends on the sign of the wave frequency, two different cases are considered, i.e. , the case where the wave propagates in the direction of the particle drift motion and the case in the opposite direction. We made numerical calculations under various particle and wave conditions for the two cases. The results are shown in Fig. 1. Open circles show the condition where μ is conserved, while filled circles show the condition where μ is not conserved. In both cases, we obtained two characteristic conditions for the μ non-conservation caused by the electrostatic wave. One is independent of the wave frequency, and the other forms a spike-like structure in the wave frequency-particle energy space. Particularly, when the wave propagates in the particle drift direction the spike-like structure is larger than that in the oppositely propagating case.

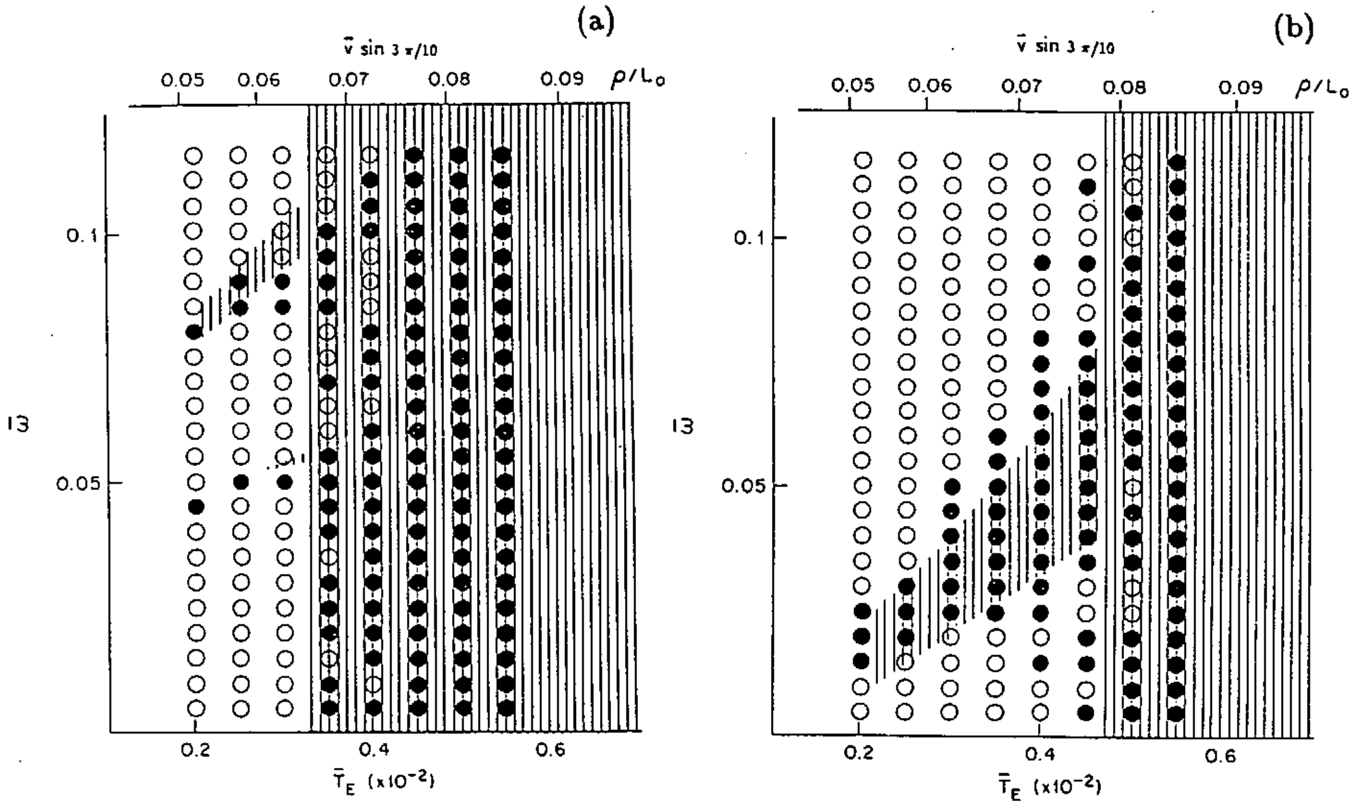

Figure 1: *A comparison of the analytical results with the numerical ones for the case where the wave propagates in the direction opposite to the particle drift(a) and in the direction of particle drift motion(b). The shaded region shows the analytical results.*

In order to study the critical condition of the adiabaticity of the magnetic moment in the presence of an electrostatic wave, we make the following conjecture. When the wave frequency is comparable to the drift frequency, the μ-breaking mechanism can still be independent of the existence of the wave. Hence the critical condition for the μ conservation in the absence of a wave, Eq. (1), is also applicable to the case where a low frequency wave is present. The critical condition may be satisfied with the modification of the perpendicular velocity in the nonresonant case, and with the modification of the parallel velocity in the resonant case. Thus we analytically study the velocity change due to the electrostatic wave for two cases; the direct interaction case and the resonant cases.

In the direct interaction case, we estimate the decrease of the perpendicular velocity due to the electrostatic wave during the particle gyromotion. Assuming that the electric field is constant during the gyromotion, we obtain the maximum change of the perpendicular velocity. In the resonant case, we estimate the increases of the parallel velocity due to the resonances between the wave and particle motions. By means of the Hamiltonian for the guiding center, we found that the parallel velocity is maximized by two types of resonance, i.e., the bounce-$E \times B$ drift resonance and the wave-drift resonance. The bounce-$E \times B$drift resonance is a resonance between particle bounce motion and $E \times B$ drift motion, and the wave-drift resonance is a resonance between the wave motion and the particle $\nabla \mathbf{B}$ drift motion.

Substituting the perpendicular velocity change and the parallel velocity change into the critical condition in Eq. (1), we can obtain the non-adiabatic condition in the presence of an electrostatic wave. We compare the numerical results with the analytical ones for the case where the wave propagates in the direction opposite to the particle drift and in the direction of particle drift motion (Fig. 1). The unstable conditions obtained by theoretical consideration showed good agreements with those of numerical results in both cases. Consequently, it is concluded that the frequency independent characteristic condition is caused by the direct interaction between the particle and the electrostatic wave during the gyromotion and that the frequency dependent one is caused by two kinds of resonances, i.e., the bounce-$E \times B$ drift resonance and the wave-drift resonance.

REFERENCES

1. S. Murakami, T. Sato, and A. Hasegawa, Phys. Fluids B **2**, 715 (1990).
2. A. J. Dragt, Rev. Geophysics **3**, 255 (1965).
3. T. G. Northrop, Ann. Phys. **15**, 79(1961).
4. T. G. Northrop, in *The Adiabatic Motion of Charged Particles* (John Wiley, New York, 1963).
5. B. V. Chirikov, Sov. J. Plasma Phys. **4**, 289 (1978).
6. B. V. Chirikov, in *Reviews of Plasma Physics Vol. 13* (Consulatnts Bureau, New York,1987), p. 1.

NUMERICAL STUDY OF ION TEMPERATURE GRADIENT MODES IN A TOKAMAK

M. Yagi and M. Azumi

Japan Atomic Energy Research Institute
Muko-yama, Naka-machi, Naka-gun, Ibaraki-ken, Japan 311-01

Understanding of anomalous transport processes in a tokamak is the key issue for improving the energy confinement and realizing a fusion reactor. From this point of view, the microturbulence caused by ion temperature gradient modes (η_i modes) has been extensively studied as a possible candidate for degrading the ion energy confinement. Some recent experimental results, however, show that the energy confinement time does not differ from the standard one even when η_i becomes much greater than the threshold value; that is, the η_i mode is linearly unstable. These results suggest that , when we employ the quasilinear expression of ion thermal flux as $q_i=[e\phi/T_i]^2F(n_e,T_i, \ldots.)(\eta_i-\eta_i^{crit})^{1/2}$, the numerical factors such as the saturation level and the value of function F may change, depending on the change of plasma parameters. We are now studying the three different regimes of η_i modes, based on the fluid model by Horton. The first regime is the normal density profile case (positive η_i modes), which is related with the standard L-mode confinement. The second regime is the flat density profile case (weak density gradient η_i modes), which is related with the H-mode confinement. The third regime is the inverted density gradient case (negative η_i modes), which is considered to be related with phenomena observed in H -mode discharges in D-III-D. By the kinetic theory based on the weak turbulent approximation, Harm and his coworkers found that the saturation level of the negative η_i mode does not show the strong dependence on the η_i parameter. We are now checking their results in the framework of the fluid model. We will also discuss the relationship between the result of nonlinear fluid simulations and the tokamak transport analysis.

Nonlinear Behavior and Transport Property of Multiple-Helicity Resistive Interchange Modes near Marginally Stable States

H. Sugama

National Institute for Fusion Science
Nagoya 464–01, Japan

MODEL EQUATIONS AND THEIR SYMMETRY PROPERTY

Resistive interchange modes are described by the following reduced MHD model in the electrostatic limit, which consists of the following equations:

$$\frac{\rho_m c}{B_0}\left(\frac{\partial}{\partial t} - \nu\nabla_\perp^2 + \frac{c}{B_0}\hat{z}\times\nabla\phi\cdot\nabla\right)\nabla_\perp^2\phi = -\frac{B_0}{c\eta}\nabla_\parallel^2\phi - \Omega'\frac{\partial p}{\partial y} \tag{1}$$

$$\left(\frac{\partial}{\partial t} - \chi\nabla_\perp^2 + \frac{c}{B_0}\hat{z}\times\nabla\phi\cdot\nabla\right)p = \frac{c}{B_0}P_0'\frac{\partial\phi}{\partial y} \tag{2}$$

where ϕ is the electrostatic potential, p the pressure fluctuation, B_0 the component of the static magnetic field along the z-axis, ρ_m the average mass density, c the light velocity in the vacuum, η the resistivity, ν the kinematic viscosity, χ the pressure diffusivity, $P_0' \equiv dP_0/dx$ (< 0) the average pressure gradient and $\Omega' \equiv d\Omega/dx$ (> 0) the average curvature of the magnetic field line. $\nabla_\perp^2 = \partial_x^2 + \partial_y^2$ denotes the two-dimensional Laplacian. The gradient along the the static sheared magnetic field line is given by $\nabla_\parallel = \partial_z + (x/L_s)\partial_y$. Here B_0, L_s, ρ_m, η, ν, χ, P_0' and Ω' are assumed to be constant since we treat a local transport problem. The electrostatic approximation is used in Eqs.(1) and (2) since we consider the low beta plasma in the peripheral region and futhermore we are most concerned with the transport of the stationary state, in which the time variation of the magnetic field vanishes as well as those of the other physical variables.

Choosing the units:

$$\begin{array}{ll} [t] = (-P_0'\Omega'/\rho_m)^{-1/2} & [x] = [y] = cL_s\eta^{1/2}(-\rho_m P_0'\Omega')^{1/4}/B_0 \\ [z] = L_s & [\chi] = [x]^2/[t] = c^2\eta(-P_0')\Omega' L_s^2/B_0^2 \\ [\phi] = c\eta(-P_0')\Omega' L_s^2/B_0 & [p] = cL_s\eta^{1/2}\rho_m^{1/4}(-P_0')^{5/4}\Omega'^{1/4}/B_0 \end{array} \tag{3}$$

we obtain model equations in non-dimensional variables from Eqs.(1) and (2) as follows

$$\partial_t\nabla_\perp^2\phi + [\phi, \nabla_\perp^2\phi] = -\nabla_\parallel^2\phi - \partial_y p + \chi P_r\nabla_\perp^4\phi \tag{4}$$

$$\partial_t p + [\phi, p] = -\partial_y\phi + \chi\nabla_\perp^2 p \tag{5}$$

where $\nabla_\parallel = \partial_z + x\partial_y$, $[f, g] = (\partial_x f)(\partial_y g) - (\partial_x g)(\partial_y f)$ and $P_r = \nu/\chi$(the Prandtl number).

Let us expand the electrostatic potential ϕ and the pressure fluctuation p into the Fourier series with respect to y and z as

$$\begin{pmatrix} \phi(x,y,z) \\ p(x,y,z) \end{pmatrix} = \sum_{n=0}^{\infty}\begin{pmatrix} \phi_{0n}(x)\sin kn\Delta z \\ p_{0n}(x)\cos kn\Delta z \end{pmatrix} + \sum_{m=1}^{\infty}\sum_{n=-\infty}^{\infty}\begin{pmatrix} \phi_{mn}(x)\sin k(my + n\Delta z) \\ p_{mn}(x)\cos k(my + n\Delta z) \end{pmatrix}. \tag{6}$$

where $\Delta = (k_z)_{min}/(k_y)_{min}$ denotes the interval between the neighboring $m = 1$ mode ratinal surfaces.

We consider the following transformation T:

$$\mathrm{T}:\begin{pmatrix}\phi_{m,n}(x)\\ p_{m,n}(x)\end{pmatrix}\to\begin{pmatrix}(T\phi)_{m,n}(x)\\ (Tp)_{m,n}(x)\end{pmatrix}=\begin{pmatrix}\phi_{m,m+n}(x-\Delta)\\ p_{m,m+n}(x-\Delta)\end{pmatrix}. \tag{7}$$

Equations (4) and (5) are invariant with the transformation **T**. We should note that not only Eqs.(4) and (5) but also other reduced fluid model equations based on the local sheared slab geometry with constant magnetic shear are invariant under the transformation T.

PERTURBATION THEORY OF MULTIPLE-HELICITY RESISTIVE INTERCHANGE MODES

Here the perturbation theory of the single-helicity nonlinear problem near marginally stable states by Hamaguchi and Nakajima [1-3] is extended to the multiple-helicity case and applied to the resistive interchange modes. Equations (4) and (5) have the trivial equilibrium solution $\phi = p = 0$. Solving the linearized equation gives the spectrum of the eigenvalue or the linear growth rate γ for the perturbaton which varies in the form $\exp\gamma t$ and vanishes as $x \to \pm\infty$. When k and P_r are given, a critical diffusivity χ_c exists such that all the Fourier modes in Eq.(6) are linearly stable for $\chi > \chi_c$, only one of the eigenvalues of the $m = 1$ modes becomes $\gamma = 0$ for $\chi = \chi_c$ and the system is linearly unstable for $\chi < \chi_c$. Since the neighborhood of the marginally stable states $\chi = \chi_c$ is considered, the magnitudes and the temporal variations of $\phi(x,y,z)$ and $p(x,y,z)$ are small and therefore we make the following perturbation expansion with the parameter λ

$$\begin{aligned}\begin{pmatrix}\phi\\ p\end{pmatrix} &= \lambda\begin{pmatrix}\phi_1\\ p_1\end{pmatrix}+\lambda^2\begin{pmatrix}\phi_2\\ p_2\end{pmatrix}+\cdots\cdots\\ \frac{\partial}{\partial t} &= \lambda\frac{\partial}{\partial\tau_1}+\lambda^2\frac{\partial}{\partial\tau_2}+\cdots\cdots\\ \chi &= \chi_c+\lambda\chi_1+\lambda^2\chi_2+\cdots\cdots.\end{aligned} \tag{8}$$

Substituting Eq.(8) into Eqs.(4) and (5) yields in $O(\lambda)$

$$\mathrm{L}\begin{pmatrix}\phi_1\\ p_1\end{pmatrix}\equiv\begin{pmatrix}-\nabla_{\parallel}^2\phi_1+\chi_c P_r\nabla_{\perp}^4\phi_1 & -\partial_y p_1\\ \partial_y\phi_1 & -\chi_c\nabla_{\perp}^2 p_1\end{pmatrix}=0. \tag{9}$$

Equation (9) is just the linear equation for the marginally stable state. We find that the solution of Eq.(9) consists of the linear combination of the $m = 1$ modes

$$\begin{pmatrix}\phi_1\\ p_1\end{pmatrix}=\sum_{n=-\infty}^{\infty}A_n\begin{pmatrix}\phi_1(x+n\Delta)\sin k(y+n\Delta z)\\ p_1(x+n\Delta)\cos k(y+n\Delta z)\end{pmatrix}. \tag{10}$$

Here we used the fact that since the linear equation (9) is also invariant with the transformation **T**, we can produce the linear solutions from one set of eigenfunctions $(\phi_1(x)\sin ky, p_1(x)\cos ky)^T$ by operating **T** successively

$$\mathrm{T}^n\begin{pmatrix}\phi_1(x)\sin ky\\ p_1(x)\cos ky\end{pmatrix}=\begin{pmatrix}\phi_1(x-n\Delta)\sin k(y-n\Delta z)\\ p_1(x-n\Delta)\cos k(y-n\Delta z)\end{pmatrix}\qquad(n=0,\pm1,\pm2,\cdots). \tag{11}$$

Thus the marginally stable state is degenerate with the m=1 mode eigenfunctions (11). Here we employ the boundary condition that $\phi_1(x) \to 0$ as $x \to \pm\infty$. The eigenfunction $\phi_1(x)$ has a peak at $x = 0$ so that the m=1 modes (11) are localized around the mode rational surfaces $x = n\Delta \quad (n = 0, \pm 1, \pm 2, \cdots)$. In Eq.(10) A_n is a real-valued function of the time $A_n = A_n(\tau_1, \tau_2, \cdots)$.

From the solvability condition of the $O(\lambda^2)$ equation, we can assume that $\chi_1 = \partial_{\tau_1} A_n = 0$. The sovability condition of $O(\lambda^3)$ equation gives

$$D_0 \partial_{\tau_2} A_n + \chi_2 D_1 A_n + \sum_{n_1, n_2} D_{n-n_2, n-n_1} A_{n-n_1+n_2} A_{n_1} A_{n_2} = 0. \tag{12}$$

Rewriting $\lambda A_n \to A_n$, $\tau_2 \to \lambda^2 t$ and $\lambda^2 \chi_2 \to (\chi - \chi_c)$ we obtain

$$D_0 \partial_t A_n + (\chi - \chi_c) D_1 A_n + \sum_{n_1, n_2} D_{n-n_2, n-n_1} A_{n-n_1+n_2} A_{n_1} A_{n_2} = 0 \tag{13}$$

where

$$D_0 = \int_{-\infty}^{\infty} dx [|\partial_x \phi_1(x)|^2 + k^2 \phi_1^2(x) + p_1^2(x)] \tag{14}$$

$$D_1 = \int_{-\infty}^{\infty} dx [P_r |(\partial_x^2 - k^2) \phi_1(x)|^2 + |\partial_x p_1(x)|^2 + k^2 p_1^2(x)] \tag{15}$$

$$\begin{aligned} \sum_{n_1, n_2} D_{n-n_1, n-n_2} A_{n-n_1+n_2} A_{n_1} A_{n_2} &= \int_{-\infty}^{\infty} dx [-\phi_1(x + n\Delta) \{[\phi_1, \nabla_\perp^2 \phi_2]_{1n} + [\phi_2, \nabla_\perp^2 \phi_1]_{1n}\} \\ &\quad + p_1(x + n\Delta) \{[\phi_1, p_2]_{1n} + [\phi_2, p_1]_{1n}\}]. \end{aligned} \tag{16}$$

Equation (13) determines the behavior of the amplitude A_n in the solution of the leading order (10) near the marginally stable state.

COMPARISON BETWEEN THEORY AND NUMERICAL SIMULATIONS OF SYMMETRIC SOLUTION

In this section the results of the perturbation theory in the previous section are compared with those of the numerical simulations of Eqs.(4) and (5). Here we consider the symmetric solutions which are invariant under the transformation **T**: $\mathbf{T\Phi} = \mathbf{\Phi}$. Then it follows that $A_n = A \quad (n = 0, \pm 1, \pm 2, \cdots)$ and Eq.(13) reduces to the Landau equation:

$$D_0 \partial_t A + (\chi - \chi_c) D_1 A + D_3 A^3 = 0. \tag{17}$$

The solution of the Landau equation is easily obtained and written as

$$A^2 = A_\infty^2 / [1 + (A_\infty^2 / A_0^2 - 1) \exp(-2\sigma t)] \tag{18}$$

where $A_0 = A(t = 0)$, $\sigma = (\chi_c - \chi) D_1 / D_0$ and $A_\infty^2 = (\chi_c - \chi) D_1 / D_3$. Equations (14) and (15) show that $D_0 > 0$ and $D_3 > 0$. We find that if $\chi > \chi_c$ then $\sigma < 0$ and $A \sim A_0 \exp(\sigma t)$, i.e., the linear theory holds as $t \to \infty$ for sufficiently small A_0. As will be found in the detailed calculations, D_3 is positive in the cases treated here. When $\chi < \chi_c$, we have $\sigma > 0$ and $A \sim A_0 \exp(\sigma t)$ as $t \to -\infty$ for sufficiently small A_0. In this case, $A \to A_\infty$ as $t \to \infty$ for arbitrary magnitudes of A_0. The volume-averaged convective flux $\langle p v_x \rangle$ in the stationary state, in which the contributions from the $m = 1$ modes are dominant, is $O(\lambda^2)$ and given by

$$\begin{aligned} \langle p v_x \rangle &= -\langle p \partial_y \phi \rangle = -\frac{kA^2}{2\Delta} \sum_{n=-\infty}^{\infty} \int_0^{\Delta} dx p_1(x + n\Delta) \phi_1(x + n\Delta) \\ &= -\frac{kA^2}{2\Delta} \int_{-\infty}^{\infty} dx p_1(x) \phi_1(x) = -(\chi_c - \chi) \frac{k}{2\Delta} \frac{D_1}{D_3} \int_{-\infty}^{\infty} dx p_1(x) \phi_1(x). \end{aligned} \tag{19}$$

Figures 1 show the electrostatic potential in the saturated state of the multiple-helicity resistive interchange mode obtained from the numerical simulation of Eqs.(4) and (5). Here we put $P_r = 1$, $k = \pi$, $\Delta = 3$, $\chi = 5 \times 10^{-2}$ ($\chi_c = 7.79 \times 10^{-2}$) and included the modes with $0 \leq m \leq 6$. Figure 1(a) shows the contours of the electrostatic potential. In this case the $m = 1$ mode structures appear dominantly, the profiles of which are shown in Fig.1(b). The $m = 1$ mode structures are similar to those of the linear eigenfunctions obtained from Eq.(9) except that the former is somewhat broader than the latter due to the nonlinear interaction through the overlapping of the neighboring m=1 modes.

Figure 2 shows the dependence of the convective flux $\langle pv_x \rangle$ in the saturated state on the diffusivity χ obtained from the theoretical expression Eq.(19) and the simulations of Eqs.(4) and (5). Here $P_r = 1$, $k = \pi$ and $\Delta = 10$. The theoretical results are in good agreement with the simulation results. For small χ the convective flux obtained from the simulations is smaller than that obtained from the theory due to the higher order nonlinear corrections.

Figure 3 shows the dependence of the saturated convective flux $\langle pv_x \rangle$ multiplied by Δ on Δ^{-1}. Here $P_r = 1$, $k = \pi$ and $\chi = 7 \times 10^{-2}$. As seen from Eq.(19), $\langle pv_x \rangle \Delta = -\frac{1}{2} k A^2 \int_{-\infty}^{\infty} dx p_1(x) \phi_1(x)$ denotes the convection of a single $m = 1$ mode integrated over $-\infty < x < \infty$. Since the values of k and χ are fixed here, the linear mode structures remain unchanged and therefore Δ^{-1} represents the measure for the ratio of the width of the $m = 1$ mode structure to the interval between the neighboring $m = 1$ mode rational surfaces (or the extent to which the neighboring $m = 1$ modes overlap). Here the results of the theory [Eq(19)] and the simulations of Eqs.(4) and (5) are shown. The simulation results are well described by the theoretical predictions but for larger Δ^{-1} the former shows the more rapid increase of $\langle pv_x \rangle \Delta$ than the latter. Thus we see that the higher order nonlinear corrections enhance the saturation amplitude for larger Δ^{-1} while they lower that for smaller χ as seen from Fig.2.

[1] S. Hamaguchi, Phys. Fluids B 1, 1416(1989).
[2] N. Nakajima, Phys. Fluids B 2, 1170(1990).
[3] N. Nakajima and S. Hamaguchi, Phys. Fluids B 2, 1184(1990).

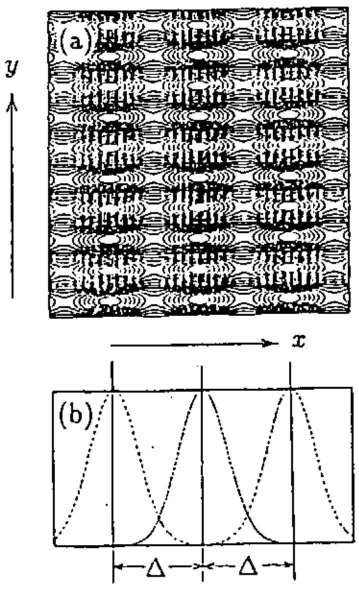

FIG.1

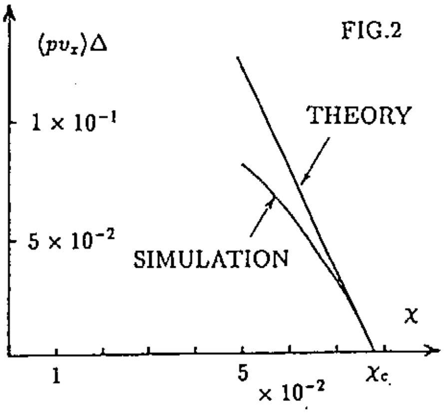

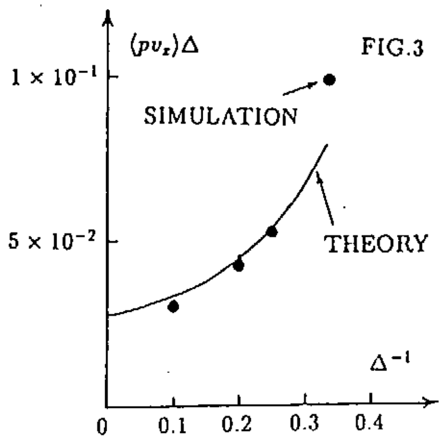

Nonlinear Computer Analysis of Backward Wave Oscillator

T. Watanabe, K. Ogura*, M. M. Ali*, M. Itakura**,
and
K. Minami**

National Institute for Fusion Science, Nagoya, 464-01
*Graduate School of Science and Technology,
Niigata University, Niigata, 950-21
**Faculty of Engineering, Niigata University, Niigata, 950-21

Abstract: A new treatment for nonlinear analysis for backward wave oscillator is developed. A new scheme, Higher order Implicit Difference Method (HIDM) to solve partial differential equation is applied to study the propagation of electromagnetic wave in a corrugated wave guide and its coupling with relativistic electron beam. The computational results is compared with the linear dispersion relation and good agreement is obtained.

High-power microwave sources driven by intense relativistic electron beam have been studied extensively in U. S. and U. S. S. R. in last two decade[1]. Backward oscillators (BWOs) are an example of such devices.

A few years ago, significant enhancement of radiation from a plasma filled backward oscillators were observed at the University of Maryland[2, 3]. Recently, Lin and Chen[4] have reported a numerical simulation of Maryland Plasma BWO, and they attributed the mechanism of enhanced efficiency to be a decrease in the phase velocity of most unstable mode which traps the beam electrons. They concluded that beam- backward plasma wave instability was unlikely to be the major reason of the improved oscillation. They used, however, an artificial periodic boundary condition along the axial direction which did not correspond to the experiments[2, 3]. In real experiments, the length of the interaction region of BWOs are finite, and the end condition of the structure for reflection of radiation are believed to affect seriously the oscillation.

We here try to analyze numerically the nonlinear behavior of a plasma BWO with finite length. Relativistic fluid equation of motion and Maxwell equations are solved numerically in cylindrical coordinates assuming axisymmetric electromagnetic TM01 mode and an infinitely strong external axial magnetic field. We consider a waveguide whose wall radius varies with the axial coordinate z according to a(z) as shown in Fig. 1. The set of the nonlinear partial differential equations includes three independent variables, (r, z, t). In order to make the equations tractable, we try to reduce 2D (r, z, t) boundary value problem to 1D (z, t) problem. We device a power expansion method, which is one of the Galerkin method. All physical quantities are expanded in power series in r;

$$E_r(r,z,t)=E_{r1}(z,t)\,r + E_{r3}(z,t)\,r^3 + \cdots \qquad (1)$$

$$E_z(r,z,t)=E_{z0}(z,t) + E_{z2}(z,t)\,r^2 + E_{z4}(z,t)\,r^4 + \cdots \qquad (2)$$

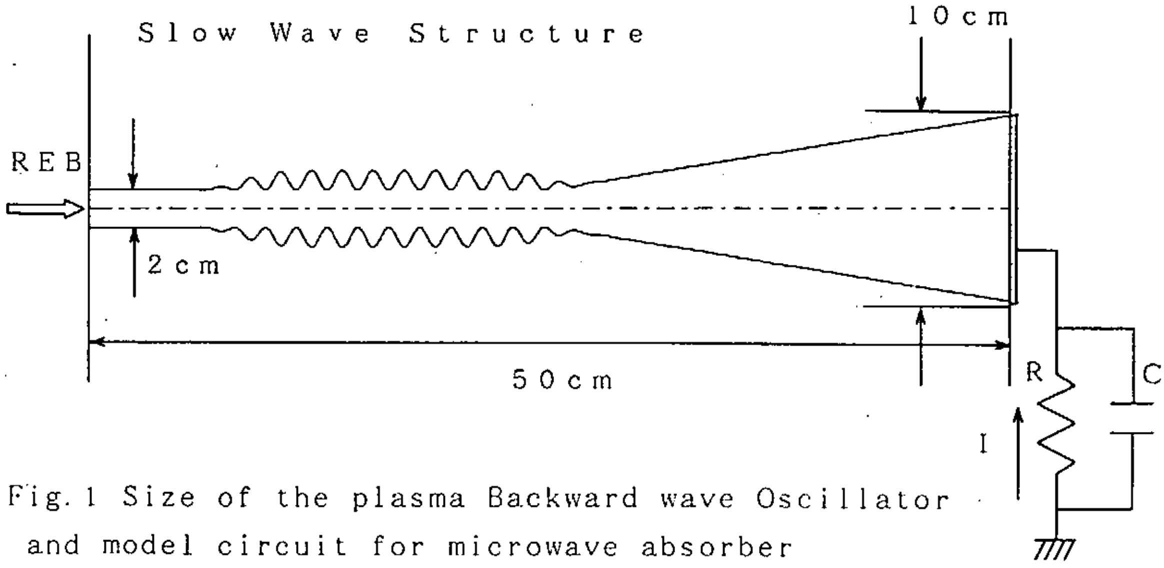

Fig. 1 Size of the plasma Backward wave Oscillator and model circuit for microwave absorber

$$B_\theta(r,z,t)=B_{\theta 1}(z,t)\,r + B_{\theta 3}(z,t)\,r^3 + \cdots \qquad (3)$$

$$v_z(r,z,t)=v_{z0}(z,t) + v_{z2}(z,t)\,r^3 + \cdots \qquad (4)$$

$$n(r,z,t) = n_0(z,t) + n_2(z,t)\,r^2 + \cdots \qquad (5)$$

where notations are standard.

Putting eqs. (1)~(5) into the Maxwell and fluid equations, we find a hierarchy system of equations in which $E_{z2}(z,t)$ has to be known to solve $E_{z0}(z,t)$. The hierarchy can be closed and equations become solvable, if we impose the boundary conditions at surface of the waveguide,

$$E_z(r,z,t)+a'(z)E_r(r,z,t)\Big|_{r=a(z)} = 0 \ . \qquad (6)$$

i.e.,

$$E_{z0}(z,t) + a(z)^2E_{z2}(z,t) + a'(z)\cdot a(z)E_{r1}(z,t) = 0 \ . \qquad (7)$$

Hatched terms in eqs. (1)~(5) are neglected as higher order parts in the lowest order approximation. The final form of the equation is given by

$$\frac{\partial^2 E_{z0}}{\partial t^2} - c^2\frac{\partial^2 E_{z0}}{\partial z^2} + \frac{4c^2}{a^2}E_{z0} + \sum_j 4\pi e_j\left[\frac{\partial(n_{j0}v_{jz0})}{\partial t} + c^2\frac{\partial n_{j0}}{\partial z}\right]$$

$$- \frac{2c^2a'}{a}\left[\frac{\partial E_{z0}}{\partial z} - \sum_j 4\pi e_j n_{j0}\right] = 0 \ . \qquad (8)$$

In order to check the validity eq. (8), we consider the simplest case of TM01 mode in a straight cylinder ($a'=0$) without the beam and plasma. From eq. (8) one can gets dispersion relation $\omega^2 = c^2k^2+(2c/a)^2$ which means the cutoff frequency to be $2c/a$. As is well known, the exact cutoff value is $2.4048\cdots \times c/a$. This means suggests that our (8) may be correct within an error of 20%. It must be emphasized that our scheme does not include any artificial assumptions contradictory to physical processes, and that accuracy can be improved, if we pick up more higher order terms in expansion in eqs. (1)~(5).

The reduced 1D equations are solved numerically by newly developed algorithm of Higher order Implicit Difference Method (HIDM) which is a generalized scheme to solve system of equations with wide applicability, high accuracy and

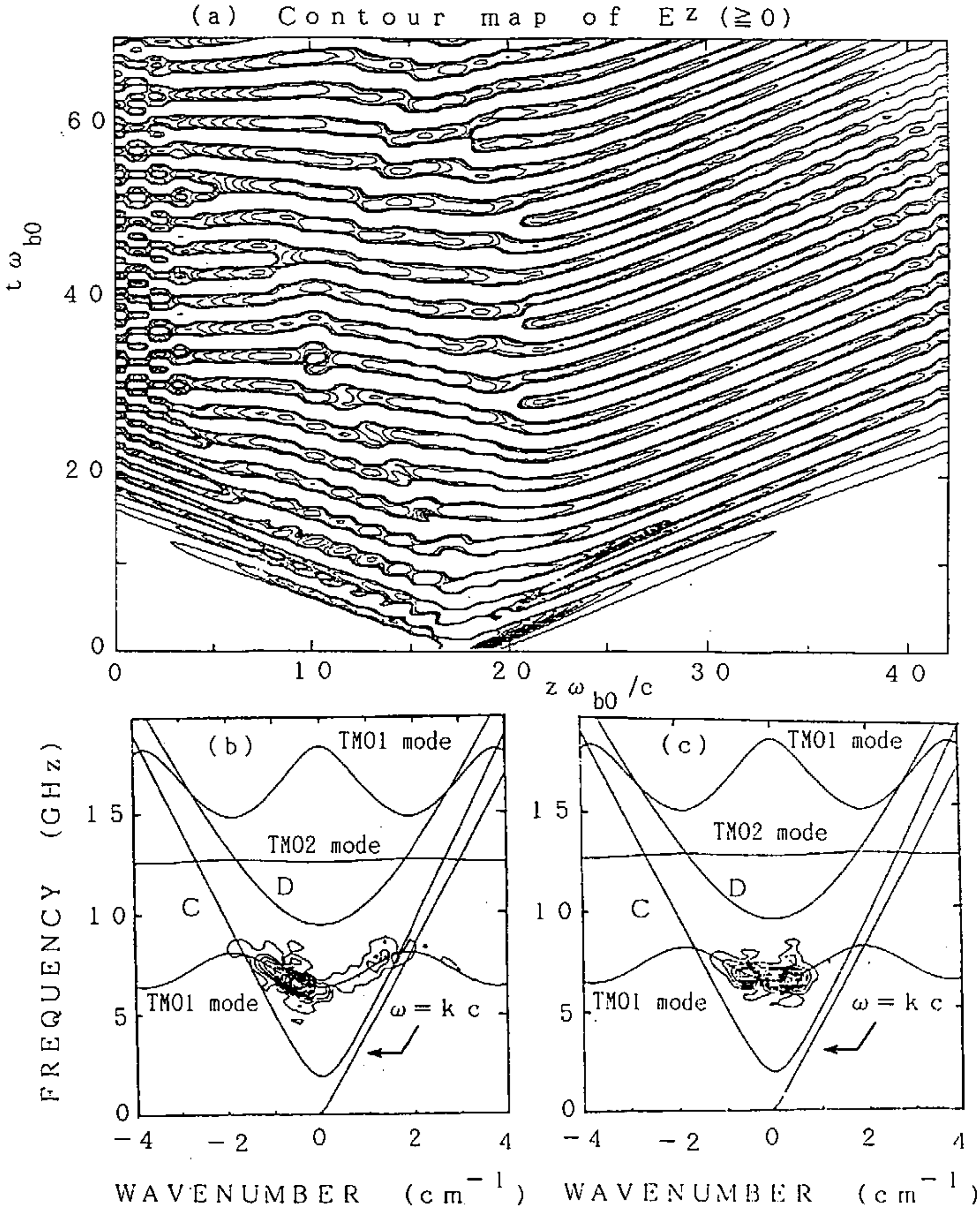

Fig. 2 (a) Spatial and temporal evolution of a localized initial disturbance for the slow wave structure shown in Fig. 1 without beam and plasma. (b) Fourier spectrum obtained from (a) at a period of $\omega_{b0}t$=20-60. (c) the same as (b) for $\omega_{b0}t$=100-140.

strong numerical stability.

The sizes of the plasma BWO used in the analysis are shown in Fig. 1, which has identical size to those in the experiments[2, 3]. The beam of 630 keV(v=0.9c) and density $n_{b0}=2\times10^{11}cm^{-3}$ is incidents from the left. At right end, a microwave absorber, expressed by appropriate C and R, minimize the reflection of output radiation. The beam and plasma densities can be assumed to change in radial direction, but in our scheme only the values on the axis are included in the computation as shown in (8). The beam is cold and the plasma temperature is 100eV. In real computation, terms with a small amount of viscosity are introduced to damp out the modes with short wavelength.

First, linear dispersion relation is checked in the case without beam and plasma. A highly localized Gaussian type disturbance of E_z is initially imposed at the exit of the slow wave structure, and spatial and temporal evolution of the fields are followed as shown in Fig. 2(a). Contour map of Fourier spectrum in frequency and wavenumber space is depicted in Fig. 2(b) for $\omega_{b0}t=20-60$ and (c) for $\omega_{b0}t=100-140$, respectively, in corrugated region. In these Figures, TM01 and TM02 modes are linear dispersion relations[6], when, in the latter, the average radius 1.445 cm is multiplied by a factor 1.202. It is shown in (b), that the contour lines coincides mainly with a linear dispersion relation of TM01 mode with negative group velocity. This results correspond to the early stage of propagation of disturbances exited at exit region (right hand side) of corrugation. In the later periods of (c), only components with small group velocity remain in the structure.

Figure 3 shows structure and time development of electromagnetic field exited by injected beam in backward wave oscillator. We found that in early stage, Fourier spectrum of exited wave is in good agreement with linear dispersion. When oscillation amplitude become large, sideband in frequency appear. Plasma electrons are gathered in nodal parts of corrugation of waveguide by ponderomotive force of exited electromagnetic wave. We found efficiency of BWO is large if injected beam is cold. When plasma electron density become large, for example, $n_{e0} \geq 5\times10^{11}\mathrm{cm}^{-3}$, strong coupling between injected electron beam and Trivelpiece-Gould mode appear.

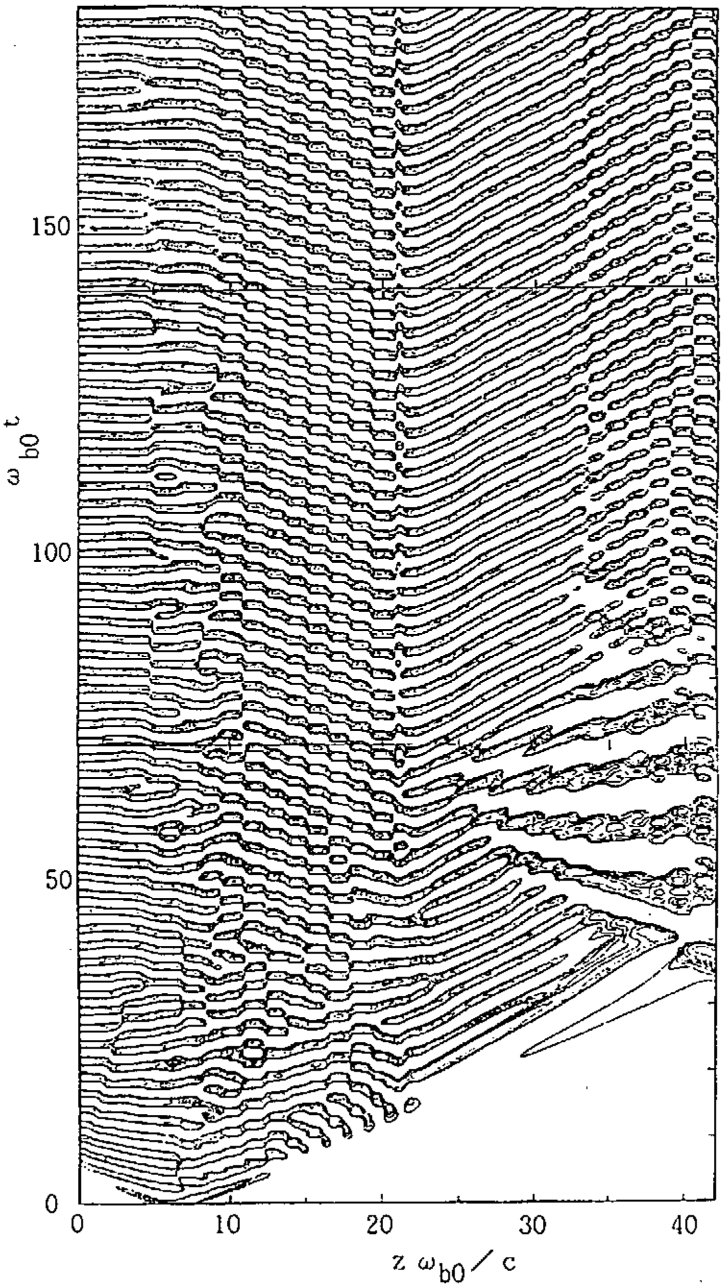

Fig. 3 Structure and time development of electromagnetic field exited in plasma filled backward wave oscillator. Contour map of $E_z(\geq0)$ is shown. $n_{b0}=2\times10^{11}\mathrm{cm}^{-3}$, $v_{b0}=0.9c$, $n_{e0}=5\times10^{9}\mathrm{cm}^{-3}$

References

[1] V. L. Granatstein and I. Alexeff, High-Power Microwave Sources (Altech House, Boston, 1987).

[2] K. Minami et. al., Appl. Phys. Lett. 53, 559 (1988).

[3] Y. Carmel et al., Phys. Rev. Lett. 62, 2389 (1989).

[4] A. T. Lin and L. Chen, Phys. Rev. Lett. 63, 2308 (1989).

[5] J. Swegle, J. W. Poukey and G. T. Leifeste, Phys. Fluids 28, 2882 (1985) and references therein.

[6] K. Minami et. al., IEEE Trans. P-S 18, 537.

MODE CONVERSION OF ALFVÉN WAVES INDUCED BY QUADRUPOLE MAGNETIC FIELD MODULATION

H.HOJO, M.INUTAKE, M.ICHIMURA AND S.MIYOSHI

Plasma Research Center, University of Tsukuba
Tsukuba 305, Japan

Abstract

A new type of the mode conversion of Alfvén waves in ICRF is presented, which is induced by the spatial modulation of a quadrupole magnetic field. It is shown that the physical mechanism is analogous to a resonant parametric mode coupling and the coupling coefficient depends on the ellipticity of the cross section of flux surface and vanishes when the magnetic field is axisymmetric.

Mode conversion of waves in a plasma is a important elementary process on plasma heating by waves. Recently a large number of theoretical studies on mode conversion have been done in the ion cyclotron range of frequency (ICRF) and in the electron cyclotron resonance heating (ECRH).

In this paper we present a new type of the mode conversion of Alfvén waves in ICRF[1]. We show here that one Alfvén mode can convert to another Alfvén mode due to the spatial modulation of a quadrupole magnetic field. We obtain coupled mode equations between two Alfvén waves via the spatial quadrupole field modulation. If we suppose the quadrupole magnetic field modulation as a 'virtual' mode, we can see that the conversion prcess is analogous to a resonant parametric mode coupling among two Alfvén and the virtual modes. The solutions of the coupled mode equations show that the efficient mode conversion takes place when a resonant condition with respect to an axial wavenumber among these modes is satisfied.

We now study the mode conversion of Alfvén waves propagating in a quadrupole magnetic field geometry. The basic equation to be analyzed is Maxwell's wave quation given by

$$\nabla \times \nabla \times \underline{E} - (\omega/c)^2 \underline{\underline{\varepsilon}}\,\underline{E} = 0 , \tag{1}$$

where $\underline{\underline{\varepsilon}}$ is the dielectric tensor of plasma, which is calculated from a cold plasma model. If we use the flux coordinates (ψ, θ, z), where the magnetic field is defined by $\underline{B} = B\underline{b} = \nabla\psi \times \nabla\theta$ and the wave electric field $\underline{E}$ is expressed in the covariant form as $\underline{E} = E_\psi \nabla\psi + E_\theta \nabla\theta + E_z \underline{b}$, we obtain

$$\frac{\partial}{\partial z}\left[\frac{|\nabla\psi|^2}{B}\frac{\partial E_\psi}{\partial z} + \frac{(\nabla\psi\cdot\nabla\theta)}{B}\frac{\partial E_\theta}{\partial z}\right] - B\frac{\partial}{\partial\theta}\left(\frac{\partial E_\theta}{\partial\psi} - \frac{\partial E_\psi}{\partial\theta}\right)$$
$$+ \left(\frac{\omega}{c}\right)^2 (S-1)\frac{|\nabla\psi|^2}{B}E_\psi + \left(\frac{\omega}{c}\right)^2\left[(S-1)\frac{(\nabla\psi\cdot\nabla\theta)}{B} - iD\right]E_\theta = 0\ , \tag{2}$$

$$\frac{\partial}{\partial z}\left[\frac{|\nabla\theta|^2}{B}\frac{\partial E_\theta}{\partial z} + \frac{(\nabla\psi\cdot\nabla\theta)}{B}\frac{\partial E_\psi}{\partial z}\right] + B\frac{\partial}{\partial\psi}\left(\frac{\partial E_\theta}{\partial\psi} - \frac{\partial E_\psi}{\partial\theta}\right)$$
$$+ \left(\frac{\omega}{c}\right)^2 (S-1)\frac{|\nabla\theta|^2}{B}E_\theta + \left(\frac{\omega}{c}\right)^2\left[(S-1)\frac{(\nabla\psi\cdot\nabla\theta)}{B} + iD\right]E_\psi = 0\ , \tag{3}$$

where S and D are given by

$$S = 1 - \sum_{i,e}\frac{\omega_p^{\,2}}{\omega^2 - \omega_c^{\,2}} = 1 + \frac{c^2}{V_A^{\,2}}\,\frac{1}{1-(\omega/\omega_{ci})^2}\ , \tag{4}$$

$$D = \sum_{i,e}\frac{\omega_c}{\omega}\,\frac{\omega_p^{\,2}}{\omega^2 - \omega_c^{\,2}} = -\frac{c^2}{V_A^{\,2}}\,\frac{1}{1-(\omega/\omega_{ci})^2}\ ,$$

ω_c being the cyclotron frequency, ω_p the plasma frequency and V_A the Alfvén velocity. E_z is neglected as $E_z \ll E_\psi,\ E_\theta$.

We express the magnetic field line by $x(z) = \sigma(z)x_0$ and $y(z) = \tau(z)y_0$, where (x_0, y_0) denotes the radial position at $z = z_0$ with a circular cross section of flux surface. The x_0 and y_0 are given by $x_0 = (2\psi/B_0)^{1/2}\cos\theta$ and $y_0 = (2\psi/B_0)^{1/2}\sin\theta$, respectively, and satisfy $x_0^{\,2} + y_0^{\,2} = r_0^{\,2} = = 2\psi/B_0$, where $B_0 = B(z_0)$. Then $|\nabla\psi|^2$, $|\nabla\theta|^2$ and $(\nabla\psi\cdot\nabla\theta)$ are expressed as

$$\begin{aligned}
|\nabla\psi|^2 &= (2\psi B_0)[h(z) + \alpha(z)\cos 2\theta]\ ,\\
|\nabla\theta|^2 &= (B_0/2\psi)[h(z) - \alpha(z)\cos 2\theta]\ ,\\
(\nabla\psi\cdot\nabla\theta) &= -B_0\alpha(z)\sin 2\theta\ ,
\end{aligned} \tag{5}$$

with

$$h(z) = (1/2)(1/\sigma^2 + 1/\tau^2)\ , \qquad \alpha(z) = (1/2)(1/\sigma^2 - 1/\tau^2).$$

We can see that the mode coupling with respect to the azimuthal mode number arises in Eqs.(2) and (3) due to the θ − dependence of $|\nabla\psi|^2$, $|\nabla\theta|^2$ and $(\nabla\psi\cdot\nabla\theta)$. That is, a mode with mode number m couples to modes with $m \pm 2$ through the quadrupole field component with mode ± 2.

We here restrict to study one-dimensional wave propagation along the field line. If we define X_m and Y_m by

$$X_m = E_\theta(m) - 2i\psi E_\phi(m) \;, \qquad Y_m = -E_\theta(m) - 2i\psi E_\phi(m) \;, \tag{6}$$

where $E_\phi(m)$ and $E_\theta(m)$ are the Fourier components of E_ϕ and E_θ, respectively. X_m and Y_m describe left-hand and right-hand circularly polarized wave compoments, respectively and are governed by

$$\frac{d}{dz}[p\frac{d}{dz}X_m] + k_S{}^2 X_m + \frac{d}{dz}[2\beta\frac{d}{dz}Y_{m+2}] + 2\beta k_T{}^2 Y_{m+2} = 0 \;, \tag{7}$$

$$\frac{d}{dz}[p\frac{d}{dz}Y_m] + k_F{}^2 Y_m + \frac{d}{dz}[2\beta\frac{d}{dz}X_{m-2}] + 2\beta k_T{}^2 X_{m-2} = 0 \;, \tag{8}$$

with $\Theta = \tau / \sigma$ and

$$\begin{aligned}
&p(z) = h(z)[B_0/B(z)] = (\Theta + 1/\Theta)/2 \;, \\
&2\beta(z) = \alpha(z)[B_0/B(z)] = (\Theta - 1/\Theta)/2 \;, \\
&k_S{}^2 = (\omega/V_A)^2(p + \omega/\omega_{ci})/[1 - (\omega/\omega_{ci})^2] \;, \\
&k_F{}^2 = (\omega/V_A)^2(p - \omega/\omega_{ci})/[1 - (\omega/\omega_{ci})^2] \;, \\
&k_T{}^2 = (\omega/V_A)^2/[1 - (\omega/\omega_{ci})^2] \;.
\end{aligned} \tag{9}$$

Equations (7) and (8) are coupled mode equations between X_m and Y_{m+2} (or, X_{m-2} and Y_m). If the magnetic field is axisymmetric, the coupling coefficient β, which depends on the ellipticity of the cross section of flux surface, vanishes since $\Theta = 1$ ($\sigma = \tau$) and then X_m and Y_{m+2} decouple each other.

As a model of the magnetic field, we consider a periodic quadrupole field mirror described by $\sigma(z) = 1 - \varepsilon\cos(k_0 z)$ and $\tau(z) = 1 + \varepsilon\cos(k_0 z)$ with $\varepsilon \ll 1$ and k_0 being a wavenumber characterizing the spatial modulation of the quadrupole magnetic field. We see that the slow wave of $m = -1$ being left-hand polarized is described by X_{-1} ($= X$) and the fast wave of $m = +1$ being right-hand polarized by Y_{+1} ($= Y$). In this case, Eqs.(7) and (8) with Eq.(9) are reduced to

$$[\frac{d^2}{dz^2} + k_S{}^2]X + 2\varepsilon\{\frac{d}{dz}[\cos(k_0 z)\frac{dY}{dz}] + k_T{}^2\cos(k_0 z)Y\} = 0 \;, \tag{10}$$

$$[\frac{d^2}{dz^2} + k_F{}^2]Y + 2\varepsilon\{\frac{d}{dz}[\cos(k_0 z)\frac{dX}{dz}] + k_T{}^2\cos(k_0 z)X\} = 0 \;. \tag{11}$$

These equations are analogous to parametric coupled mode equations[2], if we suppose the spatial modulation of the quadrupole magnetic field as a 'virtual' wave with zero frequency and axial wavenumber k_0.

Fourier-analyzing Eqs.(10) and (11) and also assuming the resonant condition given by $k_0 = k_S - k_F$, we obtain approximately the propagating coupled solutions as follows:

$$Y = Y_0 \cos(\Delta z) \exp(i k_F z) \ , \qquad (12)$$

$$X = (k_F / k_S) Y_0 \sin(\Delta z) \exp(i k_S z) \ , \qquad (13)$$

with

$$\Delta = \varepsilon\, (k_T{}^2 - k_F k_S)^{1/2} / 2 (k_F k_S)^{1/2} \ , \qquad (14)$$

where Y_0 is the wave amplitude of the fast wave in the absence of the slow wave. The slow(fast) wave amplitude increases when the fast(slow) wave amplitude decreases. Then we can see that these solutions express the mode conversion between the fast and slow waves, satisfying the following conservation relation:

$$k_F |Y_0|^2 = k_F |Y|^2 + k_S |X|^2 \ , \qquad (15)$$

which is analogous to the Manley-Rowe relation.

We have observed the polarization reversal of Alfvén waves in the recent GAMMA 10 experiment[3]. In the experiment, the fast wave with $m = +1$, which is observed to be right-hand polarized in a core region, is excited in the axisymmetric central cell. The wave field observed in the anchor cell with a quadrupole magnetic field is left-hand polarized in the core region and heating of the anchor-cell ions is also observed, which is due to the ion cyclotron resonance. Therefore, the wave observed in the anchor cell is considered to be the slow wave with $m = -1$.

As another interesting case, we briefly discuss the case of $k_0 = k_S + k_F$. In this case, we find that the eigenvalue the of axial wavenumber obtained from Eqs.(10) and (11) becomes complex. This shows that the Alfvén wave can not propagate in the quadrupole mirror field with the spatial modulation of $k_0 = k_S + k_F$. The complex eigenvalue of the wavenumber just corresponds to the exsistence of a forbidden energy band in solid state physics.

In conclusion, we presented a new type of Alfvén mode conversion due to the spatial modulation of the quadrupole field in ICRF. The mechanism of the mode conversion is analogous to the resonant parametric mode coupling. The present model of the mode conversion can resonably explains the experiment results on the polarization reversal of Alfvén waves in GAMMA 10.

This work was partially supported by a Grant-in-Aid for Scientific Research from the Ministry of Education, Science and Culture.

References

[1] H.Hojo, et al.: submitted to Phys. Rev. Lett.
[2] K.Nishikawa: J. Phys. Soc. Jpn. 24 (1968) 916, 1152.
[3] M.Inutake, et al.: submitted to Phys. Rev. Lett.

NUMERICAL SIMULATION OF POTENTIAL-DRIVEN ION CYCLOTRON OSCILLATION

S. Ishiguro, K. Nakagawa and N. Sato
Department of Electronic Engineering, Tohoku University,
Sendai 980, Japan

Abstract

Using two-dimensional electrostatic particle simulation code, we study the ion cyclotron oscillation driven by applying a positive potential to a small electrode in a magnetized plasma. It is confirmed that a direct plasma response to a two-dimensional potential structure is essential.

Electrostatic ion cyclotron oscillations are typically observed in magnetized plasmas in both space and laboratory. D'Angelo and Motly$^{1)}$ reported the first clear-cut observation of electrostatic ion cyclotron oscillations in a laboratory plasma. The oscillations are induced by applying a positive potential to the small electrode immersed in a single ended Q-machine with uniform magnetic field. An electric current is generated along the mgnetic field under this configuration and the oscillations are therefore considered to be caused by the current driven electrostatic ion cyclotron instability predicted by Drummond and Rosenbluth.$^{2)}$

On the other hand, Hatakeyama *et al.*$^{3)}$ made mesurements on the ion cyclotron oscillation in nonuniform magnetic fields under the similar expermental configuration to that of ref. 1. The oscillation frequency observed is around the ion cyclotron frequency defined by a local magnetic field at the position of the electrode biased positively to drive the oscilation. This result is not consistent with the current driven model. Hatakeyama and Sato pointed out that the two-dimensional potential structure near the electrode could be essential in the generation of the oscillations and they poposed the mechanism of 'two-dimensional potential driven oscillations' on the basis of further detailed mesurements.$^{4,5)}$ In this paper we present the numerical simulation of the electrosatic ion cyclotron oscillation driven by applying a positive potential to the small electrode in a magnetized plasma.

A two-dimensional magnetized electrostatic particle simulation code is employed. The simulation model is schematically shown in Fig. 1. A uniform external magnetic field $\vec{B}_0$ is pointing in the positive x-direction. We assume that a plasma reservoir are placed $x \geq L_x$ and plasma particles are continuously injected from the region $x = L_x$ and $0.2L_y \leq y \leq 0.8L_y$ into the simulation system with half-Maxwellian in v_x and full-Maxwellian in v_x and v_y. At $y = 0$, $y = L_y$ and $x = L_x$ electric potential $\phi(x, y = 0) = \phi(x, y = L_y) = 0$ and $\phi(x = L_x, y) = 0$. Initially the potential of the collecter which is placed at $x = 0$ is set negative $\phi = \phi_0 = -2.3T_0/e < 0$. After plasma particles fill the simulation system, a positive potential $\phi_a = 40T_0/e$ is started to be applied in the center of the collector with width $L_a = 64\Delta$. The parameters of simulation are following: a 256×256 spatial grid, the ion to electron mass ratio $m_i/m_e = 100$, $\omega_{ce}/\omega_{pe0} = 0.5$ where ω_{ce} is the electron gyrofrequency, $\omega_{ce} = |e|B/m_e c$

and ω_{pe0} is the plasma reservoir electron plasma frequency, $\omega_{pe0} = (4\pi n_0 e^2/m_e)^{1/2}$, the ion Larmor radius $r_{Li} = 20\Delta$ where Δ is the grid size. The Debye length of the plasma reservoir λ_{De0} is taken equal to the grid size.

At first we present the time development of the potential structure about one-cycle of the oscillation in Fig. 2(a). It is observed that the electric potential in front of the electrode oscillates. The potential at $x \sim 25\Delta$ and $y \sim 128\Delta = L_y/2$ increases from $\omega_{pe0}t = 9000$ to 9300, decreases from 9300 to 9500, and increases from 9400 to 9700. It is interestingly observed that the potential dip is created at $\omega_{pe0}t = 9500$. As shown in Fig. 2(b), the electric current oscillation is synchronized with the variation of the potential profile. Next, let us see the time variation of the potential structure in detail with the model of the potential driven ion-cyclotron oscillation$^{4)}$ in mind. We show a cut at $x = 64\Delta$ in Fig. 3(a) and the cut through the center of the system at $y = 128\Delta$ in Fig. 3(b). Potential slopes in the y-direction from the center of the system to the edge are observed from $\omega_{pe0}t = 9100$ to $\omega_{pe0}t = 9300$. The magnitude of the potential peak is about $3T_0/e$ and the width of the slope is about 15Δ. Since the gyroradius of the ions is larger than the scale length of the transverse E_y field, they can move across the magnetic field lines. Thus the ions in front of the electrode are accelerated in the y-direction away from the center of the system. An electron rich region thereby is formed. As a result, a negative potential dip is created, as observed at $\omega_{pe0}t = 9500$ in Fig. 3(b). Its depth is about $2T_0/e$. It limits the electron flow along the magnetic field, and thus the electric current is decreased. The ions return to the central region after the ion cyclotron period. The negative potential region thereby disappers. The electron flow along the magnetic field increases, and the current channel is formed. This results in the increase of the potential there.

Finally we show the macroscopic ion flow pattern at $\omega_{pe0}t = 9300$ and $\omega_{pe0}t = 9500$ in Fig. 4. Flows of ions in the y-direction away from the central region are observed at $\omega_{pe0}t = 9300$. On the contrary flows of ions in the y-direction into the center of the system are observed at $\omega_{pe0}t = 9500$. These results is consistent with previous explanation of the oscillation.

In conclusion, the potential driven oscillation with frequency around the ion cyclotron frequency is driven by applying a large positive potential to the electrode. The ion motion across the magnetic field is synchronized with the electron motion along the magnetic field through the two-dimensional potential structure.

References

1) N. D'Angelo and R. W. Montley: Phys. Fluids **5** (1962) 633; R. W. Montley and N. D'Angelo: Phys. Fluids **6** (1963) 296.
2) W. E. Drummond and M. N. Rosenbluth: Phys. Fluids **5** (1962) 1507.
3) R. Hatakeyama, N. Sato, H. Sugai and Y. Hatta: Phys. Lett. **63A** (1977) 28 and Plasma Phys. **22** (1980) 25; N. Sato: *Proc. 1980 Int. Conf. on Plasma Physics Nagoya, 1980* (Fusion Research Association of Japan, Nagoya, 1980) Vol. II, p.138.
4) N. Sato and R. Hatakeyama: J. Phys. Soc. Jpn. **54** (1985) 1661.
5) R. Hatakeyama and N. Sato: Jpn. J. Appl. Phys. **24** (1985) L285.

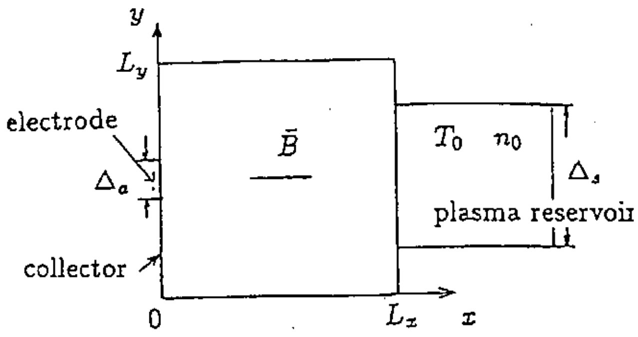

Fig. 1. Sketch of the simulation model.

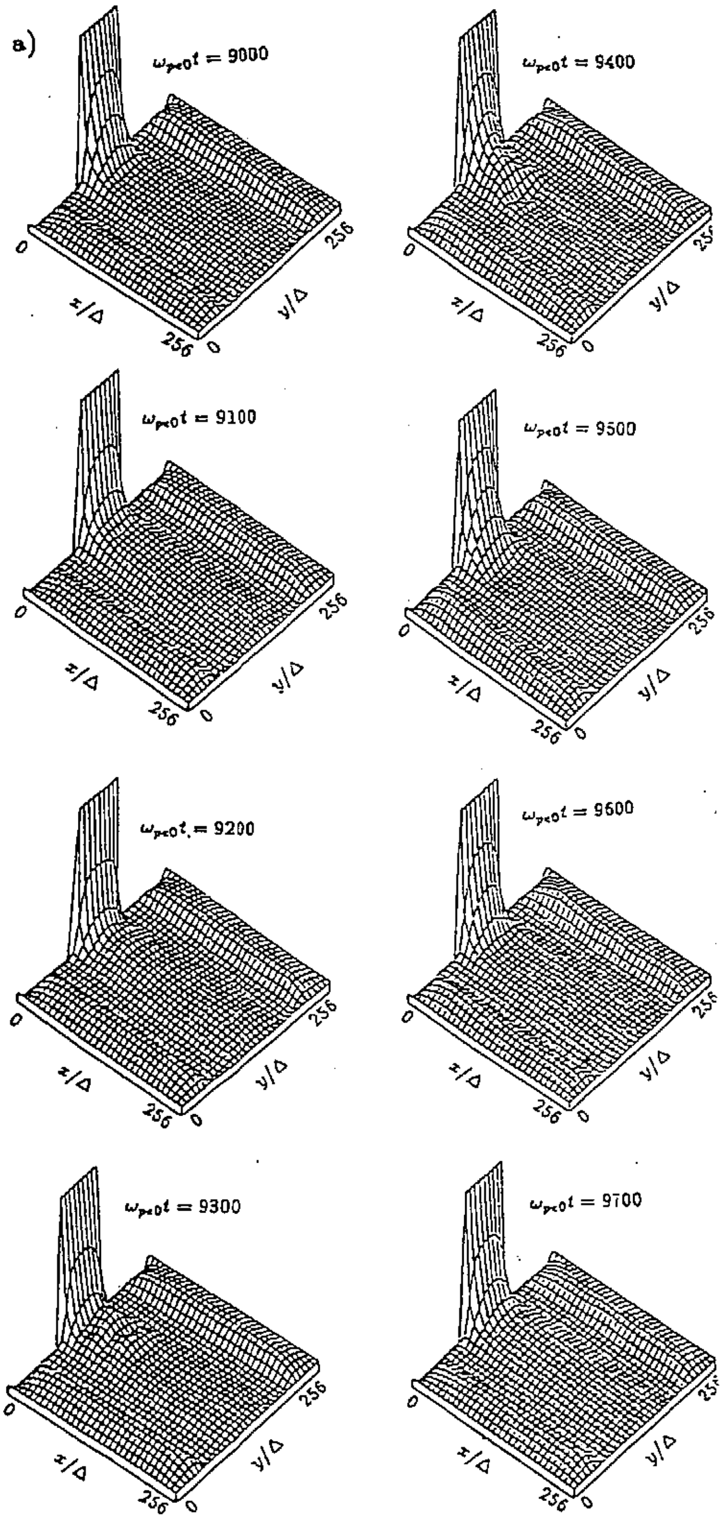

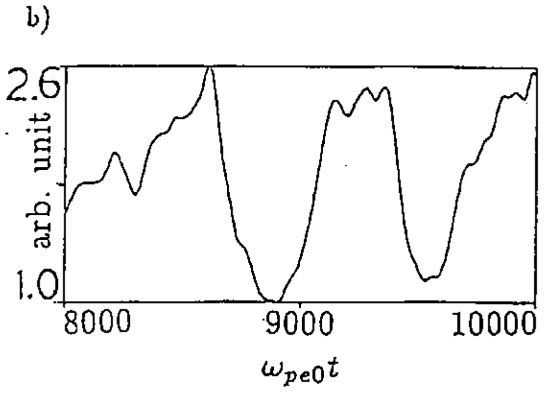

Fig. 2. Time development of the potential structure(a). Time development of the electric current along the magnetic field(b).

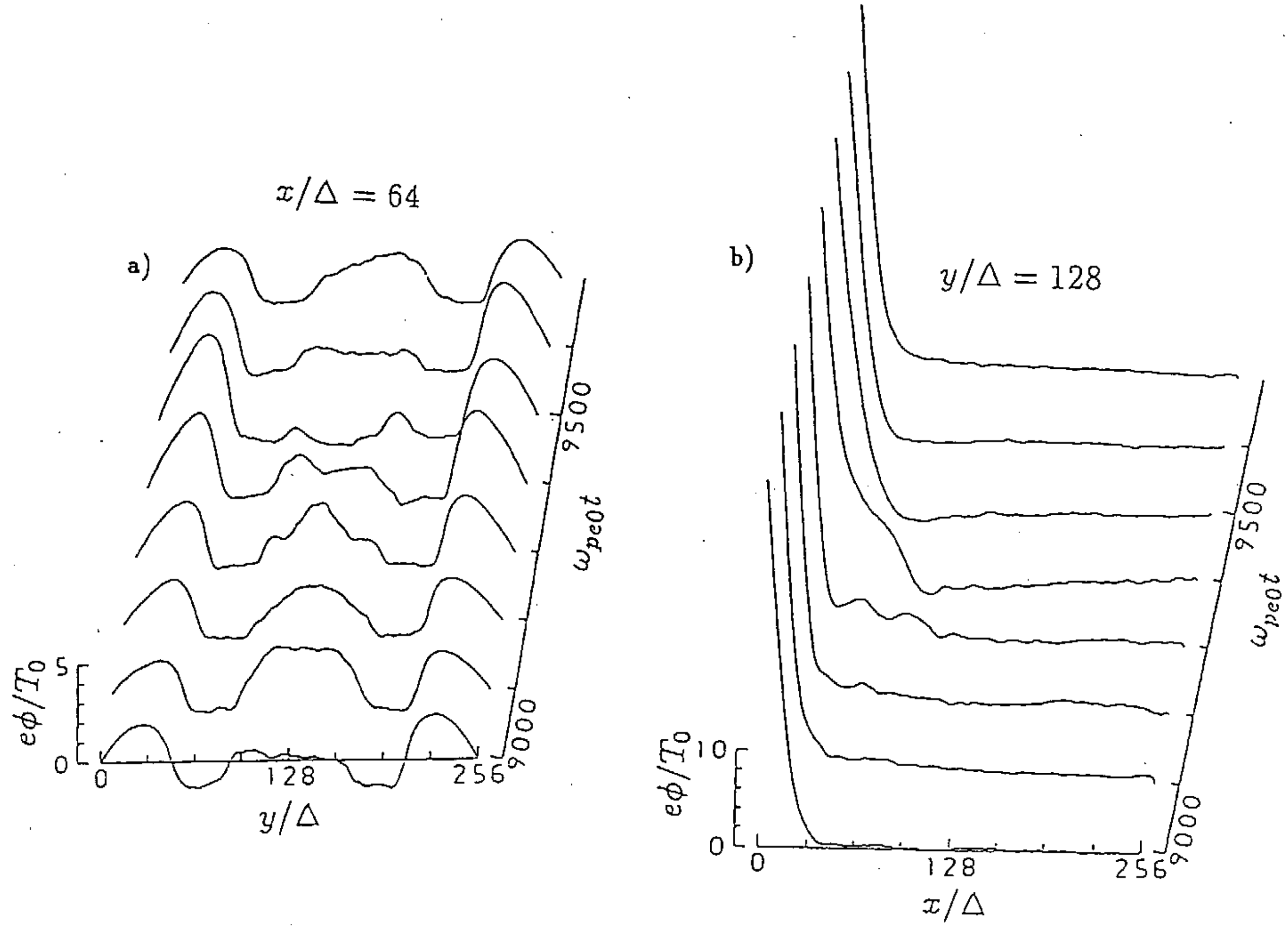

Fig. 3. Time development of the potential profile $\phi(x = 64\Delta, y)$(a), and $\phi(x, y = 128\Delta)$(b).

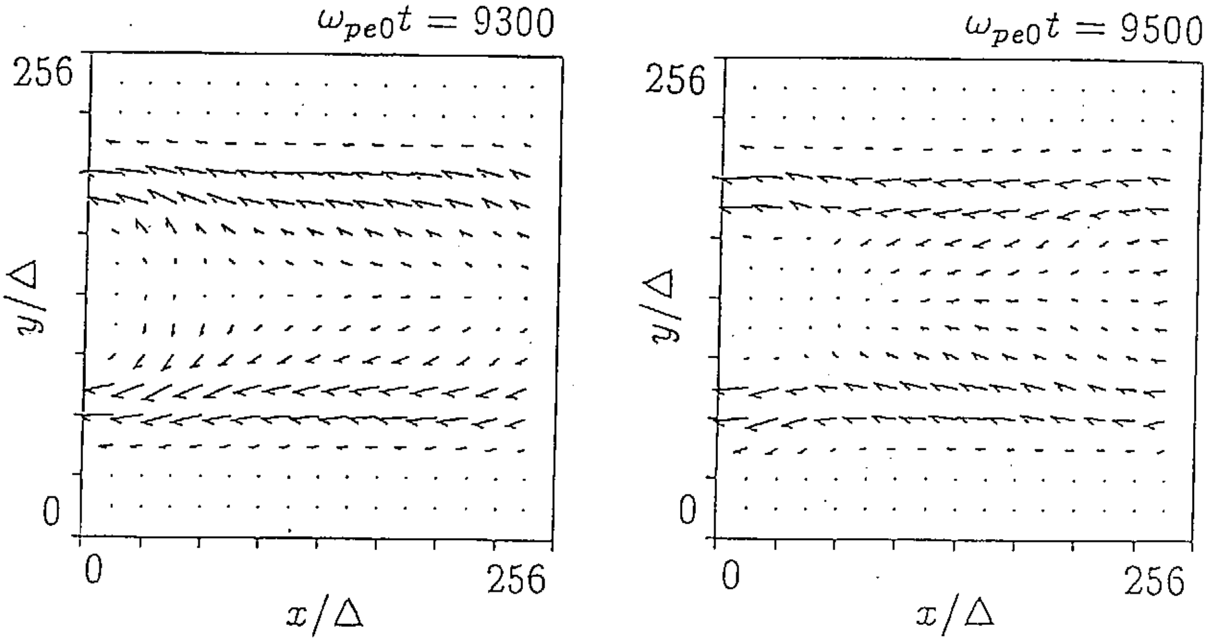

Fig. 4. Macroscopic ion flow pattern.

DYNAMICS OF INTERFACES WITH INTERNAL STRUCTURES

Toshihiro Kawakatsu and Kyozi Kawasaki

Department of Physics, Kyushu University 33, Fukuoka 812, Japan.

ABSTRACT We develop computer simulation methods dealing with dynamical models for interfaces (or discontinuities) having internal structures, where for instance, other particles are attracted to the discontinuities.

It is well known that topological defects, such as interfaces, play an important role in the dynamics of nonlinear systems [1,2]. For example, let us consider the so-called time dependent Ginzburg-Landau (TDGL) equation, which is a simple model to describe the temporal evolution of phase separation processes in binary fluid mixtures. In the late stage of the phase separation process, the system becomes to be divided into many domains separated by interfaces. At this stage, the time evolution of the system is practically dominated by the motion of these interfaces. In the last decade, there have been extensive investigations on the dynamics of such topological defects, which have brought us to considerable understanding of many nonlinear phenomena. Compared to these successful understandings of the simple model for the phase separation processes, little is known about more complex systems, where the topological defects have internal structures. In this report, we consider the dynamics of such complex topological defects [3].

As an example, we investigate the dynamics of interfaces between two immiscible phases, onto which other particles are adsorbed [4-6]. Particles which can easily be adsorbed to interfaces, are generally called as surfactants. We can easily find examples of surfactants in the biochemical and the engineering fields. Although we cannot find a direct counterpart of the surfactant in the field of plasma physics at present, it should be important to investigate mathematical aspects of surfactants in order to understand the nature of interfaces in nonlinear systems. The most important character of the surfactants is its amphiphilic nature. Let us consider surfactant particles in an AB immiscible binary fluid mixture. The amphiphilic nature of the surfactant originates from the fact that the surfactant particle has two distinct parts, one part likes A phase and the other part likes B phase, and therefore the surfactant particles are easily adsorbed onto interfaces between these two phases. Such an internal structure of the surfactant particle is similar to an electric dipole, and therefore it can be regarded as a particle with spin.

We have proposed a mathematical model of surfactant particles in a binary fluid mixture, which retains essential features of the surfactant. Our model is a combination of a continuous scalar field and discrete particles with spins. The former describes the immiscible binary fluid mixture and the latter corresponds to surfactant particles. Our model is, therefore, a hybrid model. We assume TDGL equation for the temporal evolution of the scalar field and also assume purely dissipative equations of motion (Aristotle's equations of motion) for the surfactant particles. We solve this set of equations of motion numerically with the use of the finite-difference method and the molecular dynamics method. Our method is, therefore, similar to the technique of particle-particle particle-mesh

(PPPM) method, which is a well-known technique for computer simulations of dense plasmas [7].

Computer simulations on the phase separation processes of a binary fluid mixture containing surfactant particles have been performed. It has been proved by these simulations that the dynamics of phase separation processes is changed considerably. In Fig.1, we show a typical example of the phase separation processes. By comparing the case without surfactant particles, we have observed a quick phase separation in the early stage and a slowing down of the coarsening in the late stage [5,6]. Both of these two features can qualitatively be explained by a simple theoretical analysis, which shows that these features are common to all the systems containing surfactant particles.

In summary, we presented a model, which is convenient to study the dynamics of systems containing surfactant particles both analytically and numerically. We have shown that the surfactant particles have an important role in the phase separation processes. Such features should be utilized in controlling the phase separation processes in immiscible fluids.

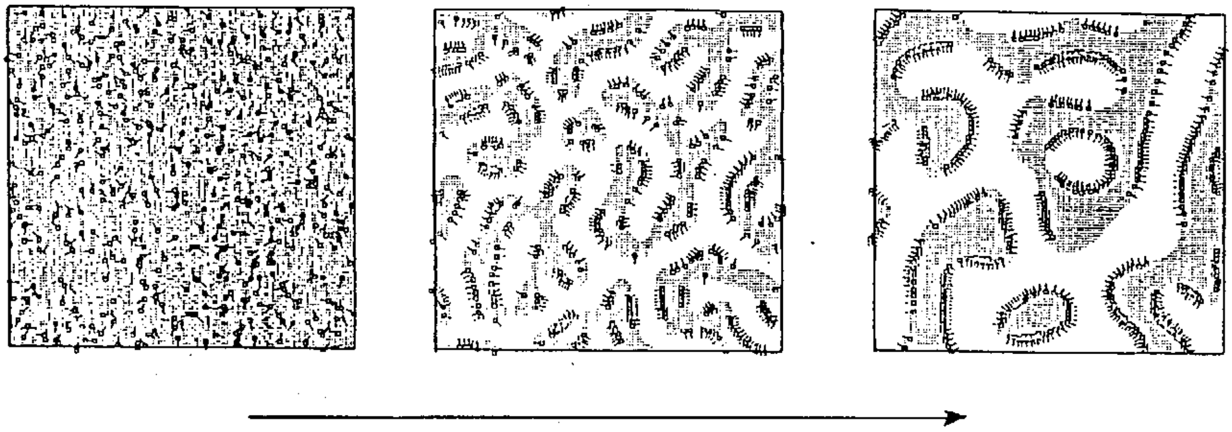

Fig.1 An example of the phase separation processes is shown. Shaded regions and white regions show A-domains and B-domains, respectively, and the small particles show surfactant particles.

References

1) K.Kawasaki and T.Ohta; Physica 116A (1982) 573.
2) K.Kawasaki; Ann. Phys. 154 (1984) 319.
3) Physics of Complex and Supermolecular Fluids; eds. S.Safran and N.Clark, (Wiley, New York, 1987).
4) K.Kawasaki and T.Kawakatsu; Physica 164A (1990) 549.
5) T.Kawakatsu and K.Kawasaki; Physica 167A (1990) 690.
6) T.Kawakatsu and K.Kawasaki; to be published in Molecular Dynamics Simulations, Proceedings of the Taniguchi Symposium, ed. F.Yonezawa, (Springer,1991).
7) J.W.Eastwood, R.W.Hockney and D.Lawrence; Comput. Phys. Commun. 19 (1980) 215.

Nonlinear equations for weakly unstable modes

N.Nakajima, National Institute for Fusion Science

For some interesting nonlinear systems, the eigenvalue in the linearized system is degenerate, i.e, there are a number of eigenfunctions for a single eigenvalue. For a nondegenerate case, two types of nonlinear equations are derived by applying the perturbation theory to weakly unstable modes near the marginally stable states together with the multiple-time-scale expansion[1,2]. This method is extended to degenerate cases.

Consider the following nonlinear system of equations:

$$\overleftrightarrow{\mathcal{L}}\vec{u} + \vec{N}(\vec{u},\vec{u}) = 0, \tag{1}$$

where $\overleftrightarrow{\mathcal{L}}$ and $\vec{N}(\vec{u},\vec{u})$ are a linear and a nonlinear operator, respectively. Introducing an ordering parameter λ we expand $\vec{u}$ and a characteristic parameter in the system p as follows:

$$\begin{aligned} \vec{u} &= \sum_{j=1} \lambda^j \vec{u}_j, & (2)\\ p &= p_c \pm \lambda^2, & (3) \end{aligned}$$

where $\vec{u}_j$ is a real function and we assume that p_c corresponds to the marginally stable state. The marginally stable state is defined as the situation where the imaginally part of the eigenvalue ω (frequency of the linear mode) vanishes, i.e., Im(ω_c) = 0. When p is specified so that p indicates the situation of the system to be considered the ordering parameter λ is determined from Eq.(3).

Using the multiple-time-expansion

$$\begin{aligned} &\tau_1 = \lambda t, \tau_2 = \lambda^2 t, \cdots, \tau_j = \lambda^j t, \cdots, \\ &\frac{\partial}{\partial t} = \frac{\partial}{\partial \tau_0} + \lambda\frac{\partial}{\partial \tau_1} + \lambda^2\frac{\partial}{\partial \tau_2} + \cdots \end{aligned} \tag{4}$$

and expanding the linear term $\lambda\vec{\phi}_1(i\frac{\partial}{\partial t}, p; x) \equiv \overleftrightarrow{\mathcal{L}}\lambda\vec{u}_1$, we have the following expanded form :

$$\lambda\vec{\phi}_1(i\frac{\partial}{\partial t}, p; x)$$

$$\begin{aligned} &= \lambda\vec{\phi}_1(\omega_c,p_c;x) \\ &\quad +i\lambda^2\frac{\partial}{\partial\tau_1}\frac{\partial}{\partial\omega}\vec{\phi}_1(\omega_c,p_c;x) \\ &\quad +\lambda^3\{\frac{\partial}{\partial\tau_2}\frac{\partial}{\partial\omega}\vec{\phi}_1(\omega_c,p_c;x)-\frac{1}{2}\frac{\partial^2}{\partial\tau_1^2}\frac{\partial^2}{\partial\omega^2}\vec{\phi}_1(\omega_c,p_c;x)\pm\frac{\partial}{\partial p}\vec{\phi}_1(\omega_c,p_c;x)\} \\ &\quad +\cdots. \end{aligned} \tag{5}$$

Substitution of Eqs.(2) and (5) into Eq.(1) gives the following equations for each order of λ :

λ - order

$$\overleftrightarrow{\mathcal{L}}(\omega_c,p_c;x)\vec{u}_1(\omega_c,p_c;x)=0, \tag{6}$$

λ^2 - order

$$\begin{aligned} &\overleftrightarrow{\mathcal{L}}(\frac{\partial}{\partial\tau_0},p_c;x)\vec{u}_2+i\frac{\partial}{\partial\tau_1}\frac{\partial}{\partial\omega}\{\overleftrightarrow{\mathcal{L}}(\omega_c,p_c;x)\vec{u}_1(\omega_c,p_c;x)\} \\ &+\vec{N}(\vec{u}_1(\omega_c,p_c;x),\vec{u}_1(\omega_c,p_c;x))=0, \end{aligned} \tag{7}$$

λ^3 - order

$$\begin{aligned} &\overleftrightarrow{\mathcal{L}}(\frac{\partial}{\partial\tau_0},p_c;x)\vec{u}_3+i\frac{\partial}{\partial\tau_1}\frac{\partial}{\partial\omega}\{\overleftrightarrow{\mathcal{L}}(\frac{\partial}{\partial\tau_0},p_c;x)\vec{u}_2\} \\ &+i\frac{\partial}{\partial\tau_2}\frac{\partial}{\partial\omega}\{\overleftrightarrow{\mathcal{L}}(\omega_c,p_c;x)\vec{u}_1(\omega_c,p_c;x)\}-\frac{1}{2}\frac{\partial^2}{\partial\tau_1^2}\frac{\partial^2}{\partial\omega^2}\{\overleftrightarrow{\mathcal{L}}(\omega_c,p_c;x)\vec{u}_1(\omega_c,p_c;x)\} \\ &\pm\frac{\partial}{\partial p}\{\overleftrightarrow{\mathcal{L}}(\omega_c,p_c;x)\vec{u}_1(\omega_c,p_c;x)\} \\ &+\vec{N}(\vec{u}_1(\omega_c,p_c;x),\vec{u}_2)+\vec{N}(\vec{u}_2,\vec{u}_1(\omega_c,p_c;x))=0. \end{aligned} \tag{8}$$

As p_c is determined to correspond to the marginally stable state, the linear equation (6) gives the eigenfunction at the marginally stable state. Also, the linearized system is degenerate so that the eigenfunction $\vec{u}_1$ is written as follows:

$$\vec{u}_1=\sum_n\vec{u}_{1n}. \tag{9}$$

Introducing the complex eigenfunction $\vec{\varphi}_n$ and the complex coeficient A_n, we put $\vec{u}_{1n}$ as follows:

$$\vec{u}_{1n}=A_n\vec{\varphi}_n+A_n^*\vec{\varphi}_n^*,\quad \overleftrightarrow{\mathcal{L}}\vec{\varphi}_n(\omega_c,p_c;x)=0,\quad A_n=A_n(\tau_1,\tau_2,\cdots), \tag{10}$$

where complex eigenfunction $\vec{\varphi}_n$ has the same eigenvalue ω_c not depending on n and we assume complex coefficient A_n is dependent on the multiple-time scale.

From the solvability condition of the λ^2 - order equation, following conditions on the coefficients A_n are obtained :

$$\frac{\partial A_n}{\partial \tau_1} = 0 \quad \text{for} \quad < \frac{\partial}{\partial \omega}\{\overset{\leftrightarrow}{\mathcal{L}}(\omega_c, p_c; x)\vec{\varphi}_n(\omega_c, p_c; x)\}, \vec{\varphi}_n^{\dagger} > \neq 0, \tag{11}$$

$$\frac{\partial A_n}{\partial \tau_1} \neq 0 \quad \text{for} \quad < \frac{\partial}{\partial \omega}\{\overset{\leftrightarrow}{\mathcal{L}}(\omega_c, p_c; x)\vec{\varphi}_n(\omega_c, p_c; x)\}, \vec{\varphi}_n^{\dagger} >= 0. \tag{12}$$

And the solution of the second order equation is given by

$$\vec{u}_2 = \sum_n \vec{u}_{2n}, \tag{13}$$

$$\vec{u}_{2n} = \sum_j A_j A_{n+j}^* \vec{\varphi}_{20,j,n+j} + C.C. + \sum_j A_j A_{n-j} \vec{\varphi}_{22,j,n-j} + C.C. \tag{14}$$

Using above results and the solvability condition of the λ^3 - order equation, we have the two types of nonlinear equations as follows:

CASE 1)

$$d_0 \frac{\partial A_n}{\partial \tau_2} \pm d_1 A_n + \sum_l \sum_m d_{3lmn} A_l A_m^* A_{m-l+n} = 0 \tag{15}$$

for $< \frac{\partial}{\partial \omega}\{\overset{\leftrightarrow}{\mathcal{L}}(\omega_c, p_c; x)\vec{\varphi}_n(\omega_c, p_c; x)\}, \vec{\varphi}_n^{\dagger} > \neq 0$, where

$$d_0 = i < \frac{\partial}{\partial \omega}\{\overset{\leftrightarrow}{\mathcal{L}}(\omega_c, p_c; x)\vec{\varphi}_n(\omega_c, p_c; x)\}, \vec{\varphi}_n^{\dagger}(\omega_c, p_c; x)\} >, \tag{16}$$

$$d_1 = < \frac{\partial}{\partial p}\{\overset{\leftrightarrow}{\mathcal{L}}(\omega_c, p_c; x)\vec{\varphi}_n(\omega_c, p_c; x)\}, \vec{\varphi}_n^{\dagger}(\omega_c, p_c; x)\} >, \tag{17}$$

$$d_{3lmn} = < \vec{N}(\vec{\varphi}_l, \vec{\varphi}_{20,m,m-l+n}^*) + \vec{N}(\vec{\varphi}_m, \vec{\varphi}_{22,l,m-l+n}) \tag{18}$$

$$+ \quad \vec{N}(\vec{\varphi}_{20,m,m-l+n}^*, \vec{\varphi}_l) + \vec{N}(\vec{\varphi}_{22,l,m-l+n}, \vec{\varphi}_m), \vec{\varphi}_n^{\dagger}(\omega_c, p_c; x)\} > . \tag{19}$$

Note that $\vec{\varphi}_n^{\dagger}$ is the adjoint solution. Using the original variables : $\frac{\partial}{\partial t} = \lambda^2 \frac{\partial}{\partial \tau_2}$, $\mathcal{A}_n = \lambda A_n$ Eq.(15) becomes

$$d_0 \frac{d\mathcal{A}_n}{dt} + (p - p_c) d_1 \mathcal{A}_n + \sum_l \sum_m d_{3lmn} \mathcal{A}_l \mathcal{A}_m^* \mathcal{A}_{m-l+n} = 0. \tag{20}$$

If the eigenvalue of the linear equation is nondegenerate, Eq.(20) reduces to

$$d_0 \frac{d\mathcal{A}}{dt} + (p - p_c) d_1 \mathcal{A} + d_3 \mid \mathcal{A} \mid^2 \mathcal{A} = 0 \tag{21}$$

This is a Landau equation well known in fluid dynamics. This situation corresponds to global resistive MHD modes (nondegenerate) and to micro-instabilities (nondegenerate or degenerate).

CASE 2)

$$c_0 \frac{\partial^2 A_n}{\partial \tau_1^2} \pm c_1 A_n + \sum_l \sum_m c_{3lmn} A_l A_m^* A_{m-l+n} = 0 \tag{22}$$

for $< \frac{\partial}{\partial \omega}\{\overleftrightarrow{\mathcal{L}}(\omega_c, p_c; x)\vec{\varphi}_n(\omega_c, p_c; x)\}, \vec{\varphi}_n^\dagger >= 0$, where

$$\begin{aligned}
c_0 &= i < \frac{1}{2}\frac{\partial^2}{\partial \omega^2}\{\overleftrightarrow{\mathcal{L}}(\omega_c, p_c; x)\vec{\varphi}_n(\omega_c, p_c; x)\}, \vec{\varphi}_n^\dagger(\omega_c, p_c; x)\} >, &(23)\\
c_1 &= < \frac{\partial}{\partial p}\{\overleftrightarrow{\mathcal{L}}(\omega_c, p_c; x)\vec{\varphi}_n(\omega_c, p_c; x)\}, \vec{\varphi}_n^\dagger(\omega_c, p_c; x)\} >, &(24)\\
c_{3lmn} &= < \vec{N}(\vec{\varphi}_l, \vec{\varphi}_{20,m,m-l+n}^*) + \vec{N}(\vec{\varphi}_m, \vec{\varphi}_{22,l,m-l+n}) &(25)\\
&+ \vec{N}(\vec{\varphi}_{20,m,m-l+n}^*, \vec{\varphi}_l) + \vec{N}(\vec{\varphi}_{22,l,m-l+n}, \vec{\varphi}_m), \vec{\varphi}_n^\dagger(\omega_c, p_c; x)\} > . &(26)
\end{aligned}$$

Using the original variables $\frac{\partial}{\partial t} = \lambda \frac{\partial}{\partial \tau_1}$, $\mathcal{A}_n = \lambda A_n$ Eq.(22) becomes

$$c_0 \frac{d\mathcal{A}_n}{dt^2} + (p - p_c)c_1 \mathcal{A}_n + \sum_l \sum_m c_{3lmn} \mathcal{A}_l \mathcal{A}_m^* \mathcal{A}_{m-l+n} = 0 \tag{27}$$

If the eigenvalue of the linear equation is nondegenerate, Eq.(27) reduces to

$$c_0 \frac{d\mathcal{A}}{dt^2} + (p - p_c)c_1 \mathcal{A} + c_3 \mid \mathcal{A} \mid^2 \mathcal{A} = 0. \tag{28}$$

This situation corresponds to ideal nonresonant MHD modes (nondegenerate).

The condition (11) corresponds to the fact that the eigenvalue ω has a single root, so that the obtained nonlinear equation has the first order time derivative. Contrastively, the condition (12) corresponds to the case that the eigenvalue ω has a double root. In this case the obtained nonlinear equation has the second order time derivative.

References

1) N.Nakajima Phys.Fluids B, Vol.2, No.6, 1170-1183, 1990
2) N.Nakajima and S.Hamaguchi Phys.Fluids B, Vol.2, No.6, 1184-1189, 1990

Hole Dynamics of One-Dimensional Plasma

K. Kitahara, N. Ishibashi and K. Tanno
Department of Applied Physics
Tokyo Institute of Technology
Tokyo 152

Although steady state solutions of the Vlasov equation are known as BGK solutions, the stability of these solutions is not fully investigated. So, we performed an exact particle simulation in order to see the dynamics of holes in phase space. Dawson's model of electron sheets in the uniform positive back ground is transformed into an 2N-dimensional discrete-time mapping, which can be treated numerically exactly. The formation and persistence of a big hole from two-stream instability is analyzed.

Shock and Soliton Structures Induced by Poloidal Flow in Tokamaks

T.Taniuti
Department of Engineering, Natural Science Mathematics, Chubu University
K.Watanabe, Y.Ishii and M.Wakatani
Plasma Physics Laboratory, Kyoto University

When poloidal flow velocity, Up, becomes close to ϵC_S in tokamaks, fluid motion inside the flux surface is governed by forced KdV equation in the small dissipation limit, where ϵ is an inverse aspect ratio and C_S is a sound velocity. This implies that a stationary soliton structure appears at the inside region of toroidal plasma or $\theta \simeq \pi$, where θ is a poloidal angle.

In the limit of large dissipation a forced Burgers equation is more appropriate. This case corresponds to an appearance of shock structure. When an averaged poloidal flow velocity is very close to ϵC_S, a shock may be seen in the outer region of toroidal plasma or $\theta \simeq 0$. With the increase of $\mid Up - \epsilon C_s \mid$ the shock position moves from $\theta \simeq 0$ to $\theta \simeq \pi$.

Recent tokamak experiments show the existence of poloidal flow with $Up \simeq \epsilon C_S$ in the transition phase from the L mode to the H mode. Implication of our results in the experiment will be discussed.

Soliton Phenomena in Electron Beam Plasma

Tetsu Yajima
Department of Applied Physics, Faculty of Engineering, University of Tokyo,
Hongo 7-3-1, Bunkyo-ku, Tokyo 113, Japan.

Abstract

As a model equation for an electron beam plasma system, the unstable nonlinear Schrödinger (UNS) equation, $iq_x + q_{tt} + 2|q|^2 q = 0$, is proposed. Recent works on this equation are reported. The UNS equation is a canonical equation which describes nonlinear modulations of wave amplitude in unstable media. In the electron beam plasma system, near the critical wave number, the wave amplitude obeys the UNS equation. Results derived by investigating this equation show that solitons can be caused in the system. In addition, the roles of solitons in unstable media is clarified.

It is well known that soliton phenomena occur as a result of competition between dispersion and nonlinearity. We shall make some considerations on systems where instability and nonlinearity coexist, and shall study the properties and the roles of localized solitary wave mode (soliton) in such systems.

The model equation is the unstable nonlinear Schrödinger (UNS) equation :

$$iq_x + q_{tt} + 2|q|^2 q = 0. \tag{1}$$

Let us consider the derivation of (1). There are two systems; one is a plasma system where an electron beam is injected under high frequency electric field (electron beam plasma)[1,2], and the other is the Rayleigh-Taylor (RT) system[3]. Here the former case is considered, and those who are interested in the RT problem are recomended to refer to the Ref.[3].

The basic equation is the continuum relation and the Bernoulli equation for electrons in plasma. Denoting the density and the velosity of electrons as n and u, and using subscript p and b for plasma and beam electrons, we have

$$\frac{\partial n_p}{\partial t} + \nabla\cdot(n_p \boldsymbol{u}_p) = 0\,, \qquad \frac{\partial \boldsymbol{u}_p}{\partial t} + (\boldsymbol{u}_p\cdot\nabla)\boldsymbol{u}_p = -\frac{e}{m}\boldsymbol{E}^{(h)} - \frac{T_p}{mn_p}\nabla n_p\,, \tag{2a}$$

$$\frac{\partial n_b}{\partial t} + \nabla\cdot(n_b \boldsymbol{u}_b) = 0\,, \qquad \frac{\partial \boldsymbol{u}_b}{\partial t} + (\boldsymbol{u}_b\cdot\nabla)\boldsymbol{u}_b = -\frac{e}{m}\boldsymbol{E}^{(h)}\,. \tag{2b}$$

Here $\boldsymbol{E}^{(h)}$ is the high frequency electric field, T_p the temperature of electrons, m the electron mass and $-e$ the electron charge. The term including the temperature for electron beam is neglected since the beam velosity is sufficiently large. Equations for ion are left out because ions are too heavy to undergo high frequency motion. We shall devide the densities into three parts: the average, the high frequency fluctuation and the low frequency parts. The low frequency parts for velocities will be neglected. These will be distinguished by the superscripts 0, h, and l.

Higher order terms of high frequency parts are considered to be small, so eliminating $\boldsymbol{u}_p$ and $\boldsymbol{u}_b$, and using Gauss's law for electric field, $\nabla\cdot\boldsymbol{E}^{(h)} = -4\pi e(n_p^{(h)} + n_b^{(h)})$ in (2), we have

$$\nabla\cdot\left(\frac{\partial^2}{\partial t^2} - \frac{T_p}{m}\nabla^2 + \omega_e^2\left(1 + \frac{n_p^{(l)}}{n_p^{(0)}}\right)\right)\boldsymbol{E}^{(h)} = -\left(\frac{\partial^2}{\partial t^2} - \frac{T_p}{m}\nabla^2\right)4\pi e n_b^{(h)}, \tag{3a}$$

$$\left(\frac{\partial}{\partial t} + \boldsymbol{u}_0\cdot\nabla\right)^2 n_b^{(h)} = \frac{\alpha\omega_e^2}{4\pi e}\nabla\cdot\left(1 + \frac{n_b^{(l)}}{n_b^{(0)}}\right)\boldsymbol{E}^{(h)}. \tag{3b}$$

where $\alpha = n_b^{(0)}/n_p^{(0)}$, $\omega_e = 4\pi e^2 n_p^{(0)}/m$. We call α beam constant and ω_e electric plasma frequency, and $\boldsymbol{u}_0$ is the avarage velocity of the beam. We introduce complex variables $\boldsymbol{E}$ and ρ instead of $\boldsymbol{E}^{(h)}$ and $n_b^{(h)}$, such as $\boldsymbol{E}^{(h)} = (\boldsymbol{E} + \boldsymbol{E}^*)/2$. The frequency of electric field can be approximated as ω_e, so $\boldsymbol{E}$ and ρ are written as products of $e^{-i\omega_e t}$ and slowly varying function in time. And we think ρ as a travelling wave with long wavelength. Therefore, the higher order derivatives can be neglected. Then from (3), we have a set of equations:

$$\nabla\cdot(i\frac{\partial}{\partial t}-\omega_e+\frac{T_p}{2m\omega_e}\nabla^2-\frac{\omega_e|\boldsymbol{E}|^2}{32\pi n_p^{(0)2}T_p})\boldsymbol{E}=-\frac{\omega_e}{2}\rho,\qquad(\frac{\partial}{\partial t}+\boldsymbol{u}_0\cdot\nabla)^2\rho=\alpha\omega_e^2\nabla\cdot\boldsymbol{E}. \tag{4}$$

In deriving (4), we take into consideration the ponderomotive force $n_p^{(I)}/n_p^{(0)}=-|\boldsymbol{E}|^2/16\pi n_p^{(0)}T_p$. Hereafter, we shall consider one dimensional problem. Let us take the direction of the beam volisity $\boldsymbol{u}_0$ and the wave propagation as parallel to x-axis. We think longitudinal mode for ρ then the non-zero element of $\boldsymbol{E}$ is E_1. Integrating (4), we have

$$(i\frac{\partial}{\partial\tau}-1+\frac{1}{2}\frac{\partial^2}{\partial\xi^2}+|f|^2)f=-\frac{4}{27}\kappa^3 g,\qquad(\frac{\partial}{\partial\tau}+V\frac{\partial}{\partial\xi})^2 g=f. \tag{5}$$

Setting $N=1/\alpha\sqrt{32\pi n_p^{(0)}T_p}$, we have defined the variables as

$$\xi=x\sqrt{2m\omega_e/T_p},\qquad\tau=\omega_e t,\qquad f=\alpha NE_1,\qquad g=\int^x N\rho\,dx,\qquad V=u_0\sqrt{m/T_p},\qquad\kappa^3=27\alpha/8. \tag{6}$$

The dispersion relation of the linearized (5) yields a cubic equation for ω:

$$\omega-4\kappa^3/27(\omega-kV)^2=1+k^2/2. \tag{7}$$

The unstable mode is realized when ω is complex. When $V^2<2(1+\kappa)$, there always exist complex solutions. When $V^2>2(1+\kappa)$, complex ω's exist only for the k satysfying $k<k_c\equiv V(1-\sqrt{1-2(1+\kappa)/V^2})$. We investigate the region near the critical wave number k_c. We define critical frequency as $\omega_c=k_cV-2\kappa/3$. We express the solutions of (5) as

$$f=\phi_1\exp i(k_c\xi-\omega_c\tau),\qquad g=\phi_2\exp i(k_c\xi-\omega_c\tau). \tag{8}$$

Around the critical point where the wave number and the frequency are near k_c and ω_c, the emvelopes ϕ_1 and ϕ_2 are slowly varying functions of ξ and τ. Using this approximation in the second equation of (5), we have

$$\phi_2=-\{\frac{9}{4\kappa^2}+\frac{27i}{4\kappa^3}(\frac{\partial}{\partial\tau}+V\frac{\partial}{\partial\xi})-\frac{243}{16\kappa^4}(\frac{\partial}{\partial\tau}+V\frac{\partial}{\partial\xi})^2-O((\frac{\partial}{\partial\tau}+V\frac{\partial}{\partial\xi})^3)\}\phi_1. \tag{9}$$

Then, we obtain

$$-iV\frac{\partial\phi_1}{\partial\xi}+\frac{9}{4\kappa}\frac{\partial^2\phi_1}{\partial\tau^2}+|\phi_1|^2\phi_1=0. \tag{10}$$

Finally, a suitable transformation of variables in (10), gives the UNS equation (1). To summarize, under the conditions that the beam velocity is sufficiently large and that the system is one dimensional, the envelope of the high frequency electric field near the critical wave number k_c obeys the UNS equation.

Before solving the initial value problem of (1), let us consider a perturbation analysis of time development of small disturbance caused in the system. When the amplitude of $q(x,t)$ is small, we have a linearized equation:

$$iq_{0,x}+q_{0,tt}=0. \tag{11}$$

Substitution of $q_0(x,t)=A\exp(ikx-i\omega t)$ into (11) yields a dispersion relation $\omega^2+k=0$. Therefore, a small disturbance with positive k will exponentially grow. Then we set $k=4\eta^2$, $\omega=2i\eta$, ($\eta>0$) and $q_0(x,t)=A\exp(4i\eta^2x+2\eta t)$. We expand $q(x,t)$ as

$$q(x,t)=e^{4i\eta^2x}(A\,e^{2\eta t}+\varepsilon\,B_1(t)+\varepsilon^2B_2(t)+\cdots). \tag{12}$$

The constant ε denotes a "smallness" parameter for a perturbative calculation which expresses magnitude of nonlinear effect and finally we take $\varepsilon=1$. Substituting this into eq.(1), we have a set of differential equations, which can be solved iteratively. Upon summing up contributions from all orders and setting $\epsilon = 1$, we get

$$q(x,t) = e^{4i\eta^2 x}\, e^{2\eta t}\, A\,(1 + \sum_{n=1}^{\infty} (-\frac{|A|^2}{16\eta^2})^n\, e^{4n\eta t}\,) = -\frac{2i\eta\, e^{4i\eta^2 x + i\phi}}{\cosh\,(2\eta t + \rho)}, \tag{13}$$

where, in terms of real constants ρ and ϕ, we have set $A = -4i\eta\, e^{\rho + i\phi}$. This shows that the instability will not grow forever. The exponential growth in the linear regime is suppressed by the nonlinearity and the system returns to the unstable equilibrium state. This behavior is reasonable since the UNS equation (1) is invariant under the time reversal $t \to -t$.

Let us consider this stabilizing mechanism. The system is unstable in a sense of that the zero-field configuration is not at the minimum energy state. When a disturbance is caused, it will grow because of the instability of the system. The fact that the disturbance does not grow forever shows that there are some mechanism to carry away the surplus energy. We recall solitary localized wave mode (soliton) as such a nonlinear exitation that can carry energy in an effective way.

The UNS equation can be solved by the inverse scattering method, and as a result, we have N-soliton solution of the system[1]. Owing to a limited space, we shall only give the gist on the inverse scattering. We introduce a set of auxiliary linear equations:

$$\frac{\partial v}{\partial x} = \begin{pmatrix} i|q|^2 - 2i\zeta^2 & iq_t + 2\zeta q \\ iq_t^* - 2\zeta q^* & -i|q|^2 + 2i\zeta^2 \end{pmatrix} v, \qquad \frac{\partial v}{\partial t} = \begin{pmatrix} -i\zeta & q \\ -q^* & i\zeta \end{pmatrix} v, \qquad v = \begin{pmatrix} v_1 \\ v_2 \end{pmatrix}. \tag{14}$$

The spectral parameter $\zeta = \xi + i\eta$ is generally a complex constant corresponding to the eigenvalue. We assume a boundary condition $q(x,t) \to 0$ for $|x| \to \infty$.

For a while, we shall fix t and consider the eigenvalue problem of the first equation of (14). For real $\zeta \equiv \xi$, we introduce the Jost functions, with the following asymptotic forms:

$$\begin{array}{llllll} \phi(x,\xi) & \to & \begin{pmatrix} e^{-2i\xi^2 x} \\ 0 \end{pmatrix} & \bar{\phi}(x,\xi) & \to & \begin{pmatrix} 0 \\ -e^{2i\xi^2 x} \end{pmatrix} \quad x \to -\infty, \\ \psi(x,\xi) & \to & \begin{pmatrix} 0 \\ e^{2i\xi^2 x} \end{pmatrix} & \bar{\psi}(x,\xi) & \to & \begin{pmatrix} e^{-2i\xi^2 x} \\ 0 \end{pmatrix} \quad x \to +\infty. \end{array} \tag{15}$$

In conplex ζ-plane, ϕ and ψ can be analitically continued into the regions which satisfy $\mathrm{Im}(\zeta^2) \geq 0$, and $\bar{\phi}$ and $\bar{\psi}$ into $\mathrm{Im}(\zeta^2) \leq 0$. We define Wronskian as $W[f,g] \equiv f_1 g_2 - f_2 g_1$. For Jost functions which belong to the same eigenvalue, $W[\phi,\bar{\phi}]$ and $W[\psi,\bar{\psi}]$ are not equal to zero, so each of the sets $\{\phi,\ \bar{\phi}\}$ and $\{\psi,\ \bar{\psi}\}$ consists a fundamental system of solutions. Then the following relations holds:

$$\phi(x,\xi) = a(\xi)\bar{\psi}(x,\xi) + b(\zeta)\psi(x,\xi), \qquad \bar{\phi}(x,\xi) = -\bar{a}(\xi)\psi(x,\xi) + \bar{b}(\xi)\bar{\psi}(x,\xi). \tag{16}$$

The coefficients $a(\xi)$, $\bar{a}(\xi)$, $b(\xi)$ $\bar{b}(\xi)$ corresponds to scattering amplitudes and they do not depend on space variable x. We enumerate some important properties of these amplitudes.

(1) These amplitudes can be expressed in terms of Wronskians of Jost functions: $a(\xi) = W[\phi,\psi]$, $\bar{a}(\xi) = W[\bar{\phi},\bar{\psi}]$, $b(\xi) = -W[\phi,\bar{\psi}]$, $\bar{b}(\xi) = W[\bar{\phi},\psi]$.

(2) From the analytic continuation of Jost functions, the amplitude $a(\xi)$ $(\bar{a}(\xi))$ can be analytically continued into $\mathrm{Im}\zeta^2 \geq 0$ $(\mathrm{Im}\zeta^2 \leq 0)$ in the complex ζ-plane. On the other hand, $b(\xi)$ and $\bar{b}(\xi)$ are generally defined on the real and imaginary axes.

(3) At zeroes of $a(\zeta)$ in the region $\xi\eta > 0$, ζ_j, $(j = 1, 2, \cdots, N)$, the functions $\phi(x,\zeta)$ and $\psi(x,\zeta)$ become linearly independent so it is thought that a bound state occurs. At $\zeta = \zeta_j$, $\phi(x,\zeta_j) = b_j\psi(x,\zeta_j)$. A set of quantities $\{a(\zeta), b(\zeta), b_j, \zeta_j\}$ is called scattering data.

(4) The scattering data except ζ_j's depend not only on ζ but also on t. This time dependences give the time dipendence of the solution.

In this analysis, we assume that the N zeroes of $a(\zeta)$, ζ_j, $j = 1, 2, \cdots, N$ are simple. The scattering data are derived from the initial conditions for $q(x,t)$ and $q_t(x,t)$. After a straightforward but lengthy calculatoins[1], we have the solution for the UNS equation as

$$q(x) = -2i\sum_{k=1}^{N} \gamma_k^* e^{-2i\zeta_k^{*2} x}\, \psi_2^*(x,\zeta_k) - \frac{1}{\pi}\int_{-\infty}^{\infty} d\xi\, \phi_2^{(1)*}(\xi) - \frac{i}{\pi}\int_{-\infty}^{\infty} d\eta\, \phi_2^{(2)*}(\eta), \tag{17}$$

where $\gamma_k = b_k/a'(\zeta_k)$, $\psi_2(x,\zeta)$ is the second component of the Jost function $\psi(x,\zeta)$ and the functions $\phi_2^{(1)}$ and $\phi_2^{(2)}$ are the second components of the vector functions defined as

$$\phi^{(1)}(\xi) = \begin{cases} \dfrac{b(\xi)}{a(\xi)}\psi(x,\xi)e^{2i\xi^2 x} & \xi > 0 \\ -\dfrac{b(\xi)}{a(\xi)}\psi(x,\xi)e^{2i\xi^2 x} & \xi < 0 \end{cases}, \qquad \phi^{(2)}(\eta) = \begin{cases} \dfrac{b(i\eta)}{a(i\eta)}\psi(x,i\eta)e^{-2i\eta^2 x} & \eta > 0 \\ -\dfrac{b(i\eta)}{a(i\eta)}\psi(x,i\eta)e^{-2i\eta^2 x} & \eta < 0 \end{cases}. \tag{18}$$

Soliton solutions are derived under the condition $b(\zeta) \equiv 0$. From (17) and (18), we have

$$\psi_1(x,\zeta_j)e^{-2i\zeta_j^2 x} = -\sum_{k=1}^{N} \frac{\gamma_k^* e^{-2i\zeta_k^{*2} x}}{\zeta_j - \zeta_k^*}\psi_2^*(x,\zeta_k), \qquad \psi_2^*(x,\zeta_j)e^{2i\zeta_j^{*2} x} = 1 + \sum_{k=1}^{N} \frac{\gamma_k e^{2i\zeta_k^2 x}}{\zeta_j^* - \zeta_k}\psi_1(x,\zeta_k). \tag{19}$$

Then, from (17), we find that $q(x,t)$ is given by

$$q(x,t) = -2i\sum_{k=1}^{N}(\gamma_k(t)\psi_2(x,\zeta_k)e^{2i\zeta_k^2 x})^*. \tag{20}$$

For example, one soliton solution is obtained when $a(\zeta)$ has one simple zero. Denoting this zero by $\zeta = \xi + i\eta$, we obtain

$$q(x,t) = -2i\eta\frac{\exp(-4i(\xi^2 - \eta^2)x - 2i\xi t + i\phi)}{\cosh(8\xi\eta x + 2\eta t + \rho)}, \tag{21}$$

where $\phi = -2\arg(\mu(t=0))$, $\rho = \log(2|\eta|/|\mu(t=0)|^2)$. This solution, when x and t are interchanged, is the same as that of the stable (conventional) nonlinear Schrödinger equation[4]. We see that (13) is a special case of the one soliton solution (21) given by taking $\xi \to 0$.

Properties of this soliton solutions is very interesting, but for the details we refer to the Ref.[1]. Let us think an initial value problem:

$$q(x,0) = A\exp[i(kx - 2A^2\tanh x)]/\cosh x, \qquad q_t(x,0) = 0, \qquad A, k: \text{constants}. \tag{22}$$

This corresponds to a situation that an disturbance is caused in the system. Similar to the procedure given for the conventional nonlinear Schrödinger equation[5], we can express the Jost functions by the Gauss's hypergeometric functions, and the scattering coefficients by Gamma functions[1]. The number of zeroes of $a(\zeta)$ at $\xi\eta \geq 0$ (the number of solitons) is not zero only for $k < 0$ and it is expressed as

$$N = 2n, \qquad 1 \leq n < A^2\sqrt{2|k|} + 1/2.$$

The number of solitons increases as A^2. This fact seems to has a close relation to that the system is unstable, and corresponds to a situation that solitons carry the energy of disturbance proportinal to the initial amplitude. It is interesting that a pure sech-type potential does not evolve into solitons. Analyses of other initial conditions are in progress.

In conclusion, we emphasize that solitons can be caused in the unstable system, and they play important roles in stabilizing the unstable media.

Acknowledgment

The author is very grateful to Professor M. Wadati and Dr. T. Iizuka for collaboration in this work. Thanks are also due to Professor J. Satsuma, Professor K. Yamagiwa and Dr. M. Tanaka for their interests in this work and stimulating discussions on electron beam plasma systems.

References

[1] T. Yajima and M. Wadati: J. Phys. Soc. Jpn. **59** (1990) 41, J. Phys. Soc. Jpn. **59** (1990) 3237.
[2] M. Tanaka and N. Yajima: Prog. Theor. Phys. Suppl. **94** (1988) 138.
[3] T. Iizuka and M. Wadati: J. Phys. Soc. Jpn. **59** (1990) 3182.
[4] V. E. Zakharov and A. B. Shabat: Sov. Phys. -JETP. **34** (1972) 62.
[5] J. Satsuma and N. Yajima: Prog. Theor. Phys. Suppl. **55** (1974) 284.

Point vortex description of a modon solution

Chihiro Matsuoka and Kazuhiro Nozaki

Department of Physics,
Nagoya University, 464-01, Japan

Abstract. Using the point vortex approximation, an exact solution corresponding to a modon solution in the Hasegawa-Mima equation is obtained. The stability of this solution is discussed.

The basic equation adopted in our study is the Hasegawa-Mima equation [1][2]:

$$\left(\frac{\partial}{\partial t} + \hat{z} \times \nabla\phi\cdot\nabla\right)(\Delta\phi - \phi) + v^{*}\frac{\partial\phi}{\partial y} = 0, \tag{1}$$

where v^{*} is the constant drift velocity and $\hat{z}$ is the unit vector in the z direction. This equation describes an electrostatic two-dimensional drift wave in inhomogeneous plasmas and has a dipole solution, called a modon, which propagates with a constant speed in the y direction.

We seek a discrete vortex solution to eq.(1), which is rewritten as

$$\left(\frac{\partial}{\partial t} + \hat{z} \times \nabla\phi\cdot\nabla\right)(\Delta\phi - \kappa^2\phi) + (\kappa^2 - 1)\left(\frac{\partial}{\partial t} + u\frac{\partial}{\partial y}\right)\phi = 0, \tag{2}$$

where $u = \frac{v^{*}}{\kappa^2 - 1}$ and κ is a constant. Let we set

$$\Delta\phi - \kappa^2\phi = \sum_{j=1}^{N} \gamma_j(t)\delta(\mathbf{r} - \mathbf{r}_j(t)), \tag{3}$$

where $\gamma_j(t)$, the strength of the vortex and is a constant for the special case of the modon, and $\mathbf{r} = (x,\ y)$, then we have

$$\phi = \sum_{j=1}^{N} \phi_j, \qquad \phi_j = -\frac{\gamma_j}{2\pi}K_0(\kappa|\mathbf{r} - \mathbf{r}_j|). \tag{4}$$

Equation (4) gives a solution to eq.(2) when the following equations are satisfied

$$\frac{d\mathbf{r}_j}{dt} = \hat{z} \times \nabla \left(\sum_{h \neq j} \phi_h \right)_{\mathbf{r}=\mathbf{r}_j}, \tag{5}$$

and

$$\left(\frac{\partial}{\partial t} + u \frac{\partial}{\partial y} \right) \phi_j = 0. \tag{6}$$

From eq.(6), we have

$$(x_j, y_j) = (\bar{x}_j, ut + \bar{y}_j), \tag{7}$$

where $\bar{x}_j$ and $\bar{y}_j$ are constants.

Now we consider the following equation:

$$A\mathbf{g} = \mathbf{u}, \tag{8}$$

where

$${}^t\mathbf{g} = (\gamma_1, \gamma_2, \ldots, \gamma_N), \qquad {}^t\mathbf{u} = (u, u, \ldots, u),$$

and

$$A = \frac{\kappa}{2\pi} \begin{bmatrix} 0 & K_1(\kappa l_{12}) & \ldots & K_1(\kappa l_{1N}) \\ -K_1(\kappa l_{21}) & 0 & \ldots & K_1(\kappa l_{2N}) \\ \vdots & \vdots & \ddots & \vdots \\ -K_1(\kappa l_{N1}) & -K_1(\kappa l_{N2}) & \ldots & 0 \end{bmatrix},$$

$$l_{jk} = |\bar{x}_j - \bar{x}_k|,$$

The configuration is shown in Fig.1.

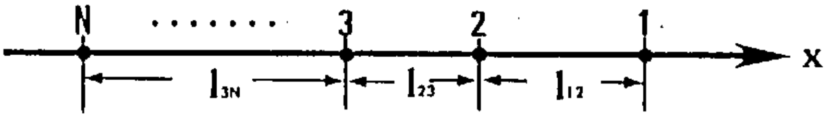

Fig. 1 Configuration.

For odd N, there are no solutions to eq.(8). In the simplest case, $N = 2$, we obtain an exact dipole solution corresponding to a modon [3][4]. For $N = 2n(n \geq 2)$, there exist also solutions which propagate uniformly in the y direction.

The strength of a vortex $\gamma_j(t)$ is given as

$$\gamma_j = \gamma_{j0} + \delta \left[v^* x_j - \frac{1}{2\pi} \sum_{k \neq j} \gamma_k (\kappa_k^2 - 1) K_0(\kappa_k |\mathbf{r}_j - \mathbf{r}_\mathbf{k}|) \right], \qquad (9)$$

$$k \neq j; \qquad k, j = 1, 2$$

where $\delta(\delta << 1)$ and γ_{j0} are constants.

Applying the linear stability theory to eqs.(5) and (9), we can examine the stability of a modon(, which corresponds to $\gamma_1 = -\gamma_2 = \gamma$ and $\kappa_1 = \kappa_2 = \kappa$). Then we get the result that the system is marginaly stable for $\kappa > 1$. The phase velocity v_p in the original system is given as

$$v_p = -\frac{v^*}{1 + k^2},$$

where k is the wave number. Therefore, we see that the system is stable when the velocity of the modon has the opposite sign to the phase velocity.

References

[1] A Hasegawa and K Mima, Phys. Fluids **21**, 87 (1978).

[2] W. Horton, Phys. Fluids **B1**, 524 (1989).

[3] G. Flierl, V. Larichev, J. McWilliams and G. Reznik, Dyn. Atm. Oceans 5, 1 (1980).

[4] N. J. Zabsky and J. C. McWilliams, Phys. Fluids **25**, 2175 (1982).

Structures of Magnetic Field Lines In the Helical Torus

T. Hatori and T. Watanabe
National Institute for Fusion Science
Nagoya 464-01, Japan

ABSTRACT

Equation of magnetic field line can be written in the form of Hamiltonian equation. An explicit form for the Hamiltonian applicable to the first order of ρ/R is obtained ,where ρ and R are minor and major radii.

Breakdown of magnetic surface in the periphery of helical torus is the typical phenomenon in the Hamilton dynamics with two degrees of freedom that the nested KAM torii are limited by the chaotic region in phase space. It is well known that the helically symmetric field constitutes the magnetic surface near the magnetic axis and the separatrix in the outer region. Since the symmetry breaking perturbations increase in the outer area for the toroidal field, the separatrix and the neighbouring surface disapear and become chaotic. The structure of transition regime from the regular surface to chaos is analogous to the critical phenomena and worth examining.

There have been a number of calculations for the rearlistic helical toroidal magnetic field. All of them are large and expensive, which include the calculation of magnetic field through the Biot-Savart law from a realistic coil, construction of magnetic field by the data of a MHD code, and so on. To study the detailed structure near the outermost magnetic surface, however, we need to develope an analytic model which enable us to track many field lines long enough to obtain precise statistical properties. The stochastic magnetic field is a typical chaos in the conservative dynamical system, so that retainment of the symplecticity ($\mathrm{div}\boldsymbol{B} = 0$) is crutial to develope a simple model. To this end, we adopt a canonical formalism for the magnetic field and obtain an explicit expression for the Hamiltonian describing the helical toroidal magnetic field.

The general magnetic field can be expressed in a canonical form

$$\boldsymbol{B} = \nabla\Psi \times \nabla\Theta - \nabla\Psi_p \times \nabla\varphi, \tag{1}$$

where φ is the geometrical toroidal angle, (Θ, Ψ) are generalization of (θ, φ), and Ψ_p is the counterpart of ψ. In the new coordinate system (Ψ, Θ, φ), the equation of the field line becames the following canonical form,

$$\frac{d}{d\varphi}\Psi = -\frac{\partial}{\partial\Theta}\Psi_p(\Psi, \Theta, \varphi), \tag{2}$$

$$\frac{d}{d\varphi}\Theta = \frac{\partial}{\partial\Psi}\Psi_p(\Psi, \Theta, \varphi). \tag{3}$$

Clearly $\Psi_p(\Psi, \Theta, \varphi)$ plays a role of Hamiltonian, (Ψ, Θ) are action and angle variables. The left-hand sides of eqs.(2) and (3) are

$$\frac{d}{d\varphi}\Psi = \frac{B \cdot \nabla\Psi}{B \cdot \nabla\varphi}, \tag{4}$$

$$\frac{d}{d\varphi}\Theta = \frac{B \cdot \nabla\Theta}{B \cdot \nabla\varphi}. \tag{5}$$

The present ploblem is to obtain Hamiltonian Ψ_p on the right-hand sides of eqs.(2) and (3) from the left-hand sides given by eqs.(4) and (5). The ordinary dynamical problem is to obtain Ψ and Θ from the right-hand sides of eqs. (2) and (3), where it is usually easy to write explicitly Hamiltonian. Thus the presnt task is to solve the inverse problem.

We know much information about the helical toroidal magnetic field in the ordinary coordinate system. The well-known analytical model for the vacuum helical toroidal field is given in Refs.1 and 2. When β value of plasma is negligible,the vacuum field, $B = \nabla\Phi$,is a good approximation. The scalar potential Φ has to be a harmonic function, $\Delta\Phi = 0$, which is a direct result from div$B = 0$. A solution for the scalar potential is

$$\begin{aligned}\Phi &= B_0 R\varphi + \sqrt{\frac{R}{r}}\frac{bR}{l}\{I_n(\frac{nl\rho}{R})\sin n\theta + f_+(\rho)\sin[(n+1)\chi - nl\varphi] \\ &\quad + f_-(\rho)\sin[(n-1)\chi - nl\varphi]\} + \cdots,\end{aligned} \tag{6}$$

and the functions $f_\pm(\rho)$ are solutions of the following inhomogeneous equations,

$$[\frac{1}{\rho}\frac{d}{d\rho}\rho\frac{d}{d\rho} - \frac{n \pm 1}{\rho^2} - \frac{(nl)^2}{R^2}]f_\pm = -\frac{(nl)^2}{R^3}\rho I_n(\frac{nl\rho}{R}). \tag{7}$$

Here the coordinate system is illustrated in the figure, the helical angle is defined by $\theta = \chi - l\varphi$, and I_n is the modified Bessel function. Note that $f_\pm$ is of the order of $(\frac{nl\rho}{R})^3 I_n(\frac{nl\rho}{R})$. In case of LHD, periodicity in φ is $2\pi/10$, so l should be 5 when $n = 2$. Divide the solution (6) into two parts ,the unperturbed plus the perturbed, as $\Phi = \Phi^{(0)} + \delta\Phi$, where

$$\Phi^{(0)} = B_0 R\varphi + \frac{Rb}{l} I_n(\frac{nl\rho}{R})\sin n\theta. \tag{8}$$

The unperturbed $B^{(0)}$ is given by $B^{(0)} = \nabla^{(0)}\Phi^{(0)}$, where $\nabla^{(0)} = (\partial/R\partial\varphi, \partial/\rho\partial\chi, \partial/\partial\rho)$.

After some analysis, we finally get an explicit expression for Hamiltonian Ψ_p, correct to the first order of ρ/R,

$$\begin{aligned}&\Psi_p(\Psi, \Theta, \varphi) = \psi(\Psi) + \\ &\quad \epsilon\sum_{n=0}^{\infty}\{G_n^{(1)}(\Psi)\sin[(2n+1)\Theta + l\varphi] + G_n^{(2)}(\Psi)\sin[(2n+1)\Theta - l\varphi] + \\ &\quad G_n^{(3)}(\Psi)\sin[(2n+1)\Theta]\cos l\varphi + G_n^{(4)}(\Psi)\cos[(2n+1)\Theta]\sin l\varphi\}.\end{aligned} \tag{9}$$

Here $G_n^{(i)}(\Psi)(i = 1, \ldots 4)$ are increasing elementary functions of Ψ and satisfy $G_n^{(i)}(0) = 0$ .The smallnes parameter ε is the inverse aspect ratio, and b/B_0 is the ratio of the typical poloidal field to the toroidal field. The unpertuebed Hamiltonian $\psi(\Psi)$ cannot be written explicitly ,but its derivative,the unperturbed frequency ω , is given by

$$\omega(\Psi) = \frac{d\psi}{d\bar{\psi}} = -\frac{\pi l}{2} \frac{\sqrt{1 + \Psi + 2\frac{b}{B_0}}}{K(m)} \tag{10}$$

where m is defined in eq.(21), and.$K(m)$ is the elliptic integral

$$K(m) = \int_0^{\frac{\pi}{2}} \frac{d\theta}{\sqrt{1 - m\sin^2\theta}}. \tag{11}$$

REFERENCES

1.N.N.Filonenko, R.Z.Sagdeev and G.M.Zaslavsky; Nuc.Fusion 7,253(1967).
2.A.I.Morozov and Solov'ev; Rev. of Plasma Phys. Vol.2.

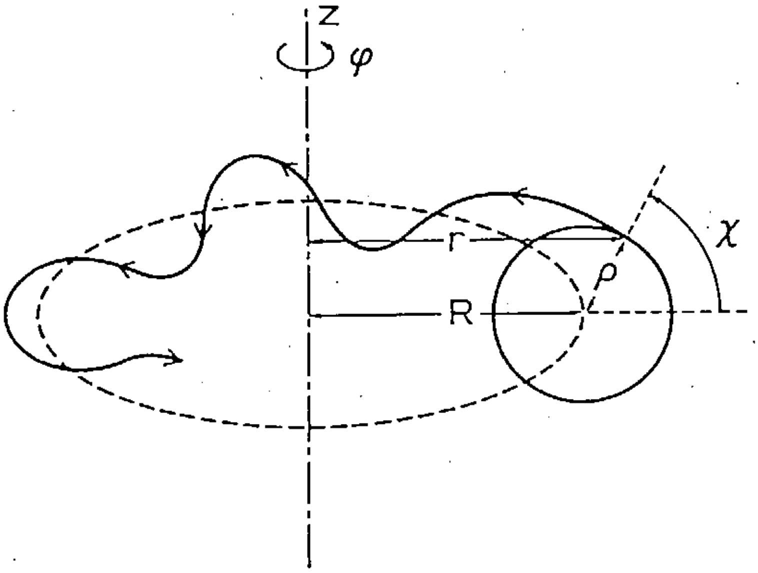

REGULAR MOTION AND SYMMETRY IN THE RELATIVISTIC STANDARD MAP$^{1)}$

Y. Nomura and Y. H. Ichikawa
National Institute for Fusion Science, Nagoya 464-01, Japan

W. Horton
Institute for Fusion Studies, The University of Texas at Austin,
Austin, Texas 78712-1060, U. S. A.

EXTENDED SUMMARY

In nonlinear dynamical systems, area-preserving maps have been investigated extensively as useful method for characterizing the non-integrable Hamiltonian systems. Especially, the nonrelativistic acceleration of charged particles by an infinite sequence of constant amplitude longitudinal waves with equally spaced phase velocities is represented by the standard map. This map exhibits regular and chaotic motion and has been studied in various fields of physics. The central problem of the standard map is a transport process under the coexistance of regular motion and chaos. Recently, Chernikov et al.$^{2)}$ introduced the relativistic generalization of the standard map. They have found that the chaotic motion is restricted to the vicinity of the fixed points and the breakup of last KAM torus occurs at higher wave amplitude than that for the standard map.

The purpose of this work is to clarify the relativistic effects on the nonlinear motion of particles by varying the wave phase velocity in a wide range and to discuss properties of the regular motion by constructing the families of symmetry lines.

1. REGULAR MOTION AND CHAOS IN THE RELATIVISTIC STANDARD MAP

Relativistic motion of charged particles in an infinite sequence of electrostatic waves with constant amplitude and equally spaced phase velocities is described by the relativistic standard map$^{1, 2)}$ in the normalized form :

$$P_{n+1} = P_n + F(X_n), \quad X_{n+1} = X_n + G(P_{n+1}), \tag{1}$$

$$F(X) = -(K/2\pi)\sin(2\pi X), \quad G(P) = P/\sqrt{1+\beta^2 P^2}$$

where K is the stochastic parameter which corresponds to the wave amplitude and the relativistic parameter β is defined as the ratio of phase velocity v_0 of the slowest wave to the speed of light c, $\beta \equiv v_0/c$. In the limiting case of $\beta \to 0$, the map (1) is reduced to the usual standard map. Fundamental properties of the relativistic standard map such as the stability of fixed points or the Poincare-Birkhoff period-p/q multifurcation condition have been derived in Ref. 1).

Particle trajectories in the relativistic standard map are shown in Fig. 1 for various values of β at K = 1.3. In these figures, particles are initially distributed uniformly at P = 0 and advanced according to the map (1) till T = 5000. For weekly relativistic case $\beta \ll 1$, diffusion of particles at low momentum region is qualitatively the same as that in the standard map. The stochastic region, however, is bounded by an invariant KAM surface at high momentum and global chaos is suppressed. As the parameter β increases, the maximum attainable momentum decreases rapidly and the particle diffusion is restricted to a thin layer.

In the ultra-relativistic case, $\beta \gg 1$, particle trajectory becomes quite regular. Secondary island chains with very high period are formed inside the separatrix KAM surface and the stochastic layer in the peripheral region of island chains is observed. In order to characterize this regular structure of the phase space, it is useful to analyze symmetry property of the map introduced by Birkhoff.[3] In the next section, we identify the periodic orbits by means of symmetry analysis.

2. SYMMETRY OF THE RELATIVISTIC STANDARD MAP

We consider a 2D area-preserving map T of the form given by Eq. (1). A map T is called reversible[3] if there exists an involution I_0 which satisfies the relation

$$T \cdot I_0 \cdot T = I_0 , \qquad I_0 \cdot I_0 = Id. \tag{2}$$

This relation indicates that the reversible map can be expressed as the product of two involutions:

$$T = I_1 \cdot I_0 , \qquad I_1 \cdot I_1 = Id. , \qquad I_1 \equiv T \cdot I_0 \tag{3}$$

and the inverse transformation T^{-1} is given by

$$T^{-1} = I_0 \cdot I_1 \tag{4}$$

If we define I_j as the jth iteration of the map T on the involution I_0, $I_j \equiv T^j \cdot I_0$, we immediately confirm that I_j is also an involution. Ensemble of I_j and T^k for arbitrary integers j and k forms a discrete infinite group with the relationships:

$$I_j \cdot I_k = T^{j-k} , \qquad T^j \cdot I_k = I_{j+k} , \qquad I_j \cdot T^k = I_{j-k} \tag{5}$$

It can be shown that the fixed points of the involution I_j form a line Γ_j which is called as its symmetry line,

$$\Gamma_j : \{ R \mid I_j R = R \} . \tag{6}$$

Therefore, the first equation of (5) defines that the intersection of Γ_j and Γ_k determines periodic points of T, whose period N divides $| j - k |$. From the second and the third equations of (5), we can deduce that the symmetry lines are transformed by T^N into other symmetry lines : $T^N \cdot \Gamma_j = \Gamma_{2N+j}$. This relation enables us to facilitate the construction of symmetry lines of arbitrary order.

Since the transformation function F is anti-symmetric with respect to the space inversion, $F(-X) = - F(X)$, the map (1) is expressed as the composition of the following involutions :

$$I_0 : \quad P' = P + F(X), \quad X' = -X$$
$$I_1 : \quad P' = P, \quad X' = -X + G(P) \tag{7}$$

Symmetry lines of these two involutions are given by

$$\Gamma_0 : \quad X = 0, \qquad \Gamma_1 : \quad 2X - G(P) = 0 \tag{8}$$

A factorization of the map into two involutions is not unique. Anti-symmetricity of the function G with respect to momentum inversion, G(-P) = - G(P), gives rise to another involution decomposition $T = J_1 \cdot J_0$,

$$J_0 : \quad P' = -P, \quad X' = X - G(P)$$
$$J_1 : \quad P' = -P + F[X - G(P)], \quad X' = X - G(P) - G[P - F\{X - G(P)\}] \tag{9}$$

This type of factorization defines momentum inversion symmetry as

$$\gamma_0 : \quad P = 0, \qquad \gamma_1 : \quad 2P - F[X - G(P)] = 0 \tag{10}$$

Figure 2 shows superposition of families of symmetry lines on the phase portrait of the map (1) for K = 1.3 and $\beta = 4\pi$. It can be found in Fig. 2(a) that the space inversion symmetry lines become parallel at high momentum, which indicates that phase increase of particles is almost constant for ultra-relativistic case. Momentum inversion symmetry lines in Fig. 2(b) are asymptotic to the separatrix KAM surface. In both figures, intersections of symmetry lines determine stable and unstable periodic orbits.

3. CONCLUDINIG REMARK

Particle acceleration in the relativistic standard map is studied and it is found that the relativistic correction suppresses the chaotic motion of particles. For the waves whose phase velocities extremely exceed the speed of light, particle trajectory becomes regular. In this case, periodic orbits play dominant role in the phase space and the stochasticity occurs around the secondary island chains. In order to obtain critical information on the periodic orbits, we carry out the symmetry analysis and construct families of space inversion and momentum inversion symmetry lines. Space inversion symmetry lines exhibit the constant phase increase of particle motion. These two families of symmetry lines predict stable and unstable periodic orbits of arbitrary period.

REFERENCES

1) Y. Nomura, Y. H. Ichikawa and W. Horton : Kakuyugou Kenkyu 64 (1990) 347. [in Japanese]
2) A. A. Chernokov, T. Tel, G. Vattay and G. M. Zaslavsky : Phys. Rev. A 40 (1989) 4072
3) G. D. Birkhoff : Dynamical Systems (AMS Colloquium Publications, Vol. IX, 1927) p. 115 and p.186.

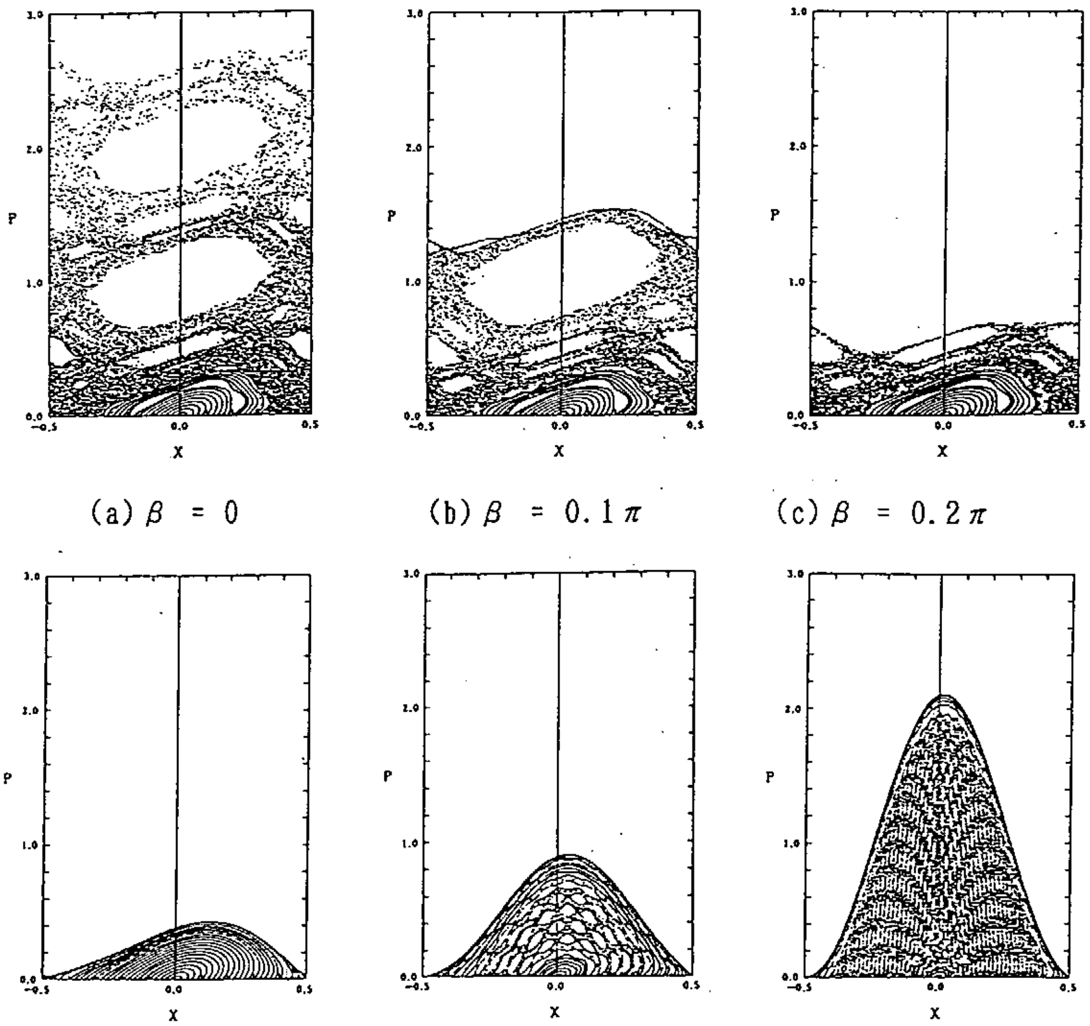

(a) β = 0　(b) β = 0.1π　(c) β = 0.2π

(d) β = π　(e) β = 4π　(f) β = 10 π

Fig. 1 Particle orbit in the relativistic standard map at K = 1.3.

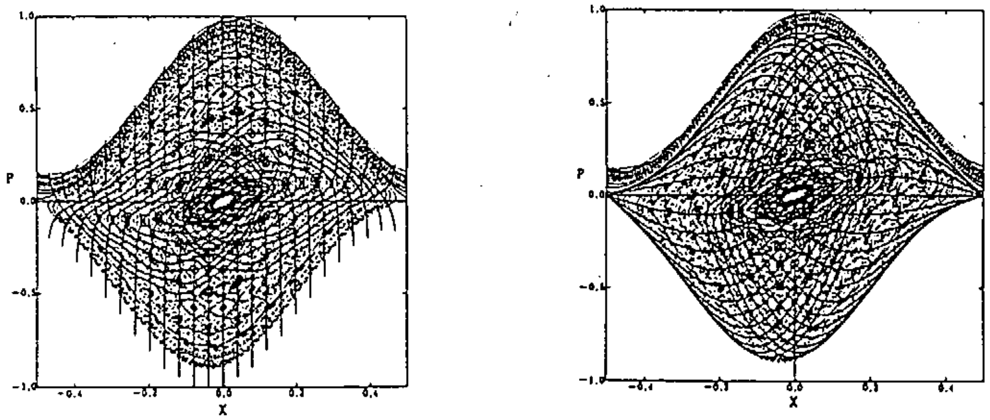

(a) Space inversion symmetry　(b) Momentum inversion symmetry

Fig. 2 Superposition of symmetry lines on the phase portrait of the relativistic standard map at K = 1.3 and β = 4π.

Diffusion and relaxation in Hamiltonian chaos

Tetsuro KONISHI
Dept. of Phys., Nagoya Univ., Nagoya, 464-01, JAPAN
E-mail address (Junet) : c42636a@nucc.cc.nagoya-u.ac.jp

Chaos in Hamiltonian systems have great importance in fundamental physics as a basis of classical statistical mechanics, as well as in application to plasma physics, solid state physics and so on [1-8]. In this paper I will introduce some results on the properties of global diffusion for Hamiltonian systems with many degrees of freedom, through numerical studies on coupled map lattices [8, 9].

Many important facts have been revealed for the chaos in area preserving mappings e.g. standard map [2].

$$p' = p + \frac{K}{2\pi}\sin 2\pi x, \quad x' = x + p' \tag{1}$$

Phase space of area preserving mapping is filled with self-similar structure of islands and cantori, which are related to dynamical properties such as anomalous diffusion and flicker noise [11, 12, 13]. Such delicate structures are expected to smeared out when the number of degrees of freedom increases. The main topic here is; "Are chaos and diffusion enhanced by making system size large?" The answer is partly yes, as we shall see below.

Our models are i) standard map (1) and ii) symplectic version of coupled map lattices [15, 16, 17, 18, 19, 20, 21, 22, 23], defined on discrete space and time; <u>a) locally interacting model;</u>

$$\begin{aligned} p_i(t+1) = &\ p_i(t) + \frac{K}{2\pi}\left\{\sin[2\pi(x_{i+1}(t) - x_i(t))] - \sin[2\pi(x_i(t) - x_{i-1}(t))]\right\}, \quad K > 0, \\ x_i(t+1) = &\ x_i(t) + p_i(t+1) \quad i = 1, 2, \cdots, N, \end{aligned} \tag{2}$$

where we take periodic boundary condition $x_{i+N} = x_i, p_{i+N} = p_i$. <u>b) globally interacting model;</u>

$$\begin{aligned} p_i(t+1) &= p_i(t) + \frac{K}{2\pi\sqrt{N-1}}\sum_{j=1}^{N}\sin[2\pi(x_j(t) - x_i(t))], \quad K > 0, \\ x_i(t+1) &= x_i(t) + p_i(t+1), \quad i = 1, 2, \cdots, N. \end{aligned} \tag{3}$$

The anomalous diffusion is observed both for area preserving mappings and for systems with many degrees of freedom, reflecting the self similar structures of phase spaces. In both cases, however, they are transients appearing only for finite time. This is easily seen if we see the convergence of diffusion coefficient[8]. After some finite time t_c the diffusion coefficient approaches to a finite value D_∞ , which is inversely proportional to t_c. Up to some time scale, the motion in phase space "sticks" to some KAM tori, and the hierarchical structure of tori and islands leads to the power-law type behavior. For longer time scales, however, the system escape from initial hierarchy and gets into another one, thus causes random phase summation of independent hierarchical motions [8].

Crossover from anomalous to normal diffusion has its origin in array-like arrangement of equivalent hierarchies of island chains in phase space, and are common to low dimentional and high dimensional systems. The difference between area preserving mappings and systems with many degrees of freedom lies in dependence of D_∞ on the coupling K [9]. It is known that $D_\infty \propto |K - K_c|^\alpha$ for standard map, and it is found that, for systems with $N \geq 3$, the diffusion coefficients obey 'Nekhoroshev form' [14, 2]

$$D \propto K \exp(-\xi(1/K)^\beta). \tag{4}$$

What is important is that the exponent β changes according to the system size [9]. The values of β's in eq.(4) which give best fit are summarized in Table 1;

Table 1 : exponent β and system size for locally interacting model

$D \propto K \exp(-\xi(1/K)^{\beta})$					
N	3	4	5	6	128
$\beta(\pm 0.05)$	0.73	0.46	0.50	0.47	0.43

For the model (2) we see that

- When the system size N is small compared to the spatial correlation length, β decreases as N gets large. This means that diffusion is enhanced as the system size is increased.
- When $N \gtrsim$ (correlation length) the value of β seems to converge to a finite value. In our model this convergence is achieved when $N \gtrsim 8$. The convergence is contrary to original estimation[14], where $\beta \to 0$ as $N \to \infty$.

For the model(3) we apply power-law fitting for D as an empirical formula. This power-law may be a manifestation of 'poor adiabacity' proposed by Chirikov[24]. The exponent of the power law again decreases as size, thus we see enhancement of the magnitude of diffusion by making system size large.

In this way we have seen the properties of global diffusion in Hamiltonian chaos with many degrees of freedom, where diffusion show a crossover from anomalous to normal and can be enhanced according to the increase of size of the system.

The model (3) shows a peculiar behavior, that is, particles get clustered and show a kind of order. Ordering process in conservative systems should attract much attention.

This work is a collaboration with Dr. K. Kaneko (Tokyo Univ., Komaba, Tokyo, Japan). We would like to thank National Institute for Fusion Science at Nagoya for the computational facility of FACOM M380 and VP200.

References

[1] R.S. MacKay and J. Meiss (eds.), *Hamiltonian Dynamical Systems* (Adam Hilger,Bristol,1987) A.J. Lichtenberg and M.A. Lieberman, *Regular and Stochastic Motion*(Springer, Berlin,1983).

[2] B. V. Chirikov, Phys. Rep. 52 (1979),263.

[3] V.I. Arnold, Sov. Math.Dokl. 5(1964), 581.

[4] V.I. Arnold and A. Avez, *Ergodic Problems in Classical Mechanics* (Benjamin-Cummings,Reading,1968).

[5] R.Livi, A.Politi, and S.Ruffo, J.of Phys. A19 (1986), 2033.

[6] I.Dana, et al., Phys.Rev.Lett. 62(1989), 233.

[7] A. B. Rechester and R. B. White, Phys.Rev. Lett.44(1980), 1586. J.D.Meiss et al., Physica 6D(1983),375. T. Hatori et al., Physica 14D(1985),193.

[8] K. Kaneko and T. Konishi, Phys. Rev. **A40** (1989) 6130.

[9] T. Konishi and K. Kaneko, J. of Phys. A **23** (1990) L715 - L720

[10] A.J.Lichtenberg and B.P.Wood, Phys.Rev.A39 (1989),2153.

[11] J. M. Greene, J. Math. Phys. **20** 1183 (1979); D. Bensimon and L.P. Kadanoff, Physica **10D** 82 (1984); R.S. Mackay, J.D. Meiss, and I. C. Percival, Physica **13D** 55 (1984)

[12] D.K. Umberger and J. D. Farmer, Phys.Rev. Lett. **55** 661 (1985)

[13] C.F.F. Karney Physica **8D** 360 (1983); B.V. Chirikov and D. L. Shepelyansky, Physica **13D** 395 (1984); T. Kohyama, Prog. Theor. Phys. **71** 1104 (1984); Y. Aizawa ibid, 1419; T. Geisel, A. Zacherl, and G. Radons, Phys. Rev. Lett. **59** 2503 (1987); J.D. Meiss and E. Ott, Physica **20D** 387 (1986)

[14] N.N. Nekhoroshev, Russ. Math. Surv. **32**(1977), 1.

[15] See e.g., K. Kaneko,*Collapse of Tori and Genesis of Chaos in Dissipative Systems*, (World Sci. Pub., Singapore,1986); J. P. Crutchfield and K. Kaneko, "Phenomenology of Spatiotemporal Chaos", in *Directions in Chaos* (World Sci.Pub., Singapore,1987), and references cited therein.

[16] C. Froeschlé, Astron. Astrophys. **16** (1972),172.

[17] K. Kaneko and R. J. Bagley, Phys. Lett. **110A** (1985),435.

[18] H-t. Kook and J. Meiss,Physica **35D**(1989),65.

[19] H. Kantz and P.Grassberger J. of Phys. A **21** (1988),L127.

[20] K. Kaneko and T. Konishi, J. Phys. Soc. Jpn. **56** (1987),2993.

[21] T. Konishi and K. Kaneko, in *Cooperative Dynamics in Complex Physical Systems*, ed. H. Takayama (Springer,Berlin,1989).

[22] G. Paladin and A. Vulpiani, Phys. Lett. **118A**(1986), 14.

[23] T. Konishi, Prog. Theor. Phys. Suppl. **98** (1989) 19

[24] B. V. Chirikov and V. V. Vecheslavov , preprint "How fast is the Arnold diffusion?", Novosibirsk 89-72

Non-linear Behaviour in Tokamaks

J.A. Wesson

JET Joint Undertaking
Abingdon, Oxfordshire, England

The range of non-linear phenomena observed in tokamaks is extensive. Rather than summarise their behaviour, it is perhaps more interesting to choose specific subjects which present clearly identifiable theoretical problems. We shall look at three such cases:

i) Fast instabilities

ii) The sequence of events in disruptions

iii) Sawtooth reconnection

The problem of fast instabilities is widely misunderstood. It is generally assumed that the experimental observation of a fast growing instability can be understood if an appropriate mode with a fast growth rate can be found. As we shall see in the next section, this is not so.

In the early days of tokamak research it was common to hear the question - "What is the cause of disruptions?" It is now recognised that a disruption is usually a complex sequence of events posing several theoretical questions. We shall find possible explanations for some of the events, but still be left with a problem regarding the energy quench phase.

When sawtooth oscillations were first observed it was immediately apparent that the relaxation phase occurred on much too short a timescale for simple resistive rearrangement of the magnetic flux to occur. Kadomtsev suggested that the timescale could be understood if the reconnection takes place in a narrow layer at the $q = 1$ surface. It turned out that Kadomtsev's proposed model is indeed the solution of the resistive mhd equations for an $m=1$ instability. However, for large tokamaks at least, the observed sawtooth collapse time is an order of magnitude shorter than predicted by Kadomtsev's model. In the third section the reconnection process is re-examined and a new model with an order of magnitude faster reconnection is described.

i) Fast Instabilities

The procedure in linear stability calculations is to take an equilibrium solution of the equations and, assuming that perturbations have a time dependence $e^{\gamma t}$, to calculate the growth rate γ. A fast instability is then associated with a strongly unstable equilibrium.

It is clear that in most cases of interest this does not represent the actual behaviour. In tokamaks it is not possible to produce strongly unstable axisymmetric equilibria because the timescales required for equilibrium development are much longer than the timescale of fast instabilities.

We can attempt a quantitative description by using the approximation for the perturbation

$$\xi = \xi_o \exp \int_o^t \gamma(t)\,dt$$

where marginal stability is passed at a time taken to be t=0 and the perturbation at that time is ξ_o. Taking as a simple example $\gamma = \dot{\gamma} t$ we obtain

$$\gamma^2 = 2\dot{\gamma}\, \ell n \frac{\xi}{\xi_o}$$

Now if ξ is first observed at a level ξ_{obs} and if the growth rate is then γ_{obs}, we can write

$$\gamma_{obs} = \frac{1}{\tau_{eq}}\, 2\,\ell n \frac{\xi_{obs}}{\xi_o} \qquad (1)$$

where $\tau_{eq}(= \gamma_{obs} / \dot{\gamma})$ is the time taken for the changing equilibrium to produce a growth rate γ_{obs}.

Equation (1) makes the problem clear. The observed growth time is a few times less than a characteristic equilibrium time and this would seem to preclude the appearance of fast instabilities.

The problem can be made even clearer by considering a particular case and the sawtooth collapse on JET provides a carefully investigated example. Figure 1 shows the measured displacement of the peak of the soft X-ray radiation profile for three sawteeth. The displacement appears out of the noise level at ~ 1 cm and then increases to ~ 50 cms with a characteristic growth time of 25 μs.

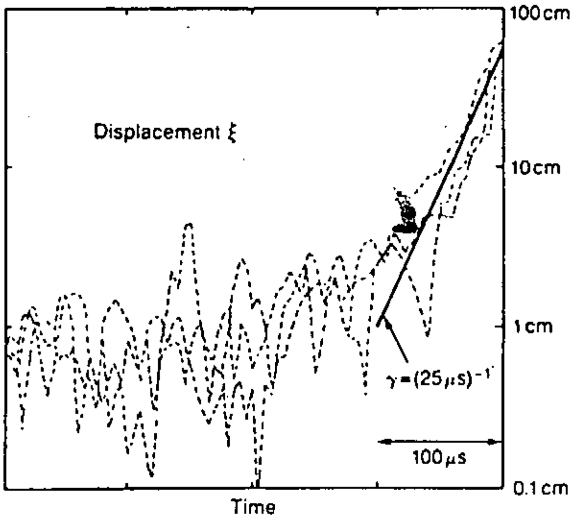

Figure 1 Graphs of the magnitude of the displacement, ξ, of the peak X-ray emission for three sawtooth collapses taken from different discharges. The initial noise level is ~ 1 cm and the growth rises out of this noise with a growth rate ~ (25 μs)$^{-1}$, increasing the displacement to ~ 50 cms in ~ 100 μs.

The expected behaviour depends somewhat on the particular instability imagined to underlie the behaviour, but the essential result does not depend on the instability. In all cases the time which would be taken for the equilibrium to evolve from marginal stability to the observed growth rate is ≥ 100 ms. Thus on a millisecond timescale the growth rate does not change. We should therefore be able to extrapolate the displacement back in time from the observed value using the observed growth rate. Looking 1 ms before the observed instability gives a displacement

$$\xi = (1\,cm)\exp - \left(\frac{1ms}{25\mu s}\right)$$

$$\sim 10^{-17} cm \quad .$$

This shows that the observed instability, even at its smallest amplitude has no connection with conventional linear theory. To say that the behaviour is non-linear does not, of course, contribute to our understanding. We need a new theoretical framework to deal with fast instabilities of this sort.

A tentative model is described in reference (1). This involves the coupling of two stability boundaries as illustrated in Fig. 2. When the first stability boundary is passed, stability is maintained by some weak stabilising effect. This allows progress to the second stability boundary where the weak effect fails to provide stability. At this point the basic instability would have a fast growth rate but this has been suppressed. After passing the second stability boundary the instability then grows slowly until, at some unobservable amplitude (~ the ion Larmor radius perhaps) the weak effect is lost and transition to the fast growth of the basic instability occurs, giving the appearance of a spontaneous fast instability.

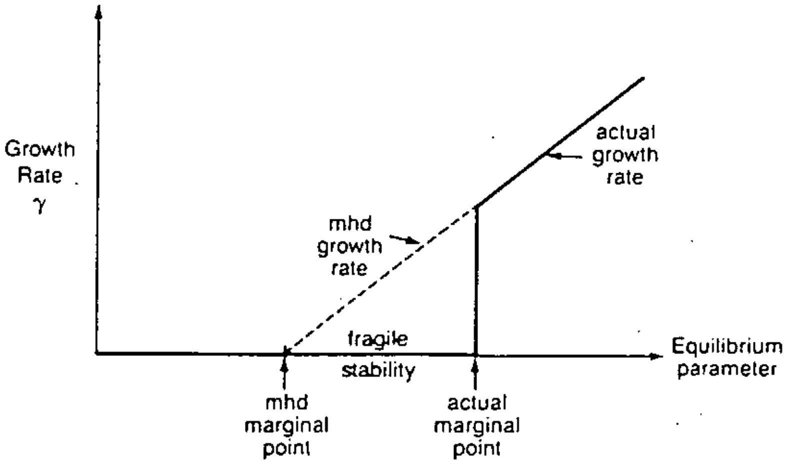

Figure 2 Illustrating a type of behaviour which would be consistent with the experimental observations. A weak stabilising effect provides a fragile stability beyond the mhd stability boundary. This allows the build up of free energy which is then suddenly released when the actual stability boundary is reached.

ii) Disruptions

Disruptions often involve a quite complex sequence of events (2). The observed growth of mhd instabilities at the time of the disruption is a clear indication that these instabilities play a crucial role. However the principal threats posed by disruptions are related to the subsequent fast current decay which transfers current to the vacuum vessel producing very large forces, and the generation of large currents of relativistic electrons. Even the basic mhd features are more complicated than expected. In JET the form of the energy loss is not consistent with any of the theoretical models and the negative voltage spike does not appear at the expected time. These issues have been addressed in a number of papers and the present understanding is outlined below.

Figure 3 shows the behaviour of the current, temperature and loop voltage in a typical JET disruption. There has been a precursor growth of mhd instability prior to the events shown and it seems likely that the mhd perturbations are responsible for the initial fall in the temperature. However careful examination of the soft X-ray behaviour reveals a spatial structure which does not appear to be consistent with the theoretical mhd models. These models predict either multi-mode turbulence or a gross non-linear behaviour in which the m=1 and m=2 modes drive each other through profile effects. What is seen experimentally is a large modification of the soft X-ray profile, this modification having an m=1 structure. However the spatial structure of the change has the form of an "erosion" of the profile and does not correspond to the displacement expected from the theory of m=1 modes. This important issue is therefore unresolved.

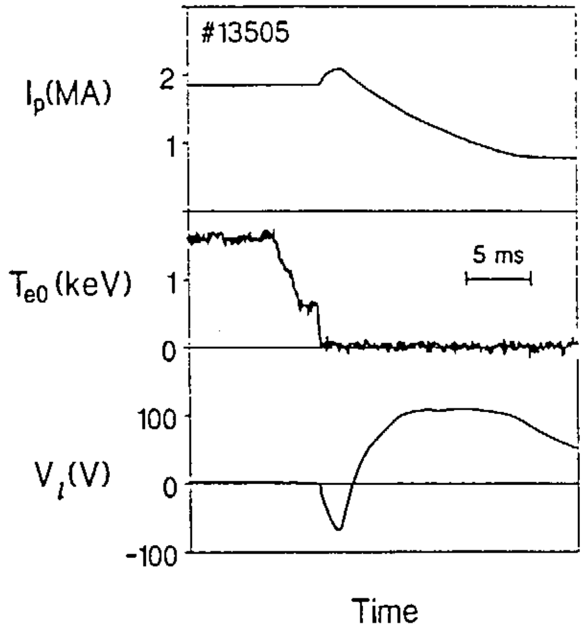

Figure 3 The temperature drop in the disruption occurs in two phases. The positive current and negative voltage spikes appear only after the second phase.

If the initial fall in temperature is due to the mhd instability then we would expect that it would also produce the observed negative voltage spike. The delay in the appearance of the spike therefore needs an explanation. A theoretical model has been developed in which the current flattening associated with the mhd instability does not extend to the plasma surface (3). This gives rise to a surrounding negative current sheet. The current configuration is frozen on the millisecond timescale because of the high electrical conductivity of the plasma. However this conductivity is suddenly reduced by orders of magnitude when the plasma temperature undergoes its second stage fall, reaching a very low temperature. The negative current then rapidly diffuses out of the plasma producing the current increase shown in figure 3 together with the associated negative voltage spike. Numerical simulations based on this model have reproduced the observed behaviour.

The final rapid fall in temperature is believed to be due to an impurity influx (4). In this model the rapid decay of the current is not due to plasma turbulence but results simply from the high resistivity of the cold plasma.

Another consequence of the increased resistivity is the production of a large current (~ MA) of runaway electrons. This arises because the critical parameter for runaway is proportional to the product, ET, of the electric field and the electron temperature. It is therefore proportional to $\eta j T$ and hence to $1/T^{1/2}$. Consequently a fall in temperature by a factor of 100 leads to an order of magnitude increase in the runaway parameter. This gives rise to a complicated runaway process which results in the observed runaway current. The velocity distribution of the electrons is unstable and calculations have been carried out to investigate the types of possible relativistic non-linear behaviour.

It is seen from the above account that disruptions can involve a complex sequence of events which have been only partly explored.

iii) Sawtooth Reconnection

It is well known that the sawtooth relaxation oscillations observed in tokamaks are not understood. In particular the Kadomtsev model appears to be in conflict with a number of experimental results. It is not clear therefore whether, or when, reconnection of the Kadomtsev type takes place. This makes it important to examine the assumptions of the model. As a result of such an examination it has been found that the assumption of resistive behaviour is seriously in question (5).

If full reconnection of the helical flux within the q=1 surface takes place on the observed timescale of the sawtooth collapse then we can calculate the resulting electric field at the reconnection layer. If we then use Ohm's law to calculate the drift-velocity of the electrons carrying the reconnection sheet current we obtain

$$v_d \sim (1-q_o)\,\frac{r_1}{R}\,\frac{\tau_e}{\tau_c}\,\omega_c\, r_1$$

Where q_o is the axial value of the safety factor, r_1 is the radius of the q=1 surface, R is the major radius, τ_e and τ_c are the electron collision time and the sawtooth collapse time and ω_c is the electron cyclotron frequency.

Using typical JET values gives $v_d \sim 3 \times 10^8$ ms^{-1} (= c). It is clear that under these circumstances the resistive model is inappropriate and that the electrons would undergo strong runaway.

A current carried by runaway electrons sees a very low resistance. However, although the electrons entering the layer rapidly acquire a large velocity in the direction of the q=1 field lines, they are immediately swept out of the layer into the magnetic island. Thus the high current density has to be maintained by the continuous acceleration of electrons entering the layer. Consequently, rather than presenting a low impedance, this form of reconnection gives a high impedance.

When electron inertia dominates, the appropriate form of Ohm's law is

$$E + \mathrm{v} \times B = \frac{m}{ne^2}\, \mathrm{v}.\nabla \mathrm{j} \quad . \tag{2}$$

The electric field in the layer is given by the rate, vB*, at which flux is brought in to the layer, B* being the helical magnetic field at the edge of the layer. Thus, using Ampere's law,

$$\nabla \mathrm{j} \sim \frac{B*}{\mu_o \delta}$$

where δ is the layer thickness, equation (2) gives

$$\delta \sim \frac{c}{\omega_p} \quad , \tag{3}$$

and the layer thickness is of the order of the collisionless skin depth.

The conventional reconnection analysis provides the expression for the reconnection time, τ, in terms of the layer thickness

$$\tau \sim \frac{r_1}{\delta}\, \tau_A$$

where $\tau_A = r_1 / (B^*/\sqrt{\mu_o \rho}\,)$ and so, using relation (3), the reconnection time is

$$\tau \sim \frac{r_1\, \omega_p}{c}\, \tau_A \quad . \tag{4}$$

Comparing numerical predictions we find that for a typical JET sawtooth collapse having a timescale of 100 μs the prediction of Kadomtsev's model is ~ 3 ms whereas relation (4) gives ~ 300 μs. It is clear that the new model gives better agreement but there are many reservations since we do not understand the sawtooth mechanism.

Summary

From the many non-linear processes occurring in tokamaks we have chosen three quite different phenomena. Firstly, the problem of fast instabilities which is quite subtle and requires some new thinking. Secondly disruptions, which are found to be rather complex. Although explanations have been provided for some of the features, the initial energy quench does not appear to be consistent with existing theoretical models. Finally, an analysis of the Kadomtsev reconnection model leads to doubts about the applicability of the resistive Ohm's law and suggests that the effect of electron inertia would be predominant.

References

1. Wesson, J.A., Edwards, A.W. and Granetz, R.S., To appear in Nuclear Fusion (1991).

2. Wesson, J.A. et al., Nuclear Fusion 29 (1989) 641.

3. Wesson, J.A., Ward, D.J., and Rosenbuth, M.N., Nuclear Fusion 30 (1990) 1011.

4. Ward, D.J., Gill, R.D., Morgan, P.D. and Wesson, J.A., in Controlled Fusion and Plasma Heating (Proc. 15th Eur. Conf. Dubrovnick, 1988), Vol. 12B, Part I, European Physical Society (1988) 330.

5. Wesson, J.A. Nuclear Fusion 30 (1990) 2545.

Fluctuation Spectrum of Ion Temperature Gradient Driven Modes in Sheared Magnetic Fields

Takashi Tuda, Masatoshi Yagi and Masafumi Azumi
Japan Atomic Energy Research Institute

Introduction

The electrostatic fluctuation due to the ion temperature gradient driven mode[1] is considered to cause the anomalous ion heat transport in L-mode discharges of a tokamak. Because of importance of this mode on the present day tokamak, many authors studied the linear properties and the nonlinear saturation mechanism of the mode. However, understanding on the saturation mechanism, the estimated fluctuation level and also the spectrum shape is not still satisfactory and the resulting expressions for the heat transport do not always agree with experimental results in the wide range of discharge parameters until now. For these reasons, we have developed several kinds of fluid simulation models, which include the toroidal effect, neoclassical effects and the impurity ion response, in order to investigate the ion temperature gradient driven mode in various situations and to analyze the experimental fluctuation measurements.

Model

As the first step of our study, we investigated the linear and nonlinear properties of η_i mode by employing the model of Hamaguchi and Horton [2]. The electron Boltzman response and the quasi neutrality condition are assumed. The ion fluid velocity perpendicular to the magnetic field consists of the ExB drift motion, the ion diamagnetic drift motion and the polarization drift motion. The normalized system of model equations is given as

$$(1-\nabla_\perp^2)\frac{\partial\phi}{\partial\tau} = -(1-K\nabla_\perp^2)\frac{\partial\phi}{\partial y} - \nabla_{//}v + \{\phi,\nabla_\perp^2\phi\} - \mu_\perp\nabla_\perp^4\phi. \quad (1)$$

$$\frac{\partial v}{\partial \tau} = -\nabla_{//}(\phi+p) - \{\phi,v\} + \mu_{\perp}\nabla_{\perp}^{2}v + \mu_{//}\nabla_{//}^{2}v. \qquad (2)$$

$$\frac{\partial p}{\partial \tau} = -K\frac{\partial \phi}{\partial y} - \Gamma\nabla_{//}v - \{\phi,p\} + \chi_{\perp}\nabla_{\perp}^{2}p + \chi_{//}\nabla_{//}^{2}p. \qquad (3)$$

Key variables are normalized as

$$x = \frac{x}{\rho_s},\ y = \frac{y}{\rho_s},\ z = \frac{z}{L_n},\ \ \tau = \frac{tc_s}{L_n}$$

and

$$\phi \equiv \frac{e\phi}{T_e}\frac{L_n}{\rho_s},\ v \equiv \frac{v_{//}}{c_s}\frac{L_n}{\rho_s},\ p \equiv \frac{p_i}{p_{i0}}\frac{L_n}{\rho_s}\frac{T_i}{T_e}$$

where $c_s \equiv (\frac{T_e}{m_i})^{1/2}$, $\rho_s \equiv \frac{c_s}{\omega_{ci}}$ and $L_n \equiv -(\frac{d}{dx} \ln n_0)^{-1}$, $L_T \equiv -(\frac{d}{dx} \ln T_{i0})^{-1}$.

Nondimensional parameters K and Γ are defined by

$$K \equiv \frac{T_i}{T_e}(1+\eta_i),\ \ \eta_i \equiv \frac{L_n}{L_T}\ \text{and}\ \ \Gamma \equiv \gamma\frac{T_i}{T_e},$$

and the Poisson bracket $\{f,g\}$ is defined by

$$\{f,g\} = e_z\cdot\nabla_{\perp}f \times \nabla_{\perp}g = \frac{\partial f}{\partial x}\frac{\partial g}{\partial y} - \frac{\partial f}{\partial y}\frac{\partial g}{\partial x}.$$

Linearlized equations (1)-(3) have two branchs of solution. One is the electron drift wave which has the maximum real frequency at $k_{\perp}\rho_s \sim 0.5$ and is stabilized by the magnetic shear effects by out-going wave propagation. Another branch corresponds to the ion drift wave (η_i-mode) unstable for $\eta>\eta_c$ and its real frequency increases monotonically with $k_{\perp}^{2}$ approximately.

Steady state solution

Equations (1)-(3) has a solitary double vortex solution similar to the electron drift wave of Meiss and Horton[3] in the uniform magnetic field when dissipative effects are absent ($\mu_{//}= \mu_{\perp}= \chi_{//}= \chi_{\perp}= \Gamma= 0$). This solitary wave can propagate oblique to the magnetic field and the fluctuation amplitude is in the the same order as the value estimated from the mixing length theory. Propagation velocity U of this solution in the y-direction is limited with the velocity $U<-K$ or $U>1$. In these regions, the linear wave is inhibited to propagate. Existence of this kind of steady state solution is important for the nonlinear behavior of ion temperature gradient driven mode.

Simulation results

We studied the saturation mechanism of the ion temperature gradient driven mode by using simple 2-D and 3-D simulation codes of fluid model. In 2-D model with single resonance surface, the fluctuation energy is transferred to the longest wave length region (the inverse cascade) at the initial stage. After the amplitude of the mode with maximum growth rate ($k_\perp\rho_s \sim 0.8$) reaches the level of a mixing length theory ($e\phi/T \sim 1/k_\perp L_n$), the spectrum becomes broad.(see figure 1) For short wavelength region($k_\perp\rho_s > 1$), the spectrum behaves $\phi^2 \propto k_\perp^{-9}$. The longest wavelength mode ($k_\perp\rho_s \ll 1$, weakly unstable) has the largest fluctuation energy.

In 3-D case, the situation is quite different. The modes which have the large radial size are stabilized by the modes on neighboring rational surfaces and the fluctuation spectrum has a peak at the shorter wavelength region ($k_\perp\rho_s \sim 0.3$). Many double vortex structures ($k_\perp\rho_s \sim 0.6$) are formed and sustained for the time interval longer than 20 L_n/c_s.

Conclusions

We studied the saturation mechanism of the ion temperature gradient driven mode by using simple 2-D and 3-D simulation codes of fluid model. Many double vortex structures ($k_\perp\rho_s \sim 0.6$) are formed and are sustained for the long time, more than 20 L_n/c_s, which is longer than the linear growth time. The resulting thermal diffusion should be much smaller than the prediction from a mixing length theory by this sturucture formation.with long life

[1] B. Coppi , M. N. Rosenbluth and R. Z. Sagdeev, Phys.Fluids 10 582 (1967)
[2] S. Hamaguchi and W. Horton, Phys.Fluids B2 1833 (1990).
[3] Meiss and Horton, Phys.Fluids 26 990 (1983).

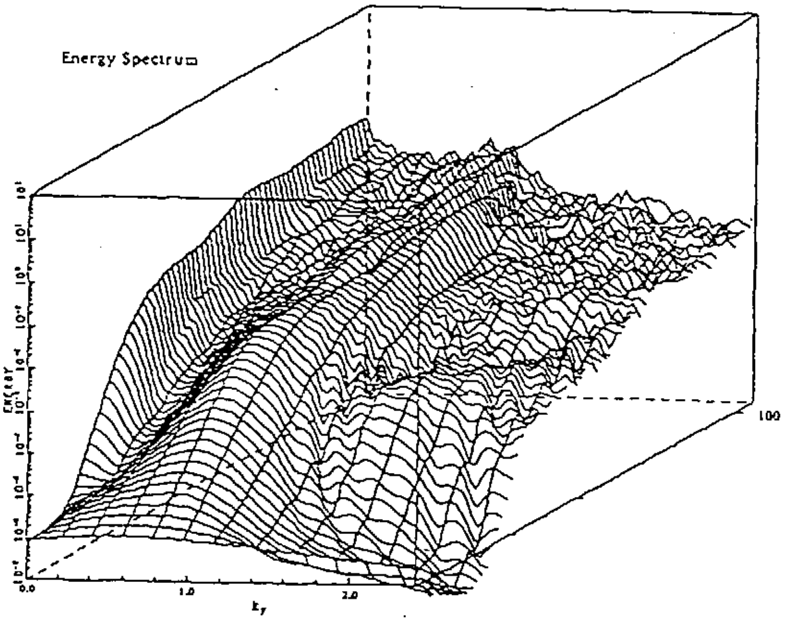

Figure 1 Time behavior of fluctuation spectrum. L_x = 80, K=2.0, $\mu_\perp$= 0.1, $\chi_\perp$=0.1, $\mu_{//}$= 1.0, $\chi_{//}$=1.0, L_n/L_s = 0.1.

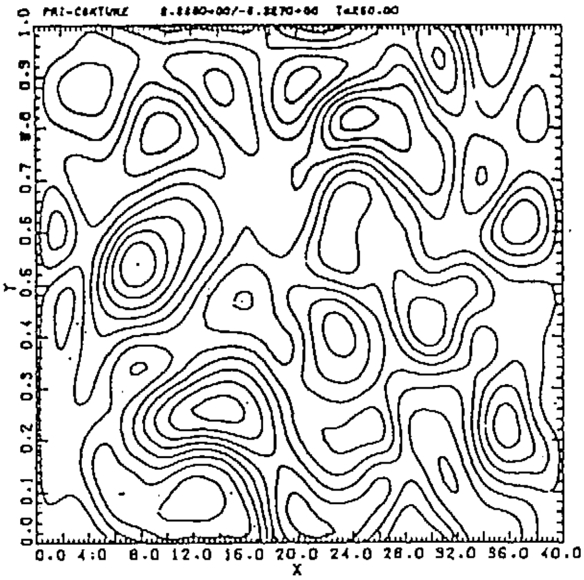

Figure 2 The contours of constant ϕ at t=250L_n/c_s by 3D simulation. L_x = 80, K=2.0, $\mu_\perp$= 0.1, $\chi_\perp$=0.1, $\mu_{//}$= 1.0, $\chi_{//}$=1.0, L_n/L_s = 0.1.

EQUILIBRIA AND DYNAMICS OF TEMPERATURE IN A FUSION REACTOR PLASMA

Hans Wilhelmsson

Institute for Electromagnetic Field Theory and Plasma Physics
Chalmers University of Technology
S-412 96 Göteborg, Sweden

1. INTRODUCTION

Equilibria and dynamics of plasma temperature profiles are central topics in present-day research on fusion plasmas. In view of future possibilities of approaching ignition in the large fusion machines extensions of prevailing theory or new methods for describing these phenomena have to be deviced. A model equation for describing the temperature evolution has to include the effects of a combination of external heating (from HF and/or NBI sources) and alpha particle heating (from light-nuclei reactions) and the effects of losses, like bremsstrahlung losses, as well as the simultaneous effects of diffusion and the presence of boundaries. The corresponding partial differential equation (PDE) is an elaborate form of a reaction-diffusion equation. It is found to exhibit interesting features from principal as well as practical points of view. Even for forms which are special cases of the one to be discussed here, it has been demonstrated [1] that no exact analytic solutions can be obtained to such equations for arbitrary initial conditions. One therefore has to resort to other methods of analysis [2-8].

2. The principle of central expansion

It is the purpose of the present paper to study reaction-diffusion equations by means of a new technique, the central expansion, which simultaneously accounts for the process of diffusion and the effects of sources, losses (represented by different powers of the temperature) as well as the effects of boundaries. Various possibilities will be discussed of using new results from the central expansion analysis for describing the dynamics of complicated realistic systems. The procedure of how these results can be obtained by means of the central expansion will be described in detail. It may be useful in this connection to consider the accompanying scheme of analysis.

SCHEME OF ANALYSIS

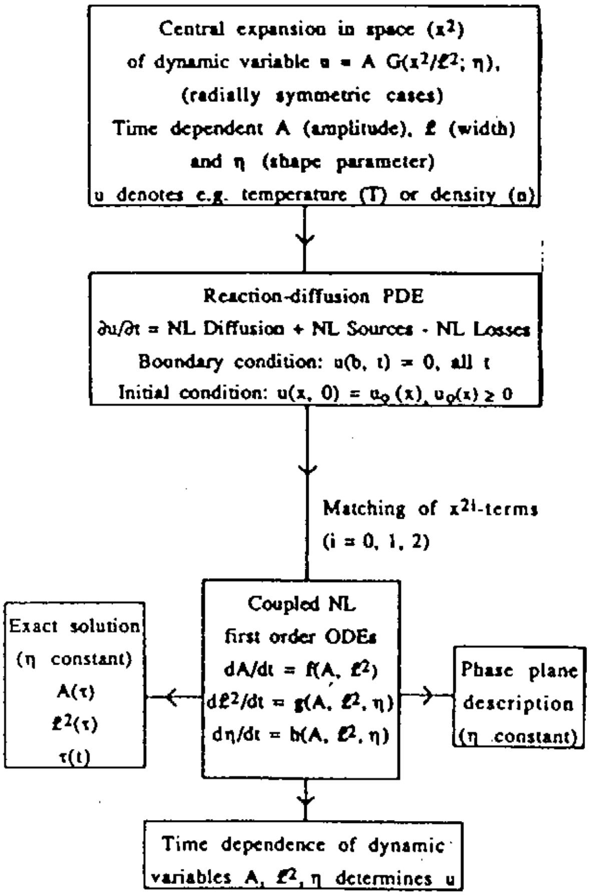

The starting point in the process of analysis is to construct a certain form of expansion, which for radially symmetric (or spatially symmetric one-dimensional) profiles contains terms of increasing powers of the spatial variable squared, where the terms have time-dependent coefficients. The expansion can be expressed as a product of the central value (amplitude) A(t) and a series in powers of x^2, including $\ell^2(t)$, where ℓ is the width of a profile, and $\eta(t)$, which is a shape parameter, with ℓ as well as η depending on time. By proper account of flux conditions at the boundary the effects of the boundary can be included directly in the form of the expansion.

The next step is to introduce the expansion into the original reaction-diffusion equation, and to carry out the differentiations in space and time and the expansions of the powers in the source and loss terms. Matching separately the terms which do not depend on x^2 as well as the x^2 terms and the x^4 terms one obtains as a result three coupled nonlinear first order differential equations in time for the time-dependent variables A, ℓ^2 and η, as indicated in the scheme of analysis. One important task in the forthcoming analysis will be to determine the forms of the algebraic expressions f, g and h, which define the right-hand membra of the three coupled equations. These equations can be used to study the equilibria and dynamics of the system. The initial values A_0, ℓ_o^2 and η_0 can be given arbitrary values. This freedom allows for consideration of a wide variety of dynamic situations, where the variables may deviate far from equilibrium values, which they may finally approach.

The three coupled nonlinear first order differential equations are well suited for computer analysis by which A, ℓ^2 and η can easily be determined as a function of time for various initial values of these variables. The dynamic variable u is accordingly determined as a function of x and t from the form of the central expansion, defining at any moment a certain spatial temperature or density profile. A unified description for one-, two-, and three-dimensional situations can be given for radially symmetric situations. Profiles of equilibria and the dynamic approach to equilibria from initial states, which deviate appreciably from the equilibrium states, can be determined with high accuracy.

There exists, however, also other possibilities of exploiting the coupled nonlinear first order ODEs. By chosing for the shape parameter η a suitable constant value, only two coupled equations for A and ℓ^2 remain to be studied. For certain cases, i.e. removed boundary and neglect of loss term, the coupled equations can be solved exactly by introducing a certain transformation in time $\tau(t)$ and expressing A and ℓ^2 in terms of τ, [2].

Alternatively, and even more interesting, the two coupled equations for A and ℓ^2, assuming η constant, can be treated by a phase plane description , where A and ℓ^2 are the co-ordinates in a Cartesian system. The evolution of the system from any initial point (A_0, ℓ_o^2) can then be easily traced by noticing the signs of the rate of change in time of A and ℓ^2 at each point of the evolution. These signs are generally easily determined by relating the position of a particular point (A, ℓ^2) to the cardinal curves defined by dA/dt = 0 or $d\ell^2/dt = 0$, i.e. $f(A, \ell^2) = 0$ or $g(A, \ell^2, \eta_e) = 0$. In particular the cross-points where $f(A,\ell^2) = g(A, \ell^2, \eta_e) = 0$ correspond to equilibria. A phase plane description may, accordingly, provide full insight into the structure of dynamic behaviour of the system for different initial states. The approximation introduced by chosing a particular value of η can obviously be relaxed by introducing at any moment, i.e. for any point of the phase trajectory, the instantaneous value of η given by the full solution of the three coupled equations.

The original reaction-diffusion equation can also be studied by direct numerical analysis. The results are in excellent agreement with those obtained by means of the central expansion approach. The initial profiles allow for more specific and complicated features in the case of direct numerical evaluation than can be specified by the central expansion including a limited number of terms. This freedom of choice is at the expense of higher complexity of the computer calculations. With due regard to the advantages of a phase-plane description, based on the central expansion approach, this method and the direct numerical analysis method may be considered complementary for the understanding and description of the results.

A remarkable result of the present investigation is the high accuracy obtained by using the central expansion, and the wide range of applicability that such an approach seems to have. It can be used for analysis of systems which are far from equilibrium, e.g. in combination with phase-plane description, in contrast to variational methods which apply to small deviations from equilibrium. It also has certain advantages in comparison with direct computer calculations from the original nonlinear PDE equation, in that insight into the roles of the physical processes in the dynamic evolution of the systems is facilitated. It furthermore aids in the determination of the number of equilibria for each case. Moreover, the computational use of the coupled equations, obtained from the central expansion, is particularly simple.

The parameter values chosen for the examples correspond to situations of interest for describing equilibria and dynamics of temperature in a future fusion reactor plasma. The results indicate the interesting fact that several different equilibria may occur for the same set of parameter values in the original equation.

REFERENCES

1. Jancel, R. and Wilhelmsson, H., Physica Scripta (to appear) (1991).
2. Wilhelmsson, H. and Jancel, R., Physica Scripta 41, 269 (1990).
3. Wilhelmsson, H., Nucl. Phys. (to appear) (1990).
4. Wilhelmsson, H., Phys. Rev. A., 38, 1482 (1988).
5. Wilhelmsson, H., Benda, M., Etlicher, B., Jancel, R. and Lehner, T., Physica Scripta 38, 863 (1988).
6. Le Roux, M.-N. and Wilhelmsson, H., Physica Scripta 40, 674 (1989).
7. Anderson, D., Elevant, T., Hamnén, H., Lisak, M., Persson, H., Physica Scripta 42, 574 (1990).
8. Galaktionov, V.A., Dorodnitsyn, V.A., Elenin, G.G., Kurdyumov, S.P. and Samarskii, A.A., Itogi Nauki i Tekniki, Ser. Sov. Probl. Mat., Nov. Dost. 28, 95 (1986); English translation: Journal of Soviet Mathematics (JOSMAR) 41, 1222 (1988).

Model for Marfe- Detached Plasma Transition in Tokamaks

P.K. Kaw, S. Deshpande, K. Avinash and S. Rath
Institute for Plasma Research,
Bhat, Gandhinagar - 382 424,
INDIA.

ABSTRACT

The nonlinear saturated state of the radiative thermal-condensation instability responsible for the phenomenon of marfes observed in tokamak edge plasmas, has been investigated. In essence, the problem is one of studying two-dimensional thermal equilibria in the tokamak edge where perpendicular and parallel heat conduction balances the radiated power and heat flux to the limiter. In certain reasonable limits, the relevant nonlinear Poisson's equation can be solved exactly and the solution displays many features of the observed marfe-Detached Plasma transition. Numerical results taking realistic temperature dependences for thermal conductivity coefficients and generally accepted coronal radiation model are also presented.

PROPAGATIONS OF DRIFT WAVES IN TOROIDAL PLASMA SYSTEMS

S. Yoshikawa and C. Z. Cheng
Princeton University, Plasma Physics Laboratory
Princeton, NJ 08543

Abstract

Drift wave patterns in toroidal plasmas are studied. The dispersion relation was simplified to retain both the shear and the toroidal coupling effects. Since the dispersion relation does not depend on the toroidal angle, ϕ, the dispersion is solved in the two-dimensional space made up with minor radius and poloidal angle. The dispertion relation can be reduced into second-order, partial differential equations of a hyperbolic type. The one–dimensional convective mode analysis, which was originated in the 1960's, was extended into the two–dimensional analysis. Depending on the strength of the magnetic shear, one can obtain either the convective or the localized solutions. The results show that the plasma is expected to be unstable for large azimuthal mode number and that the plasma instability tends to be more stabilized for large mass ions.

STATISTICAL MECHANICS USING SYMBOLIC DYNAMICS

Roscoe B. White
Princeton Plasma Physics Laboratory
Princeton, New Jersey 08543
and
Alexander B. Rechester
Massachusetts Institute of Technology
Cambridge, MA 02139

Symbolic dynamics[1] provides a means of partitioning phase space so that information concerning the particle orbits is imbedded in the partitioning. Consider a sequence of numbers $x_0, x_1, x_2 \cdots$ given by the dynamics, which we call an orbit, the subscript refering to time. Define a sequence of integers $s_0, s_1, s_2, \cdots$ associated with this orbit. If there is a unique correspondence between the symbol sequence and the orbit as the length of the orbit becomes infinite, then the set of such allowed sequences entirely describes the dynamics. Many examples of symbolic dynamics are known, the simplest being that associated with the logistic map, which exhibits the period doubling route to chaos. This map is given by

$$x_{t+1} = \alpha x_t(1 - x_t) \tag{1}$$

where $0 < x_t < 1$ and $0 < \alpha < 4$.

The symbolic sequence associated with x_t is defined by

$$s_t = \begin{cases} 0 & \text{when} \quad x_t < \frac{1}{2} \\ 1 & \text{when} \quad x_t > \frac{1}{2} \end{cases} . \tag{2}$$

We use this map as an example, but the methods are similar also for two dimensional maps such as the Henon map and the Chirikov-Taylor map, which we have also investigated.

Consider a truncated sequence $S = s_0, s_1, \cdots, s_{n-1}$ and let $D(S)$ be the set of all x_0 which produce the sequence S as time is advanced. Each of the 2^n sequences S defines a coarse grain element of phase space. Upon advancing in time we have

$$s_0, s_1, \cdots s_{n-1} \longrightarrow s_1, s_2 \cdots s_n \tag{3}$$

and in the case of the logistic map there are two possible resulting sequences, corresponding to $s_n = 0, 1$. That is, all points in one phase space element $D(S)$ move in one time step to at most two other elements.

Now introduce a coarse–grain approximation, i.e. approximate the distribution function $f(x,t)$ as constant in each coarse grain domain $D(S)$. Similarly, let $D(S, S')$ be the image of the set $D(S)$ in coarse grain element $D(S')$ in one time step. The coarse–grain approximation to the branching ratios is then given by

$$\gamma(S, S') = \frac{D(S, S')}{\sum_{S''} D(S, S'')} \tag{4}$$

The sets $D(S)$ and the branching ratios $\gamma(S, S')$ are easily found numerically.

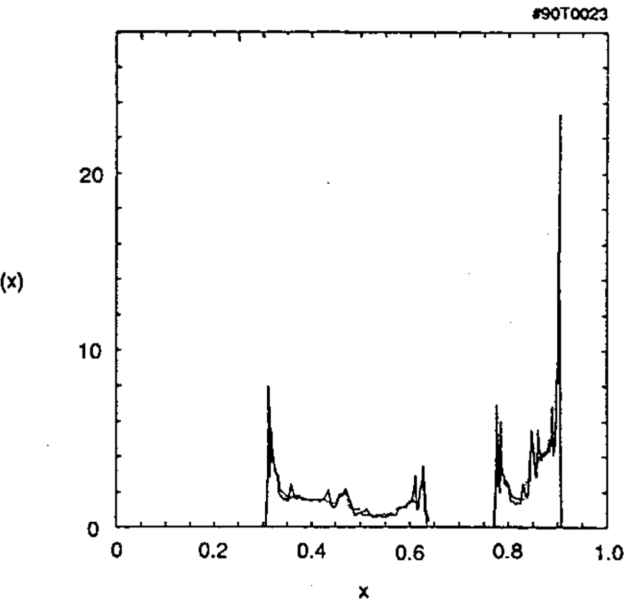

Figure 1: Invariant distribution $f(x)$ for the chaotic attractor produced by the logistic map, $\alpha = 3.62$. Shown is the result from orbit averaging (solid line) and that from solving Eq. 5, $n = 18$

The symbolic kinetic equation[2] for the coarse grain probabilites $P_t(S)$ takes the form

$$P_{t+1}(S) = \sum_{S} P_t(S')\gamma(S,S') \tag{5}$$

and this equation can be readily solved for the steady state probabilities $P(S)$. An example is shown in Fig. 1, which shows the solution to Eq. (5) as well as the result of directly averaging over a long orbit. We find that the solution of the symbolic kinetic equation generally requires much less computing then orbit averaging over the necessarily long particle orbits.

Any statistical quantity can be readily computed from the probabilities $P(S)$ and the branching ratios $\gamma(S,S')$. For example the correlation function is given by

$$C(\tau) = \sum_{s_\tau} x_\tau \Pi_{t=1}^{\tau} \sum x_0 P(s_0)\gamma(s_0,s_t). \tag{6}$$

An example is shown in Fig. 2.

The branching ratios $\gamma(S,S')$ define a network, or Markov chain, whose topological properties are related to the physical properties of the system. Systems with long correlation time have networks with relatively few closed loops, whereas systems with short correlation time have networks with high topological connectivity. An example is shown in Fig. 3 for the logistic map for $\alpha = 3.71$, $n = 6$. This network has high topological connectivity, corresponding to the short correlation time apparent from Fig. 2.

In Fig. 4 is shown the power spectrum $P(w)$, which is the Fourier transform of the correlation function, for the logistic map, $\alpha = 3.94$. The "fluctuations" have a broad spectrum with two peaks.

This technique has also been applied to the Henon map (strange attractor) and the Chrikov–Taylor map (Hamiltonian), with similar agreement found between orbit averages and the solution

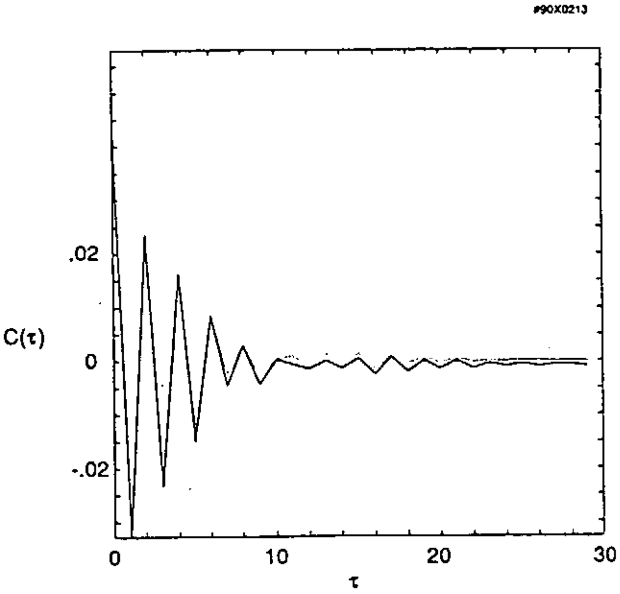

Figure 2: Correlation function for the logistic map, $\alpha = 3.71$. Shown is the result of orbit averaging (solid line) and the coarse grain result from Eq. (6).

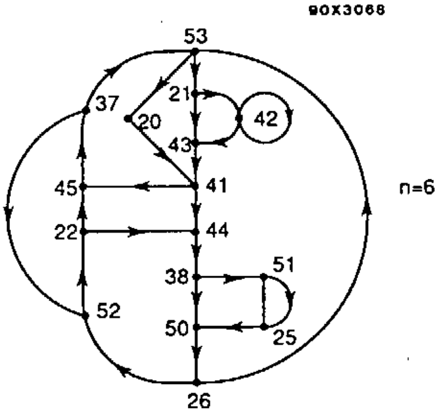

Figure 3: Network diagram for the logistic map, $\alpha = 3.71$, $n = 6$. The points indicate coarse grain elements, labelled using a shorthand designation[2] for the sequences, and the arrows show the effect of advancing in time.

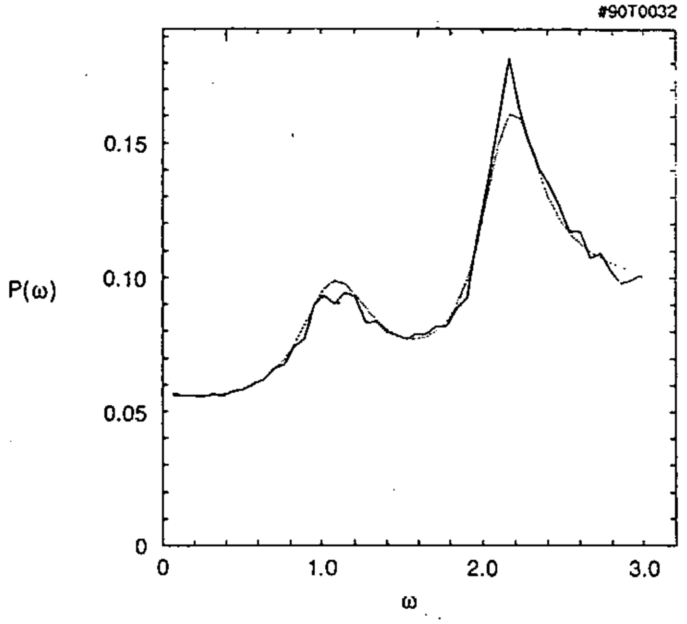

Figure 4: The power spectrum $P(w)$ obtained from the correlation function for the logistic map, $\alpha = 3.94$. The line is the result of an orbit average and the dotted line the coarse–grain result from Eq. (6).

to the symbolic kinetic equation. The results indicate that the use of symbolic dynamics can lead to a rapid calculation of the statistical properties of chaotic sytsems, and give insight into their dynamical properties.

Acknowledgments This work is supported by U.S. Department of Energy Contract No. DE–AC02–76–CHO3073.

References

[1] R.L. Devaney, **An Introduction to Chaotic Dynamical Systems**, (Addison Wesley, 1989), p.184, 189.

[2] A.B. Rechester and R.B. White, *Symbolic Kinetic Equation for a Chaotic Attractor*, submitted to Phys. Rev. Lett.

Diffusion Through Stochastic Webs in Two and More Dimensions

by

Allan J. Lichtenberg
EECS Dept. University of California, Berkeley, CA 94720

Extended Summary

Hamiltonian systems of coupled oscillators or their related area preserving mappings will have a connected web of stochasticity in the action space if the system has three or more degrees of freedom. This intrinsic property of higher-dimensional systems is known as the Arnold web and the diffusion through the web is called Arnold diffusion [1]. A connected web of stochasticity can also be obtained in two degrees of freedom from a mapping derived from a linear oscillator that is perturbed by a periodic force which is harmonically related to the linear oscillator [2, 3]. However, the phase space topology and the diffusion are quite different in the two degree of freedom system than in the higher degree system.

With three or more degrees of freedom resonances of all order between the primary oscillators are coupled together, making a web dense within the phase space [4]. Since stochasticity exists generically along the separatrices of these resonances, and particles in a stochastic phase space are free to explore all parts of it, it is possible for particles within the stochastic web to eventually approach arbitrarily close to all other points in the phase space. The diffusion rate along the stochastic layers is exponential in the ratio of the harmonic resonance frequencies, and is therefore generally extremely slow [4, 5].

The topology and the diffusion through a stochastic web in two degrees of freedom has quite different properties from the higher degree-of-freedom system. Near-resonance exists everywhere in the phase plane, but is broken by the interaction term. This leads to a mesh of exactly resonant elliptic and hyperbolic fixed points. The elliptic fixed points are surrounded by Kolmogorov Arnold Moser (KAM) curves which isolate the phase space in their vacinity. The hyperbolic points are joined by the stochastic web. The transport through the web occurs by diffusion across the stochastic layer, from one web to another, rather than along the layers as in the Arnold diffusion. Since the web, as well as the diffusion rate, is exponentially thin in the harmonic ratio, the effective diffusion rate is not exponential but rather follows a power law of the frequency ratio [6].

We illustrate these contrasting behaviors with two mapping systems. For the two degree of freedom problem we consider the motion of a charged particle in a magnetic field perturbed by a periodic δ-function electric field. The differential equation for the motion then has a mapping representation [3]

$$\begin{aligned} u_{n+1} &= (u_n + K_\alpha \sin\upsilon_n)\cos\alpha + \upsilon_n \sin\alpha, \\ \upsilon_{n+1} &= -(u_n + K_\alpha \sin\upsilon_n)\sin\alpha + \upsilon_n \cos\alpha, \end{aligned} \tag{1}$$

where $\alpha = \omega_c T$ is the rotation angle between kicks, K_α is the stochasticity coefficient, and u and υ are the normalized velocity components. At a resonance we have $\alpha = 2\pi p/q$. Taking $p = 1$ for simplicity, we see that q is the number of δ-function kicks per gyroperiod. There is an approximate q-fold rotational symmetry, and, for $q = 2$, 3, 4, and 6, there is also translational symmetry. The combination of these symmetries tiles the phase space by the separatrix joining the unstable periodic points of the mapping. For example, a piece of the resulting phase space is shown in Fig. 1, for $q = 4$ and $K_\alpha = 0.5$, for a few initial conditions, showing both the KAM surfaces within a tile, and the stochastic continuous web surrounding the separatrix. A blow up of the phase space near a hyperbolic fixed point is shown in Fig. 2.

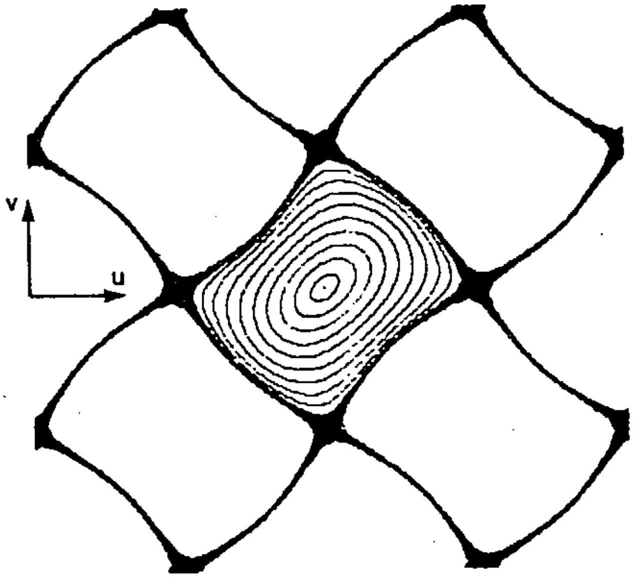

FIG. 1. A portion of the phase space with a 4:1 resonance, showing the stochastic web and a few curves of constant Hamiltonian within a tile.

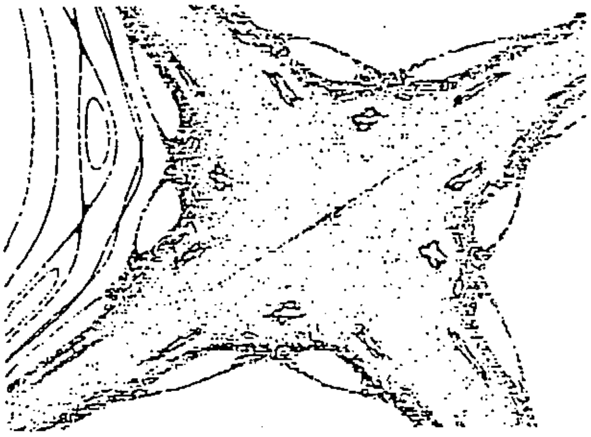

FIG. 2. Structure of the phase space in the neighborhood of an x point of the stochastic web for $K_\alpha = 0.4$.

The basic assumption made for calculating the global diffusion is that the stochastic region is ergodic. This implies that the stochastically available canonical phase space out to the KAM barrier is uniformly occupied in the asymptotic (long time) limit [4]. The number of steps n needed for a separatrix crossing is, then, just the ratio of the total stochastic phase space area within a single square to the phase space crossing the separatrix on each step. Although both are exponentially small in the frequency ratio π/K_α, the ratio of these areas gives the simple result $n = \pi^2/4K_\alpha$. Using this we calculate the spreading from

$$L_{\mathrm{rms}} = L_{\mathrm{step}} T^{1/2}/(n\tau_{\mathrm{av}})^{1/2}, \tag{2}$$

where T is the number of iterations and τ_{av} is the average rotation period. This result gave excellent agreement with numerical calculations [6].

For a higher dimensional system we use as the model coupled pendula in which gravity is applied as a periodic delta function. For a single pendulum the resulting mapping equations are the well studied standard map [4, 5]. A convenient coupling for study is obtained by coupling the phases through a sinusoid, giving

$$\begin{aligned} I_{n+1} &= I_n + K_i \sin\theta_n + \mu \sin(\theta_n + \phi_n), \quad & \theta_{n+1} &= \theta_n + I_{n+1}, \\ J_{n+1} &= J_n + K_j \sin\phi_n + \mu \sin(\theta_n + \phi_n), \quad & \phi_{n+1} &= \phi_n + J_{n+1}. \end{aligned} \tag{3}$$

The phase space is now four dimensional. However, for small coupling, which we consider here, the phase space of two variables, over short times, looks very similar to the phase space of a single standard map, as shown in Fig. 3. However, over longer time periods an initial phase point within the stochastic region will explore the entire phase plane of Fig. 3. In particular, a phase point in the main stochastic web in J, ϕ, and on a rotational orbit in I, θ, will slowly Arnold-diffuse across the I-space. The global nature of this diffusion is shown in the I, J space in the surface of section $\theta = \phi = 0$, in Fig. 4. The shaded areas indicate the main resonance layers and the thinner lines indicate the positions of the secondary resonance layers. The diffusion along resonance layers is clearly seen.

The local diffusion rate along a main resonance layer can be calculated from the three resonance model [4, 5], giving

$$\Delta I_{\rm rms} = 4\mu Q_0 \exp(-\pi Q_0/2) n^{1/2} \tag{4}$$

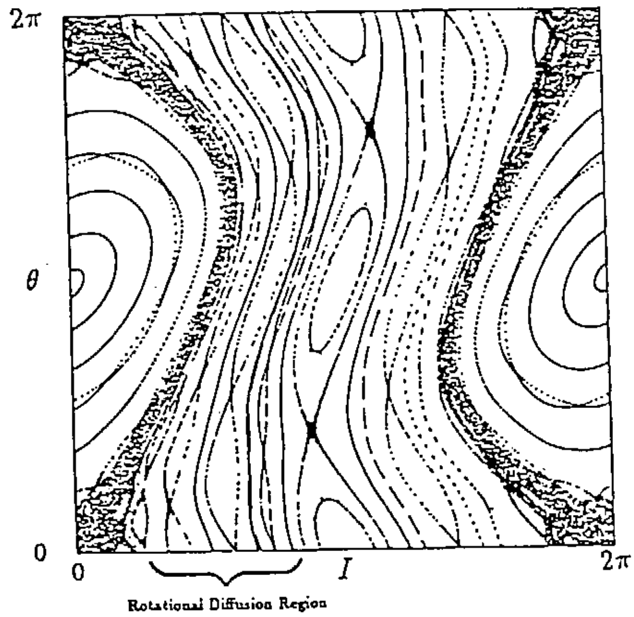

FIG. 3. The phase space of the standard map with $K = 0.8$ and small coupling.

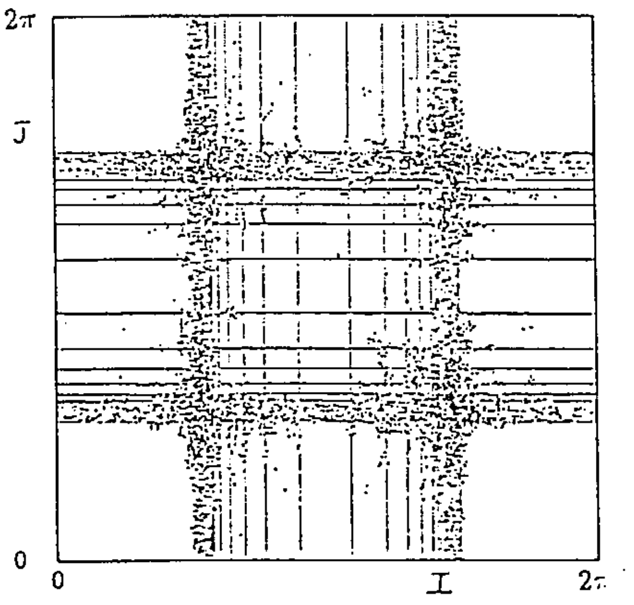

FIG. 4. Arnold diffusion in the I, J plane with $K_i = K_j = 0.8$ and $\mu = 0.003$ 1000 particles were run for two million iterations.

where $Q_0 = \omega_I/\omega_J \simeq I/K_j^{1/2}$. We note the exponentially slow nature of the diffusion. To calculate global diffusion we again make the ergodic assumption that the local stochastic phase space has a uniform density distribution. This is difficult to satisfy on intermediate time scales because of the slow diffusion through the secondary resonances. Nevertheless, it gives a reasonable first approximation to the diffusion. The global diffusion is then calculated by dividing the coupled phase space into the following regions:

1. **Primary Stochastic – stochastic:** particles are rapidly transported a distance in action equal to the width of the island chain around which the stochastic region lies, contributing to the diffusion with a very high diffusion rate. 2. **Primary Stochastic – librational:** the motion of particles averages to the fixed point as it librates around the island, removed from the global diffusion while in the region. 3. **Primary Stochastic – rotational:** particles Arnold diffuse slowly through both the regular and secondary stochastic layers. 4. **Regular – regular:** the phase space is inaccessible to particles which begin in a stochastic region.

Applying these properties to the relative amounts of phase space in each category the global diffusion is calculated. It is found to agree well, asymptotically, with the corresponding numerical determination of the diffusion [7].

In summary, the topology and diffusion rate through a stochastic web in two degrees of freedom is quite different from the Arnold diffusion in higher degrees of freedom. Nevertheless, the ergodic assumption of the uniformity of an equilibrium stochastic phase space of a Hamiltonian system can be applied to both systems to relate local to global diffusion. The results of the three degree coupled standard maps can be extended to higher degree coupled mappings Strong coupling can also be investigated numerically [8], but the results lose their straightforward interpretation from the three resonance model.

1. V. I. Arnold, *Russian Mathematics Surveys* **18,** 85 (1964).
2. C. F. F. Karney, *Phys. Fluids* **21,** 1584 (1978); **22,** 2188 (1979).
3. G. M. Zaslavskii, M. Yu Zakharov, R. Z. Sagdeev, D. A. Usikov, and A. A. Chernikov, *Zh. Eksp. Teor. Fiz.* **91,** 500 (1986) [*Sov. Phys. - JETP* **64,** 294 (1986)].
4. A. J. Lichtenberg and M. A. Lieberman, *Regular and Stochastic Motion* (Springer-Verlag, New York, 1983).
5. B. V. Chirikov, *Physics Reports* **52,** 263 (1979).
6. A. J. Lichtenberg and B. P. Wood, *Physical Review A* **39,** 2153 (1989).
7. B. P. Wood, A. J. Lichtenberg, and M. A. Lieberman, "Arnold Diffusion in Weakly Coupled Standard Maps," *Phys. Rev. A* (1990), in press.
8. K. Kaneko and T. Konishi, *Phys. Rev. A* **40,** 6130 (1989).

The work was collaborative with M. A. Lieberman and B. P. Wood. We acknowledge the support of ONR Grant N00014-84-K-0367 and NSF Grant ECS-8517364.

Formation and Dynamics of Solitary Waves and Vortices in Driven and Damped Systems

K.H. Spatschek, P. Heiermann, E.W. Laedke, V. Naulin, H. Pietsch
Heinrich-Heine-Universität Düsseldorf
D-4000 Düsseldorf, F.R.Germany

Abstract: In the first (introductory) part, near-integrable model equations which allow spatially coherent solutions with temporal chaos are reviewed. In the second (main) part, this contribution focusses on nonlinear drift waves. The adequate model equations in simple (density and temperature) inhomogeneous situations are presented. Without driving and damping, the stability of spatially coherent structures (monopoles, dipoles, etc.) are summarized. Also structural perturbations are included. The self-organization hypothesis is tested for two different situations. The formation of large-scale-structures on the one hand and of zonal flow on the other hand are discussed. In both cases, numerical simulations as well as analytical predictions are presented.

1. INTRODUCTION

During the last years, the solitary wave solutions of integrable nonlinear field equations experienced a *renaissance* because of the fact that they can play a decisive role also in non-integrable driven and damped systems. For example, more general nonlinear Schrödinger (NLS) equations (for higher space dimensions, or with non-cubic nonlinearity, or when damping and driving terms are incorporated) do not posses the integrability property but many interesting new phenomena can occur with spatially coherent soliton-like solutions playing an important role [1]. Let us just mention the paradigm of a perturbed NLS equation. As has been first demonstrated by Nozaki and Bekki [2], in the model for damped nonlinear Langmuir waves driven in a rf capacitor field,

$$iq_t + q_{xx} + 2|q|^2 q = -i\gamma q - iae^{i\omega t} , \tag{1}$$

the period-doubling route to temporal chaos can occur for phase-locked solitary waves. Analyzing (1), we can derive the existence condition for a phase-locked solitary wave as $2\gamma\omega^{1/2}/\pi a \ll 1$. The stability of this phase-locked solitary wave was investigated analytically [1]; at finite driving amplitudes a (for fixed damping rate γ and prescribed frequency ω) an instability in form of a Hopf bifurcation takes place and a regulary pulsating solitary wave appears. In a reduced phase space, the phase-locked solitary wave corresponds to a limit-cycle. With increasing values of driving amplitudes, the system undergoes a series of torus-doubling bifurcations for which the universal Feigenbaum constants $\delta_\infty = 4.6692...$ and $\alpha_\infty = 2.50291...$ could be recovered quite accurately. The situation changes when two space dimensions are taken into account. Then the collapsing solutions can be new attractors and analytical proofs exist for this behavior [3]. On the other hand, the whole scenario depends on the form of the "perturbations". If, e.g., we change from (1) to

$$iq_t + q_{xx} + |q|^2 q = -i\alpha q - \beta q - \gamma q^* \tag{2}$$

or

$$iq_t + q_{xx} + p|q|^2 q = 1 - xq \tag{3}$$

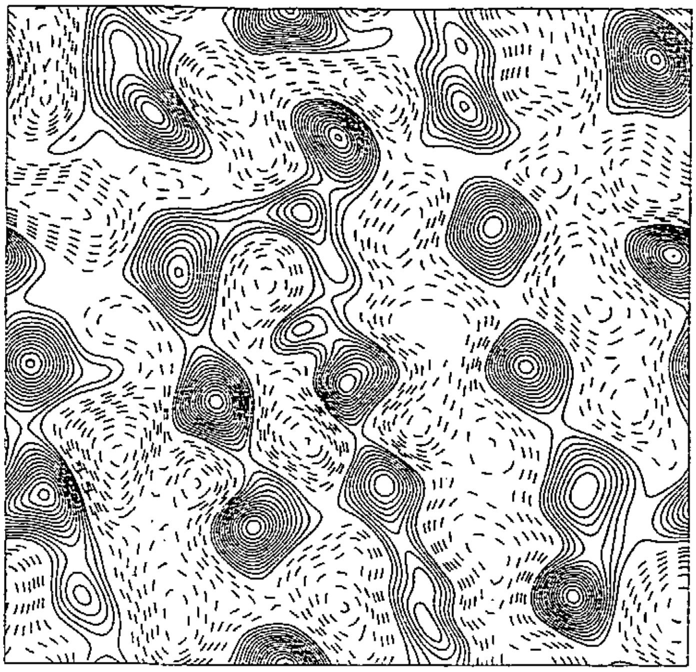

Fig.1 Contour plot of the potential ϕ in x,y-space at t=1200.

for nonlinear modulated cross-waves in Faraday resonance [4] or radiation in laser-irradiated inhomogeneous plasmas [5], we can find bifurcations in space or quasi-periodic soliton generation, respectively. These results clearly show that in any theoretical investigation the perturbation terms and the dimensionality should be carefully chosen when a close contact with experimental results is aimed for.

In this contribution we concentrate on new results for nonlinear drift waves; we directly use 2d models and include driving and damping selfconsistently in a similar way as Kono and Miyashita [6] did. Compared to the latter investigation we allow for density as well as temperature inhomogeneities and test the self-organisation hypothesis.

2. NONLINEAR COLLISIONAL DRIFT MODES

When dissipative and driving terms are ignored it is now straightforward to derive a generalized Hasegawa-Mima equation when both density and temperature inhomogeneities exist [7]. For vortices scaling on the ion Larmor radius at the electron temperature and weak density and temperature inhomogeneities the original Hasegawa-Mima equation [8] is the correct model. A different situation occurs when we look for vortices on a long scale compared with the ion Larmor radius. Then, by the multiple-scale technique, also a scalar nonlinearity appears. Collisional effects can be included in the same way as done by Kono and Miyashita. For the normalized potential ϕ we obtain the equation

$$\partial_t \left(1 - \nabla^2 - \tfrac{\kappa_n}{Dk_{\|}^2}\partial_y\right)\phi + \Big[-\kappa_n\partial_y + \tfrac{\kappa_n^2}{Dk_{\|}^2}\partial_y^2 \\ - (\delta\kappa_n\partial_y - \mu\nabla^2)\nabla^2\Big]\phi + \kappa_T\phi\partial_y\phi = \hat{z}\times\nabla\phi\cdot\nabla\nabla^2\phi\,, \qquad (4)$$

where κ_n and κ_T are the density and temperature inhomogeneity coefficients, respectively, and $D=\Omega_e/\nu_e$ characterizes the collisional contributions. For $D \to \infty$, $\delta=T_i/T_e=0$, $\mu=0$, and $\kappa_T=0$ the original Hasegawa-Mima model [8] appears. It has dipolar vortex solutions whose stability properties can be investigated. The dipolar vortices are structurally un-

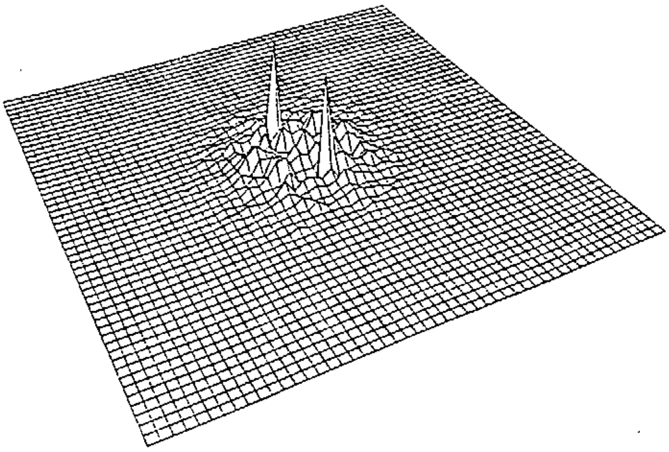

Fig.2 Fourier components corresponding to Fig.1 in k_x, k_y−space.

stable [7,9], whereas monopolar vortices (for $\kappa_T \neq 0$) are stable. The latter facts let us pose the questions: What will be the self-organized state of (4)? Can a zonal flow exist in drift-wave-turbulence? In answering these questions we have first confirmed the results of Kono and Miyashita for κ_T=0. A big dipolar vortex being the final state of the simulation is identified as the appropriate self-organized state; in this case no zonal flow exists. However, we should remember that for large-scale-structures the scalar nonlinearity cannot be ignored anymore. Simulation results of the full equation (4) [with one unstable mode as initial condition] show completely new results; see Figs.1 and 2. A zonal flow exists. Energy condensation occurs into small k_y- but finite k_x-values whereas the density can cascade to large k-values. As shown in Fig.3, a series of monopolar structures appears. It is very interesting to note that such a self-organization can already be observed in the dissipation-free case when one starts from the 2d KdV (ZK) equation including the vector nonlinearity as shown in Fig. 4.

Summarizing, for collisional drift waves a new self-organized state with zonal flow has been found. Spatially coherent structures are important in drift-wave-turbulence. The structural instability of dipolar vortices could be the reason for absence of dipolar vortices in plasma turbulence.

REFERENCES

[1] K.H. Spatschek, H.Pietsch, E.W. Laedke, and Th. Eickermann, in *Nonlinear World*, V.G. Baryakhtar et al. eds., Vol.2, p. 978 (World Scientific, Singapore 1990).

[2] K.Nozaki and N. Bekki, Physica D 21, 381 (1986).

[3] R. Blaha, E.A. Kuznetsov, E.W. Laedke, and K.H. Spatschek, in *Nonlinear World*, V.G. Baryakhtar et al. eds., Vol. 1, p. 10 (World Scientific, Singapore 1990).

[4] E.W. Laedke and K.H. Spatschek, J. Fluid Mech., in press.

[5] K.H. Spatschek, H. Pietsch, and E.W. Laedke, Europhys. Lett. 11, 625 (1990).

[6] M. Kono and E. Miyashita, Phys. Fluids 31, 326 (1988).

[7] K.H. Spatschek, E.W. Laedke, Chr. Marquardt, S. Musher, and H. Wenk, Phys. Rev. Lett. 64, 3027 (1990).

[8] A. Hasegawa and K. Mima, Phys. Fluids 21, 87 (1978).

[9] X. Su, W. Horton, P.J. Morrision, and V.P. Pavlenko, Institute for Fusion Studies Report ♯ 328, The University of Texas, Austin, Texas (1988).

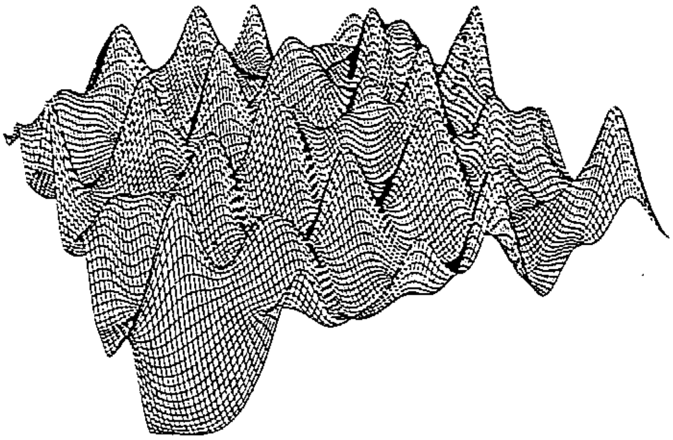

Fig.3 3d-plot of the potential ϕ at t=1200.

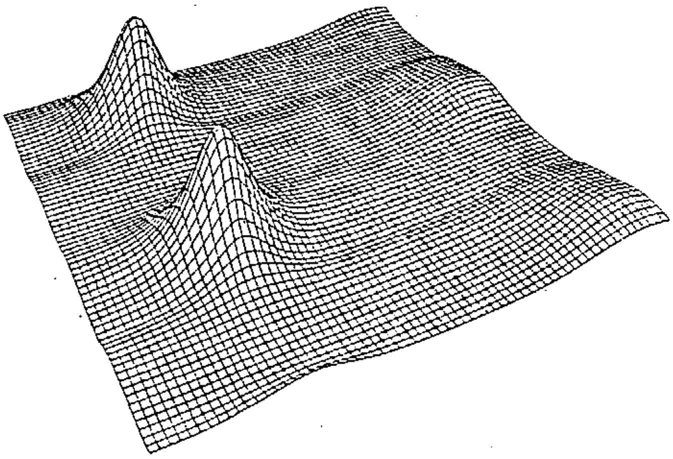

Fig.4 Monopoles as self-organized states of the modulational instability of the KdV-equation with vector nonlinearity.

SOLITONS AND CHAOS IN PLASAMA

Yoshi H ICHIKAWA
National Institute for Fusion Science
Nagoya, 464-01, Japan.

ABSTRACT

Plasma exhibits a full of variety of nonlinear phenomena. Active research in nonlinear plasma physics contributed to explore the concepts of soliton and chaos. Structure of soliton equations and dynamics of low dimensional Hamiltonian systems are discussed to emphasize the universality of these novel concepts in the wide branch of science and engineering.

1. Evolution of Fundamental Concepts in Plasma Physics

Plasma is a treasure land of instabilities$^{1)}$, which give rise to a full variety of nonlinear phenomena. Endeavor of plasma research during the past four decades may be best characterized as studies of collisionless plasma, i. e. physics of conservative systems. Here, I will speak on solitons and chaos in plasma as a summary report of what plasma physics contributed to advancement in the field of fundamental physics during the past half centuries.

When nuclear fusion reaction occurs in the high temperature plasma, species of the constituent particles change into other species and produced energy is carried away. Thus, we are confronted with dissipative systems, where such concept as strange attractors are coming to play key rolles.

2. Birth of Soliton and Quest for Chaos

Upon the introduction of high speed electronic computer in the early 1950's, as one of the research program in the Sherwoods Project, Fermi, Pasta and Ulam$^{2)}$ undertook numerical experiment to observe the equipartition of energy among the normal modes of one dimensional coupled system of anharmonic oscillators. On the contrary to their expectation, energy is not distributed over the entire mode of the system, but is shared among the lowest modes and after a finite time of elapse the system returns to the original state. This observation of the Fermi-Pasta-Ulam recurrence acted as a holy spring of the novel concepts of soliton and chaos.

Examining the long wave length behavior of the discrete coupled oscillator equation, Zabusky and Kruskal$^{3)}$ have reduced it to the K-dV equation, and numerically examined the collision processes of solitary wave solutions. In spite of its nonlinearity, two solitary waves retains their original form after the collision. Thus, they were led to propose to call the K-dV solitary wave as "soliton".

At the same time,the observation of Fermi-Pasta-Ulam recurrence phenomena renewed active interest to investigate the ergodic behavior of dynamical systems, and led us to examine "chaos" in the low dimensional nonlinear dynamical systems.

3. Inverse Scattering Transformation

The mysterious secret of K-dV soliton has been uncovered by the genius discovery of the inverse scattering transformation for the K-dV equation$^{4)}$. Subsequent extension of the method to the cubic nonlinear Schrodinger equation inspired Ablowitz et al.$^{5)}$ to formulate the 2 2 matrix representation of the inverse scattering transformation, which succeeded to unify the K-dV equation, the modified K-dV equation, the cubic nonlinear Schrodinger equation and the sine-Gordon equation as the completely integrable soliton equations. Generalizing the A-K-N-S scheme , we$^{6)}$ have shown that the superposition of A-K-N-S and K-N scheme valid for the generalized nonlinear Schrodinger equation and also derived the the new types of soliton equation such as

$$i\frac{\partial}{\partial t}q + \frac{\partial^2}{\partial x^2}\left\{\frac{q}{(1+|q|^2)^{1/2}}\right\} = 0 \qquad 1)$$

and

$$\frac{\partial}{\partial t}q + \frac{\partial^2}{\partial x^2}\left\{\frac{1}{(1+q^2)^{3/2}}\frac{\partial q}{\partial x}\right\} = 0 \qquad 2)$$

Extending eq.2), we$^{7)}$have studied propagation of a loop soliton along a string. El Naschie$^{8)}$,referring to the Euler elastica, noticed the close similarity of this soliton looping and buckling of compressed strut and emphasized that the study of elastic models will provide useful informations on the interaction between the integrable soliton and the non-integrable chaos.

4. Dynamics of Vortex Filament

As for the first type of WKI equation, eq.1), we have shown that the self induction equation for a thin vortex filament is reduced to a modified WKI equation. We obtained analytic soliton solutions[9] , which are in agreement with the numerical solutions given by Aref and Flinchem.[10]

5. Discretized Soliton Equations and Integrable Mapping

Although we have emphasized success of the analytical approach in the soliton theory, advancement of computational physics plays the key role in development of nonlinear science. In this regard, there have been extensive studies on the discretized soliton equations and the nonlinear differential-difference equations. Following the IST theory of the Toda lattice, Ablowitz and Ladik have presented the extensive theory to construct soliton solutions for various nonlinear differential-difference equations.[11] It would be worth to notice that Ross and Thompson[12]have discussed integrability of nonlinear mapping by examining several choices of dicretization of the nonlinear terms. Extending their approach, Quispel et al.[13] have been discussing relationship between the soliton equations and the integrable mappings.

6. Chaos in Low Dimensional Hamiltonian Systems

Having discussed a connection between the soliton equations and integrable mapping, we are now led to study non-integrable mapping in low dimensional Hamiltonian systems. Helleman[14] emphasized that mechanics is not in good shape,contrary to the preoccupation implanted through the present day physics course on classical mechanics. The most Hamiltonian systems are non-integrable, and many orbits exhibit sensitive dependence on the initial condition, (though their temporal evolution is deterministic). Hence, the chaotic behavior appears already in systems with only 2 or 3 degrees of freedom.

7. Concluding Remark

In the present discussion on soliton and chaos in plasma, I have tried to picturize the universality of the novel concept of soliton and chaos in dealing with nonlinear phenomena in science and engineering. With regards to the proper problems in plasma physics, I will refer to several investigators on interplay of soliton and chaos, such as on the process of chaotic emission of solitons in nonlinear inhomogeneous media[15]. Though these works are based on computational analysis, their observation provides us clear insight to develop strong plasma turbulence theory. Furthermore, I should mention that a number of experimental studies on chaos in plasma[16)-17)] awaits further investigation to explore the true understanding of the nonlinear phenomena in plasma.

REFERENCES

1. H. Haken ; *Advanced Synergetics* (Springer, 1983)
2. E. Fermi,J.Pasta and S. Ulam ; Studies of Nonlinear Problems, in *Collected Works of Enrico Fermi* (Univ. of Chicago Press, Chicago, 1965)
3. N.J.Zabusky and M.D.Kruskal; Phys. Rev. Lett. 15,(1965)240
4. C.S. Gardner, J. M. Greene, M. D. Kruskal and R. Miura ; Phys. Rev. Lett. 19, (1967) 1095
5. M.J. Ablowitz, D.J. Kaup, A.C. Newell and H. Segur ; Stud. Appl. Math.53,(1974) 249
6. M. Wadati,K. Konno and Y.H. Ichikawa ; J. Phys. Soc. Japan 47,(1979) 1968
7. K. Konno, Y.H. Ichikawa and M. Wadati ;J. Phys. Soc. Japan 50, (1981) 1025
8. M. S. El Naschie; ZAMM.Z. angew. Math. Mech. 69, (1989) T376
9. K. Konno, M. Mitsuhashi and Y. H. Ichikawa; Chaos, Solitons and Fractals, to be published
10. H. Aref and E. P. Flinchen, J. Fluid Mech. **148** (1984) 477
11. M.J. Ablowitz and J.F. Ladik; J. Math. Phys. 17, (1976) 1011
12. K.A. Ross and C.J. Thompson; Physica 135A, (1986) 551
13. C.R.W. Quispel, J.A.G. Robert and C.J. Thompson; Phys. Lett 126, (1988) 419, and Physica D 34, (1989) 183
14. R. H. G. Helleman, Self-generated Chaotic Behavior in Nonlinear Mechanics, in *Fundamental Problems in Statistical Mechanics* ed. E.G. D. Cohen (North Holland,1980)
15. W. Shyu, P.N. Guzdar, H.H. Chen, Y.C. Lee and C.S. Liu; Phys. Lett. A 147, (1990) 49
16. P.Y.Cheung,S.Donovan and A.Y.Wong; Phys. Rev. Lett.61, (1988) 1360
17. N. Ohno, M. Tanaka, A. Komori and Y. Kawai; J. Phys. Soc. Japan 58 (1989) 28

PROGRAM of SECOND INTERNATIONAL TOKI CONFERENCE on
PLASMA PHYSICS and CONTROLLED NUCLEAR FUSION

NONLINEAR PHENOMENA IN FUSION PLASMAS
— THEORY AND COMPUTER SIMULATION —

November 27 (Tuesday) – 30 (Friday), 1990
Toki-shi Bunka Plaza, Toki City, Japan

27 Tuesday	28 Wednesday	29 Thursday	30 Friday
9:00–10:30 Registration 10:30–11:00 Opening 11:00–12:00 Session I Keynote Lecture	9:00–12:00 Session III Transport (I)	9:00–10:30 Session VI Transport (II) 10:50–12:00 Session VII Space Plasmas	9:00–12:00 Session IX Tokamak
13:30–17:00 Session II MHD Relaxation	13:30–15:00 Session IV Helical Systems 15:20–17:00 Session V Laser Plasmas 18:30–20:30 Banquet at Wakamiya Kaikan	13:00–15:00 Session VIII Poster Session 15:00–17:00 Tour to New Toki Site Lectures for Public Audience	13:30–16:00 Session X Chaos · Soliton 16:00–16:20 Closing

PROGRAM of SECOND INTERNATIONAL TOKI CONFERENCE on PLASMA PHYSICS and CONTROLLED NUCLEAR FUSION

NONLINEAR PHENOMENA IN FUSION PLASMAS – THEORY AND COMPUTER SIMULATION –

November 27(Tuesday)-30(Friday), 1990
Toki-shi Bunka Plaza, TOKI City, Japan

Tuesday, November 27, 1990

9:00-10:30	Registration
10:30-11:00	Opening
Session I	**Keynote lecture** (Chairman: M.Okamoto)
11:00-12:00	Basic Transport and Other Processes in the Physics of Fusion Burning Plasmas B.Coppi (MIT)
12:00- 1:30	Lunch
Session II	**MHD Relaxation** (Chairman: R.White)
13:30-14:15	Self-Organizing Processes in Magnetically Confined Plasma T.Sato (NIFS)
14:15-14:45	Current Sheet Formation and Rapid Reconnection in the Solar Corona A.Bhattacharjee (Columbia Univ.)
14:45-15:15	Log-Stable Distribution of Energy Dissipation in Turbulence S.Kida (Kyoto Univ.)
15:15-15:35	Coffee Break
	(Chairman: J.A.Krommes)
15:35-16:05	Statistical Properties of Two-dimensional Magnetohydrodynamic Turbulence D.Biskamp (Max Plank Inst.)
16:05-16:35	Subgrid-Scale Modeling of Magnetohydrodynamic Turbulence A.Yoshizawa (Tokyo Univ.)

Wednesday, November 28, 1990

Session III	**Transport I** (Chairman: A.J.Lichtenberg)
9:00- 9:40	Hybrid Fluid/Kinetic Descriptions of Tokamak Plasmas J.D.Callen (Univ. of Wisconsin)
9:40-10:20	The Theory of Turbulence and Anomalous Transport in Plasmas: Past, Present, and Future J.A.Krommes (PPPL)
10:20-10:40	Coffee Break
	(Chairman: S. Yoshikawa)
10:40-11:05	Ion Temperature Gradient Turbulence and Coherent Structures D.Choi (Korea Advanced Inst.)
11:05-11:30	Three-Dimensional Particle Simulation of Trapped Electron Instabilities in Tokamaks C.Z.Cheng (Princeton Univ.)
11:30-12:00	Studies of Anomalous Transport Driven by G and η i modes in Heliotron/Torsatron M.Wakatani (Kyoto Univ.)
12:00-13:30	Lunch
Session IV	**Helical Plasmas** (Chairman: M.Wakatani)
13:30-14:00	Optimization, MHD-Mode, and α-Particle Confinement Behaviour of Helias Equilibria J.Nuhrenberg (Max Planck Inst.)
14:00-14:25	Equilibrium Beta Limit of Helical Systems and Suppression of Magnetic Surface Breaking T.Hayashi (NIFS)
14:25-14:40	Suppression and Control of Magnetic Islands in Toroidal Plasmas A.Bhattacharjee (Columbia Univ.)
14:40-15:00	Theoretical Studies of Nonlinear Sheath Dynamics J.K.Lee (POSTECH)
15:00-15:20	Coffee Break

Session V **Laser Plasmas** (Chairman: K.Nishikawa)

15:20-16:00 Hydrodynamic Instabilities in Laser Driven Implosion
K.Mima (Osaka Univ.)

16:00-16:30 Solitons and Chaos in Laser-Plasma Interaction
C.S.Liu (Univ. of Maryland)

16:30-17:00 Nonlinear Evolution of 2D and 3D Rayleigh-Taylor Instability at Stagnation Phase in Laser Implosion
K.Nishihara (Osaka Univ.)

18:30-20:30 Banquet (Wakamiya-Kaikan)

Thursday, November 29, 1990

Session VI **Transport II** (Chairman: J.A.Wesson)

9:00- 9:40 Models for Transport in Configuration with Destroyed Magnetic Surfaces
G.Laval (Ecole Polytechnique)

9:40-10:05 Issues in Direct Numerical Simulation of Plasma Turbulence and Transport
A.Thyagaraja (Culham Lab.)

10:05-10:30 Anomalous Electron Thermal Diffusivity and Particle Pinch Due to Short Wavelength Electromagnetic Toroidal Drift Mode
A.Hirose (Univ. of Saskatchewan)

10:30-10:50 Coffee Break

Session VII **Space Plasmas** (Chairman: P.K.Kaw)

10:50-11:20 Magnetohydrodynamical Formation of Astrophysical Jets from Gravitationally Collapsing Objects
Y.Uchida (Univ. of Tokyo)

11:20-11:40 Computer Simulation of Solar Wind-Magnetosphere Interaction
K.Watanabe (NIFS)

11:40-12:00 Rapid Acceleration of Protons in a Nonlinear Magnetosonic Wave
K.Ohsawa (Nagoya Univ.)

12:00-13:00 Lunch

Session VIII **Poster Session**

13:00-15:00

1 Effect of Pressure on Mode Transition Point of Partially Relaxed States with Peripheral Loss
Y. Kondoh (Gunma Univ.)

2 Relaxed State and Entropy Production
T. Kato (Waseda Univ.)

3 Simulation Study of MHD Relaxation and Reconnection Processes
K.Kusano (Hiroshima Univ.)

4 Finite β Equilibrium for A Pressure Configuration
S. Kajita (Gifu Univ.)

5 Application of 'Mathematica' to Energy Principle
T. Yamagishi (Fukui Inst. of Technology)

6 Direct Ion Heating in MHD Relaxation
Z. Yoshida (Univ. of Tokyo)

7 Structure of Outer-Heliosphere
H. Washimi (Nagoya Univ.)

8 Self-Similar Evolution of Nonlinear Magnetic Buoyancy Instability
K. Shibata (Aichi Univ.)

9 Turbulent Mixing due to Rayleigh-Taylor Instabilities in Laser Driver Implosion
H. Takabe (Osaka Univ.)

10 Particle Simulation of the Toroidal Plasma
M. LeBrun (Univ. of Texas)

11 Internal Kink Mode Simulation by 3-D Gyrokinetic Code
H. Naitou (Yamaguchi Univ.)

12 Particle Simulation Study on the Tilt Stabilization of the FRC Plasma
R. Horiuchi (NIFS)

13 3-D Macroscale Electromagnetic Particle Simulation of Inhomogeneous, Magnetized Plasmas
M. Tanaka (NIFS)

14 Study of Kink Instability by Three Dimensional Macroscale Particle Simulation
H. Takamaru (NIFS(Hiroshima Univ.))

15 Nonadiabatic Behavior of the Magnetic Moment of a Charged Particle in a Dipole Magnetic Field
S. Murakami (NIFS(Hiroshima Univ.))

16 Sheared Electric Field Effects on the Resistive
Pressure-Gradient-Driven Turbulence
L. Garcia (Fisica Teorica)

17 Numerical Study of Ion Temperature Gradient Modes in a Tokamak
M. Yagi (JAERI)

18 Nonlinear Behavior and Transport Property of Multiple-Helicity
Resistive Interchange Modes
H. Sugama (NIFS)

19 Nonlinear Computer Analysis of a Backward Wave Oscillator
T. Watanabe (NIFS)

20 Mode Conversion of Alfven Waves Induced by Quadrupole
Magnetic Field Modulation
H. Hojo (Univ. of Tsukuba)

21 Numerical Simulation of Potential-Driven Ion Cyclotron
Oscillation
S. Ishiguro (Tohoku Univ.)

22 Dynamics of Interfaces with Internal Structures
T. Kawakatsu (Kyushu Univ.)

23 Nonlinear Equations for weakly unstable modes
N. Nakajima (NIFS)

24 Hole Dynamics of One-Dimensional Plasma
K. Kitahara (Tokyo Institute of Tech.)

25 Shock and Soliton Structures Induced by Poloidal Flow in Tokamaks
T. Taniuti (Chubu Univ.)

26 Soliton Phenomena in Electron Beam Plasma
T. Yajima (Univ. of Tokyo)

27 Point Vortex Model of Modons
C. Matsuoka (Nagoya Univ.)

28 Structure of Magnetic Field Lines in the Helical Torus
T. Hatori (NIFS)

29 Regular Motion and Symmetry in the Relativistic Standard Map
Y. Nomura (NIFS)

30 Relaxation and Diffusion in Hamiltonian Chaos
T. Konishi (Nagoya Univ.)

15:00-15:30	Coffee Break
15:30-17:30	Tour to New Toki Site
15:00-17:00	Lectures for Public Audience

Friday, November 30, 1990

Session IX	**Tokamak** (Chairman: J.D.Callen)
9:00- 9:40	Non-Linear Behaviour in Tokamaks J.A.Wesson (JET)
9:40-10:10	Fluctuation Spectrum of Ion Temperature Gradient Driven Mode: in Sheared Magnetic Fields T. Tuda (JAERI)
10:10-10:40	Equilibria and Dynamics of Temperature in a Fusion Reactor Plasma H.Wilhelmsson (Univ. of Technology)
10:40-11:00	Coffee Break
	(Chairman: G.Laval)
11:00-11:35	Model for Marfe-Detached Plasma Transition in Tokamak P.K.Kaw (Inst. for Plasma Research)
11:35-12:00	Propagations of Drift Waves in Toroidal Plasma Systems S. Yoshikawa(PPPL)
12:00-12:30	Energy confinement as nonlinear coupling of macroscopic motion with transport processes Huo Yu-ping (ASIPP)
12:30-13:30	Lunch
Session X	**Chaos-Soliton** (Chairman: C.S.Liu)
13:30-14:10	Dynamical Networks of Nonlinear Systems R.White (Princeton Univ.)
14:10-14:50	Diffusion Through Stochastic Webs in Two and More Dimensions A.J.Lichtenberg (UC Berkeley)
14:50-15:10	Coffee Break
	(Chairman: K.Mima)
15:10-15:40	Formation and Dynamics of Solitary Waves and Vortices in Driven and Damped Systems K.H.Spatschek (Universitat Dusseldorf)
15:40-16:00	Solitons and Chaos in Plasma Y.Ichikawa (NIFS)
16:00-16:20	Closing

LIST OF PARTICIPANTS

A. Hirose	Plasma Physics Lab. University of Saskatchewan Department of Physics Saskatoon, Saskatchewan S7N 0W0 Canada
G. Laval	Centre de Physique Theorique Ecole Polytechnique 91128 Palaiseau Cedex France
D. Biskamp Jurgen Nuhrenberg	Max-Planck-Institut fur Plasmaphysik D-8046 Garching bei Munchen F. R. G.
Sh. M. Khalil	Institute for plasma physics forschungszentrum Julich GMBH Postfach 1913-D-5170 Julich F. R. G.
K. H. Spatschek	Universitat Dusseldorf Institut fur Theoretische Physik I Universitatsstr.1, D-4000 Dusseldorf 1 F. R. G.
P. K. Kaw	Institute for Plasma Reserch Bhat Gandhinagar,382424 India
D. I. Choi	Korea Advanced Inst. of Science & Technology P.O.Box 150 Chongyang, Seoul Korea
Jae Koo Lee	POSTECH PO Box 125, Pohang, Kyungbuk 790-600 Korea
Huo Yu-ping	Director Institute of Plasma Physics Academia Sinica Hefei China

L. Garcia	Dpto. Fisica Teorica : Facultad cc. Fisicas Universidad Complutense 28040 Madrid Spain
H. Wilhelmsson	Institute for Electromagnetic Field Theory and Plasma Physics Chalmers University of Technology S-41262 Goteborg Sweden
J. Wesson	JET Undertaking Abingdon Oxfordshire OX14 3EA U. K.
A. Thyagaraja	Theory Division AEA Fusion Culham Laboratory Abingdon, Oxon, OX14 3DB U. K.
B. Coppi	Department of Physics Massachusetts Institute of Technology Cambridge Massachusetts 02139 U. S. A.
C. Z. Cheng John A. Krommes R. White S. Yoshikawa	Plasma Physics Laboratory Princeton University P.O. Box 451 Princeton, NJ 08543 U. S. A.
A. Bhattacharjee	Columbia University Dept. of Applied Physics New York, N.Y. 10027 U. S. A.
J. D. Callen	Kerst Professor of Nuclear Engineering and Engineering Physics and Physics University of Wisconsin 1500, Johnson Drive Madison, WI 53706-1687

	U. S. A.
M. LeBrun	Institute for Fusion Study University of Texas Austin, Texas 78712 U. S. A.
A. J. Lichtenberg	University of California Elect. Engr. & Computer Science Dept. Berkeley, CA 94720 U. S. A.
C. S. Liu	Dept. of Physics University of Maryland College park, MD 20742 U. S. A.
S. Ishiguro	Faculty of Engineering Tohoku University Aramaki, Aoba, Aoba-ku, Sendai, Japan
K. Tani T. Tuda M. Yagi	Japan Atomic Energy Research Institute 801-1 Mukoyama, Naka-machi, Nakagun, Ibaraki, Japan
H. Hojo	Plasma Research Center University of Tsukuba 1-1-1 Tenodai, Tsukuba, Ibaraki, Japan
T. Honzawa	Faculty of Engineering Utsunomiya University 2753 Ishii-cho, Utsunomiya, Japan
Y. Kondoh	Faculty of Engineering Gunma University 1-5-1 Tenjin-cho, Kiryu, Gunma, Japan
K. Minami	Faculty of Engineering Niigata University 2-8050 Igarashi, Niigata, Japan
M. Ali K. Ogura	Graduate School of Science and Technology Niigata University 2-8050 Igarashi, Niigata, Japan

N. Ishibashi K. Kitahara K. Tanno	Faculty of Science Tokyo Institute of Tech. 2-12-1 Oh-okayama, Meguro-ku, Japan
A. Yoshizawa	Institute of Industrial Science University of Tokyo 7-22-1, Roppongi, Minato-ku, Tokyo 106, Japan
Y. Uchida	Faculty of Science University of Tokyo 7-3-1 Hongoh, Bunkyo-ku, Tokyo 113, Japan
S. Kaneko M. Taguchi T. Yajima Z. Yoshida	Faculty of Engineering University of Tokyo 7-3-1 Hongoh, Bunkyo-ku, Tokyo 113, Japan
Y. Hirano	Electrotechnical Latboratory 1-14 Umezono, Tsukuba, Ibaraki 305, Japan
T. Kato	School of Science and Engineering Waseda University 3-4-1 Ohkubo, Shinjyuku-ku, Tokyo 169, Japan
T. Taniuti	College of Engineering Chubu University 1200 Matsumoto-cho, Kasugai, Aichi 487, Japan
K. Shibata	Aichi University of Education 1 Hirosawa, Igatani, Kariya, Aichi 448, Japan
K. Ohsawa Y. Terashima	Plasma Science Center Nagoya University Furo-cho, Chikusa-ku, Nagoya 464-01, Japan
T. Konishi C. Matsuoka	Faculty of Science Nagoya University Furo-cho, Chikusa-ku, Nagoya 464-01, Japan
T. Tsukishima	Faculty of Engineering Nagoya University Furo-cho, Chikusa-ku, Nagoya 464-01, Japan
H. Washimi	Solar-Terrestrial Environment Laboratory Nagoya University

	3-13 Honohara, Toyokawa, Aichi 442, Japan
S. Okamoto K. Fukui S. Kajita K. Maekawa	Engineering Department Gifu University 1-1 Yanagito, Gifu 501-11, Japan
T. Yamagishi	Faculty of Engineering Fukui Institute of Technology 3-6-1 Gakuen, Fukui 910, Japan
S. Kida	Research Institute for Mathematical Sciences Kyoto University Kitashirakawa-oiwake-cho, Sakyo-ku, Kyoto, Japan
K. Hanatani K. Ichiguchi K. Nagasaki Y. Nakamura M. Wakatani K. Watanabe	Plasma Physics Laboratory Kyoto University Gojasho, Uji 611, Japan
S. Masamune	Faculty of Engineering and Design Kyoto Institute of Technology Matsugasaki, Sakyo-ku, Kyoto 606, Japan
K. Mima K. Nishihara H. Takabe	Institute of Laser Engineering Osaka University 2-6 Yamadaoka, Suita, Osaka 565, Japan
J. Mizushima	Faculty of Education Wakayama University 930 Sakaetani, Wakayama 640, Japan
J. Fukuyama	School of Engineering Okayama University 3-1-1 Tsushimanaka, Okayama 700, Japan
G. Gnudi K. Kusano K. Nishikawa	Faculty of Science Hiroshima University 1-1-89 Higashisenda-cho, Naka-ku, Hiroshima 730, Japan
T. Tamaru	Hiroshima Institute of Technology 2-1-1 Miyake, Saeki-ku, Hiroshima 731-51, Japan
H. Naitou	Faculty of Engineering

	Yamaguchi University 2557 Tokiwadai, Ube, Yamaguchi 755, Japan
T. Kawakatsu M. Nambu	Faculty of Science Kyushu University 6-10-1 Hakozaki, Higashi-ku, Fukuoka 812 Japan
H. Sakagami	Institute for Supercomputing Research 1-13-1 kachidoki, Chuuoh-ku, Tokyo 104, Japan
H. Fujita M. Miura T. Morikawa K. Saka K. Tsujiyama T. Tsukamoto	Mitsubishi Electric Corporation 3-18-2 Meieki, Nakamura-ku, Nagoya 450, Japan
N. Asami	Mitsubishi Heavy Industries, Ltd. 10 Ooe-cho, Minato-ku, Nagoya 455, Japan
Iwai M. Nishikawa	Mitusbishi Atomic Power Industries, Inc. 2-4-1 Shiba-koen, Minatoku, Tokyo 105, Japan
Kakizawa Y. Sawada	Power & Fusion Technology Development Dept. Toshiba Corporation 1-1-6 Uchisaiwai-cho, Chiyoda-ku, Tokyo 100, Japan
S. Suzuki	The Chubu Electric Power Co., Inc. 1 Toshin-cho, Higashi-ku, Nagoya 461, Japan
Y. Tarumoto	The Kansai Electric Power Co., Inc. 3-3-22 Nakanoshima, Kita-ku, Osaka 530, Japan
T. Inoue E. Kurihara	Kurihara Industry Corp. 1-1-2 Sonezaki, Kita-ku, Osaka, Japan

T. Amano
Y. Hamada
R. Horiuchi
T. Kamimura
K. Masai
Y. Mizuno
Y. Nomura
H. Sanuki
M. Tanaka
J. Fujita
T. Hatori
Y. Ichikawa
T. Kawamura
O. Motojima
N. Nakajima
H. Obayashi
T. Sato
K. Toi
M. Fujiwara
T. Hayashi
A. Iiyoshi
T. Kuroda
A. Miyahara
C. Namba
M. Okamoto
H. Sugama
K. Watanabe

T. Watanabe
A. Kageyama
A. Takei

T. Watari
S. Murakami
A. Usadi

J. Yamamoto
H. Takamaru

National Institute for Fusion Science
Furo-cho, Chikusa-ku, Nagoya 464-01, Japan

Recent Issues of NIFS-PROC Series

NIFS PROC-1	*U.S.-Japan Workshop on Comparison of Theoretical and Experimental Transport in Toroidal Systems Oct. 23-27, 1989* ; Mar. 1990
NIFS-PROC-2	*Structures in Confined Plasmas –Proceedings of Workshop of US-Japan Joint Institute for Fusion Theory Program–* ; Mar. 1990
NIFS-PROC-3	*Proceedings of the First International Toki Conference on Plasma Physics and Controlled Nuclear Fusion –Next Generation Experiments in Helical Systems– Dec. 4-7, 1989* ; Mar. 1990
NIFS-PROC-4	*Plasma Spectroscopy and Atomic Processes –Proceedings of the Workshop at Data & Planning Center in NIFS–*; Sep. 1990
NIFS-PROC-5	*Symposium on Development of Intensed Pulsed Particle Beams and Its Applications*; Oct. 1990